Stiffened aluminium plates subjected to impact loading

by

Hilde Giæver Hildrum

Dr ing. thesis

Department of Structural Engineering
Norwegian University of Science and Technology
N-7491 Trondheim
Norway

June 2002

URN:NBN:no-3315

URN:NBN:no-3315

Abstract

An experimental investigation has been carried out to study the behaviour of stiffened aluminium plates subjected to large mass (55 kg) projectiles in the low velocity regime. The stiffened aluminium plates were fabricated from aluminium alloy AA6082 temper T6 extrusions MIG-welded together to form flat stiffened plates. The study was made on the variation of failure mode and the energy-absorbing capacity with various combinations of projectile nose shape (blunt and hemispherical) and load application point (between two stiffeners, on a stiffener and next to a stiffener).

The estimated incipient fracture velocity (giving cracks in the target) was significant less for the hemispherical ended nose than the blunt ended nose. The impact between the stiffeners gave lowest incipient fracture velocity followed by impact next to the stiffener and impact on a stiffener in that order. The estimated ballistic limit velocity was almost equal for impact between two stiffeners using both nose shapes and for impact next to a stiffener with the blunt ended projectile. The hemispherical ended projectile impacting next to a stiffener lead to significant higher ballistic limit.

The observed differences in the ballistic limit velocity and incipient fracture velocity were mainly attributed to the change in failure mode (and energy absorption). The blunt projectile caused failure by plugging, while petaling failure modes were observed for impact with a hemispherical ended projectile.

In addition to impact tests, static punch tests were carried out to study any possible relationship between the dynamic and quasi-static capacities before fracture occurs. In the studied velocity range and for the blunt ended projectile, it seems that the static tests may give a conservative estimate of the incipient fracture impact energy. For the hemispherical ended projectile this method may lead to non-conservative results.

A metallurgical examination of cross sections of the target at the impact point was carried out to reveal details of internal changes of configuration such as deformations and changes of microstructure, and the generation of fractures. The fracture was initiated on the rear side impacting next to a stiffener or between the stiffeners (on the weld) with both nose shapes. Ductile fracture was observed in all test specimens except for fracture in the welds. No evidence of temperature effects and no pronounced shear localisation through the thickness of the plate were seen.

Numerical simulation of perforation of a stiffened plate impacted with a hemispherical ended projectile between two stiffeners (on the weld) has been performed using the non-linear finite element code LS-DYNA. Inverse modelling of tensile test specimens was performed to identify the material parameters. The weld and heat affected zone were modelled with reduced strength compared to the parent material. The main objective with these numerical simulations was to study whether the Lemaitre damage material model could predict the response of the impacted plate when taking failure into account. The numerical simulation described the maximum force quite well. Furthermore, the model predicts the instability phenomenon and fracture process as observed in the experiments reasonably well.

URN:NBN:no-3315

URN:NBN:no-3315

Acknowledgements

The author would like to express her deep gratitude to Professor Kjell Arne Malo and Professor Magnus Langseth, Department of Structural Engineering, NTNU, for their initiation and supervision of this study, for their continuos support and engagement in the project as well as several proposals for improvements of the original manuscript.

My fellow Dr ing. students and colleagues at "Stålhjørnet" (the steel and aluminium research group at the department) merit special appreciation for creating an inspiring working environment. The assistance from Dr Torodd Berstad and Dr Odd-Geir Lademo during the numerical work is greatly appreciated. Dr Arild H. Clausen is acknowledged for his helpful comments on the manuscript.

The experimental work has been carried out in the laboratories at Department of Structural Engineering, NTNU. The assistance of the laboratory staff and particular Mr Olav Haldorsen, Mr Hans Tømmervold, and Mr Øystein Langnes are acknowledged. Special credits are given to Mr Trygve Meltzer for assisting with the laboratory experiments and for checking the English language. Credits also go to Mr Eirik Fyhn and Ms Randi Sæther at the Faculty of Engineering Science and Technology, NTNU, for preparing the drawings.

In connection with the metallurgical investigations, I acknowledge the fruitful and instructive collaboration with Mr John Rasmus Leinum, Department of Materials Technology and Electro Chemistry, NTNU. The advice on the same section and the English editing support from Professor Walter Milligan, Department of Materials Science and Engineering, Michigan Technological University is acknowledged.

This research was made possible by financial support by Norwegian Defence Estate Agency and the NORLIGHT project: Capacity of Multistiffened Aluminium Plates financed by The Research Council of Norway and Hydro Aluminium. This support is gratefully acknowledged. Hydro Marine Aluminium AS has contributed with the material used in the experimental tests.

Finally, I would like to thank my husband Knut for his support, encouragement and patience throughout these years, and our daughter Marie for her impatience, which has kept me in touch with the part of life that is most important. The support from the rest of my family has been appreciated throughout this exciting and challenging period.

URN:NBN:no-3315

Notation

Notations and symbols are defined in the text where they first occur. The symbols and their meaning are listed below:

A_0	initial cross section
C_i	hardening parameters, $i = 1, 2$
d	diameter of the punch
D	isotropic damage variable
D_C	critical damage
$\dot{D}$	evolution of damage
e	nominal strain
e_l	nominal strain in longitudinal direction
e_w	nominal strain in transverse direction
E	Young's modulus
f	yield function
F	force
F_d	dynamic interface force between the projectile and the plate
F_{dc}	critical dynamic interface force
F_{dm}	maximum dynamic interface force
F_{du}	dynamic interface force at incipient fracture
F_s	static interface force between the punch and the plate
F_{su}	maximum force at incipient fracture
g	acceleration of gravity
l	gauge length
l_0	initial gauge length
L_1	= 200.2 mm, distance between the two photocells
L_2	= 100 mm, distance from the lower photocell to the test specimen
m	projectile mass below the strain gauges
m_1	projectile mass below the strain gauges, blunt nose
m_2	projectile mass below the strain gauges, hemispherical nose
M	projectile mass above the strain gauges
M_p	total mass of projectile
P	measured force in the projectile at the location of strain gauges
Q_i	hardening parameters, $i = 1, 2$
r	damage accumulated plastic strain
$\dot{r}$	ratio of damage accumulated plastic strain
r_D	strain threshold for damage initiation
R	ratio of plastic strain

R^*	isotropic strain hardening variable
s	nominal stress
S	positive material constant
T_p	impact energy, kinetic energy of projectile at impact
T_{pc}	critical impact energy
T_{pu}	incipient fracture energy, impact energy at incipient fracture
t	time
t_l	measured time
t_d	duration of impact
t_{tot}	fictive time period
U_{du}	calculated dynamic strain energy absorbed by the target at maximum force
U_{dm}	calculated maximum dynamic strain energy absorbed by the target
U_{su}	critical static strain energy at maximum force
v	velocity of projectile
v_l	velocity of projectile at the lower photocell
v^*	prescribed velocity of pins
v_i	impact velocity of projectile
v_{ic}	ballistic limit velocity (critical impact velocity of projectile)
v_{iu}	incipient fracture velocity, impact velocity of projectile at incipient fracture
v_r	residual velocity, projectile velocity immediately after impact, when the interface force is zero
w	displacement of projectile
$\ddot{w}$	acceleration of projectile
w_c	centre displacement of projectile/punch
w_{cd}	calculated centre displacement of projectile at the instant when the force is first reduced to zero
w_{cm}	maximum centre displacement of punch at incipient fracture
w_{cp}	permanent centre displacement of plate
w_{cu}	calculated displacement of projectile at maximum force
w_p	permanent displacement of plate
Y	strain energy density release rate
ε_f	rupture strain
ε_l	true longitudinal strain
ε_l^p	plastic strain in longitudinal direction
ε_t^p	plastic strain in thickness direction
ε_u	$=\varepsilon(\sigma_u)$ strain at ultimate stress
ε_w	true transverse strain
ε_w^p	plastic strain in transverse direction
ν	Poisson's ratio
σ	true stress
σ_0	proportionality limit

$\sigma_{0.2}$	$=\sigma(\varepsilon_1^p = 0.002)$ true stress at 0.2% permanent strain (proof stress)
σ_{eq}	von Mises equivalent stress
σ_u	ultimate stress
σ_Y	Yield strength in uniaxial tension
$\dot{\lambda}$	plastic multiplier
$\mathbf{C}$	fourth order tensor of elastic moduli
$\boldsymbol{\varepsilon}$	strain tensor
$\boldsymbol{\varepsilon}^e$	elastic strain tensor
$\boldsymbol{\varepsilon}^p$	plastic strain tensor
$\dot{\boldsymbol{\varepsilon}}^p$	ratio of plastic strain tensor
$\boldsymbol{\sigma}$	stress tensor
$\tilde{\boldsymbol{\sigma}}$	effective stress tensor
$\boldsymbol{\sigma}^D$	deviatoric stress tensor

URN:NBN:no-3315

Table of Contents

1 Introduction

1.1 Background

Plated components are a very common structural element in load-carrying structures, and the loading is basically in the plane of the plate. For many structures such as offshore platforms, ships, bridges and containers, reinforcements in terms of stiffening elements are very often required. For the optimisation of such structures the geometry is of primary interest, but the material choice can also be of crucial importance. Aluminium alloys have many properties that make them competitive with other materials. The development of fabrication processes, especially the extrusion process, has given large freedom to the designing engineers. In general, aluminium has advantages in applications where low self-weight, high corrosion resistance, high-energy absorption and low manufacturing costs play important roles.

The cost and weight benefits that may be achieved utilising aluminium alloys in offshore structures have become well known. Some of the recent projects are the living quarters of the Visund, Snorre A, Oseberg Øst, Troll C and Snorre B platforms in the North Sea. The Oseberg Sør platform's living quarter produced in aluminium is shown in Figure 1. Here, aluminium is used in both the walls and decks, mainly as panels made from extrusions with integrated stiffeners. The most common structural aluminium alloy is AA6082, due to its

Figure 1 *The living quarter of the Oseberg Sør platform (courtesy of Hydro Marine Aluminium AS).*

combination of high strength and resistance to corrosion, and the availability of various sections in both extruded profiles and plates. In the living quarters, built in aluminium, some stairways in steel are always used as the main escape routes. This is due to the fact that aluminium suffers from rapid strength degradation at elevated temperatures that may occur in case of accidental fires. Another use of aluminium is in helicopter decks, see illustrations in Figure 2.

In the transportation sector, i.e. trains, sea vessels, as well as the automotive and aerospace industries, low weight is essential. For high-speed boats and marine vessels stiffened aluminium plates are used in the hull and superstructure. Figure 3b shows the fabrication of friction stir welded aluminium panels used in the hull of the high speed boat Flying Cat (Figure 3a). Similar panels were also used in decks, sides and bulkheads in the Flying Cat. In addition, aluminium panels are used in applications such as containers, protection structures, offshore hatches above and below sea level, and occasionally in bridge decks.

a)

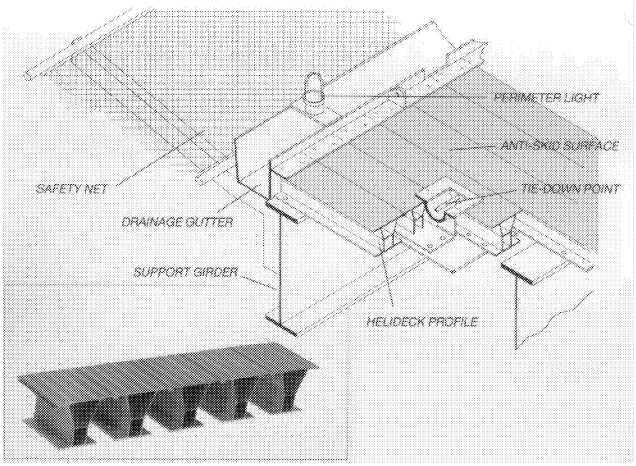

b)

Figure 2 *a) A helicopter deck in aluminium, and b) the view of the structure and the cross-section of the deck profiles (courtesy of Hydro Marine Aluminium AS).*

In addition to the obvious check of the structures in the serviceability, fatigue failure and ultimate limit states, structures such as offshore modules and mobile structures must be controlled in the progressive collapse limit state. Accidental loads on offshore platforms such as explosions and impact loads have to be considered in the design process (Norwegian Petroleum Directorate 1994).

Ships have to be designed against accidental loadings such as collision and grounding accidents. Furthermore, the increase of the number of fast marine passenger vessels has lead to increasing interest in the consequences of vessel collisions with floating objects (Simonsen and Lauridsen 2000). If the structure is in aluminium, the hull may consist of stiffened plates where the welding of the stiffeners introduces soft zones. The consequence of welds on the structural behaviour of stiffened plates has to be taken into account in the design process.

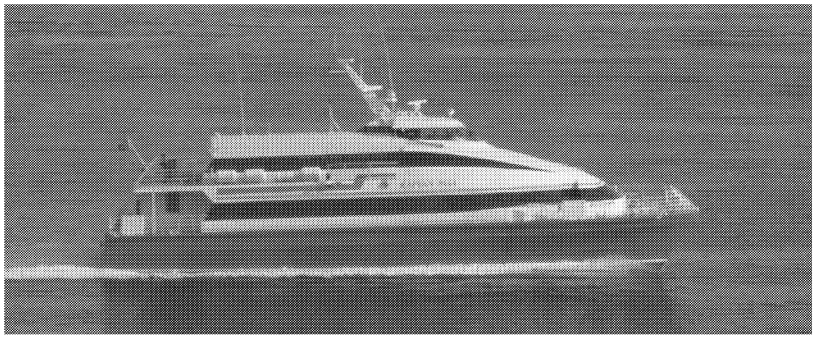

a)

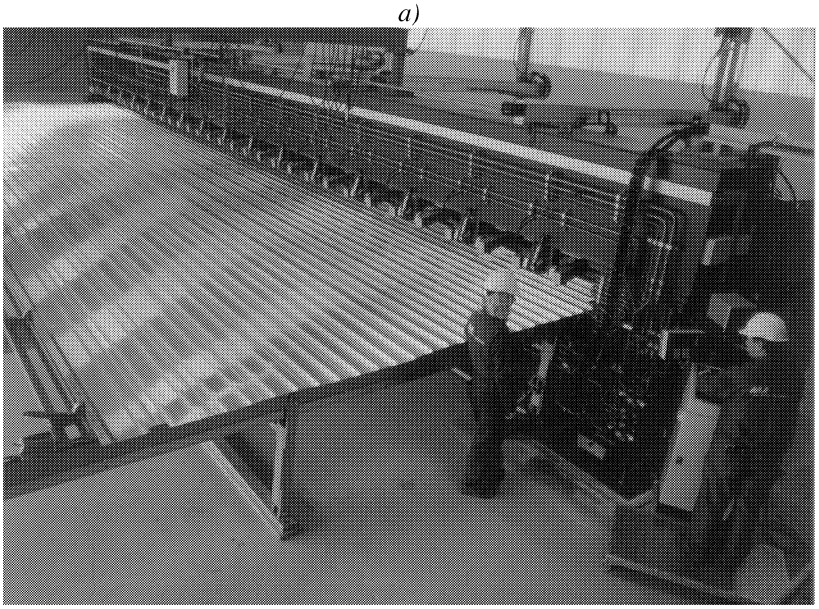

b)

Figure 3 *a) Flying Cat (courtesy of Kværner Fjellstrand AS), and b) the fabrication of friction stir welded aluminium panels used in the hull of the Flying Cat (courtesy of Hydro Marine Aluminium AS).*

Another application of aluminium plates is associated with fortification. The need for lightweight fortification as protection against terrorist attacks during peacekeeping operations is increasing. Therefore, effort has been placed on designing containers that can withstand explosions and fragments generated from explosions.

For the examples mentioned above the knowledge about the behaviour of stiffened welded aluminium plates subjected to impact loading conditions is limited. Furthermore, research is needed to provide experimental data and to gain knowledge on how to numerically simulate an impact event using the finite element method. Thus, the present research project was initiated to study the energy absorption capacity of stiffened aluminium plates subjected to projectile impact. The current work is a part of the project "Lightweight structures exposed to dynamic loading" at the Structural Impact Laboratory (SIMLab), Department of Structural Engineering, NTNU.

1.2 Definitions used in structural impact

Structural impact dynamics has some features that distinguish it from conventional quasi-static loading conditions. From a physical point of view, inertia effects must be considered in all of the governing equations. This gives rise to stress wave propagation in the impacted materials, and the recognition that most impact events are transient phenomena (Zukas et al. 1982). From a material point of view, the short time duration of the impact phenomena may introduce strain rate effects not observed in quasi-static loaded materials. Research into the field of structural impact dynamics has traditionally been of interest for the defence community, and this is obviously reflected in the terminology. The most common definitions used in structural impact phenomena are presented in this section.

1.2.1 Definition of projectile

According to Zukas et al. (1982) the term projectile can be used for any item capable of being launched. Some commonly occurring projectiles are shown in Figure 4. The projectile weight may vary from hundreds of kilograms to fractions of a gram and is often categorised as soft or hard dependent on the strength and degree of deformation during the impact event.

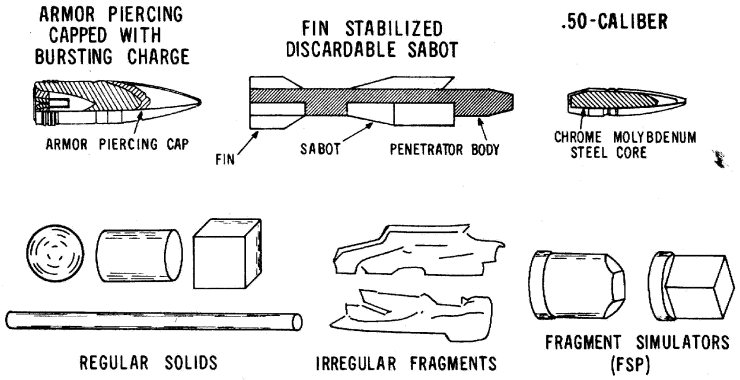

Figure 4 Examples of projectiles (Zukas et al. 1982).

1.2.2 Classification of target by thickness

The target is defined as any moving or stationary object struck by a projectile. It is convenient to classify targets by thickness, and according to Backman and Goldsmith (1978) a target is said to be:

- *Semi-infinite* if there is no influence of the distal boundary on the penetration process.
- *Thick* if there is influence of the distal boundary on the penetration process only after substantial travel of the projectile into the targets.
- *Intermediate* if the rear surface exerts considerable influence on the deformation process during nearly the entire projectile motion.
- *Thin* if stress and deformation gradients do not exist throughout the thickness.

1.2.3 Penetration cases

Penetration is defined as the entry of the projectile into any region of the target (Backman and Goldsmith 1978). Penetration involves perforation, embedment and richochet, and those terms are defined as follows:

- *Perforation* means that the projectile passed through the target with a final residual velocity.
- *Containment or embedment* means that the projectile is stopped during contact with the target.
- *Rebound or ricochet* means that the projectile is deflected from the target without being stopped or perforating, and the projectile has a final rebound velocity.

A commonly used measure of target's ability to withstand projectile impact is its ballistic limit. In general terms (Corbett et al. 1996) the *ballistic limit* of a structure is the greatest velocity the structure can withstand without perforation occurring. The ballistic limit is often given as the average of two impact velocities, one of which is the highest velocity giving a partial penetration and the other of which is the lowest velocity giving a complete perforation.

The *protection limit* is defined as the highest projectile velocity where daylight can not be seen through the plate at the point of impact.

Goldsmith (1985) defined the velocity when the first evidence of fracture was manifested on the rear side of the plate as the ballistic limit. In the present study, the average of two velocities, one of which is the highest velocity giving no cracks in the target and the other of which is the lowest velocity giving a visible crack on the surface of the target is defined as the *incipient fracture velocity*.

1.2.4 Velocity definitions

The following velocity definitions are based on Børvik (2001), Backman and Goldsmith (1978), and Langseth (1988):

- *Low velocity regime (0-50 m/s):* Elastic and plastic bending control the deformation, and with an increase of projectile mass the response is essentially plastic membrane stretching and bending with considerable plate deflection that extends to the supports. The lowest velocity domain covers dropped objects, vehicle impact, ship collisions, crashworthiness of containers for hazardous materials etc.
- *Sub-ordnance velocity regime (50-500 m/s):* Hard projectiles will normally behave in an elastic manner, while the target response is primary plastic. The rate of energy dissipated

within the target is limited by elastic and plastic waves that will tend to reduce the extent of the deformation in the target compared to the lowest domain. The sub-ordnance velocity regime covers among others the design of nuclear containments, free-falling bombs and missiles, and fragments resulting from accidental explosions.

- *Ordnance velocity regime (500-1300 m/s):* Most of the kinetic energy is converted into plastic work both in the projectile and the material. The activated part of the target is within a small zone, typically 2-3 projectile diameters from the impact point, and hardly any global deformation of the target is seen. This velocity range is of special interest for military applications and covers all kinds of military projectiles like bullets, missiles and high kinetic energy penetrators with and without explosives.
- *Ultra-ordnance velocity regime (1300-3000 m/s):* Depending on the mechanical properties of projectile and target a hydrodynamic description of the material behaviour is necessary. The target and projectile may behave like fluid when the stress level is many times the strength of the materials. This velocity regime covers e.g. warhead fragments and rocket bursted penetrators.
- *Hypervelocity regime (>3000 m/s):* The projectile and target behave like fluids, and the projectile will often be completely eroded during impact and even totally vaporised if the velocity is high enough. This velocity domain is of interest among others in designing a space vehicle to withstand meteoroid impacts.

1.2.5 Failure modes

It is common to divide the target response into non-failure and failure modes, Backman and Goldsmith (1978). As Figure 5 shows, non-failure modes involve two types of transverse displacement due to plastic deformation. Locally a bulge is formed which means that the target deforms to the shape of the penetrator nose in the contact zone, and dishing due to global bending.

According to Zukas et al. (1982), the different failure modes depend on variables such as material properties, impact velocity, projectile nose shape, target geometry and support condition as well as the masses of target and projectile. The most common failure modes for thin and intermediate thick plates are shown in Figure 6. The definitions of the different failure modes such as petaling, plugging, fracture due to initial stress wave, radial fracture behind the initial wave front, spalling, fragmentation, and ductile hole enlargement can be found in Backman and Goldsmith (1978), Zukas et al. (1982) and Langseth (1988). Although one of these failure modes may dominate the failure process, several mechanisms may interact. Petaling and plugging are of main interest in the present project, and are defined as follows (Backman and Goldsmith 1978, Zukas et al. 1982 and Langseth 1988):

- *Plugging*: A plugging failure occurs when the projectile pushes a plug of approximately the same diameter as the projectile out of the target, and the plug is set in motion by the projectile. The separation of the plug from the target may occur by a conventional fracture mode, that is, void formation and growth in shear (isothermal), or by a mechanism known as adiabatic shearing which is characterised by the formation of narrow band of intense shear. The shape of the plug depends on the triaxial stress situation; shear in combination with membrane and bending stresses. If pure shear occurs at the periphery of the projectile, a cylindrical plug is pushed out. However, small amounts of normal stresses will change the orientation of the plane of maximum shear and the truncated cone or inverted truncated cone shaped plugs can occur. This type of failure is most frequently observed when blunt or hemispherical nosed projectile impact thin or intermediate thick targets.

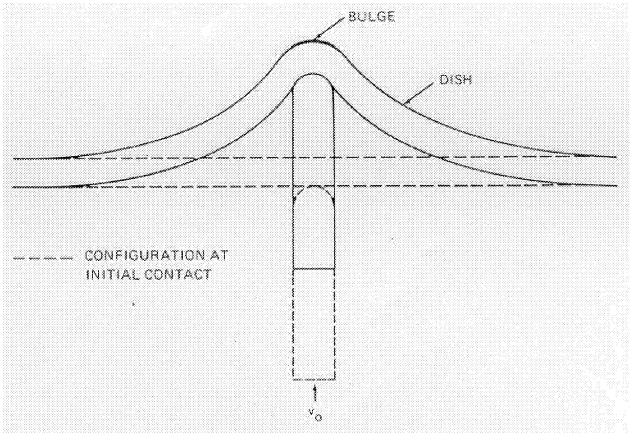

Figure 5 *Permanent deformation of a thin plate showing bulging and dishing (Backman and Goldsmith 1978).*

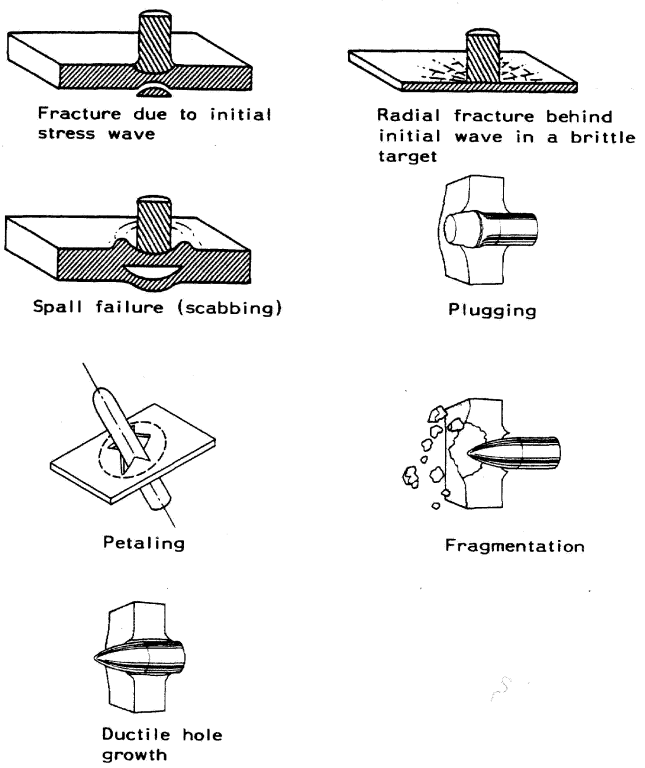

Figure 6 *Most common failure modes in thin and intermediate thick plates (Langseth 1988).*

- *Petaling*: Petaling is produced by high radial and circumferential tensile stresses after passage of the initial stress wave. The intense-stress-fields occur near the tip of the projectile. Bending moments created by the forward motion of the plate material pushed by the projectile cause the characteristic deformation pattern. In addition, the deformation mode is influenced by inhomogenities or planes of weakness of the target. Eventually, the tensile strength of the plate material is reached and star-shaped crack develops around the tip of the projectile. The sectors so formed are then pushed back by continuing motion of the projectile forming petals.

1.3 Previous work

An extensive literature on the perforation behaviour of plates is available (Backman and Goldsmith 1978, Corbett et al. 1996 and Goldsmith 1999). This concerns all sorts of impact on thin to thick targets of small to large projectiles in all velocity regimes. However, most of the experimental and theoretical studies are performed on the penetration of plates by small mass projectiles travelling with high velocities. This is of particular interest for the defence community. However, in the offshore industry large mass projectiles travelling with low velocities has to be taken into account in the design process.

In the case of high velocity impact, the plates are exposed to localised deformations and temperature and strain rate effects have to be taken into account. In the case of large masses travelling at a low speed, the duration of impact increases and the external energy is absorbed over a larger region of the plate. In particular, global displacements might develop and allow a significant proportion of the dynamic energy to be absorbed in membrane stretching before perforation occurs, Jones (1997). The behaviour of targets subjected to high and low velocity impacts are quite different and, therefore, requires different methods of analyses.

Owing to the large amount of work published in the literature, it is not feasible to give a complete review of all relevant information. Instead, this section will provide an introduction to low velocity impact on thin targets by heavy projectiles, relevant to the present project.

Among others, Langseth and Larsen (1990, 1992 and 1993) have conducted an experimental and numerical investigation of single steel plates and stiffened steel plates subjected to large mass projectiles in the low velocity regime. Two distinct phases of motion were observed: that is the transient phase where only inertia forces were present and occurred before the supports registered any loading; and a global mode phase where the supports were activated. The response was described by global plastic deformations of the plates combined with the possibility of the local failure (plugging) at the impact point. They found that the critical impact energy increased with the target thickness and decreased with increasing in-plane panel stiffness, and that an increased span length reduced the stiffness of the plate. When increasing the mass of the projectile, a decreased critical impact energy was observed, and the critical impact energy seemed to approach the static plugging energy when increasing the mass beyond a certain value. With their test set-up stiffening the plate with stringers seemed to have no effect on the critical impact energy compared to a single plate. Comparing quasi-static and dynamic force-displacement curves showed that the interface forces at perforation were approximately equal, and that the dynamic and static force-displacement curves had the same slope during the global mode phase. Langseth and Larsen (1992) also proposed a phenomenological model to calculate the energy absorption at plugging and the corresponding displacement.

Single aluminium plates subjected to blunt ended large mass projectiles have shown weight saving of as much as 40 % compared to similar steel plates (Langseth and Larsen

1994). Numerical simulations of the impacted aluminium plates were carried out using LS-DYNA (Langseth et al. 1999) and the maximum interface force and the maximum displacement at the impact point agreed quite well with the test data.

Wen and Jones (1992, 1993 and 1994) have reported an experimental investigation into dynamic plastic response and perforation of clamped mild steel and aluminium alloy circular plates stuck by a blunt cylindrical mass at any point along a radial line. They have highlighted the importance of applying empirical formulae to impact situations that lie within the low velocity impact with heavy strikers. The targets failed by plugging with a plug having approximately the same diameter as the striker. The plugs had a variable shear zone, and the diameter of the mild steel plug was less on the front side than the rear side while the angle was opposite for the aluminium alloy plug. Large elastic and plastic deformations extended to the supports. They observed that a cracked plate could absorb additional external energy before it was perforated. A significant difference in the force-time curves was observed for a plate stuck by a mass at the centre and close to the supports. This was explained by the fundamentally different plugging process for these two cases. The plate struck by a mass at its centre failed immediately and the failure was catastrophic in nature, while the plate that was impacted close to the supports was perforated relatively slowly. The energy absorbing capacity of the plates was significantly smaller when it was stuck by a mass near the supports compared to a strike at the centre.

Wen and Jones (1992 and 1994) proposed an empirical formula for the perforation of plates struck by blunt or flat-headed projectiles by using the principles of dimensional analysis. The energy absorbing mechanism of the plate was divided into two components: a local component consisting of indentation and shear; and a global component consisting of membrane stretching and bending. Good correlation was found between the predicted perforation energy and the experimental results provided that adiabatic shearing does not occur. Jones (1994) also discussed different empirical equations.

An approximate quasi-static theoretical analysis has been developed by Wen and Jones (1996) to examine the behaviour of impacted plates. Predictions of the energy absorbing capabilities of plates subjected to low velocity impacts that cause perforation have been employed based on the principle of virtual work. Provided that the influence of material strain rate sensitivity was taken into account and that perforation does not occur by adiabatic shearing, good agreement was found between the predictions and the experimental results.

Jones and Kim (1997a and 1997b) reported experimental and empirical studies of impacts by a large mass travelling with velocities in the low and sub-ordnance velocity regime. The energy required to perforate a mild steel plate decreased significantly with an increase in the striker mass and approached the corresponding static value for a large mass travelling with a low velocity. Jones et al. (1997c) have presented a theoretical analysis for a thin plate subjected to low-velocity rigid projectile having a mass which is larger than the plate mass using the rigid perfectly plastic material assumption. In the energy balance analysis, the bending energy and transverse shear energy were taken to account in the first phase of motion, while the bending and membrane energies were associated with the second phase of motion. Reasonable agreement was obtained between the experimental and theoretical predictions for projectile mass ratios larger than one.

The aim of Edwards and Mathewson's (1997) work was to examine the ballistic behaviour of commercially available high carbon steel plate at various hardness levels, and to show how the ballistic behaviour changed when welds were present. They found that when the ballistic properties of welded assemblies were considered, the key factor was the hardness of the heat affected zone.

Johnson et al. (1980) reviewed quasi-static work reported in the literature. They found that in piercing and hole-flanging processes usually four petals were created due to anisotropy in the sheet metal. The fracture directions were parallel and normal to the rolling direction.

Only limited numerical predictions of the plastic instability phenomenon leading to necking and thereafter fracture are found in the literature. Berstad et al. (1999) have implemented a continuum damage mechanics model for shell analyses in the explicit finite element code LS-DYNA. They performed a numerical simulation of perforation of a thin plate by a hemispherical projectile to demonstrate the capabilities of the continuum damage mechanics model and obtained promising results.

Simonsen and Lauridsen (2000) performed an experimental, theoretical and numerical investigation of ductile failure in metal sheets under lateral indentation by a sphere. They found that the plate failed by localised necking followed by material fracture. They modelled the plate using shell elements and defined a maximum equivalent strain at which an element was deleted when the average equivalent strain reached that level. Their numerical model predicted the response up to necking and fracture initiation.

Similar approach has also been performed by Lademo et al. (2001 and 2002) in numerical simulations of strain localisation and fracture in metal forming operations. Here, numerical simulations of instability predictions in uni-axial tension test and biaxial tension test, and in a Marciniak and Kuczinsky formability test were conducted. Lademo et al. (2002) based the numerical simulations on the classical theory of Marciniak and Kuczinsky (1967) and introduced geometric inhomogenities. They used an anisotropic yield criterion coupled with continuum damage mechanics model of Leimaitre and found good agreement between experiments and numerical simulations. They indicated that the tensile failure instability occur automatically as a function of the elasto-plastic material model, geometry and loading conditions in shell analyses with the explicit finite element code LS-DYNA independent on whether inhomogenities were present or not.

1.4 Aluminium

The plates used in the experimental tests were taken from extrusions of aluminium alloy AA6082 MIG (metal inert gas) welded to form stiffened plates. Alloying elements are usually added to aluminium to increase its strength or improvements in other properties and Magnesium and Silicon are the main alloying elements in AA6082. The process of extrusion is complex and the temperature history of the aluminium from cast billet to extruded material is important, Figure 7, and affects among others the strength of the material. The various steps from the casting of the billet to the final extrusion ready for treatment before the welding are, (Althenpohl 1982, Tibballs 1995, and Cobden 1994):

- Casting of a billet and cooling to room temperature. The melting point is in the range between 600 and 650 ^{0}C for most alloys.
- Homogenisation (soaking) to eliminate segregation from the cast structure, e.g. 3-10 hours as close as possible to the solidus (550-630 ^{0}C). The purpose is to take precipitates (particles) into solution and to distribute the solute atoms uniformly in the lattice. Precipitates not in solution lose their sharp edges and become compact and round off (“spherodized”), which improves formability significantly.
- Pre-heating of the billet to 450-500 ^{0}C immediately prior to the extrusion.
- The extrusion process means basically forcing the billet through a die that forms the aluminium to the desired shape. The extruded shape needs to be quenched immediately after exiting from the die. If the degree of deformation and temperature is high enough, a

recrystallised structure where lattice defects is eliminated, is formed. The mechanical properties are altered significantly upon recrystallisation and a soft condition appears. The tensile strength decreases and the elongation increases. In general, a fine-grained (1000 grains/mm^2) recrystallised structure is desirable. According to Altenpohl (1982), a fine-grained condition is obtained when the maximum number of recrystallisation nuclei is active at the same time. If this is not the case, fewer, coarser grains result which is most undesirable, since the condition leads to orange peeling during deformation. In this case the surface typically becomes rough and dimpled.

- Stretching to an elongation of 1-2 % and cut into delivery lengths.
- According to the certificate for the investigated extrusions, the extrusions were given a final heat treatment called artificially ageing at 185^0 for five hours. Artifical ageing strengthens the material by producing very fine precipitates.

Age-hardenable AlMgSi alloys are widely used as structural components in welded assemblies because of their strength, low density, and good resistance against general corrosion (Grong 1997). They offer tensile strength values higher than 350 MPa in the artificially aged T6 condition. However, AlMgSi alloys suffer from severe softening in the heat affected zone (HAZ) due to the weld thermal cycle.

In general, the size of the softened zone in weldment is dependent on the welding parameters and material thickness. Grong and Myhr (1993) found that the minimum strength level for 6082-T6 aluminium welded by conventional MIG of TIG procedures would be fairly constant and virtually independent of choice of welding parameters. Furthermore, in such cases it is reasonable to use a constant value for the HAZ strength reduction factor, in agreement with current practice. Figure 8 shows a typical hardness distribution for a weldment in AlMgSi alloys. The literature gives a number of formulae relating hardness to the tensile strength. Among others Dieter (1988) and Grong and Myhr (1993) have related the proof stress and ultimate stress to the Vickers Hardness.

Matusiak (1999) investigated the mechanical properties of the material in a butt weld connection by means of tensile tests of specimens taken parallel to the weld axis, as a function of the distance from the centre of the weld. He found that within a certain distance from the weld centre both the yield and ultimate strengths were significantly reduced, and the heat-affected material had lower ductility and higher strain hardening than the parent material, Figure 9. Furthermore, the weld material had considerably greater ductility and strain hardening than the parent material.

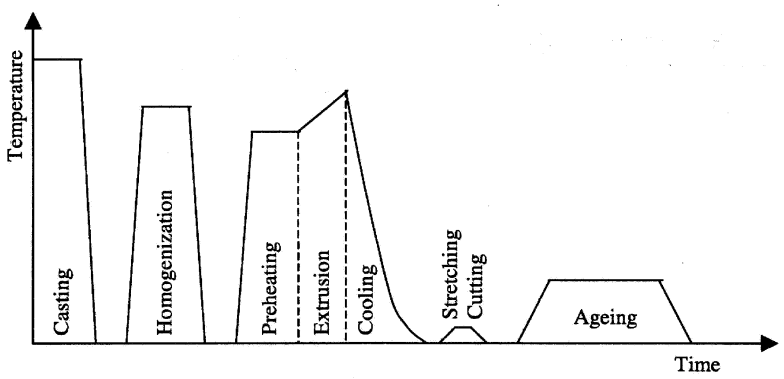

Figure 7 Schematic illustration of the process route for aluminium alloy (Tryland 1999).

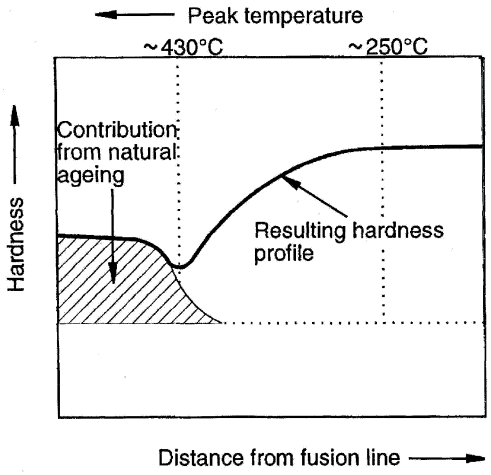

Figure 8 *Schematic hardness distribution of AA6082-T6 aluminium welds (Grong 1997).*

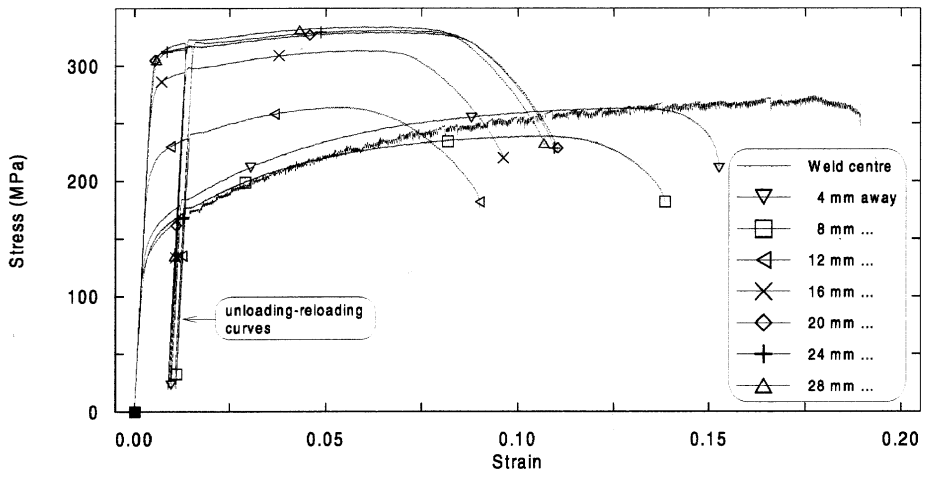

Figure 9 *Stress-strain curves in vicinity of a butt weld (MIG) in alloy AA6082-T6 with filler alloy 5183 (Matusiak 1999).*

A problem with this narrow zone with reduced strength is that all strains are localised in a rather small area. If a weld defect or a crack is present in the softened zone, this may be a critical situation. Hval et al. (1992) studied the fracture toughness properties of aluminium welds, and found that different fracture toughness is to be expected from different zones in the weldment from a 50 mm extruded AlMgSi plate (AlMg4.5Mn filler material). The results from the fracture mechanics testing indicated that the fusion line might be the problem area due to the significant lower fracture toughness properties observed there.

1.5 Objectives and scope

The main objective of the present investigation is to study the behaviour of aluminium alloy stiffened plates subjected to large mass projectiles in the low velocity regime. This objective is met by a combination of laboratory impact tests and numerical simulations using the finite element code LS-DYNA. The experiments are used to evaluate numerical models. This methodology is helpful in order to understand the physical mechanism that governs the behaviour of the panels.

The main tasks of the present investigation are as follows:

- An experimental investigation of stiffened aluminium panels subjected to projectile impact is performed. In addition to impact tests, static punch tests are carried out to study any possible relationship between the dynamic and quasi-static capacities before fracture occurs. Three different impact locations (between the stiffeners, next to a stiffener and on the stiffener) are studied. Furthermore, the projectile nose shape is varied between blunt and hemispherical ended, and the influence on the capacity and failure mode of the plate is examined.
- Uniaxial tension tests and Vickers hardness tests are carried out to provide material data for numerical analyses of the impacted plates. The base material and the material in the reduced strength zone, as well as the material in the different directions, over the cross section, and in the different panels are investigated to find the variation of the material parameters.
- A metallurgical examination of cross sections of the target at the impact point is carried out to reveal details of internal changes of configuration such as deformations and changes of microstructure, and the generation of fractures. This may provide information that is important when deciding how to perform the numerical modelling of the impacted panels.
- A numerical model of impact between two stiffeners with a hemispherical projectile travelling at a velocity above the ballistic limit is established. The objective of the numerical simulations is to study whether the Lemaitre damage model can predict the response when taking failure into account. Focus is placed on the force deformation response and the mode of failure of the stiffened plate.

URN:NBN:no-3315

2 Experimental Programme

This chapter describes the experimental test programme and the experimental set-up of the static and dynamic tests carried out on stiffened aluminium plates. Furthermore, this chapter gives a basis for the material tests carried out (Chapter 3).

2.1 Test specimen geometry

All test specimens were taken from the production of a passenger deck of a high-speed boat, and consequently the test specimen selection was limited to the geometry of the delivered panels. 70 extruded profiles were available for the dynamic, static and material tests. The extrusions with lengths of approximately 9 meters were welded together side by side to form a panel, see Figure 10 and Figure A-1. Figure 11 shows a sketch of the 70 extrusions delivered in seven parts. The different parts are separated by the dotted lines. The sketch also shows the impact test specimens (the test identification system is explained in Section 2.3) and the material used for tensile test specimens. The Arabic extrusion numbers, from 1 to 70, form the basis for the identification system of the material tests and the impact test specimens. The material marked “used for other purposes” was used in a project that deals with buckling of stiffened plates (Aalberg et al. 2001). Logistics and practical considerations gave limitations in selection of the test specimens and the sequence of testing.

The girder distance of the panels was one meter. A cross section of a panel is shown in Figure 12. The nominal width and height of the extruded profiles were 252.5 mm and 76.5 mm, respectively. The nominal thickness of the top flange of the extrusion was 5 mm.

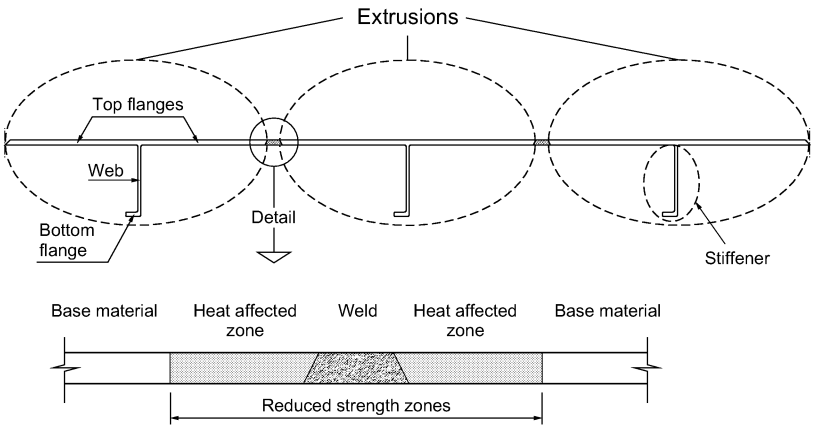

Figure 10 Sketch of a panel.

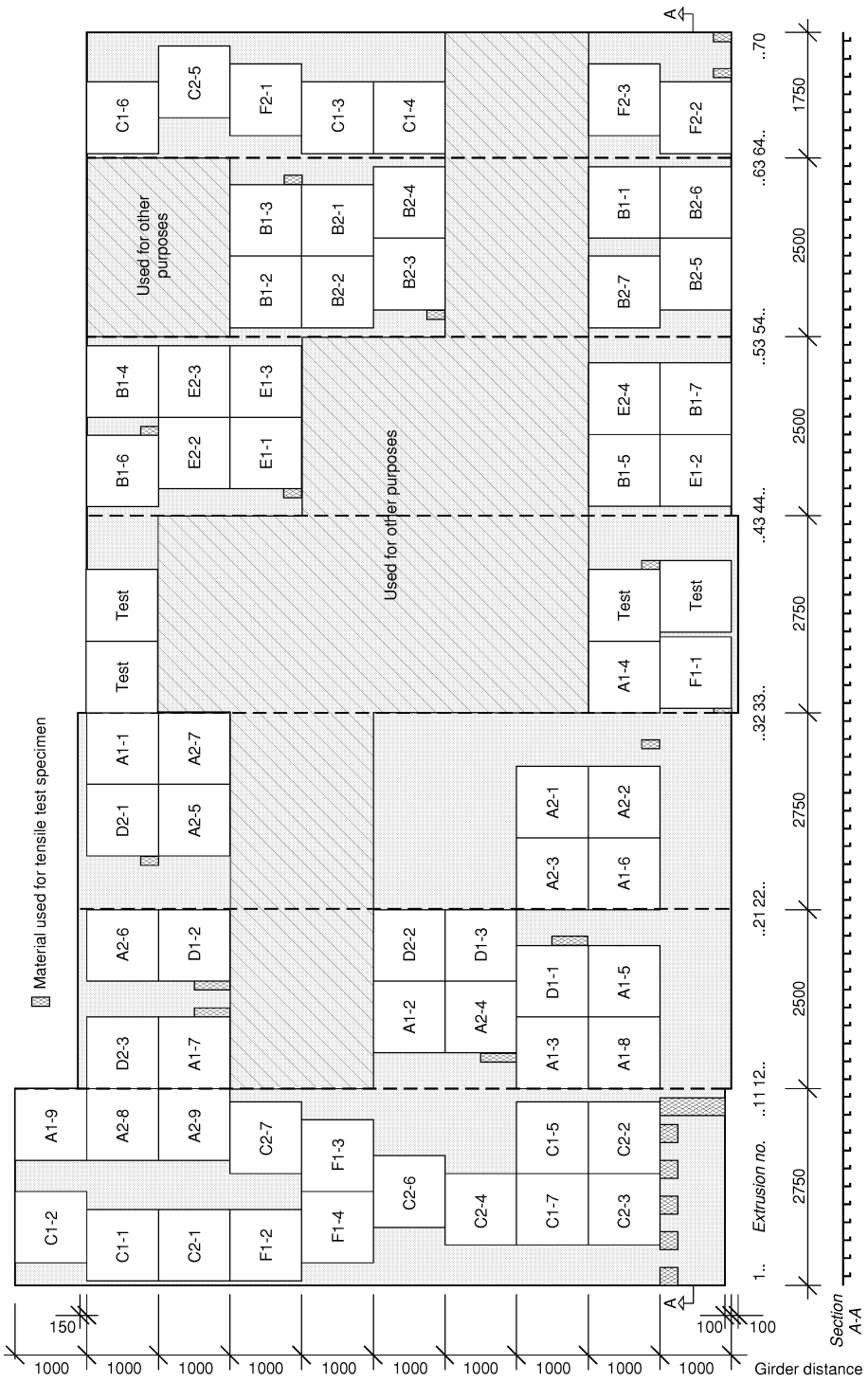

Figure 11 Sketch of the delivered panels and the test specimens.

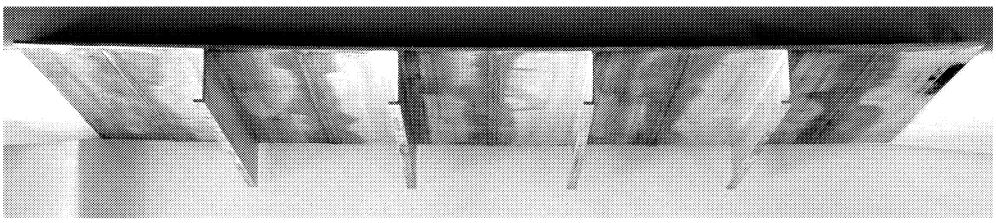

Figure 12 Photograph of a cross section of a part of a delivered panel.

The welding introduces reduced strength zones consisting of the weld and the heat affected zones on both sides of the weld as depicted in Figure 10. The material composition and the mechanical properties are described in Chapter 3. The bottom flange and the web, as defined in Figure 10, are referred to as the stiffener in the following. The term plate is used to describe the top flanges.

The girder distance of 1 meter gave an upper limit of the test specimen length. The specimens for the static and dynamic were squares with length and width equal to 970 mm, as shown in Figure 13. The specimens were equipped with edge stiffeners in order to keep the plate edges straight before and during impact testing, see Figure 13, Detail B. Owing to the possibility of shear failure of the ends of the stiffeners, the stiffeners were machined to a slope of 45 degree as shown in Figure 13, Section B-B.

2.2 Idealised support conditions

The idealised support conditions are shown in Figure 13, Section A-A and Section B-B. The support conditions shown in Figure 13 imply that only the displacements in the negative z-direction along the supports were prevented. This gave a simple support with centre-to-centre distance of 895 mm, allowing the plate overhang to rotate freely. Owing to preliminary tests where shear failure of the ends of the stiffeners occurred, inner supports with slots for the continuously stiffeners were added in the longitudinal direction, giving a inner span of 615 mm in this direction. This means that two supports in the transverse x-direction and four supports in longitudinal y-direction gave a satisfactory transmission of the force to the supports. Simple supports were chosen to avoid unknown constraints or stiffness in the numerical modelling of the impacted plates. Detailed information of the support conditions is given in Section 2.4.

2.3 Test programme

A pneumatic accelerator located at Structural Impact Laboratory (SIMLab) NTNU was used for the dynamic tests. Due to physical limitations in the laboratory equipment, the projectile mass was chosen to be approximately 55 kg. Detailed descriptions of the projectile, the dynamic test rig and the static test rig are given in the following sections.

The outline of the test programme is presented in Figure 13 with three static (series D, E and F) and three dynamic test series (series A, B and C). A total of 19 static tests and 46 dynamic tests were performed. The parameters to be varied were the point of load application (load position) on the stiffened plate and the nose shape of the punch/projectile. The three load positions were between the stiffeners, next to a stiffener, i.e. 38.5 mm from the centre of the web, and centred on the stiffeners' web. All tests were carried out as a central impact with respect to the supports. The diameter of the replaceable nose was 60 mm, and the projectile/punch nose was either blunt or hemispherical ended. The impact velocity of the

projectile was varied in the dynamic tests to determine the impact velocity leading to structural failure in the target plate.

The different test series were as follows:

Test series A (dynamic):
This test series was carried out to find the incipient fracture velocity and the ballistic limit, defined in Chapter 1, of stiffened aluminium panels subjected to projectile impact in the span **between the stiffeners** as function of the nose shape of the projectile. The load position was on the weld, and subsequently the influence of the reduced strength zone on the capacity was studied. The geometry of the test specimens is shown in Figure 13, Section A-A (series A and D).

Test series B (dynamic):
In this test series the incipient fracture velocity of stiffened aluminium panels subjected to projectile impact **centred on a stiffeners' web** as function of the projectile nose shape was studied. No attempt was made to perforate the plate in this test series. In addition, increasing the projectile velocity the propagation of the fracture was studied. The geometry of the test specimens is shown in Figure 13, Section A-A (series B and E).

Test series C (dynamic):
This test series was used to study the incipient fracture velocity and the ballistic limit of stiffened aluminium panels subjected to projectile impact **next to a stiffener** as function of the projectile nose shape. The geometry of the test specimens is shown in Figure 13, Section A-A (series C and F).

Test series D, E, and F (static):
To study any relationship between the dynamic capacities and the corresponding static ones, static punch test were carried out. As seen in Figure 13 the same test specimen geometry and support conditions were used in the static tests as for the dynamic tests. Test series D correspond to test series A, test series E correspond to test series B, and test series F correspond to test series C.

Test identification system:
The following test identification system was used: X Y – n where

X : is the test series to distinguish dynamic (A, B and C) and static (D, E and F) tests and to distinguish the different load positions (A and D: between the stiffeners, B and E: on a stiffener's web, and C and F: next to a stiffener)

Y : is the test group to distinguish the different nose shapes (1: blunt nose, and 2: hemispherical nose)

n : is the test number within a test group

Not all test specimens were produced before the first test series were carried out. The sequence of the tested panels was dependent on the manufacturing of the test specimens and it was not possible to obtain any random sampling. When performing the test program the tests were performed as described in Sections 2.4 and 2.5.

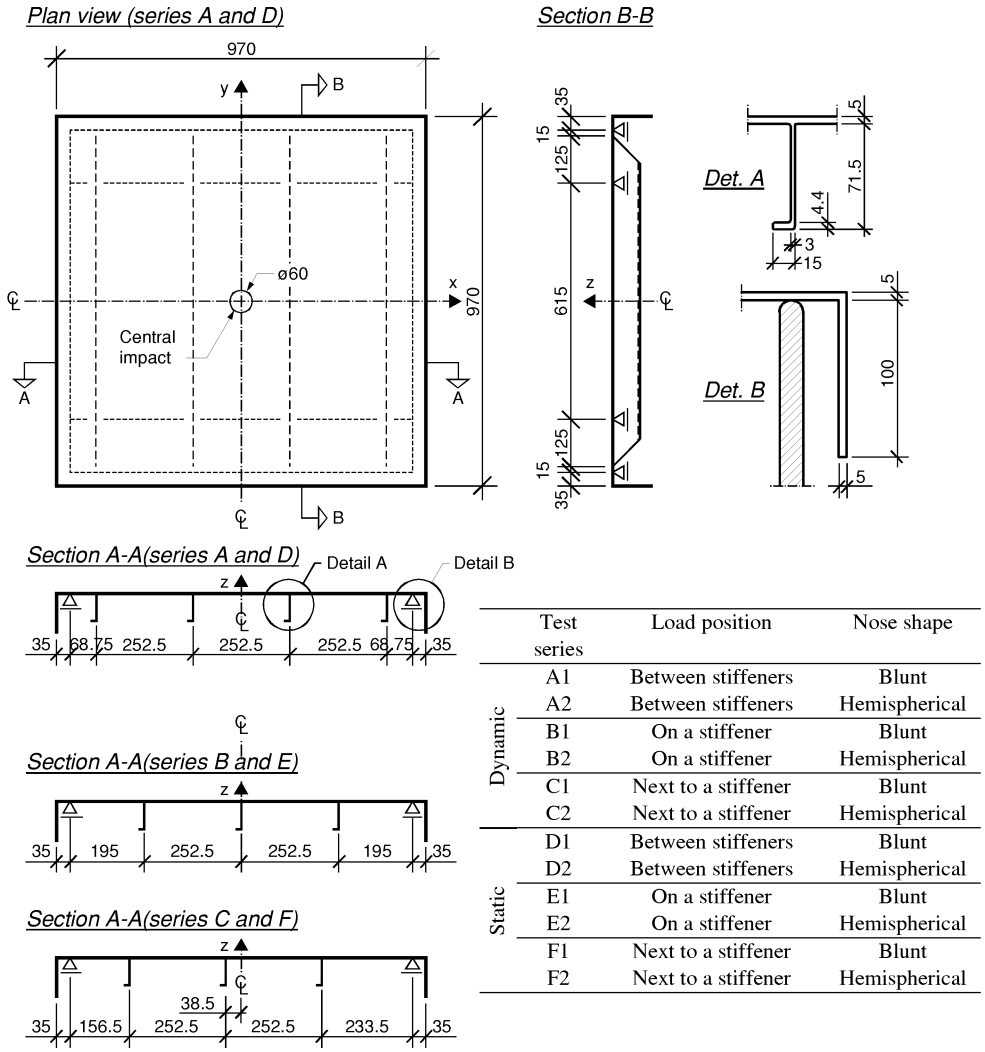

	Test series	Load position	Nose shape
Dynamic	A1	Between stiffeners	Blunt
	A2	Between stiffeners	Hemispherical
	B1	On a stiffener	Blunt
	B2	On a stiffener	Hemispherical
	C1	Next to a stiffener	Blunt
	C2	Next to a stiffener	Hemispherical
Static	D1	Between stiffeners	Blunt
	D2	Between stiffeners	Hemispherical
	E1	On a stiffener	Blunt
	E2	On a stiffener	Hemispherical
	F1	Next to a stiffener	Blunt
	F2	Next to a stiffener	Hemispherical

Figure 13 Geometry of the test specimens and the test programme.

2.4 Static test set-up

The static tests were carried out using a 1000 kN Amsler hydraulic actuator with a stroke of ± 100 mm, see the drawing in Figure 14. The cylindrical punch had a diameter equal to 36 mm, while the diameter of the nose was 60 mm, see Figure 20. The material properties of the different noses were identical (SIS 2541-03). As shown in Figure 15, the stiffened plates were simply supported with two supports in x-direction and four supports in the y-direction. The supports were greased with Teflon to minimise the friction during testing.

Each test specimen was loaded transversely at its centre in displacement control mode at a constant rate of 3 mm/min. After passing the peak load this rate was increased to 6 mm/min and kept fixed for the rest of the experiment.

The instrumentation is shown in Figure 16, see also Figure 17. The force was measured using two oil pressure transducers in differential configuration with accuracy of ±1% of the applied load. An inductive displacement transducer and an optical position transducer as shown in Figure 17 measured the displacement of the punch. The two measurements of the displacement were identical. The sampling frequency was 2 Hz.

2.5 Dynamic test set-up

The dynamic tests were carried out using a pneumatic accelerator located at the Structural Impact Laboratory (SIMLab), the Department of Structural Engineering, NTNU, as depicted Figure 18. The test rig, the instrumentation system, and data acquisition were the same as used by Langseth and Larsen (1990), and Langseth and Hopperstad (1996). Briefly, the dynamic test rig consists of a pressure chamber connected to a vertical accelerator tube. A projectile is released from the top pressure camber and fired down through the accelerator tube, subsequently impacting the test specimen. The pressure in the top chamber determines the resulting impact velocity. Figure 19 shows an overall view of the dynamic test set-up.

The projectile, Figure 20, was designed to act as a piston inside the accelerator tube. The projectile consisted of a central rod ③ and a replaceable nose ④ both of quenched and tempered steel (SIS 2541-03). This ensured an elastic behaviour during impact and made it possible to measure the impact force with strain gauges. In addition, the projectile consisted of guides of aluminium equipped with nylon rings and a gasket ring of rubber ①. The rings functioned as a seal between the accelerator tube and the projectile. To vary the mass of the projectile, although not performed in this study, the projectile was equipped with an interchangeable mass ②. The lower part of the central rod ③ was hollow to increase sensitivity for the strain gauge measurements. A cover ⑤ was added to protect the strain gauges when the projectile perforated the test specimen.

All tests were carried out as a central normal impact where the total mass of the projectile M_p were generally 55.37 kg and 55.20 kg for the projectile with a blunt and hemispherical ended nose, respectively. The exact mass of projectile is listed in Table D-1. The length of the projectile was 827 mm. The geometry of the test specimens and the supporting frame was identical in the static and dynamic tests. For safety reasons clamps were added in the dynamic tests preventing the specimens from moving upwards during impact.

The impact velocity was measured by means of a photocell system. Two photocells containing an infrared source and a detector working against a reflector on opposite side started and stopped a counter. The lower photocell was located 100 mm above the test specimen. Knowing the distance and the time elapsed between the two photocells, the velocity of the projectile at the lower photocell was calculated by

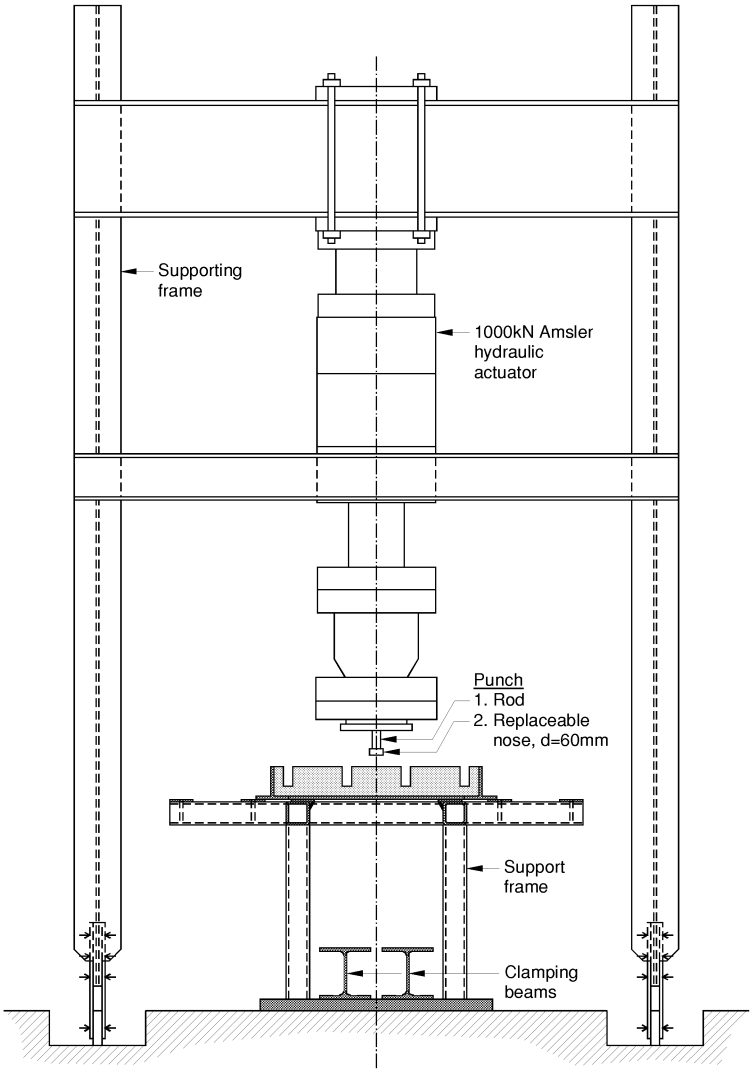

Figure 14 Static test rig.

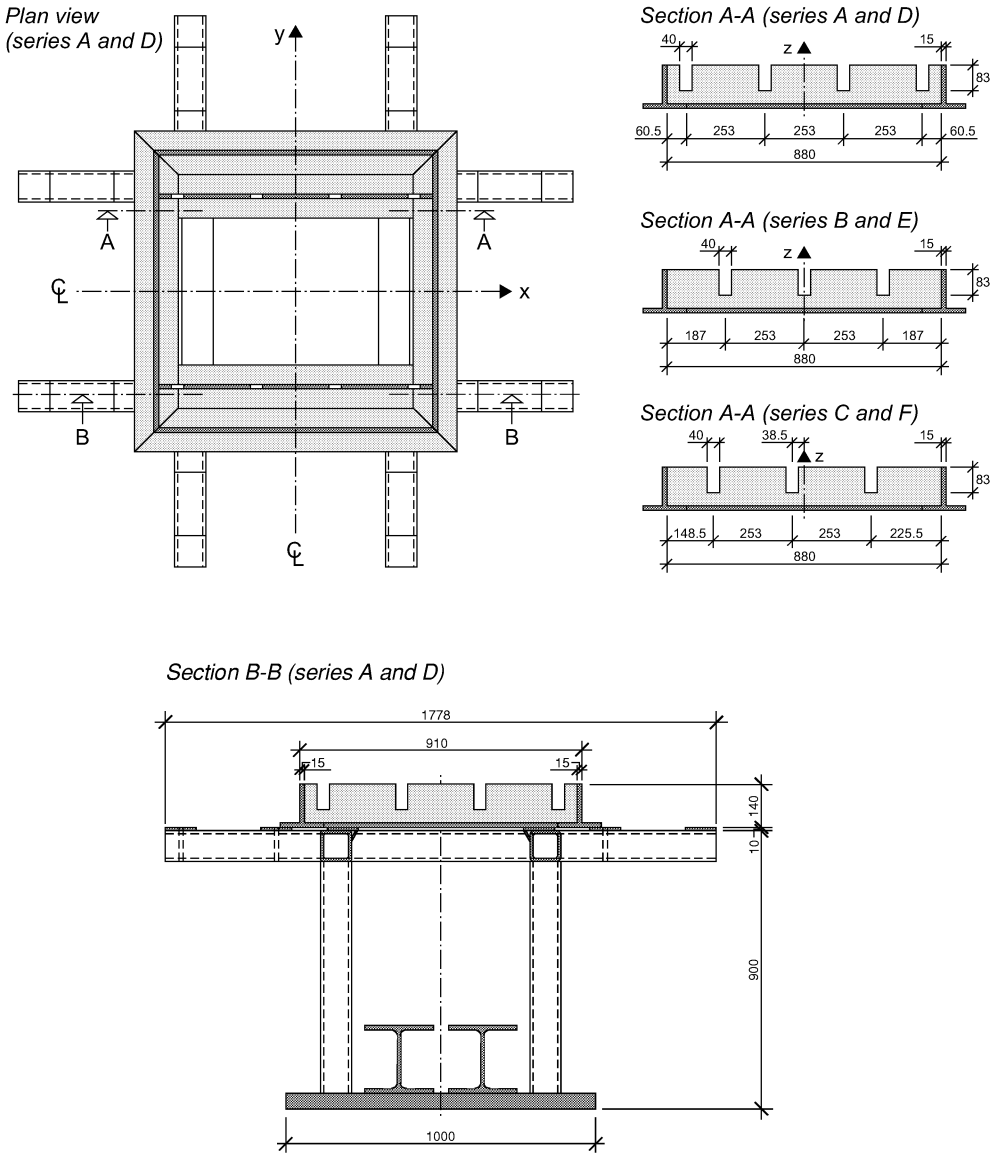

Figure 15 Support condition.

URN:NBN:no-3315

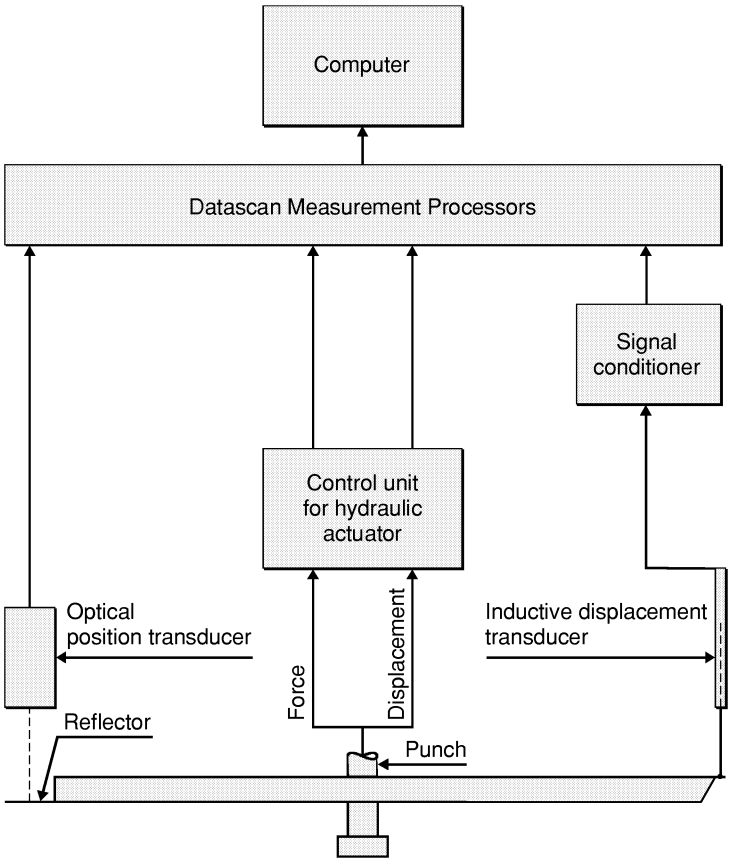

Figure 16 Instrumentation of the static test rig.

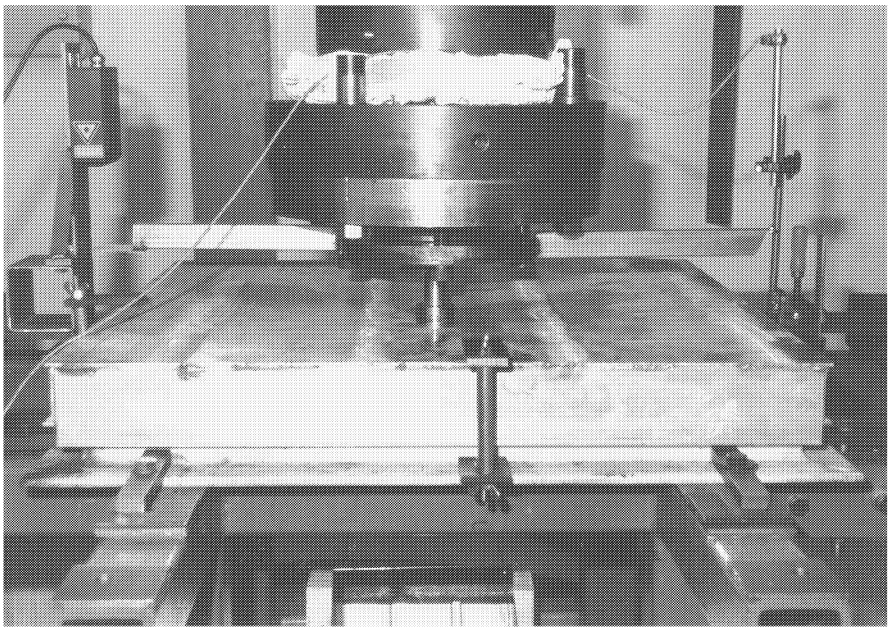

Figure 17 Photograph of a part of the static test rig. Optical position transducer to left, and inductive displacement transducer to the right.

$$v_1 = \frac{L_1}{t_1} + \frac{1}{2} g\, t_1 \tag{1}$$

where $L_1 = 200.2\,\text{mm}$ is the distance between the two photocells, t_1 is the measured time, and g is the acceleration of gravity. Assuming free fall between the lower photocell and the target plate, the impact velocity is found as

$$v_i = \sqrt{v_1^{\,2} + 2 g L_2} \tag{2}$$

where $L_2 = 100\,\text{mm}$ is the distance from the lower photocell to the test specimen.

The impacting force was measured by means of strain gauges in the nose of the projectile rod. Static calibration of the strain gauges in the projectile was carried out prior to testing in a Dartec testing machine in order to obtain the force-voltage relationship, which was a straight line. Langseth (1988) performed some additional measurements and thereby checked the static calibration. Assuming the projectile as a rigid body, Figure 21, the equations of motion for mass M and m are

$$\ddot{w} - g = -\frac{P}{M} \tag{3}$$

and

$$F_d = P - m(\ddot{w} - g) \tag{4}$$

where P is the measured compressive force in the projectile at the location of the strain gauges, m is the projectile mass below the strain gauges, $M = M_p - m$ is the projectile mass above the strain gauges, $\ddot{w}$ is the acceleration of the rigid body, and F_d is the dynamic interface force between the projectile and the test specimen. According to Langseth (1988), the accuracy of the measured interface force was within ± 3 %.

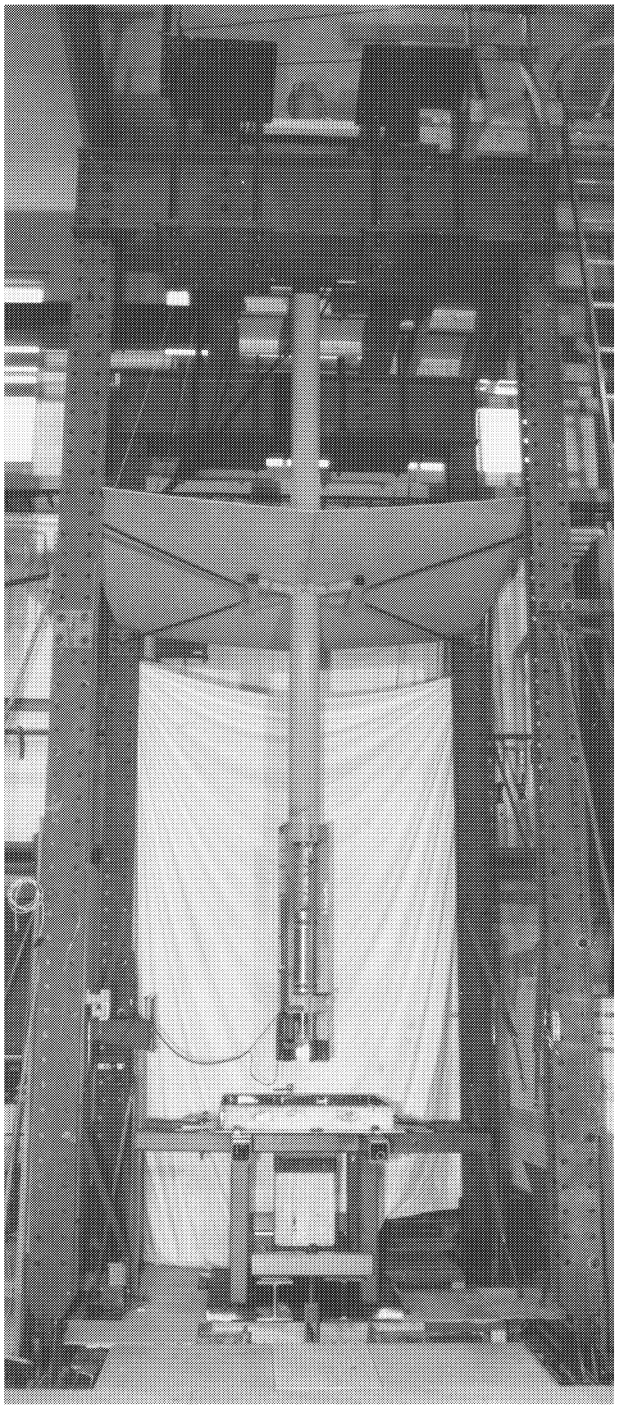

Figure 18 Photograph of the dynamic test rig.

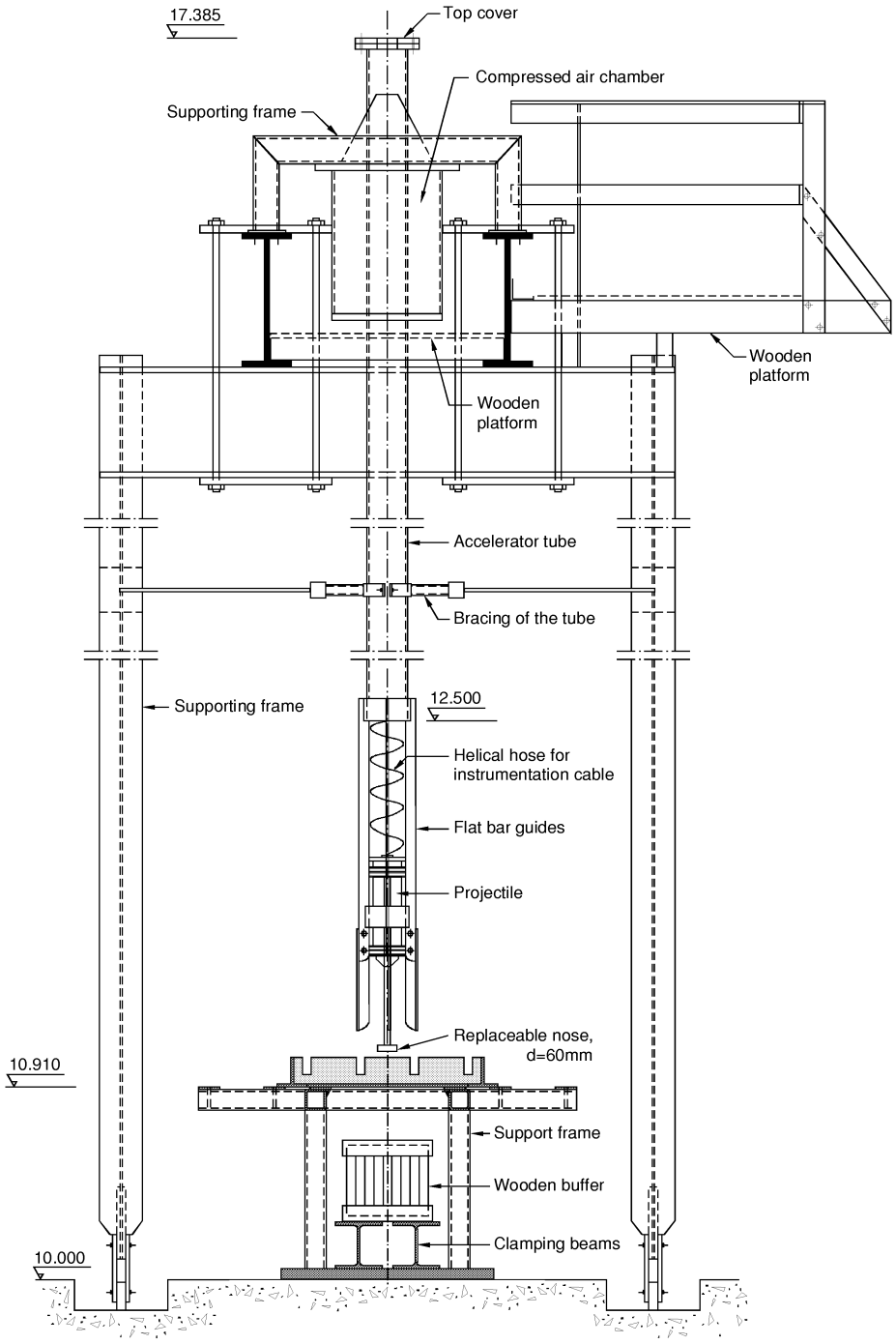

Figure 19 Dynamic test rig arrangement.

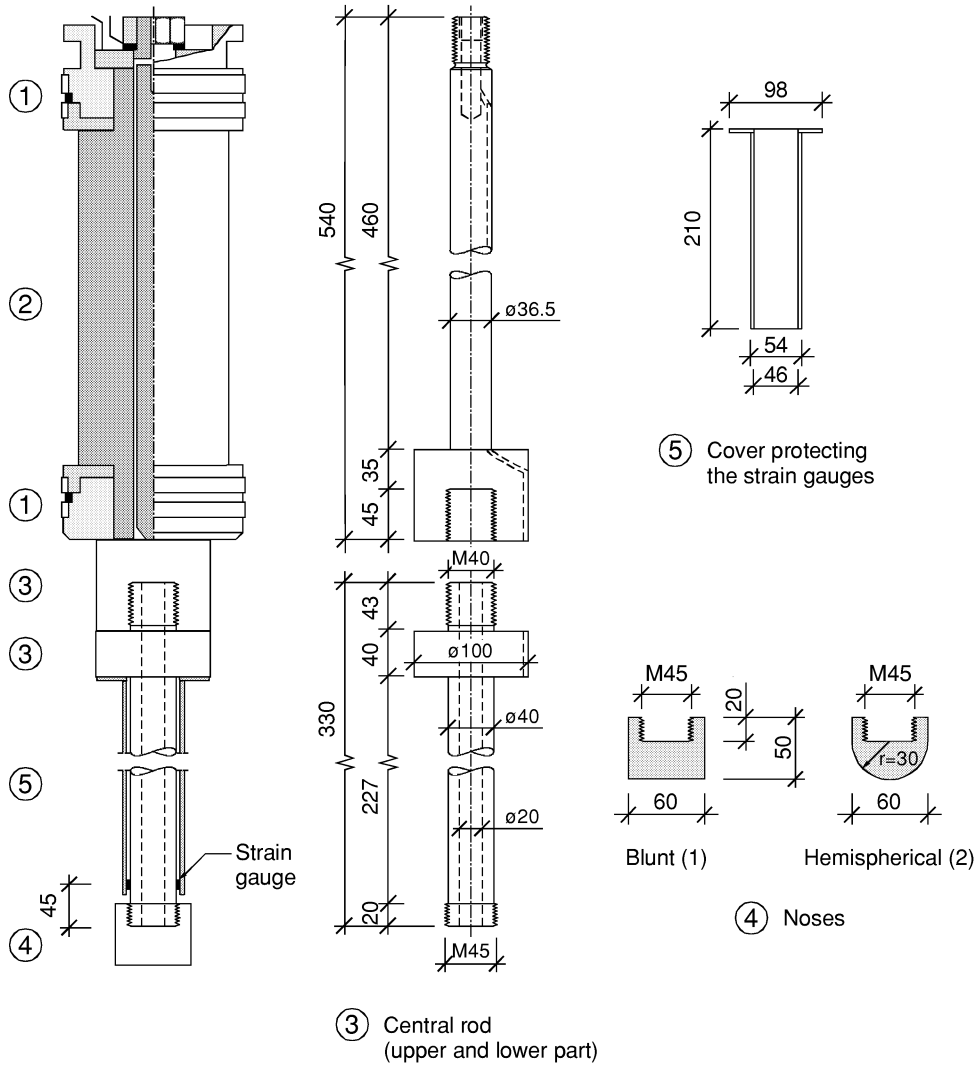

Figure 20 Geometry of projectile.

Introducing (4) into (3) yield the interface force as

$$F_d = P\left(1+\frac{m}{M}\right) \approx 1.02\,P \tag{5}$$

valid for both noses. By integration of (3) the velocity and the displacement of the rigid body were calculated as

$$v(t) = v_i + g\,t - \int_0^t \frac{P}{M}\,dt \tag{6}$$

$$w(t) = v_i t + \frac{1}{2} g\,t^2 - \int_0^t \int_0^t \frac{P}{M}\,dt\,dt \tag{7}$$

where t is the time.

The force-, velocity-, and displacement-time histories and the corresponding force-displacement curve for each test were obtained and none of the curves were filtered.

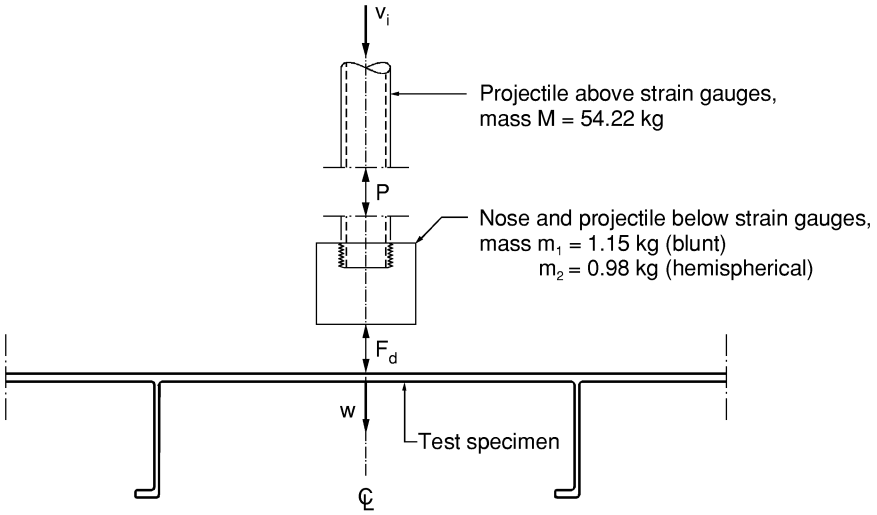

Figure 21 Rigid body diagram of projectile.

3 Material Properties

This chapter deals with material properties of panels that consist of extruded sections welded together side by side. Quasi-static material tests were performed to obtain the stress-strain characteristics of the panels in different directions as well as any spatial variation. In addition to uniaxial tensile tests of the base material in the extrusions, the reduced strength zones were examined. The widths of the weld filler material and the heat affected zones were estimated by means of Vickers hardness tests. In addition, uniaxial tensile tests of the material in the reduced strength zones were performed. The material examinations were carried out in order to calibrate material models to be used in numerical analyses of the impacted specimens.

3.1 Base material

The 70 extrusions of aluminium alloy AA6082 were artificially heat treated to obtain temper T6. The main alloying elements in AA6082 are magnesium and silicon. The minor alloying elements are manganese, iron, copper, chromium, zinc, and titanium. The nominal chemical composition is shown in Table 1. The material specifications were as follows: proof stress of 250 MPa and tensile strength of 310 MPa.

3.1.1 Test specimen and test set-up

A total of 42 uniaxial tensile tests were carried out to obtain the representative material properties as well as the variation of those properties from one extrusion to another, over the cross-section and to determine any anisotropy. It was assumed that the scatter in mechanical properties was insignificant in the extrusion direction compared to the scatter from extrusion to extrusion. Owing to that only one of the seven parts of the supplied panel was present in the laboratory at each time, it was decided that some extrusions should be examined carefully and that spot tests should be made on the other extrusions.

- **Test series A** was performed in order to examine the extent of anisotropy in the top flange of the extrusions. Tensile tests were performed on specimens taken in three different directions: 0°, i.e. the extrusion direction; 45°; and 90°, illustrated in Figure 22a. These specimens were taken from extrusion 12 to 21 as indicated in Table B-1 and Figure 11.
- **Test series B** was performed on specimens taken from extrusion 1 to 11, see Figure 11, to investigate the variation of the material in the top flanges, web and bottom flange of the extrusions, illustrated in Figure 22b. All these specimens were taken in the extrusion direction.
- **Test series C** was carried out to estimate the overall scatter of the material. Two specimens were taken from each of the five parts of the panel not tested in series A and B. The test specimens were taken from the top flange in the extrusion direction.

Table 1 Chemical composition of aluminium alloy AA6082.

	Mg	Si	Mn	Fe	Cu	Cr	Zn	Ti	Al
Min (%)	0.4	0.6	0.4						balance
Max (%)	1.4	1.6	1.0	0.5	0.1	0.1	0.2	0.1	

Figure 23a and Figure 23b show photographs of the test set-up. The geometry specifications of the small and large tensile test specimens are provided in Figure 23c and Figure 23d, respectively. The large specimens were used in all tests except the coupons from the relatively narrow bottom flange, which demanded smaller dimensions. The uniaxial tension tests were performed using a 100 kN Instron hydraulic testing machine together with a calibrated video extensiometer "ME-46 Full Image Video Extensiometer". The tests were carried out in displacement control mode at a strain rate of approximately $5 \cdot 10^{-4}$ s^{-1}. The longitudinal strains were optically determined using a gauge length of 30 mm and 12.5 mm for the large and small specimens, respectively. In addition, the width of the test specimens was used as the gauge length for optical measurement of the transverse strains. This was carried out for the long specimens only.

The sampling rate was 25 Hz. The data were processed as follows, Tryland (1999): In order to obtain the mean stress-strain curves, points were chosen in regular intervals along the strain axes using linear interpolation between neighbouring points. A straight line was fitted to the measured points between $0.17\sigma_{0.2}$ and $0.83\sigma_{0.2}$ by linear regression. The slope of this line defined the measured Young's modulus.

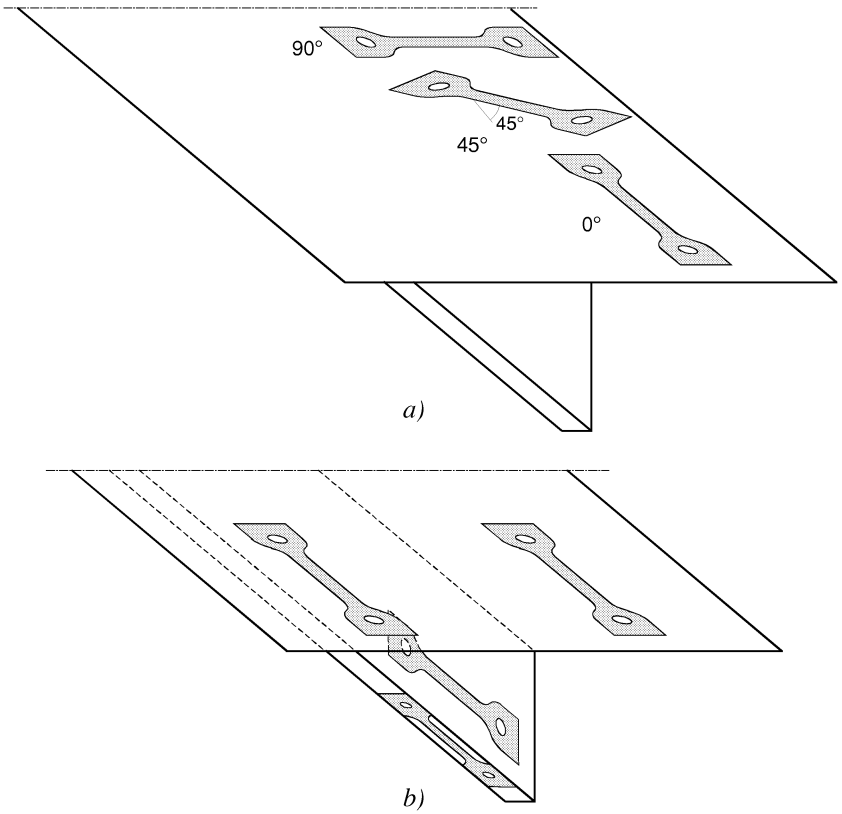

Figure 22 Position and geometry of uniaxial tensile tests: a) Series A, extrusion of panel IV, and b) Series B, extrusion of panel II.

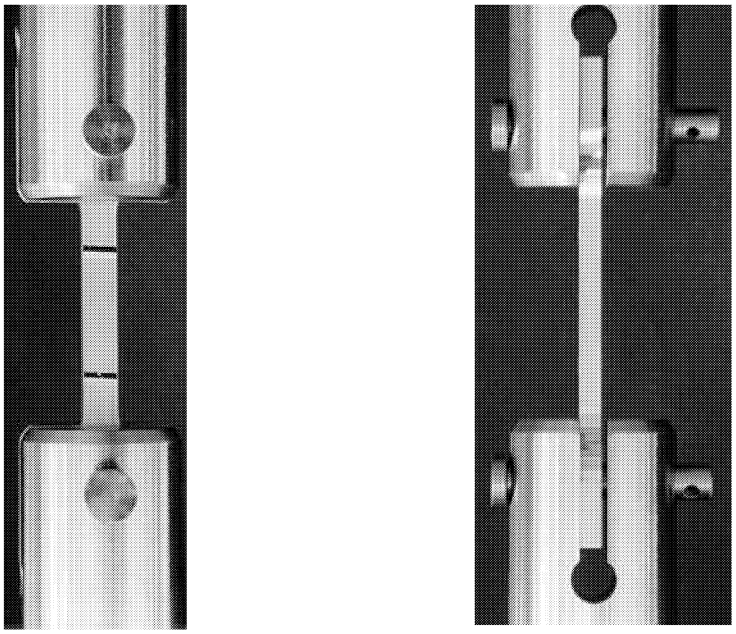

Figure 23 Uniaxial test specimens: a) front view, b) side view, c) geometry of the 80 mm long specimens, and d) geometry of the 110 mm long specimens.

The nominal stress, s, and strain, e, are defined by

$$s = \frac{F}{A_0}; \quad e = \frac{l - l_0}{l_0} \tag{8}$$

where F and A_0 are the force and initial cross section of the specimen, respectively. Furthermore, l_0 and l are the initial gauge length and the actual length, respectively. This formula is valid for both the nominal longitudinal and transverse strains, e_l and e_w, respectively. The true stress, σ, the true longitudinal strain, ε_l, and the true transverse strain, ε_w, were calculated from the nominal values as

$$\sigma = s(1 + e_l); \quad \varepsilon_l = \ln(1 + e_l); \quad \varepsilon_w = \ln(1 + e_w) \tag{9}$$

The true plastic strain in longitudinal direction, ε_l^p, and transverse direction, ε_w^p, were calculated as

$$\varepsilon_l^p = \varepsilon_l - \frac{\sigma}{E}; \quad \varepsilon_w^p = \varepsilon_w - \nu\frac{\sigma}{E} \tag{10}$$

where E is Young's modulus and ν is Poisson's ratio. The true plastic strain in the thickness direction, ε_t^p, is derived from the longitudinal and transverse strains using the incompressibility condition of the theory of plasticity, giving

$$\varepsilon_t^p = -(\varepsilon_l^p + \varepsilon_w^p) \tag{11}$$

The ratio of plastic strains, R, which can be defined as the ratio between the accumulated plastic strains in the transverse and thickness direction (Hosford and Caddell 1993), was determined from

$$R = \frac{\varepsilon_w^p}{\varepsilon_t^p} \tag{12}$$

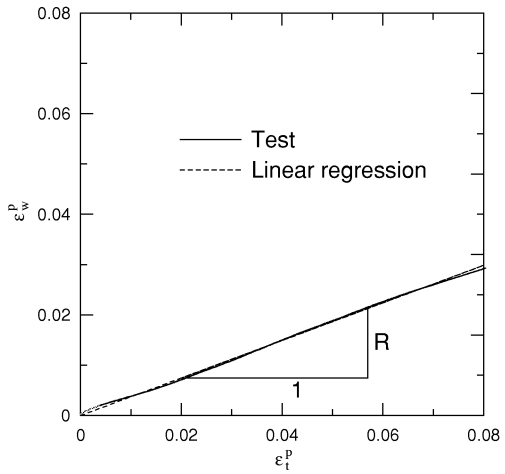

Figure 24 *R-value deduced using least squares fit. The plastic strain in the transverse direction is plotted as a function of the plastic strain in the thickness direction. One representative test.*

The plastic strain in the transverse direction plotted as a function of the plastic strain in the thickness direction is shown in Figure 24 for a representative test. The slope of the curve represents the R-value. This method gives an R-ratio that varies with the level of plastic strain, and a constant R-value is calculated using a least squares fit. The R-value is a measurement of the plastic flow properties of the material. It is noteworthy that the R-value is equal to one for isotropic materials, and an R-value different from unity signifies an anisotropic plastic flow of the material. A high R-value implies high resistance to thinning of the plates.

3.1.2 Test results

Table 2 presents mechanical characteristics of the material from the three series of uniaxial tensile tests. The data is given by mean values and coefficients of variation, i.e. standard deviation divided by mean value, for Young's modulus, E, the stress at 0.2 % plastic strain, $\sigma_{0.2}$, the ultimate stress, σ_u, the uniform strain at ultimate stress, ε_u, the strain at fracture, ε_f, and the ratio of plastic strains, R. Summary tables of all test specimen results are given in Table B-1 and Table B-2.

Table 2 Mean values and coefficients of variation (in parenthesis and given in %) for the material response parameters.

Series	Part	Direction	Extrusions	E [GPa]	$\sigma_{0.2}$ [MPa]	σ_u [MPa]	$\sigma_u/\sigma_{0.2}$	ε_u [%]	ε_f [%]	R
A	Top flange	0^0	12-21	58.9 (5.9)	275 (1.9)	305 (1.6)	1.11	7.6 (8.6)	10.5 (10.4)	0.38 (7.3)
	Top flange	45^0		59.4 (4.2)	263 (2.5)	293 (1.6)	1.11	6.0 (7.1)	6.8 (17.5)	1.05 (37.9)
	Top flange	90^0		62.4 (12.9)	274 (2.0)	307 (1.7)	1.12	7.2 (17.4)	10.3 (10.4)	0.67 (4.1)
B	Top flange	0^0	1-11	85.1 (15.0)	310 (0.6)	329 (0.6)	1.06	6.7 (5.3)	11.3 (12.1)	0.38 (10.6)
	Web	0^0		78.0 (10.5)	302 (0.9)	320 (0.3)	1.06	6.7 (1.3)	9.6 (9.7)	0.39 (2.1)
	Bottom flange	0^0		- -	289 (3.1)	314 (2.0)	1.09	7.1 (3.4)	10.0 (18.9)	- -
C	Top flange	0^0	33-43	84.9	261	289	1.11	7.4	10.9	0.39
	Top flange	0^0	22-32	91.8	258	291	1.13	8.0	11.6	0.41
	Top flange	0^0	44-53	85.5	247	281	1.14	6.5	8.5	0.46
	Top flange	0^0	54-63	88.1	263	295	1.12	6.8	11.5	0.41
	Top flange	0^0	64-70	86.1	242	274	1.13	6.4	11.3	0.40
	Top flange	0^0	22-70	87.3 (8.6)	254 (4.5)	286 (3.5)	1.13	7.0 (15.3)	10.7 (19.2)	0.41 (10.1)
All	Top flange	0^0	1-70	79.9 (18.6)	281 (9.4)	307 (6.6)	1.09	7.0 (11.6)	10.9 (14.7)	0.39 (10.3)

Table 2 shows that the Young's modulus measurements differ significant from the nominal value of 70 GPa. The scatter was large and it is obvious that it was dependent on the test set-up. The resolution of the measuring range was not high enough to achieve satisfactory measurements of E. The measured Young's modul were nevertheless employed when calculating the plastic strain and the ratio of strains.

The mean stress-strain curve derived from all tests on specimens taken from the top flange of the extrusion in the extrusion direction is shown in Figure 25a. The mean values and coefficients of variation of $\sigma_{0.2}$ and σ_u were 281 MPa and 307 MPa, and 9.4 % and 6.6 %, respectively. The mean value varied from extrusion to extrusion, and the scatter of the mean values was even larger from panel to panel as seen from Table 2. For example the coefficients of variation of $\sigma_{0.2}$ was 0.6 % for all extrusion in the panel with extrusion numbers 1 to 11, while it was 9.4 % for all extrusions in all panels. The same tendency can be seen for the thickness of the extrusions in Table B-1. Measured stress-strain curves for the top flange of each of the seven panels are given in Figure 25b visualising the scatter in material data.

The ultimate stress was about 9 % larger than the stress at 0.2 % plastic strain, thus the strain hardening of the alloy was small. The scatters of the uniform strain, ε_u, and the strain at fracture, ε_f, were significant.

Owing to the scatter in both material and geometrical properties, it is reasonable to believe that the material was from different production batches. Another effect can be different levels of recrystallisation in the extrusions. This may lead to the same variability of the material response data as observed by Tryland (1999). The measured loading response of the impact test specimens should therefore be seen in view of this spread in material properties.

The mean stress-strain curves for the three different orientations, test series A, are shown in Figure 26a. It can be seen that the strength anisotropy was small and far less than the overall variation described above. However, the anisotropy in the flow properties, represented by the R-value in Table 2 series A, seemed to be significant. The specimens taken in 45^0 direction have lower $\sigma_{0.2}$, σ_u, and ε_f, than the other directions, as have been documented by tests of the same material performed by Estensen (1998). Figure 27 shows the specimens after rupture. The picture shows one representative test specimen from each of the directions compared with a specimen before testing.

The variation in strength of the top flanges, web and bottom flange of the extrusions, given by test series B in Table 2 and Figure 26b, was not prominent in comparison with the variation between all tensile test specimens. The plate had higher $\sigma_{0.2}$ and σ_u than the web, while the flange had lower values.

It is well known that aluminium alloys exhibit small effects of strain rate upon the elastoplastic behaviour at room temperature. Thus, strain rate material tests were not carried out in the present project. Tests have, however, shown that strain rate effects (Lademo et al. 1999 and Lindholm et al. 1971) can significantly influence the fracture strain. Recent studies have also shown that some alloys exhibit negative strain rate sensitivity (Lademo et al. 1999).

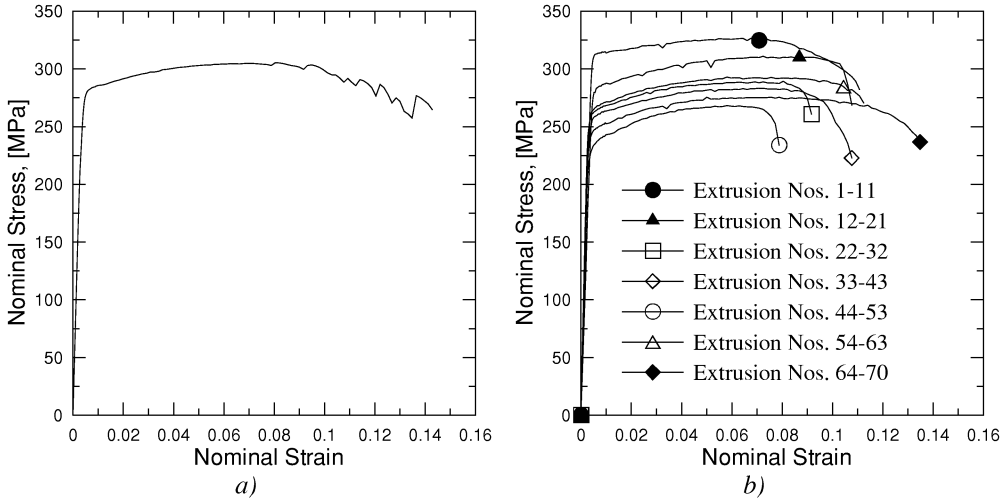

Figure 25 *a) Mean stress strain curve for all tests of the top flange of the extrusion and in the extrusion direction, b) Measured stress-strain curves from one extrusion of the seven parts of the panel to indicate the scatter in material properties.*

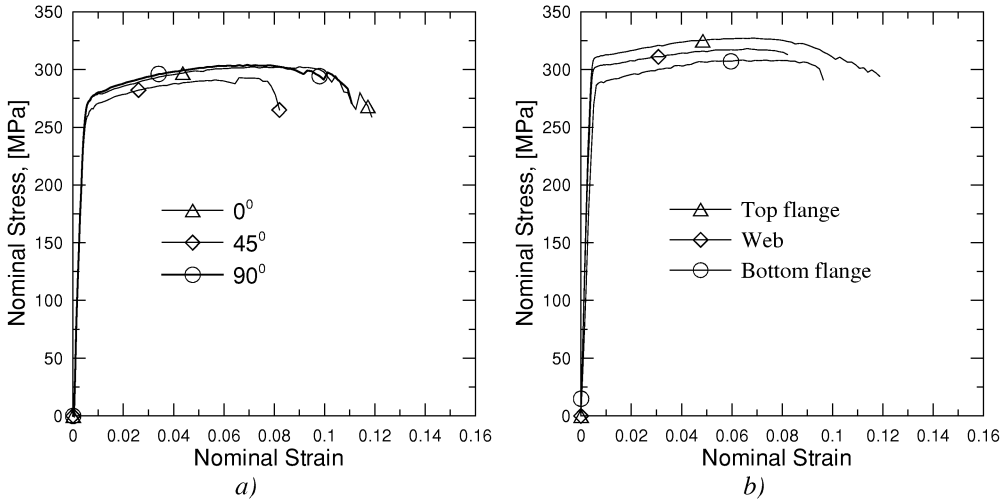

Figure 26 *Material data: a) Mean nominal stress-strain curves in three directions (series A), b) Mean nominal stress-strain curves of the top flange, web, and bottom flange (series B).*

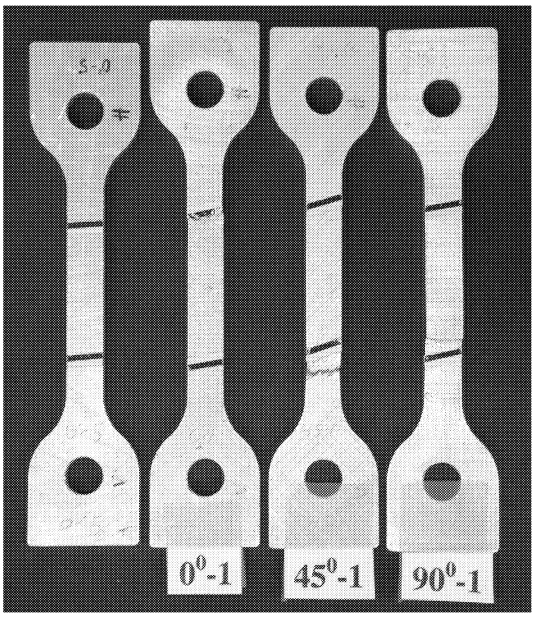

Figure 27 Fractured specimens: 0^0-1, 45^0-1, 90^0-1, and a virgin specimen (series A).

3.2 Reduced strength zones

The extrusions were pulsed MIG-welded by use of single sided welding with stainless backing. The aluminium-based filler material was in alloy AlMg4.5Mn. The welding parameters are given in Table 3. The welding introduced reduced strength zones, and material tests characterising the mechanical properties of those zones are described in this section.

It is well known that there exists a relation between the Vickers hardness and the yield strength of the material (Dieter 1988, and Ashby and Jones 1980). In order to gain information on the reduced strength zones a Vickers hardness profile was combined with tensile tests. A tensile test specimen, 90^o-w10, orientated across the weld was cut out in the vicinity of the hardness test specimen, VH-4, as indicated in Figure 28. In addition uniaxial tensile specimens in two more directions across the weld, 0°, i.e. along the weld, and 45° were cut out between extrusion 10 and 11. Owing to out-of-flatness of the specimens and thickness variations, the tensile test specimens were machined to a nominal thickness of 4.2 mm. The tensile test set-up is described in Section 3.1.1.

The nominal stress vs. the displacement of the crosshead for the three orientations is plotted in Figure 29a. As expected, the introduction of a weld decreased the strength of the tensile test compared to test from the base material. The largest ultimate stress was found in the 0° direction, along the weld, somewhat smaller in the transversal direction and smallest in 45° direction. For the 45° as well as the 90° specimens the fracture surface occurred in the heat affected zone parallel to the weld, after significant strain localisation. The 0° specimen was far more ductile than the other directions, and there was hardly any localisation of the strain before fracture occurred. Figure 30 shows the specimens after fracture compared with a specimen before testing.

The Vickers hardness profile, Figure 31a, was measured across the weld to quantify the width of the heat-affected zone and to spot the point of minimum hardness. The Vickers

hardness test specimen is shown in Figure 31b. The extent of the weld filler material was measured to approximately 7 mm from the centre line and the heat affected zone from 7 to 30 mm from the centre of the weld. Two points of minimum hardness were located; one in the centre line and one in the heat affected zone 17 mm from the centre line.

Strain gauges with gauge length of 1 mm were attached to the specimen 90°-w10, orientated across the weld, in the area of the minimum hardness in the centre line (0 mm) and the heat affected zone (17 mm). The results are plotted as the true stress-strain curves in Figure 29b for the two gauge-positions. The strength of the weld, at the centre line, was less than the strength in the heat affected zone. However, it should be noted that the overall strength of the heat affected zone was far less than in the base material. The weld material seemed to exhibit higher strain hardening than the material in the heat affected zone.

Table 3 Welding parameters.

Current [A]	Voltage [V]	Travel speed [mm/min]	Heat input [kJ/mm]	Wire feed [m/min]
235	22	410	0.76	13.8

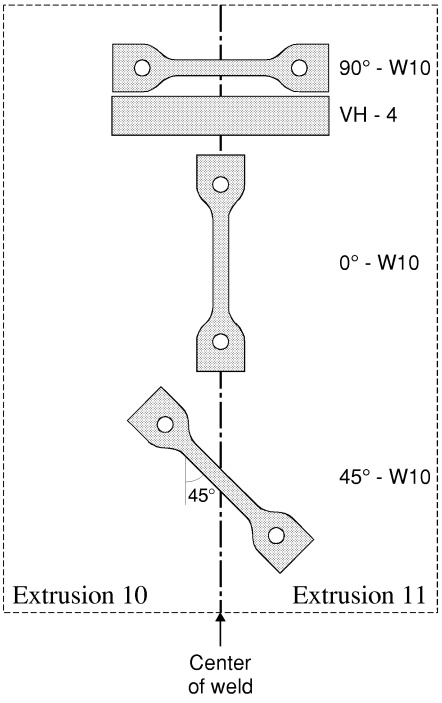

Figure 28 Test specimen selection.

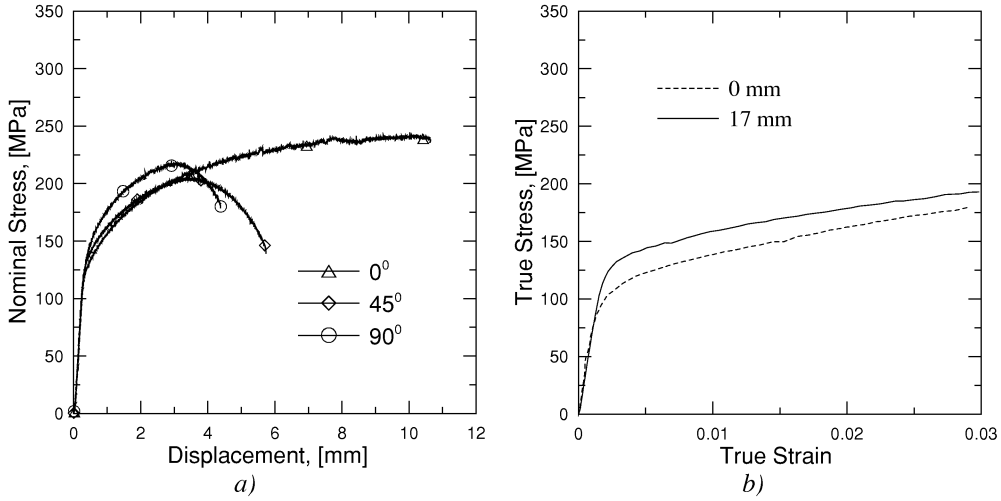

Figure 29 *Material data: a) Nominal stress vs. the displacement of welded specimens, b) True stress-strain behaviour at different positions measured from the centre line of the weld.*

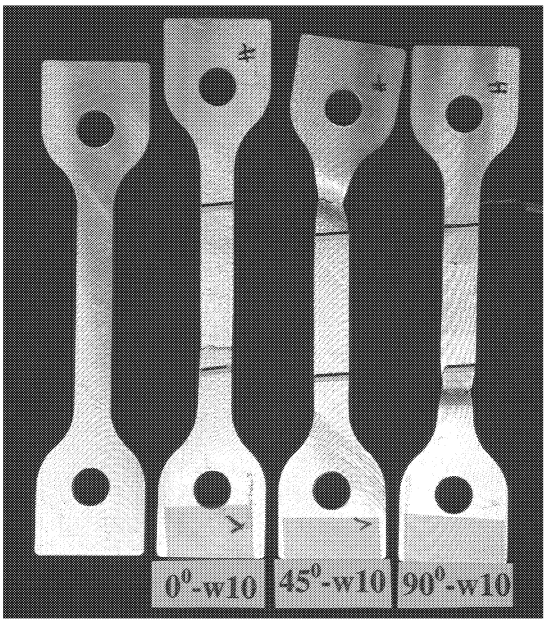

Figure 30 *Fractured specimens: 0^0-w10, 45^0-w10, 90^0-w10, and a virgin specimen.*

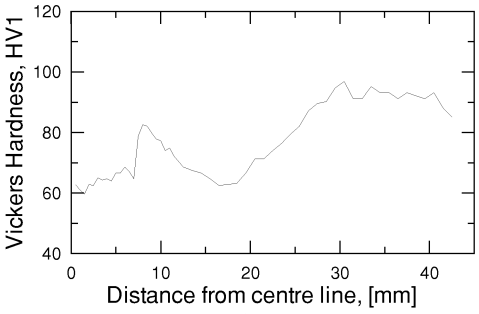

a)

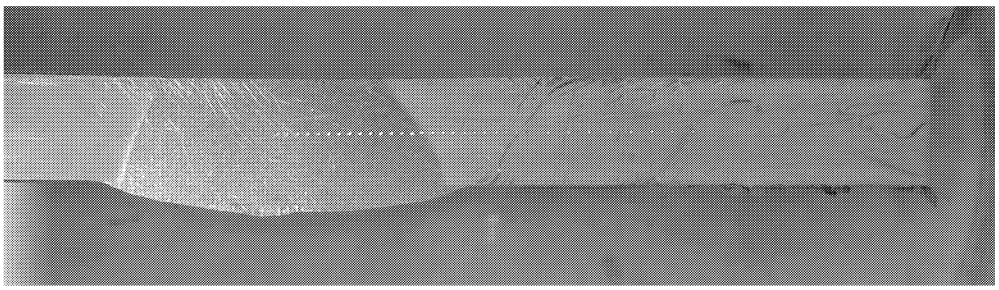

b)

Figure 31 Material data: a) Vickers Hardness profile, b) Vickers Hardness test specimen.

URN:NBN:no-3315

4 Component Tests

This chapter presents the results from impact tests on stiffened aluminium plates. The purpose of these tests was to explore the behaviour of stiffened aluminium plates subjected to large mass projectiles in the low velocity regime. Furthermore, the effects of various modelling parameters on the behaviour have been studied. In addition to impact tests, static punch tests were carried out to examine any relationship between the dynamic and quasi-static behaviour.

4.1 Static test results

A summary of the static punch tests is listed in Table 4. The force at fracture, F_{su}, is defined as the maximum force at incipient fracture, and the corresponding energy, U_{su}, is defined as the area under the force-displacement curve. The definitions are given in Figure 32. The maximum centre displacement of the punch at incipient fracture of the plate or stiffener and the permanent central displacement of the plate are denoted w_{cm} and w_{cp}, respectively. The permanent central displacement w_{cp} is only given for the tests where the test specimens were unloaded. The mean values and the coefficient of variation, i.e. standard deviation divided by mean value, for F_{su}, U_{su}, and w_{cm} is also given. The identification of the test specimens and thickness are given in Table C-1.

4.1.1 Effect of nose shape

Load between stiffeners at the weld

The local failure modes were a function of the nose shape of the punch as well as the point of load application. Applying the load in the span between the stiffeners, test series D1 and D2, two failure modes were observed. Using a blunt ended punch a shear failure mode was found as Figure 33 shows, whereas using a hemispherical nose petals were created, see Figure 34.

Figure 33a and Figure 33b show the shear failure mode, rear and front, for a test specimen loaded beyond the point of incipient fracture. The fracture started at the circumference of the blunt ended nose parallel to the weld (Point A in Figure 33a and Figure 33b and propagated subsequently across the weld and into the base material. Orange peeling of the plate was observed at the circumference of the nose and cracking occurred through the plate thickness and approximately half way around the punch's circumference. Increasing the load further a single petal was pushed aside, see Figure 33c and Figure 33d.

Applying the load using a hemispherical ended punch, fracture zones on the rear surface normal to the weld and along both fusion lines (the transitions zones between weld and heat affected zones) appeared. Increasing the load further a through thickness crack occurred across the weld and in one of the fusion lines, Figure 34a and Figure 34b, and finally four petals were created. Figure 34c and Figure 34d show the petals created after the punch has perforated the plate and the load has dropped to zero.

Force-displacement curves for the blunt and hemispherical nose are shown in Figure 35a and in Figure 35b, respectively. A non-linear behaviour for small displacements of the punch was observed, whereas in the subsequent phase a monotonic rise in the punch load with respect to the displacement nearly up to failure was found. This indicates that bending of the

Table 4 Summary table of static test results (coefficients of variation in brackets and given in %).

Test Series	Test no.	Load Position	Nose Shape	F_{su} [kN]	U_{su} [kJ]	w_{cm} [mm]	w_{cp} [mm]	Mean F_{su} [kN]	Mean U_{su} [kJ]	Mean w_{cm} [mm]
D1	D1-1	Between stiffeners	Blunt	57.6	0.590	26.4	-	57.0 (1.0)	0.587 (0.6)	25.7 (2.9)
	D1-2	Between stiffeners	Blunt	56.6	0.583	25.8	-			
	D1-3	Between stiffeners	Blunt	56.7	0.588	24.9	-			
D2	D2-1	Between stiffeners	Hemispherical	34.9	0.365	27.5	-	32.2 (7.8)	0.319 (15.4)	25.3 (11.0)
	D2-2	Between stiffeners	Hemispherical	30.0	0.267	22.2	-			
	D2-3	Between stiffeners	Hemispherical	31.6	0.324	26.3	-			
E1	E1-1	On a stiffener	Blunt	81.7	1.222	30.7	21.5	80.0 (4.5)	1.177 (7.6)	30.7 (3.1)
	E1-2	On a stiffener	Blunt	75.9	1.074	29.8	21.6			
	E1-3	On a stiffener	Blunt	82.5	1.235	31.7	-			
E2	E2-2	On a stiffener	Hemispherical	59.2	0.930	29.6	22.7	57.9 (10.3)	0.899 (18.0)	29.0 (10.4)
	E2-3	On a stiffener	Hemispherical	51.4	0.724	25.7	25.0			
	E2-4	On a stiffener	Hemispherical	63.2	1.043	31.7	-			
F1	F1-1	Next to a stiffener	Blunt	60.5	0.775	24.9	-	63.9 (8.1)	0.828 (12.4)	25.6 (5.8)
	F1-2	Next to a stiffener	Blunt	69.2	0.931	27.0	22.1			
	F1-3	Next to a stiffener	Blunt	58.5	0.711	23.9	-			
	F1-4	Next to a stiffener	Blunt	67.3	0.896	26.8	21.0			
F2	F2-1	Next to a stiffener	Hemispherical	51.8	0.785	30.9	-	51.8 (4.9)	0.791 (9.3)	31.0 (5.4)
	F2-2	Next to a stiffener	Hemispherical	49.3	0.720	29.4	-			
	F2-3	Next to a stiffener	Hemispherical	54.4	0.867	32.7	27.6			

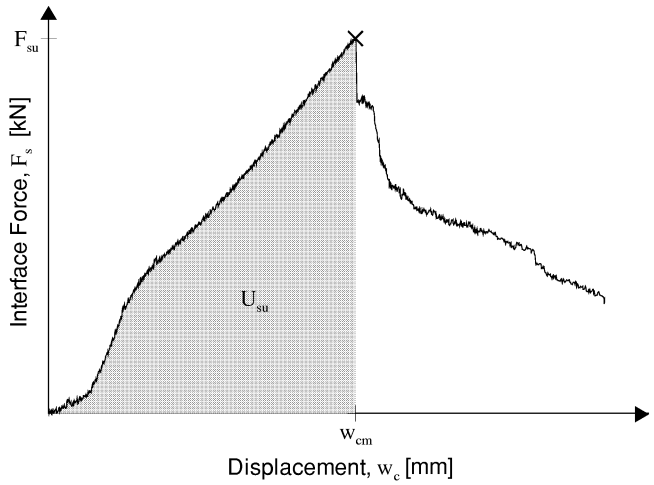

Figure 32 Symbol definitions.

plate controls the first phase, while membrane stresses control the response in the subsequent phase. The stiffness of the test specimens represented by the slope of the force-displacement curves varied throughout the test, but the variation between tests within a test series was small.

Figure 36a shows that the fracture appeared for approximately the same displacement of the punch, w_{cm}, for the two different nose shapes. The force at incipient fracture, F_{su}, and the corresponding energy, U_{su}, for the hemispherical ended punch were about 55 % of the values for the blunt ended punch, see Figure 37. Different global stiffness due to different load spread using the two nose shapes may be the reason for this. The local stress distribution will also be different and may result in different capacities using different nose shapes.

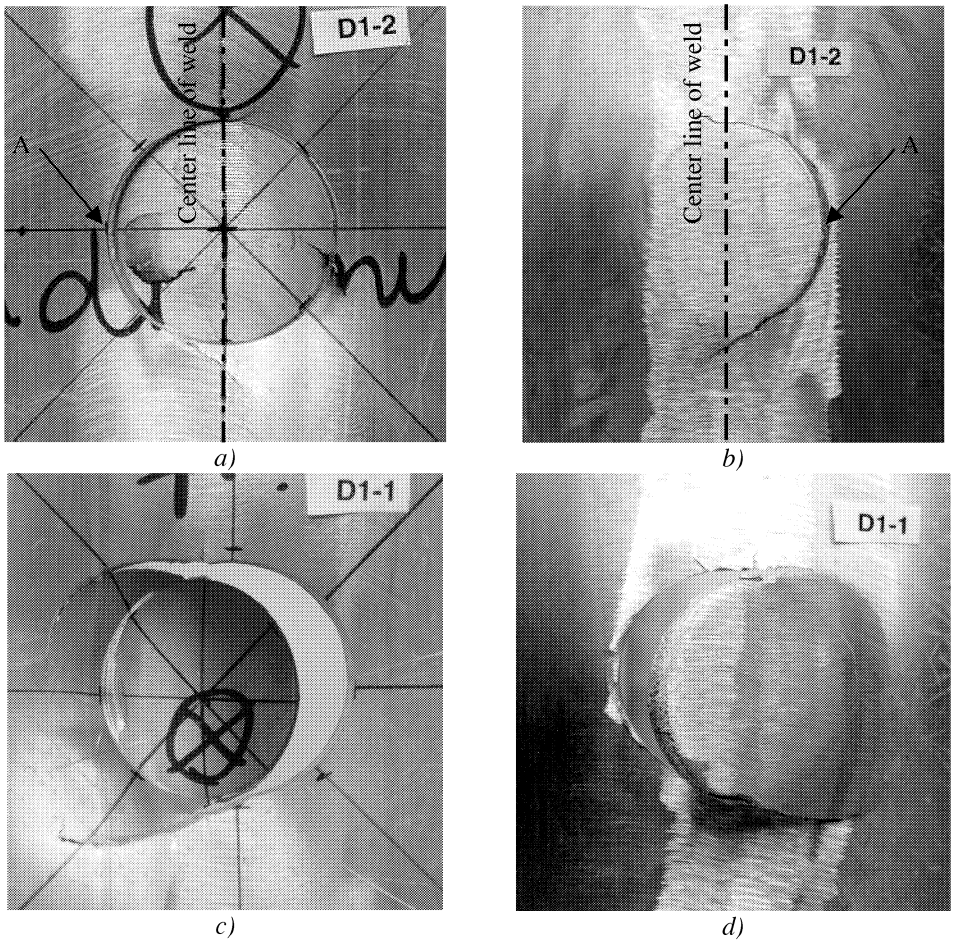

Figure 33 Shear failure mode (load position between stiffeners): a) D1-2 front, b) D1-2 rear, c) D1-1 front, d) D1-1 rear.

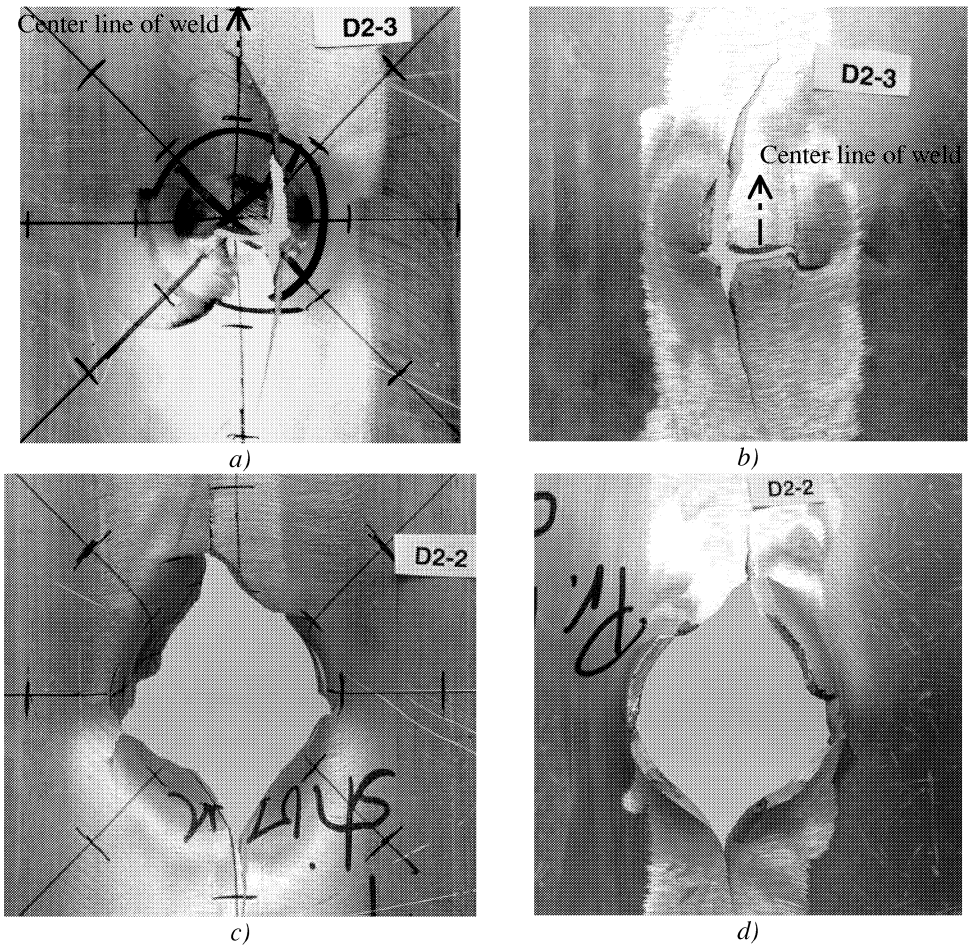

Figure 34 Petaling failure (load position between stiffeners): a) D2-3 front, b) D2-3 rear, c) D2-2 front, d) D2-2 rear.

Load on a stiffener

Load applied on the stiffener, test series E1 and E2, initiated diffuse necking of the bottom flange of the stiffener, followed by fracture which propagated into the web as shown in Figure 38b and Figure 38d for the blunt and hemispherical ended nose, respectively. Increasing the deformation of the test specimen beyond the displacement corresponding to the maximum load, the fracture propagated to the top flange. Using the blunt ended nose fracture, occurred in the top flange around the circumference of the nose as well as parallel to the stiffener, see Figure 38a and Figure 38b. For the hemispherical nose fracture occurred normal to and along the stiffener, see Figure 38c and Figure 38d.

Force-displacement curves for the blunt and hemispherical nose are shown in Figure 35c and Figure 35d, respectively. For this load position a non-linear behaviour with an overall increasing stiffness were measured. However, a distinct softening phase took place at about one quarter of the maximum displacement, w_{cm}. During the testing it was observed that the stiffener started to rotate about its longitudinal axis at a load of approximately 50 kN.

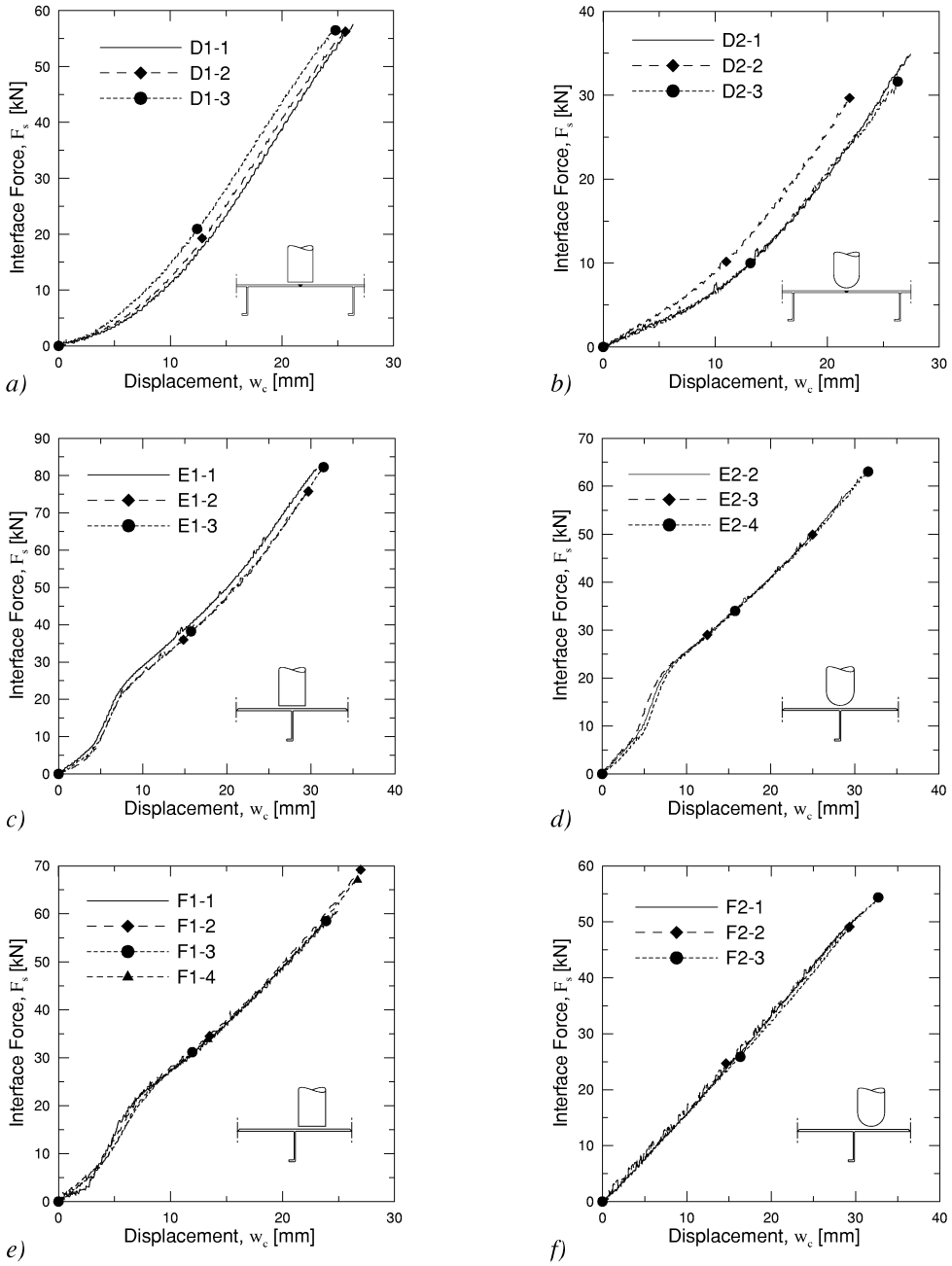

Figure 35 Force displacement curves: a) load position between stiffeners and blunt ended nose, b) load position between stiffeners and hemispherical nose, c) load position on a stiffener and blunt ended nose, d) load position on a stiffener and hemispherical nose, e) load position next to a stiffener and blunt ended nose, f) load position next to a stiffener and hemispherical nose.

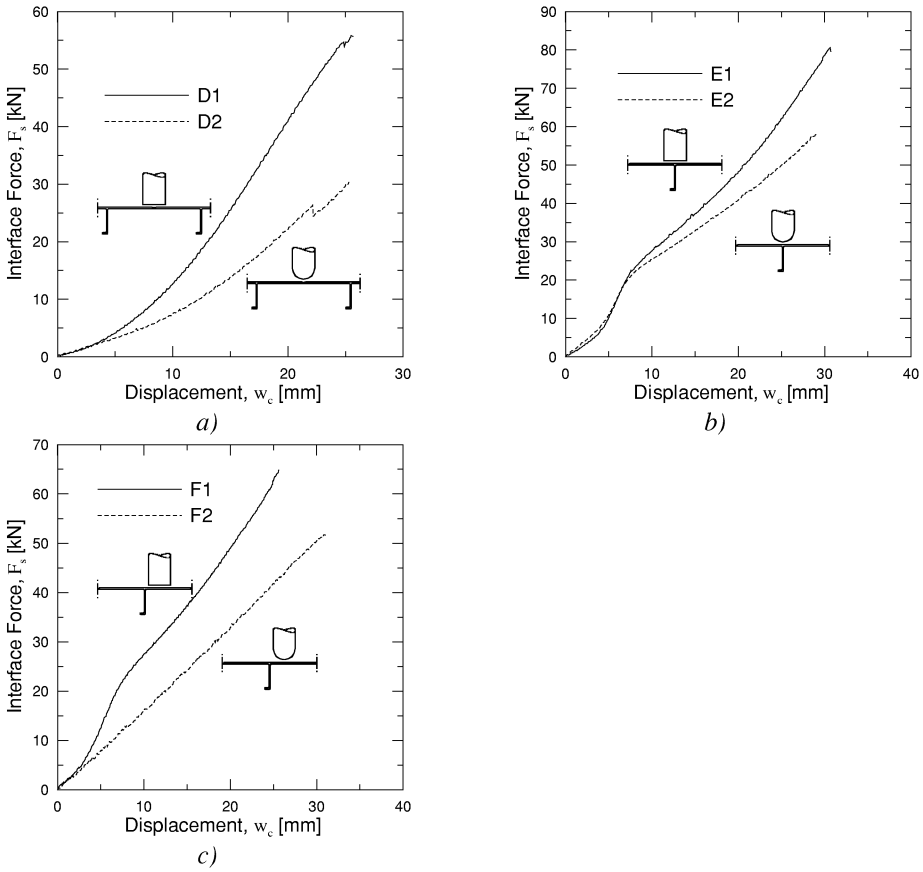

Figure 36 Mean force-displacement curves for a blunt and hemispherical ended nose: a) load position between stiffeners, b) load position on a stiffener, c) load position next to a stiffener.

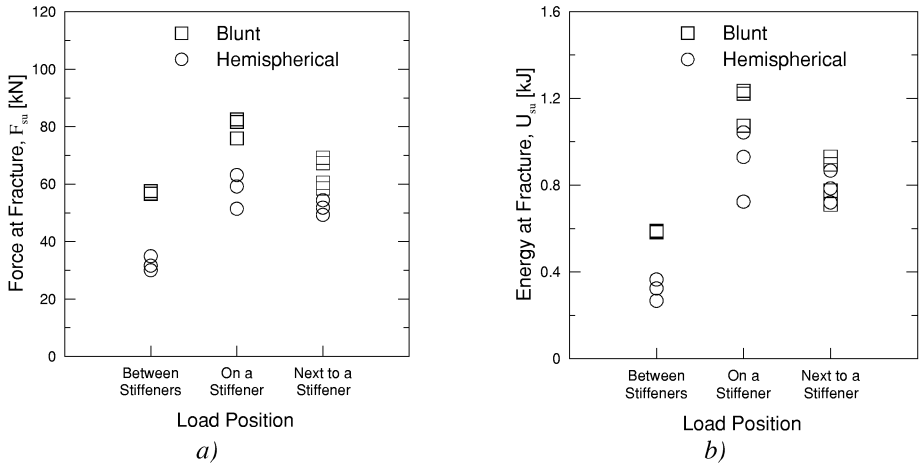

Figure 37 a) Force at fracture, and b) absorbed energy at fracture.

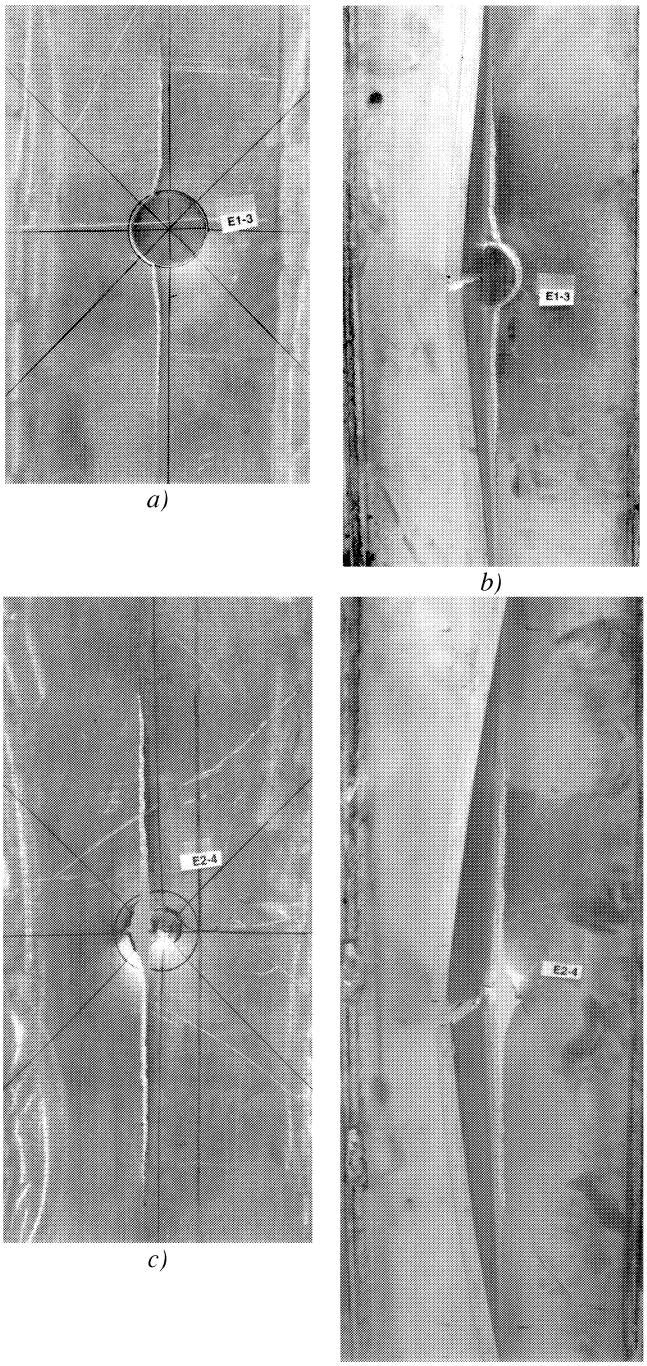

a) *b)* *c)* *d)*

Figure 38 Tensile failure of the flange of the stiffener (load position on a stiffener): a) blunt nose, front b) blunt nose, rear, c) hemispherical nose, front, d) hemispherical nose, rear.

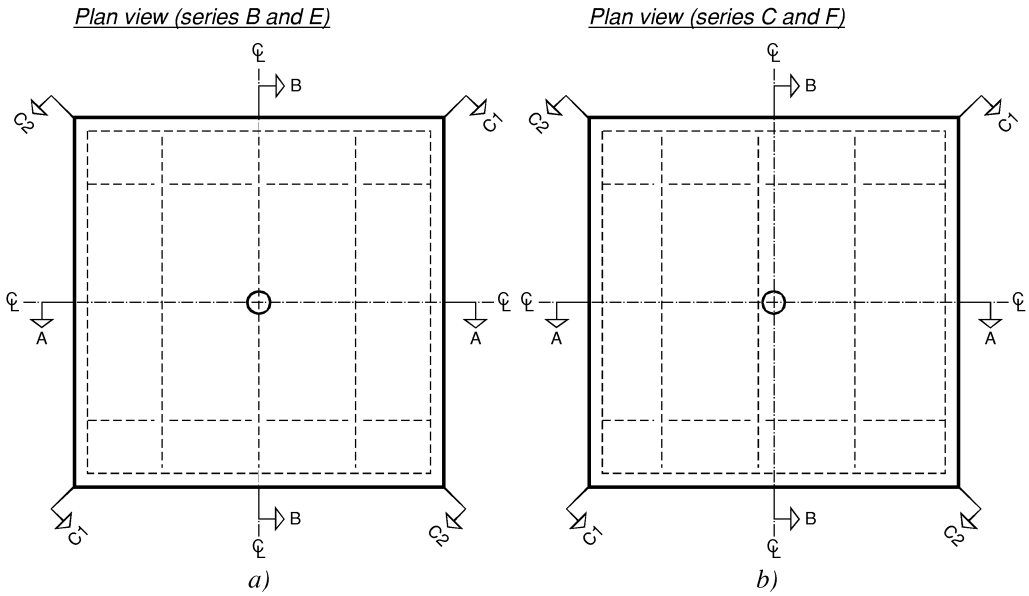

Figure 39 Sections for measurements of permanent deformations: a) load position on a stiffener, b) load position next to a stiffener.

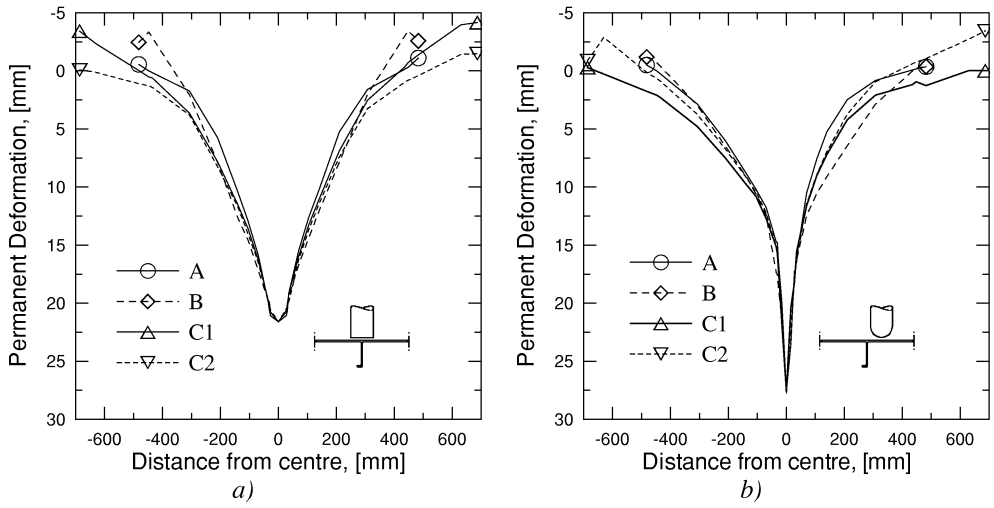

Figure 40 Permanent deformation in four different sections: a) load position on a stiffener and blunt nose (E1-2), b) load position next to a stiffener and hemispherical ended nose (F2-3).

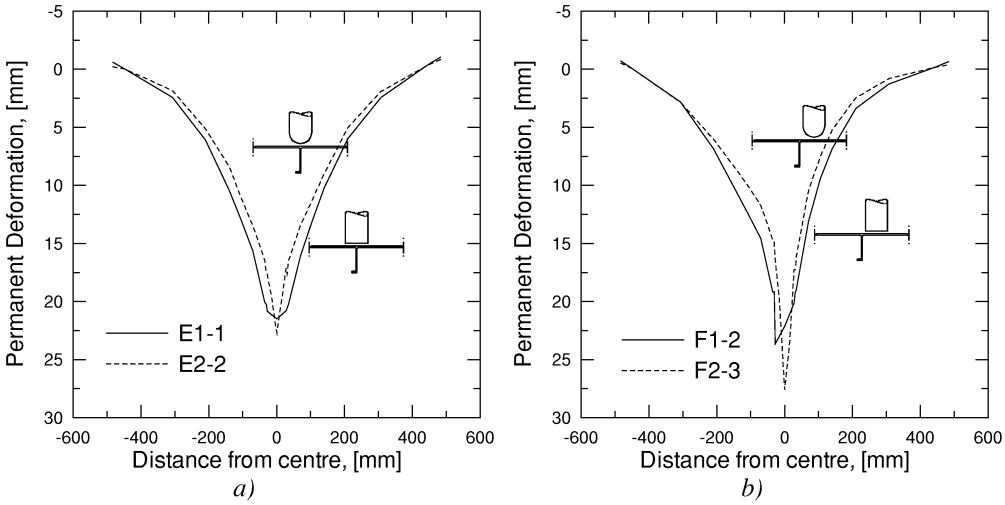

Figure 41 Permanent deformations Section A for blunt and hemispherical ended nose: a) load position on a stiffener, b) load position next to a stiffener.

Figure 36b shows that the maximum central displacement was approximately the same for the blunt and hemispherical ended nose. The mean force at incipient fracture and the corresponding energy using a hemispherical nose were approximately 75 % compared with a blunt nose, see Table 4 and Figure 37.

Large plastic deformations extended from the point of load application to the supports. The permanent deformations were measured in four different sections, in the longitudinal direction, Section B, in the transverse direction, Section A, and diagonally, Sections C1 and C2, as shown in Figure 39. Figure 40 presents the permanent deformations, w_p, of the test specimens unloaded after incipient fracture. The curves in Figure 40a show that the permanent deformation was somewhat more localised in the transverse direction (Section A) than in the longitudinal direction (Section B).

The permanent deformation in the transverse direction, Section A, for a blunt ended nose and for a hemispherical nose are shown in Figure 41a. The permanent deformation profile was symmetric about the load position. A hemispherical ended nose gave more localisation of the permanent deformation than a blunt ended nose. More than 70 % of the maximal centre displacement (w_{cm}) remained permanent after unloading, see Table 4.

Load next to a stiffener

Applying the load next to a stiffener, test series F1 and F2, resulted in similar failure modes as when the load was applied in the middle of the span between the stiffeners. A shear failure mode and considerable orange peeling of the top flange at the circumference of the nose were observed for a blunt ended nose. The fracture occurred in the top flange at the circumference of the punch next to the stiffener as seen in Figure 42a and Figure 42b. Increasing the load beyond the maximum load a single petal was pushed aside, see Figure 42c and Figure 42d.

Using a hemispherical nose, two fracture zones in the plate surface in the stiffener direction appeared. The zone next to the stiffener developed a through thickness crack at maximum load, see Figure 43a and Figure 43b. Further loading resulted in a single petal with a width approximately three times the projectile nose diameter, as seen in Figure 43c and Figure 43d.

Force-displacement curves for the blunt and hemispherical nose are shown in Figure 35e and in Figure 35f, respectively. For the blunt ended nose a similar stiffness development as observed for load position on a stiffener was found. Using a hemispherical nose an almost linear relationship between the interface force and the displacement was obtained.

Figure 37 shows that the energy at incipient fracture was nearly the same for the two noses used. The reason was that the force at incipient fracture for the hemispherical nose was 81 % compared with the blunt nose, while the maximum centre displacement of the blunt ended punch was 83 % compared with the hemispherical ended punch (Table 4 and Figure 36c).

The permanent deformation of panels loaded next to a stiffener is shown in Figure 40b for a hemispherical ended nose. The curves of the permanent deformations in the four measured sections, show that the permanent deformation was more localised in the transverse direction than in the longitudinal direction. The permanent deformation profile was only symmetric in the longitudinal direction due to the fact that the load application was next to a stiffener. The permanent deformation was less beside the stiffener than on the other side of the loading point.

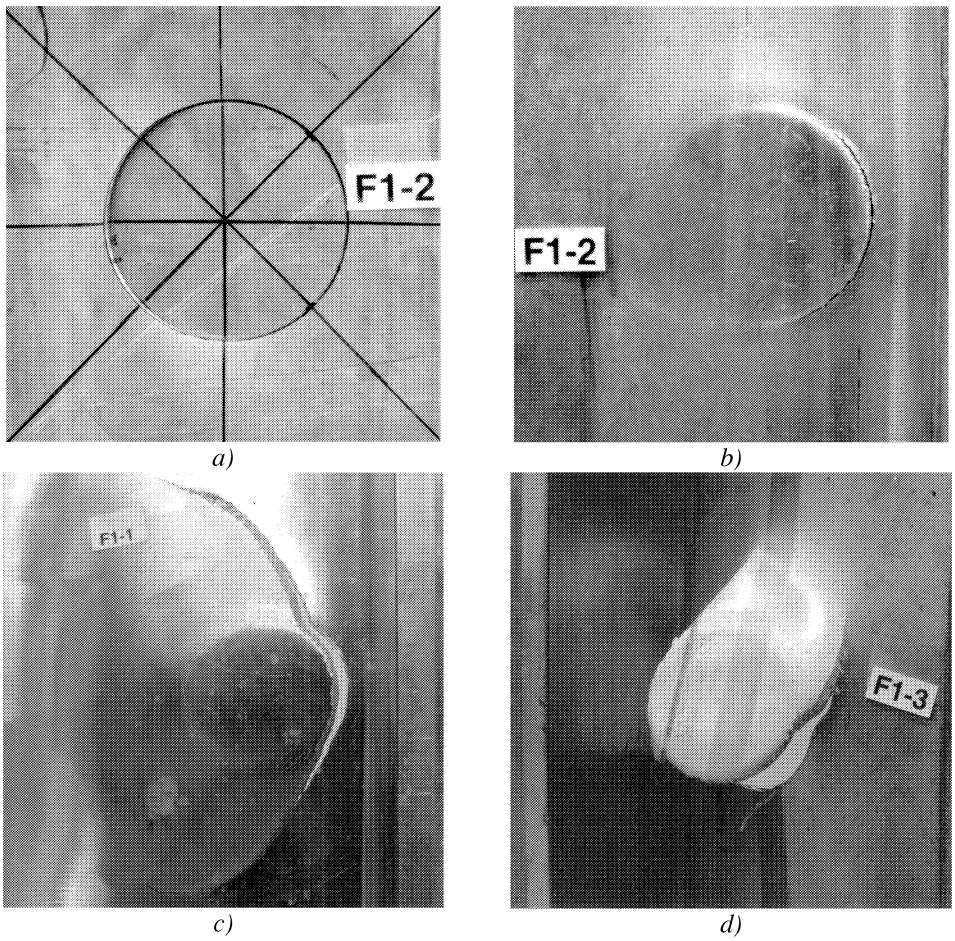

Figure 42 Shear failure mode (impact just next to the stiffener's position): a) F1-2 front, b) F1-2 rear, c) F1-1 rear, d) F1-3 rear.

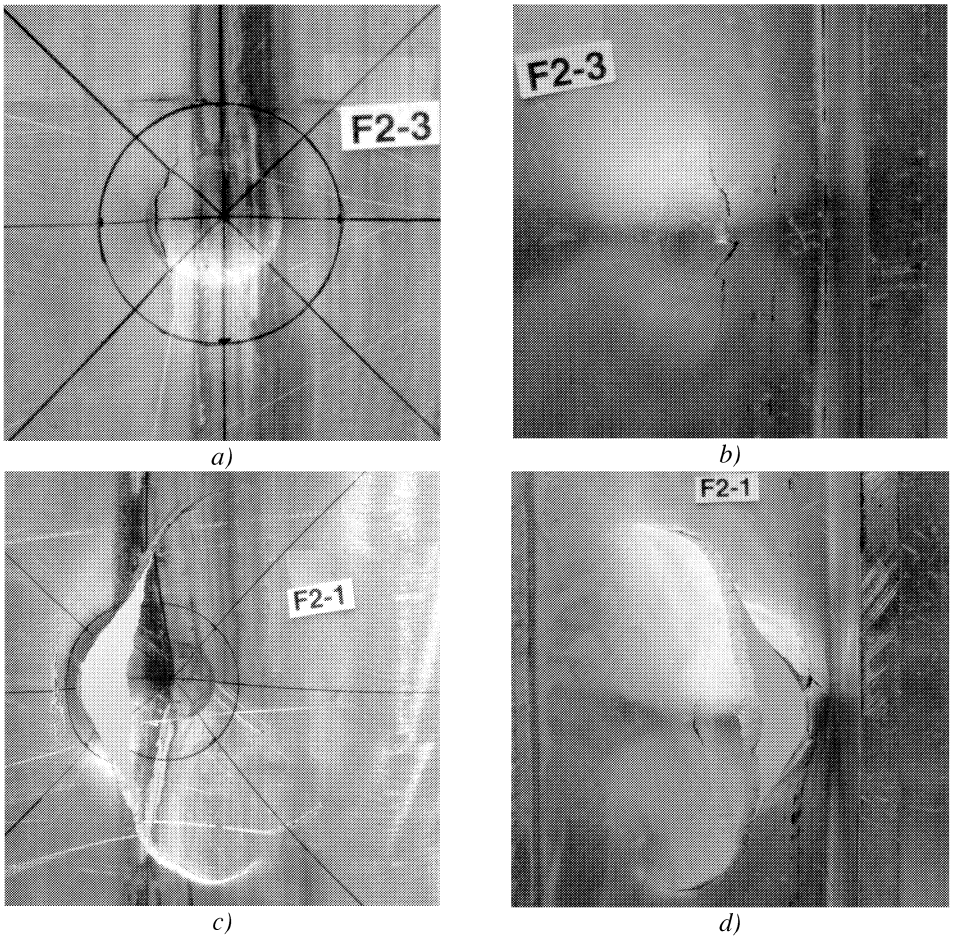

Figure 43 Petaling failure (impact just next to the stiffener's position): a) F2-3 front, b) F2-3 rear, c) F2-1 front, d) F2-1 rear.

A hemispherical ended nose, test F2-3, gave more localisation of the permanent deformation than a blunt ended nose, test F1-2, as shown in Figure 41b. More than 70 % of the maximal centre displacement (w_{cm}) remained permanent after unloading, see Table 4.

4.1.2 Effect of the point of load application

Blunt nose

Figure 44a shows the mean force-displacement curves for a blunt ended nose. The force at incipient fracture was significant larger for the load position on a stiffener, series E1, than for the two other cases. Thus the energy absorbed by the test specimen represented by the area below the force-displacement curve was significant larger for test series E1. Furthermore, it is worth noting that the force displacement curves for series E1 and F1 (next to a stiffener) were approximately equal.

The permanent deformation of two tests unloaded after incipient fracture is shown in Figure 45a. The permanent deformation profile in Section A for load position on a stiffener was nearly the same as for load position next to a stiffener. Load applied next to a stiffener gave a nonsymmetrical profile due to the nonsymmetrical geometry of the test specimen.

Hemispherical nose

The mean force-displacement curves for a hemispherical ended nose are shown in Figure 44b. The force at incipient fracture was largest for the load position on a stiffener, series E2, less for the load position next to a stiffener, F2, and least for the load position between stiffeners, D2. The energy absorbed by the test specimen when applying the load on a stiffener was 2.8 times the corresponding energy absorbed between the stiffeners.

The permanent deformation profiles for test series E2 and F2 are given in Figure 45b. The load position next to a stiffener gave a more localised deformation at the point of load application than load position on a stiffener.

4.1.3 Summary of static test results

The observation from the static tests can be summarised as follows:

- The local failure mode was a function of the model parameters; i.e. the load application point and the nose shape. Shear failure mode, tensile failure of the top flange, and tensile failure of the bottom flange were observed due to this variability.
- The energy absorbed by the test specimens and the force at incipient fracture were larger using a blunt ended nose than a hemispherical ended nose.
- The absorbed energy and force at incipient fracture were larger when applying the load on a stiffener than next to a stiffener. The weakest point occurred when the load was applied between the stiffeners, i.e. on the weld.
- The stiffness of the plate was largest using a blunt ended nose

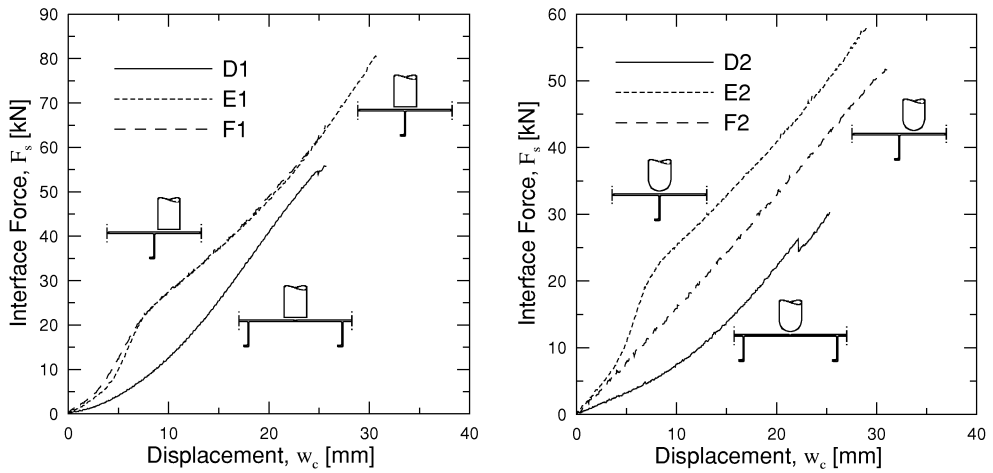

Figure 44 Mean force-displacement curves for different load positions: a) a blunt ended nose, b) a hemispherical ended nose.

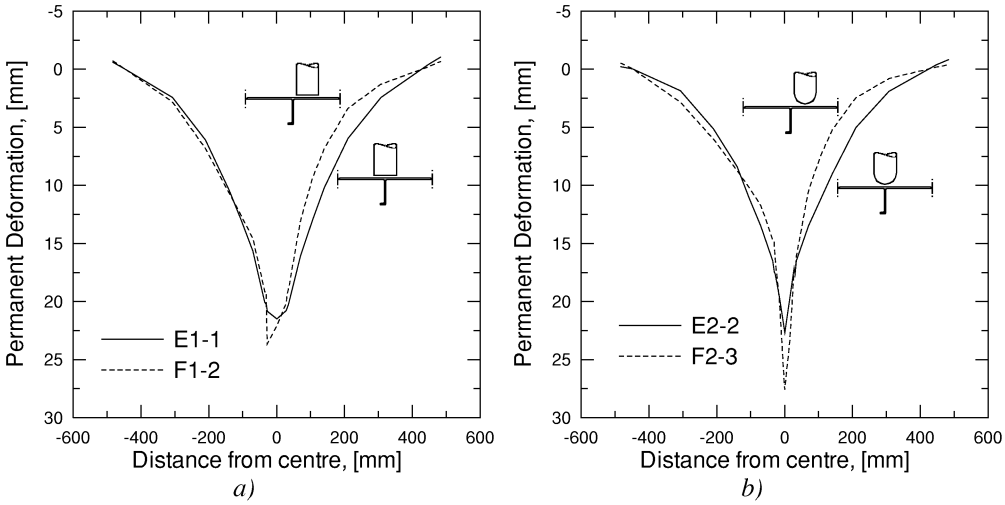

Figure 45 Permanent deformations, Section A, for load position on a stiffener and next to a stiffener: a) blunt ended nose, b) hemispherical ended nose.

4.2 Dynamic test results

A summary of the dynamic test results is presented in Table 5. The definition of the symbols in the table is as follows; v_i is the impact velocity, and T_p is the corresponding kinetic energy of the projectile at impact. The maximum force, F_{dm}, is the measured maximum interface force between the target and the projectile. Owing to oscillations caused by stress waves in the load cell, the maximum force was taken as an average of those oscillations. The centre displacement, w_{cu}, is defined as the calculated displacement of the projectile at maximum force. The residual velocity, v_r, is defined as the calculated velocity of the projectile when the interface force is equal to zero. The duration of the impact, t_d, is defined as the time elapsed from the initial impact to the instant when the force equals zero. The penetration cases called rebound, containment, and perforation are defined in Chapter 1.

The different impact locations, the shape of the projectile nose, the mass of the projectile, thickness of the target plate, and identification of the test specimens are listed in Table D-1. A complete set of response parameters from the dynamic tests is given in Table D-2.

All time histories and force-displacement curves are presented in Appendix D. The force-time curves show that the impact can be divided into two distinct phases as described by Langseth and Larsen (1994), i.e. the transient phase and the global mode phase separated by the time at which the supports were activated. In the transient phase only inertia forces were present, while in the global mode phase the supports were fully activated. An almost linear relationship was also found between the force and displacement in the global mode phase. In all test series, some oscillations with a period of approximately 0.42 ms were present, see e.g. Figure 57 and Figure 59. According to Langseth (1988), the oscillations were due to stress waves in the projectile. No separate measurements have been carried out to determine the transition between the two phases.

Table 5 Dynamic test result table.

Test no.	v_i [m/s]	T_p [kJ]	F_{dm} [kN]	w_{cu} [mm]	v_r [m/s]	t_d [ms]	Penetration	Failure mode
A1-6	3.72	0.382	46.0	20.3	-2.50	13.4	Rebound	No failure
A1-8	4.08	0.459	48.7	24.3	-2.43	13.7	Rebound	No failure
A1-9	4.90	0.666	61.9	25.3	-3.14	13.0	Rebound	Cracking
A1-5	5.07	0.709	-	-	-	-	Rebound	Cracking
A1-7	5.98	0.988	59.5	23.0	-2.42	16.1	Rebound	Cracking
A1-3	6.61	1.206	58.1	27.1	0.84	21.1	Rebound	Cracking
A1-4	7.08	1.383	69.0	30.4	1.68	10.0	Perforation	Plugging
A1-2	7.33	1.485	-	-	-	-	Perforation	Plugging
A1-1	7.67	1.624	-	-	-	-	Perforation	Single petal
A2-9	2.35	0.152	21.2	17.0	-1.60	18.4	Rebound	Cracking
A2-8	3.38	0.315	33.3	22.6	-2.09	16.6	Rebound	Cracking
A2-7	3.38	0.314	27.7	22.9	-1.59	19.6	Rebound	Cracking
A2-5	3.47	0.331	29.6	27.4	-1.66	18.9	Rebound	Cracking
A2-4	4.74	0.619	-	32.4	-0.60	17.7	Rebound	Cracking
A2-6	6.24	1.070	29.2	39.4	-1.08	26.8	Rebound	Four petals
A2-1	6.63	1.209	36.0	27.0	-0.26	25.6	Rebound	Four petals
A2-2	7.33	1.477	37.2	26.8	1.24	54.8	Perforation	Four petals
A2-3	7.85	1.695	40.6	28.3	3.10	26.2	Perforation	Four petals
B1-7	4.78	0.633	54.4	21.3	-2.50	12.4	Rebound	No failure
B1-1	6.39	1.130	77.0	29.7	-3.13	12.1	Rebound	No failure
B1-5	6.78	1.274	83.9	29.3	-3.49	11.5	Rebound	No failure
B1-2	7.12	1.403	90.0	31.9	-3.42	11.5	Rebound	No failure
B1-6	7.33	1.487	89.3	31.7	-3.19	12.2	Rebound	Failure of stiffener
B1-4	7.62	1.608	89.9	31.4	-3.76	13.0	Rebound	Failure of stiffener
B1-3	8.68	2.084	92.1	32.2	-3.94	13.2	Rebound	Failure of stiffener/top flange
B2-2	4.84	0.647	50.2	23.0	-2.16	12.6	Rebound	No failure
B2-1	5.94	0.974	61.0	27.3	-2.69	12.3	Rebound	Failure of top flange
B2-6	6.25	1.077	66.2	29.7	-2.90	12.3	Rebound	Failure of top flange
B2-5	6.54	1.181	64.6	31.1	-2.77	15.0	Rebound	Failure of top flange/stiffener
B2-4	6.85	1.296	-	-	-	-	Rebound	Failure of top flange/stiffener
B2-3	7.44	1.527	68.5	29.9	-3.26	14.1	Rebound	Failure of top flange/stiffener
B2-7	8.58	2.032	61.3	28.6	-3.19	17.3	Rebound	Failure of top flange/stiffener
C1-4	5.47	0.827	60.9	25.3	-2.61	12.6	Rebound	No failure
C1-3	6.19 *)	1.060	66.8	26.2	-2.59	13.1	Rebound	Cracking
C1-5	6.19	1.060	71.7	27.6	-3.12	12.8	Rebound	Cracking
C1-7	6.98	1.348	73.6	31.7	-2.21	14.5	Rebound	Cracking
C1-2	6.99	1.353	70.1	27.2	0.75	9.3	Containment	Plugging
C1-6	7.72	1.651	72.3	28.8	2.72	7.1	Perforation	Plugging
C1-1	8.28	1.897	69.8	27.6	3.98	5.8	Perforation	Plugging
C2-7	3.47	0.332	34.3	19.4	-2.05	15.2	Rebound	No failure
C2-3	4.34	0.520	40.9	25.4	-2.34	14.9	Rebound	Cracking
C2-2	5.68	0.891	57.9	31.2	-2.88	13.9	Rebound	Cracking
C2-1	6.22	1.069	65.9	30.3	-3.08	12.9	Rebound	Cracking
C2-4	7.41	1.513	65.4	37.1	-2.08	15.7	Rebound	Single petal
C2-5	8.53	2.008	67.2	40.0	-0.96	22.1	Rebound	Single petal
C2-6	9.57	2.525	59.8	32.8	4.68	10.4	Perforation	Single petal

*)Assumed

4.2.1 Effect of increasing velocities

The incipient fracture velocity, v_{iu}, and the ballistic limit velocity, v_{ic}, as defined in Chapter 1, were estimated by gradually varying the impact velocity of the projectile. The corresponding impact energies are the incipient fracture energy, T_{pu}, and the critical impact energy, T_{pc}. The method used to obtain these values is illustrated in Figure 46. Figure 46 shows the impact energy vs. the test series. In a target impacted with energy below the incipient fracture energy, no failure was seen. Cracks were observed in a target struck by a projectile with impact energy between the incipient fracture energy and the critical impact energy. The projectile rebounded in those cases. Increasing the impact energy further, the projectile perforated the target for an impact energy that exceeded the critical impact energy. In test series A2 where a hemispherical nosed projectile impacted between the stiffeners, the lowest velocity was taken as the incipient fracture velocity even though surface cracks was observed. No attempt was made to perforate the target in the case of impact on a stiffener (test series B1 and B2). The estimated values of the incipient fracture energy and the critical impact energy are listed in Table 6.

The maximum forces at incipient fracture and perforation (critical force) were denoted F_{du} and F_{dc}, respectively. The values were estimated in the same way as T_{pu} and T_{pc}. The maximum force, the incipient fracture force, and the critical force are plotted vs. the test series in Figure 47. The impact velocities varied from 2.35 to 9.57 m/s, and the sequence of events during crack initiation and propagation was established.

Table 6 Estimated dynamic test results.

Test Series	Impact Location *)	Nose Shape **)	v_{iu} [m/s]	T_{pu} [kJ]	F_{du} [kN]	v_{ic} [m/s]	T_{pc} [kJ]	F_{dc} [kN]	Failure Mode
A1	B	B	4.5	0.56	53.4	6.8	1.29	65.4	Plugging/Petaling
A2	B	H	<2.35	<0.15	<21.2	7.0	1.34	36.6	Petaling
B1	O	B	7.2	1.44	89.6	-	-	-	Fracture of stiffener
B2	O	H	5.4	0.81	55.6	-	-	-	Fracture of top flange
C1	N	B	5.8	0.94	63.8	7.0	1.35	68.5	Plugging
C2	N	H	3.9	0.43	37.6	9.1	2.27	58.9	Petaling

*) B means between stiffeners, O means on a stiffener, and N means next to a stiffener
**) B means blunt and H means hemispherical

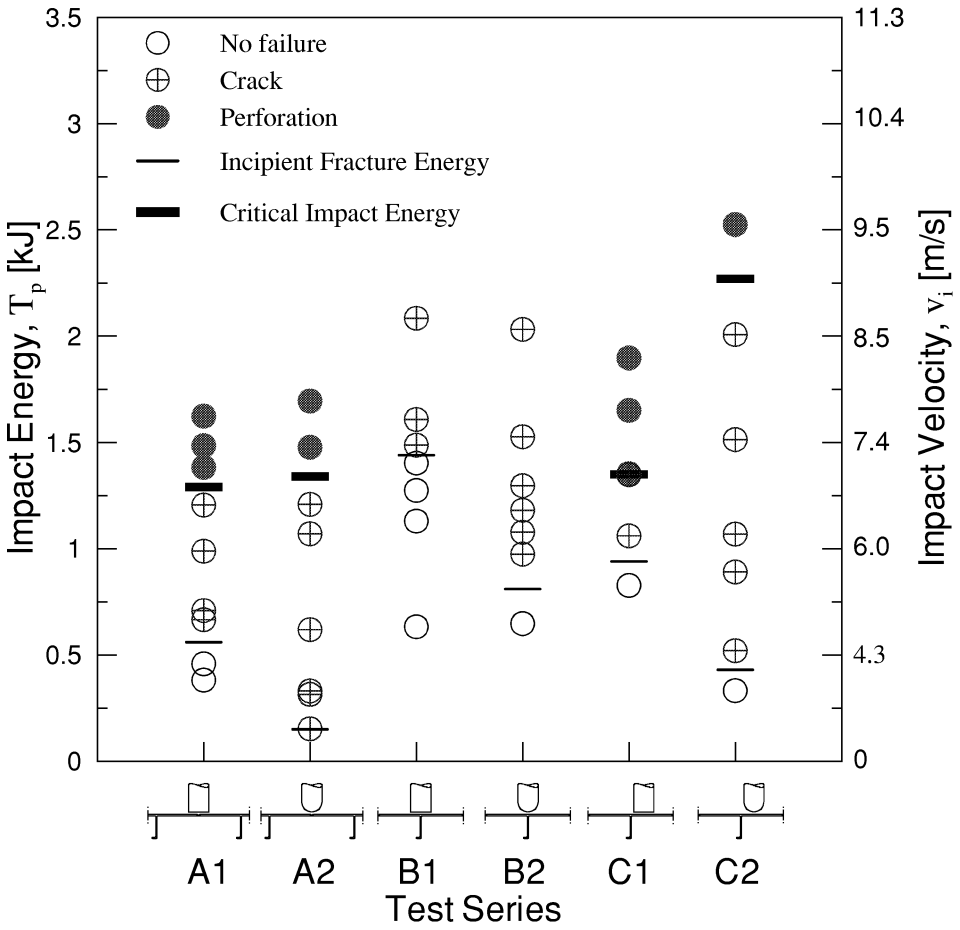

Figure 46 Impact energy vs. test series.

4.2.1.1 Test series A1

Test series A1 is the case where the blunt projectile impacted in the centre between two stiffeners. For a velocity slightly above the estimated incipient fracture velocity of 4.5 m/s, surface cracks in both fusion lines were observed on the rear side of the target plate as observed for specimen A1-9 with $v_i = 4.90\,\mathrm{m/s}$. Increasing the impact velocity, cracking occurred through the plate thickness and approximately half way around the circumference of the projectile as shown in Figure 48a and Figure 48b. When the crack reached the welding deposit it continued in the fusion line. Thus the plugs from this test series were not circular. Increasing the velocity above the estimated ballistic limit of 6.9 m/s either a plug was removed or a single petal was pushed aside as shown in Figure 48c and Figure 48d.

When a plugging failure occurred in the plate, a plug having approximately the same diameter as the projectile was completely separated from the plate. The plugs from the tests are shown in Figure 49. The shape of a plug is shown schematically in Figure 50. A thinning effect around the plug circumference was found, and the plug had a variable shear zone that

made an angle to the normal of the plate. After impact the diameter of the hole in the plate was smaller than the diameter of the projectile due to the elastic recovery of the plate.

Figure 51, Figure 52, and Figure 53 show some typical force-, velocity-, and displacement-time histories together with the corresponding force-displacement curves. The curves presented are tests where rebound, cracking with rebound, and perforation of the target plate occurred. From Figure 52 it is obvious that a cracked plate can absorb additional external energy before it is perforated. The initial failure is here seen as a sudden drop in the force-time curve from maximum force.

For a shear failure mode a sudden drop in the interface force, F_d, was found, before the final shearing of the plug from the plate took place. When a plug was separated from the plate the interface force dropped to zero. In this test series the maximum force, F_{dm}, was an increasing function of the impact velocity, v_i, see Table 5. The impact duration, t_d, was largest for impact resulting in partial fracture.

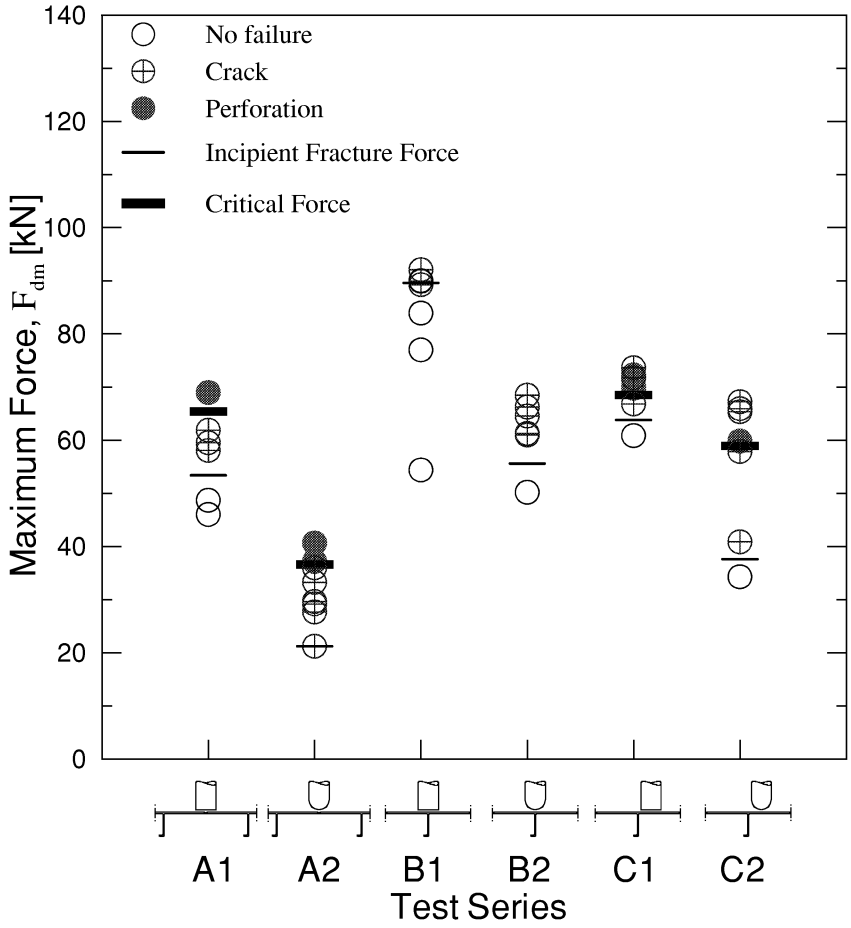

Figure 47 Maximum force vs. test series.

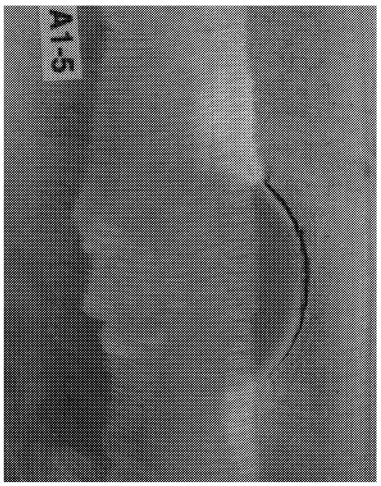

a) A1-5 rear, $v_i = 5.07\,m/s$

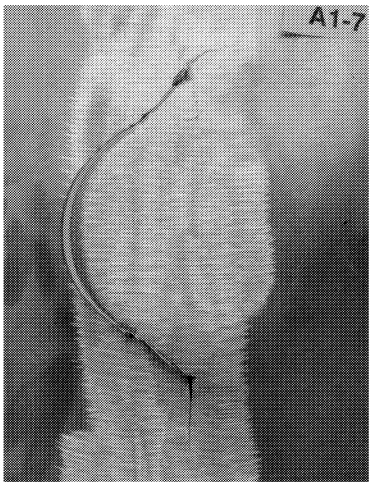

b) A1-7 rear, $v_i = 5.98\,m/s$

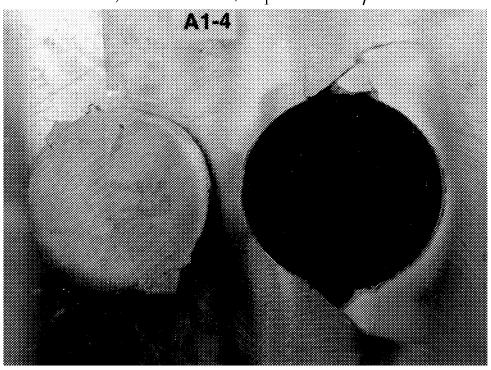

c) A1-4 rear, $v_i = 7.08\,m/s$

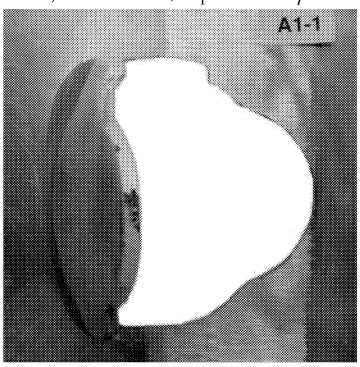

d) A1-1 rear, $v_i = 7.67\,m/s$

Figure 48 Different failure modes for increasing impact velocities impacting between the stiffeners with a blunt projectile: a) and b) shear failure mode, c) plugging, and d) single petal.

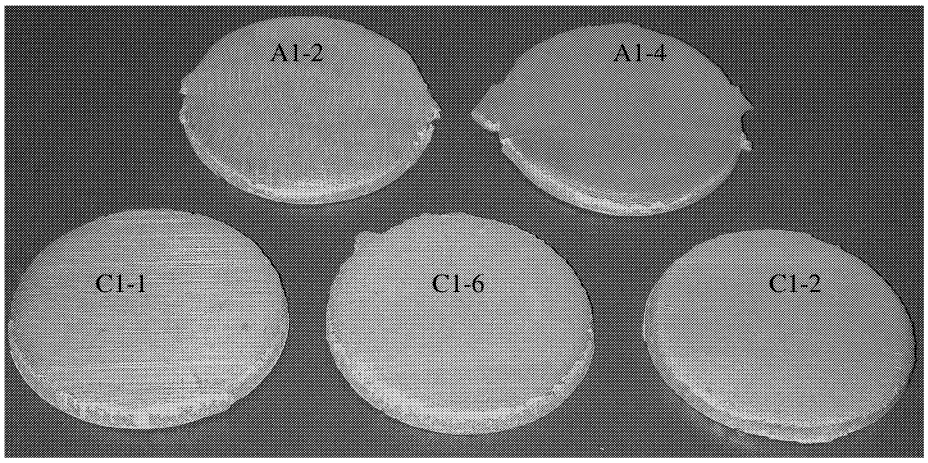

Figure 49 Plugs from dynamic tests, rear side: A1-4, A1-2, C1-2, C1-6, and C1-1.

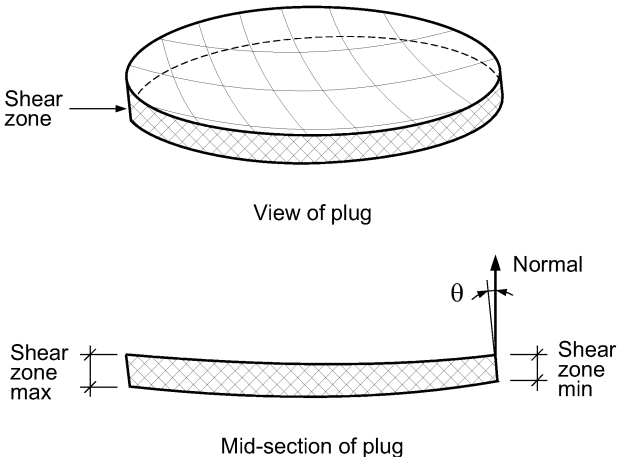

Figure 50 Characteristics of a plug.

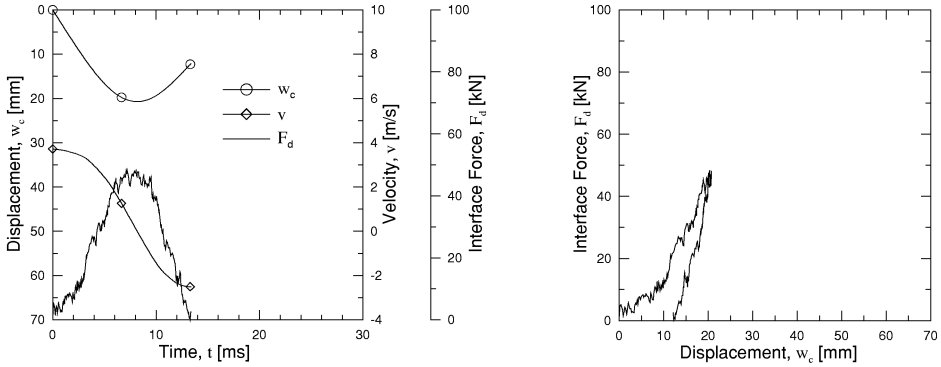

a) Displacement, velocity and force histories *b) Force-displacement curve*

Figure 51 Test A1-6; $v_i = 3.72\,m/s$ *: No cracks. Rebound.*

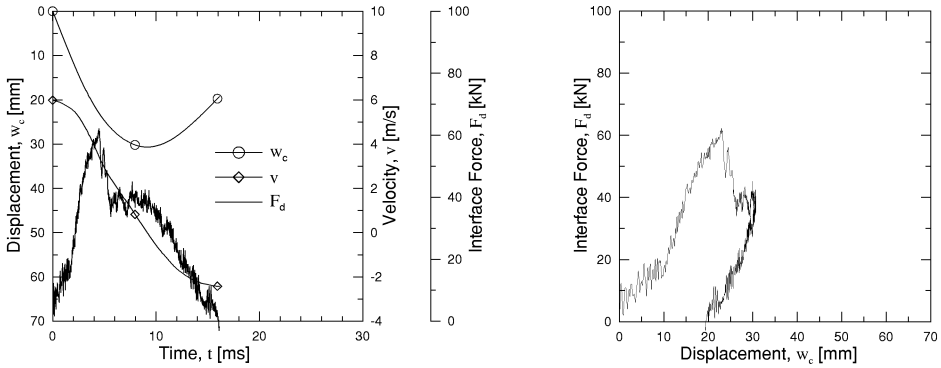

a) Displacement, velocity and force histories *b) Force-displacement curve*

Figure 52 Test A1-7; $v_i = 6.24\,m/s$ *: Shear failure. Rebound.*

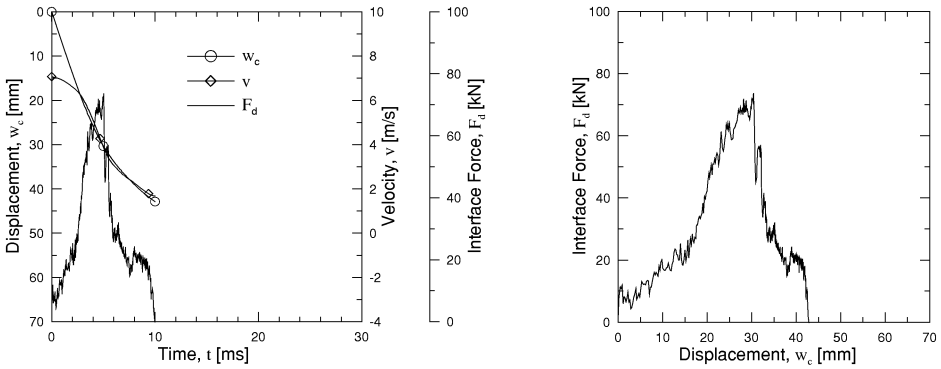

a) Displacement, velocity and force histories *b) Force-displacement curve*

Figure 53 Test A1-4; $v_i = 7.08\,m/s$ *: Plugging. Perforation.*

4.2.1.2 Test series A2

Test series A2 is the case where the hemispherical projectile impacted in the centre between the stiffeners. For low velocity impact, i.e 2.4 m/s, surface cracks in the fusion lines were observed on the rear side of the target plate, see Figure 54a. Increasing the impact velocity cracking occurred through the plate thickness and across the weld, see Figure 54b. Further increase of the impact velocity caused a petaling failure mode, Figure 54c. For velocities above the estimated ballistic limit of 7 m/s, four petals were pushed aside during the perforation of the plate as depicted in Figure 54d.

Figure 55, Figure 56, and Figure 57 show some typical force-, velocity-, and displacement-time histories together with the corresponding force-displacement curves. The presented curves are for tests where cracking and perforation of the target plate were found. Furthermore, it has been found that the difference in impact energy between the case when a crack first is visible and full perforation can be significant, confer Figure 46.

A significant difference was seen in the force-displacement curves between the case of surface cracks and the case of petaling with rebound, see Figure 55 and Figure 56, respectively. For the highest impact velocity resulting in rebound and for the lowest impact velocity leading to perforation a sudden drop in the interface force curve was found. The subsequent curve was a decreasing function with respect to for instance displacement, see Figure 56 and Figure 57.

The duration of the impact, t_d, was an increasing function of the impact energy, T_p, up to perforation. For a velocity above the ballistic limit the duration decreased.

4.2.1.3 Test series B1

Test series B1 is the case where the blunt projectile impacted on a stiffener. For an impact velocity of 6.8 m/s diffuse necking of the bottom flange was clearly visible, see Figure 58a. Increasing the velocity to 7.3 m/s fracture of the bottom flange and 60-70 % of the web height was found, see Figure 58b. Figure 58c shows the failure of the stiffener and the shear failure half way around the nose circumference for an impact velocity of 8.7 m/s. No attempt was made to perforate the target in this case.

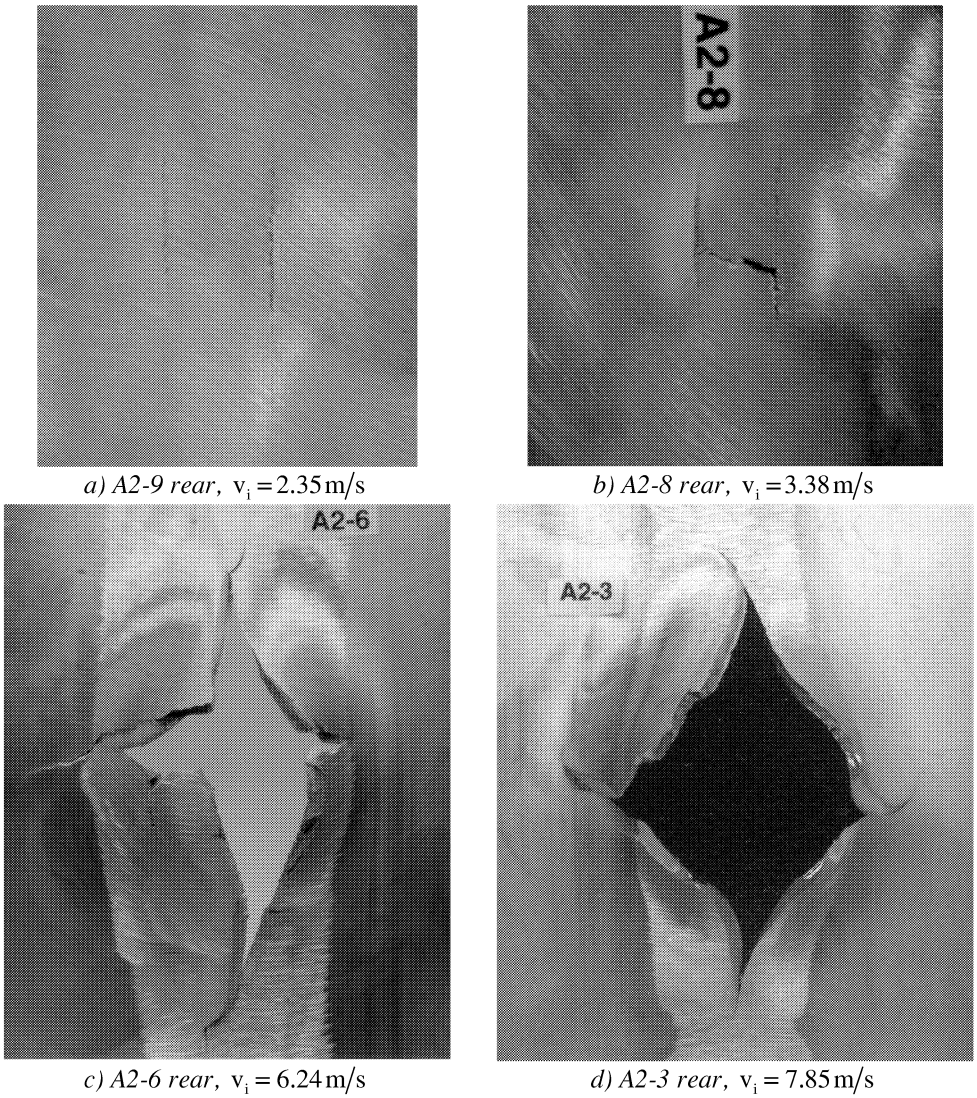

a) A2-9 rear, $v_i = 2.35\,\mathrm{m/s}$ *b) A2-8 rear,* $v_i = 3.38\,\mathrm{m/s}$

c) A2-6 rear, $v_i = 6.24\,\mathrm{m/s}$ *d) A2-3 rear,* $v_i = 7.85\,\mathrm{m/s}$

Figure 54 Different failure modes for increasing impact velocities impacting between the stiffeners with a hemispherical projectile: a) and b) cracks, c) petaling, and d) petaling with perforation.

Figure 59, Figure 60, and Figure 61 show some typical force-, velocity-, and displacement-time histories together with the corresponding force-displacement curves. The presented curves include the following cases: no fracture, fracture of the bottom flange and the web, and fracture of the bottom flange and the web together with shear failure half way around the nose circumference.

When fracture of the bottom flange took place the interface force dropped from maximum to a new smaller level. Then the interface force either remained approximately constant, see Figure 60, Figure 61 and Appendix D. No significant difference in the impact duration, t_d, for the different impact energies, T_p, was seen in this test series.

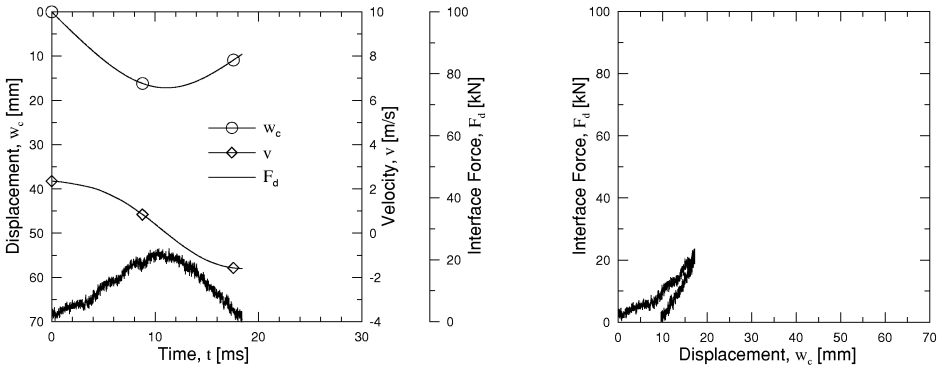

a) Displacement, velocity and force histories *b) Force-displacement curve*

Figure 55 *Test A2-9;* $v_i = 2.35\,m/s$ *: Surface cracks in the fusion lines. Rebound.*

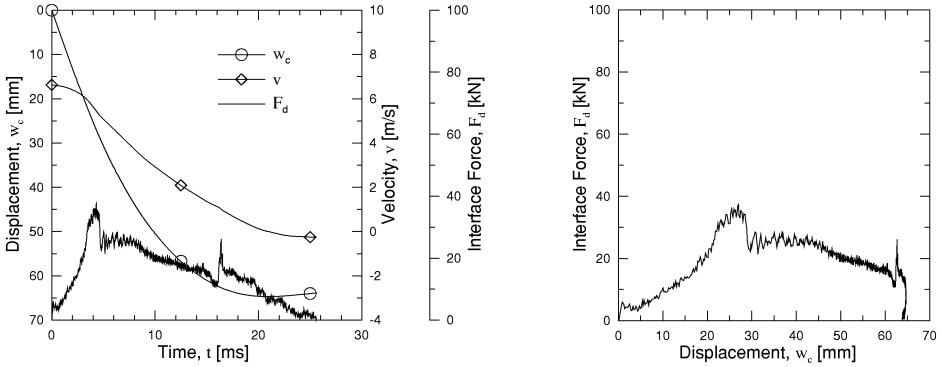

a) Displacement, velocity and force histories *b) Force-displacement curve*

Figure 56 *Test A2-1;* $v_i = 6.63\,m/s$ *: 4 petals. Rebound.*

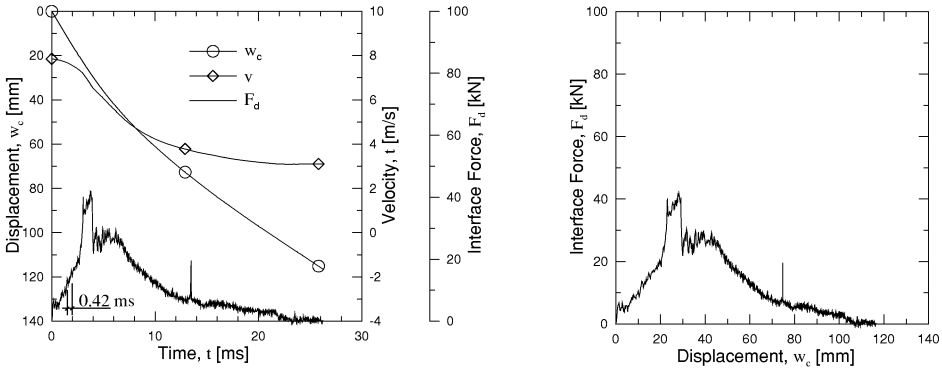

a) Displacement, velocity and force histories *b) Force-displacement curve*

Figure 57 *Test A2-3;* $v_i = 7.85\,m/s$ *: 4 petals. Perforation.*

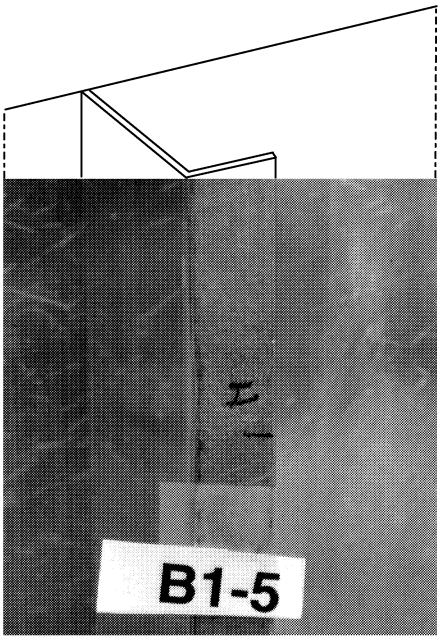

a) B1-5 rear, $v_i = 6.78\,m/s$

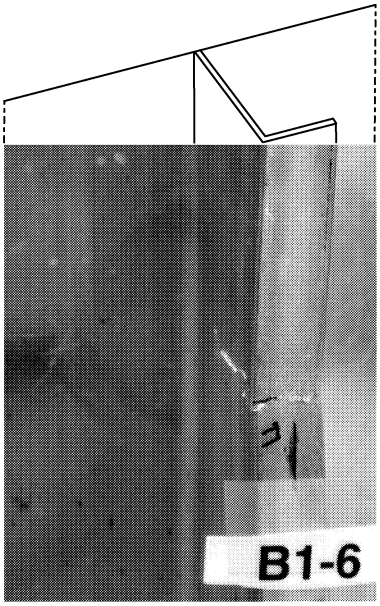

b) B1-6 rear, $v_i = 7.33\,m/s$

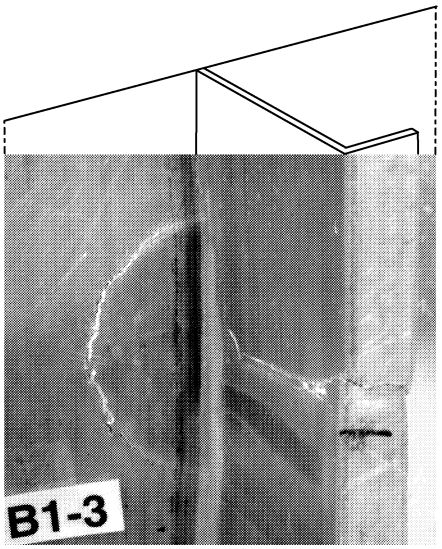

c) B1-3 rear, $v_i = 8.68\,m/s$

Figure 58 Different failure modes for increasing impact velocities impacting on a stiffener with a blunt projectile: a) necking of flange, b) failure of the web and flange, and c) failure of the web and flange and half way around the projectile circumference. (The drawings on top of the photographs are made to visualise the angles of observation.)

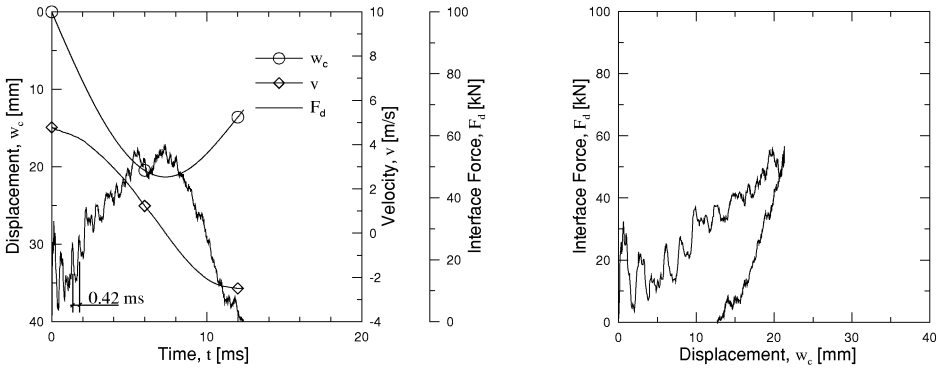

a) Displacement, velocity and force histories *b) Force-displacement curve*

Figure 59 *Test B1-7;* $v_i = 4.78\,m/s$*: No cracks. Diffuse necking of the bottom flange. Rebound.*

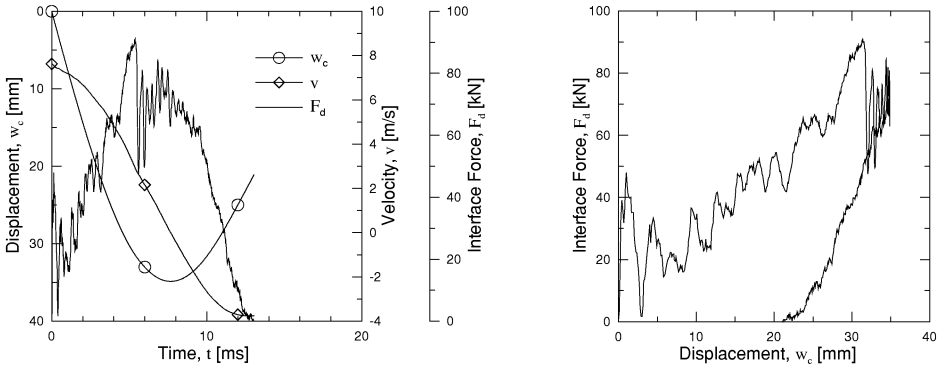

a) Displacement, velocity and force histories *b) Force-displacement curve*

Figure 60 *Test B1-4;* $v_i = 7.62\,m/s$*: Tensile fracture of the bottom flange and the web. Rebound.*

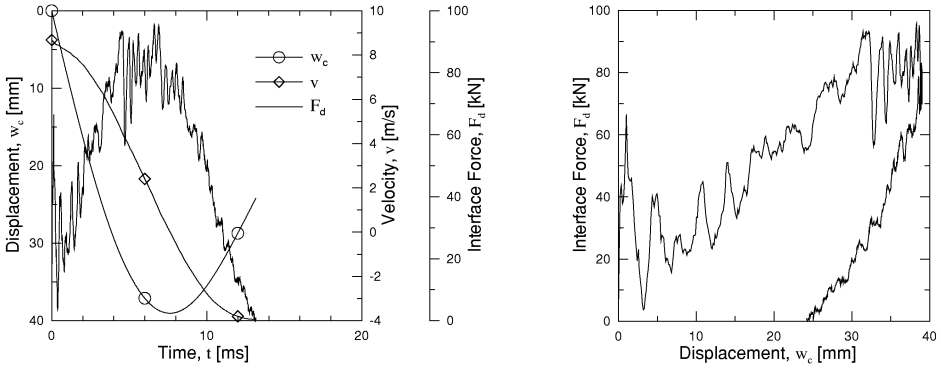

a) Displacement, velocity and force histories *b) Force-displacement curve*

Figure 61 *Test B1-3;* $v_i = 8.68\,m/s$*: Tensile fracture of the bottom flange and the web, and shear failure half way around the nose circumference. Rebound.*

4.2.1.4 Test series B2

Test series B2 is the case where the hemispherical projectile impacted on a stiffener. For an impact velocity of 4.8 m/s dishing and a local bulge in the plate was observed. Increasing the impact velocity to 6.3 m/s a crack in the plate along the web and diffuse necking of the bottom flange were found, Figure 62a. Figure 62b shows the failure of the stiffener and cracks in the plate along the web for an impact velocity of 6.5 m/s. When increasing the impact velocity the crack in the plate along the stiffener started to propagate, see Figure 62c, Figure 62d and Figure 62e. No attempt was made to perforate the target in this case.

Figure 63, Figure 64, and Figure 65 show some typical force-, velocity-, and displacement-time histories together with the corresponding force-displacement curves. The presented curves include the following cases: no cracking, fracture in the plate along the web of the stiffener, and fracture of the stiffener and fracture in the plate along the web.

No significant difference in the shape of the force-displacement curves were observed due to the cracking of the top flange, see Figure 63 and Figure 64. When the bottom flange fractured a sudden drop in the interface force curve was found. Then the interface force either remained constant or increased slightly before the force dropped to zero, see Figure 65 and Appendix D.

4.2.1.5 Test series C1

Test series C1 is the case where blunt projectiles impacted the stiffened plate next to a stiffener. For a velocity below the incipient fracture velocity of 5.8 m/s orange peeling of the bottom flange and around the nose circumference was observed. Figure 66a shows the crack through the plate thickness and approximately half way around the circumference of the projectile. The fracture occurred in the plate at the circumference of the projectile next to the stiffener. Diffuse necking of the bottom flange and lateral displacement of the bottom flange were also observed. Increasing the impact velocity above the ballistic limit of 7.0 m/s a plug was removed as depicted in Figure 66b. Figure 66c shows the projectile contained in the target plate for an impact velocity close to the ballistic limit. The plugs from this test series were almost circular as shown in Figure 49.

Figure 67, Figure 68, Figure 69, and Figure 70 show some typical force-, velocity-, and displacement-time histories together with the corresponding force-displacement curves. The presented curves include the following cases: no cracking, shear failure quarter around the circumference of the nose, plugging with containment, and plugging with perforation.

When a shear failure occurred in the top flange, a sudden drop in the interface force curve was measured, comparing Figure 67 and Figure 68. The drop in force from maximum force, F_{dm}, to zero occurred more quickly when increasing the impact velocity.

4.2.1.6 Test series C2

Test series C2 is the case where the hemispherical projectile impacted the stiffened plate next to a stiffener. A local bulge and orange peeling on the rear side were seen in the top flange for an impact velocity below the incipient fracture velocity of 3.9 m/s. For an impact velocity above the incipient fracture velocity two cracks were seen in the top flange, see Figure 71a. Diffuse necking of the bottom flange and lateral displacement of the bottom flange were also observed for that velocity. Increasing the impact velocity further one of the cracks started to expand, Figure 71b, and finally one petal was pushed aside during the perforation of the plate as depicted in Figure 71c and Figure 71d. The ballistic limit was estimated to 9.1 m/s.

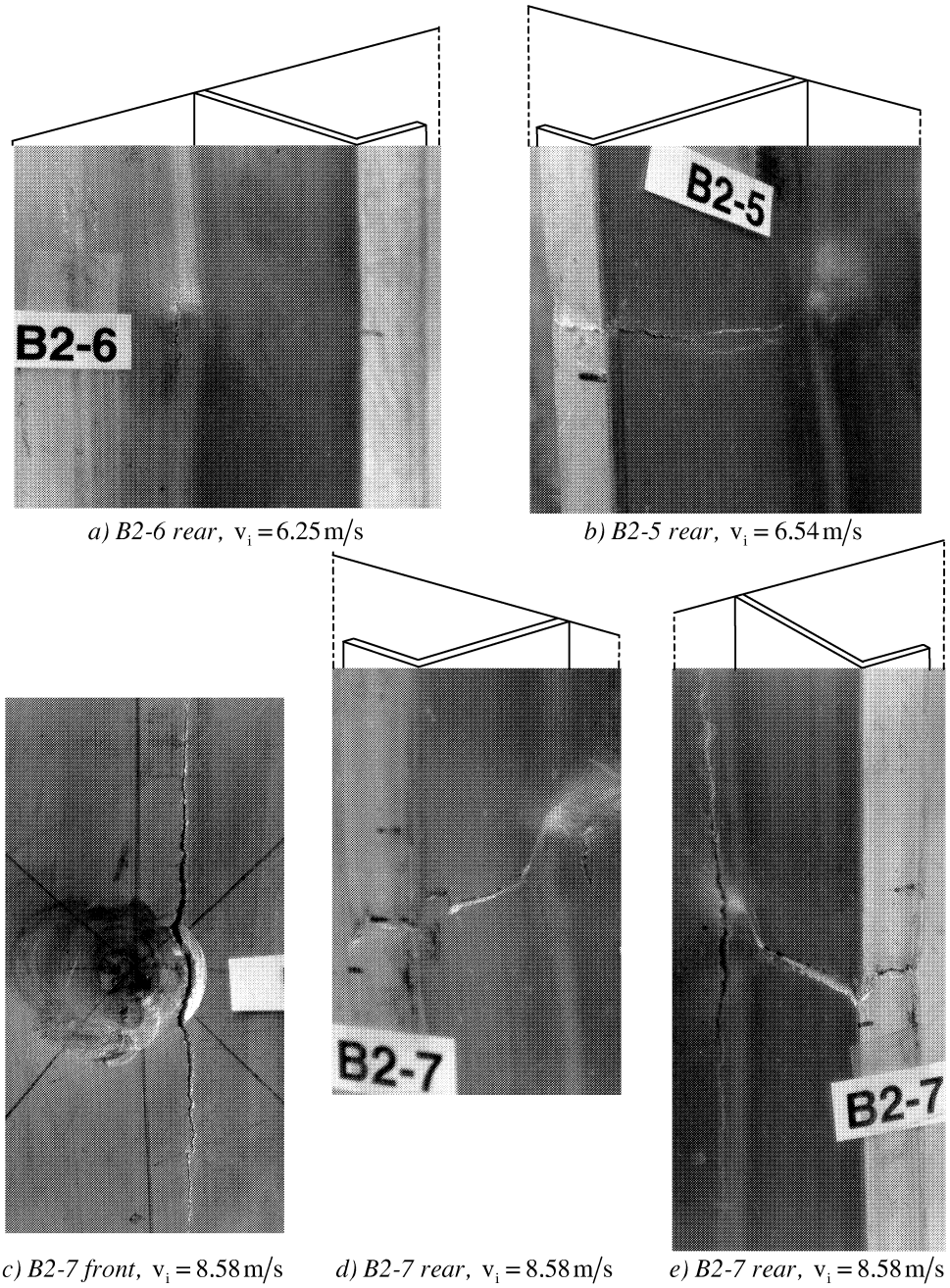

a) B2-6 rear, $v_i = 6.25\,m/s$ *b) B2-5 rear,* $v_i = 6.54\,m/s$

c) B2-7 front, $v_i = 8.58\,m/s$ *d) B2-7 rear,* $v_i = 8.58\,m/s$ *e) B2-7 rear,* $v_i = 8.58\,m/s$

Figure 62 Different failure modes for increasing impact velocities impacting on a stiffener with a hemispherical projectile: a) bulge and crack in the plate along the web in the plate, b) crack in the plate along the web and fracture of the bottom flange and the web, c), d) and e) crack in plate along the stiffener and fracture of the bottom flange and the web.

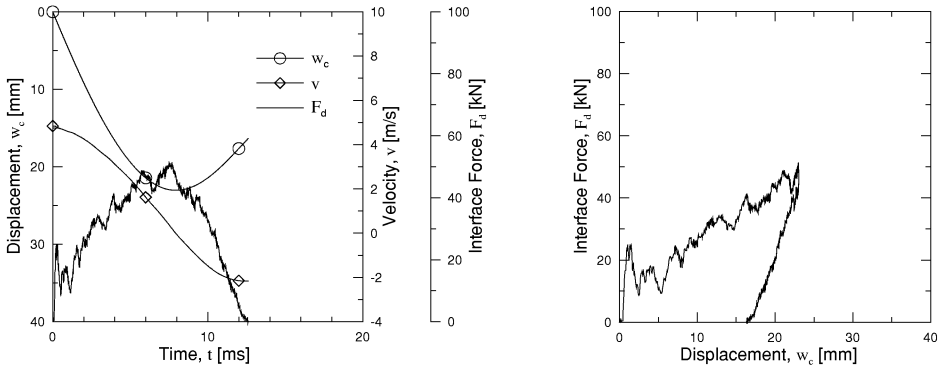

a) Displacement, velocity and force histories *b) Force-displacement curve*

Figure 63 Test B2-2; $v_i = 4.84\,m/s$ *: No cracks. Bulge. Rebound.*

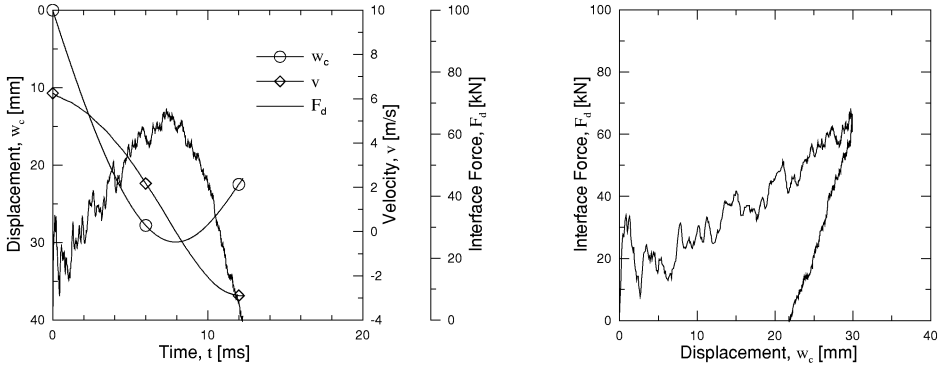

a) Displacement, velocity and force histories *b) Force-displacement curve*

Figure 64 Test B2-6; $v_i = 6.25\,m/s$ *: Fracture of the top flange along the web (20 mm). Rebound.*

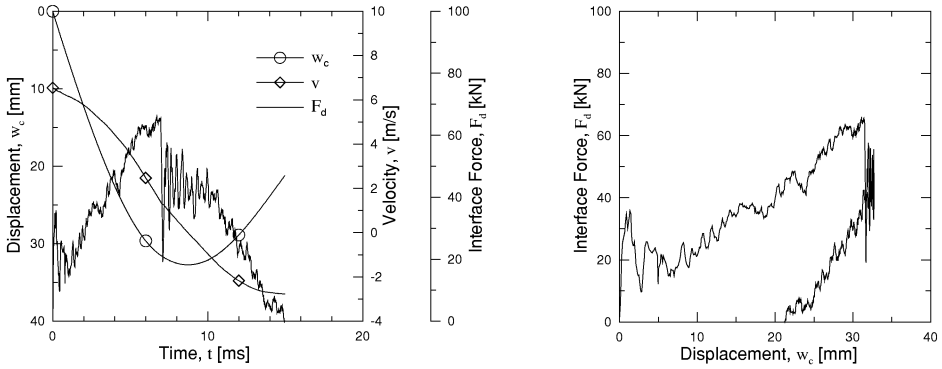

a) Displacement, velocity and force histories *b) Force-displacement curve*

Figure 65 Test B2-5; $v_i = 6.54\,m/s$ *: Fracture of the top flange along the web on both sides of the web (10-15 mm), tensile fracture of the bottom flange. Rebound.*

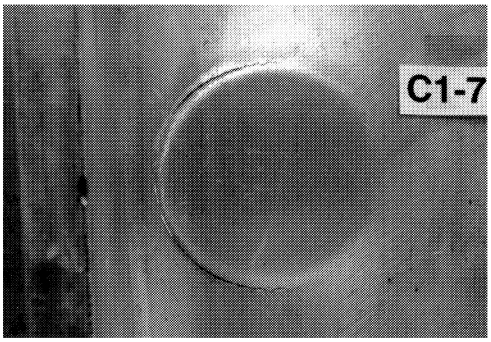

a) C1-7 rear, $v_i = 6.98\,m/s$

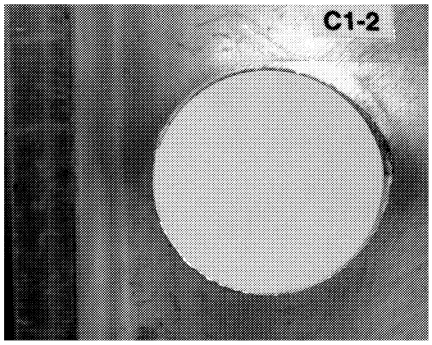

b) C1-2 rear, $v_i = 6.99\,m/s$

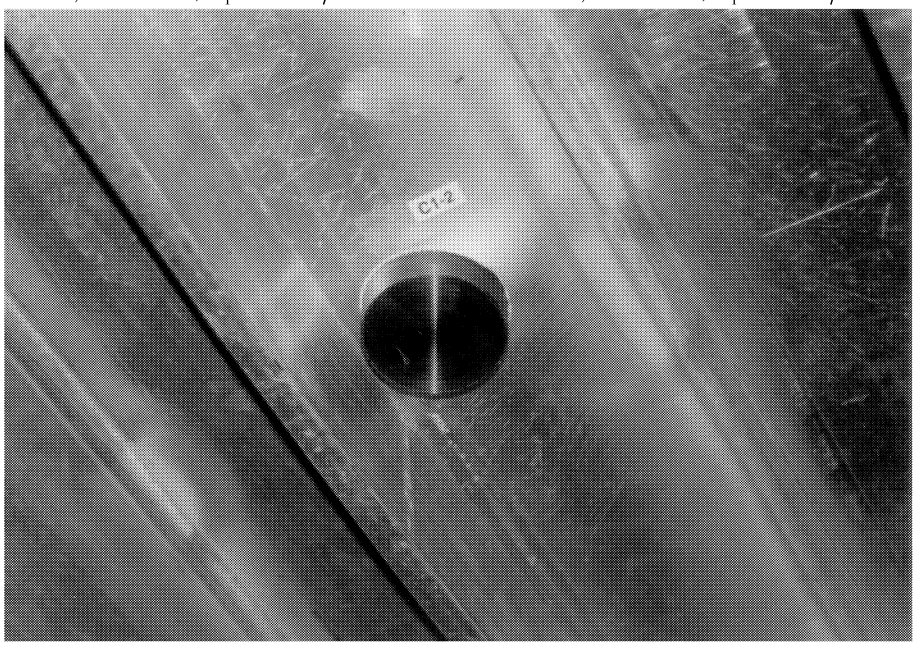

c) C1-2 rear, containment

Figure 66 Different failure modes for increasing impact velocities impacting neat to a stiffener with a blunt projectile: a) shear failure mode, b) and c), plugging with containment.

Figure 72, Figure 73, Figure 74, and Figure 75 show some typical force-, velocity-, and displacement-time histories together with the corresponding force-displacement curves. The presented curves include the following cases: no cracking, cracking in fusion line, petaling with rebound, and petaling with perforation.

For an impact velocity where one petal was created a sudden drop in the interface force was found, followed by a rather nonlinear behaviour as the projectile was rebounded from the plate, Figure 74. For the perforation case, the force decreased quite quickly from maximum force to zero, see Figure 75.

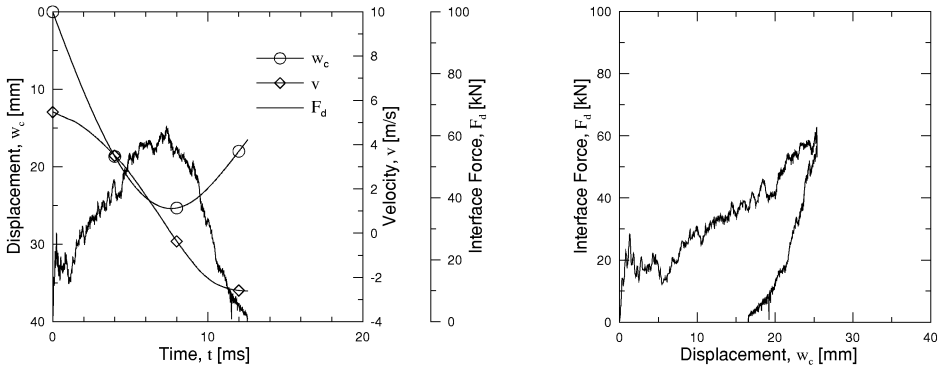

a) Displacement, velocity and force histories *b) Force-displacement curve*

Figure 67 Test C1-4; $v_i = 5.47\,m/s$*: No fracture. Rebound.*

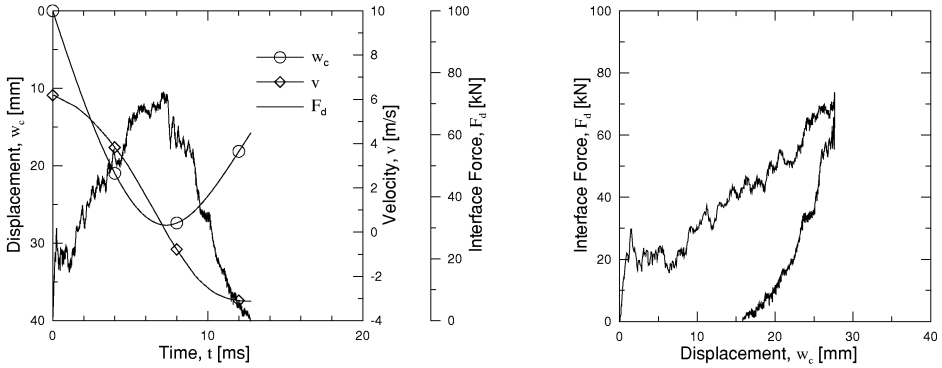

a) Displacement, velocity and force histories *b) Force-displacement curve*

Figure 68 Test C1-5; $v_i = 6.19\,m/s$*: Shear failure of the top flange a quarter around the circumference of the nose. Rebound.*

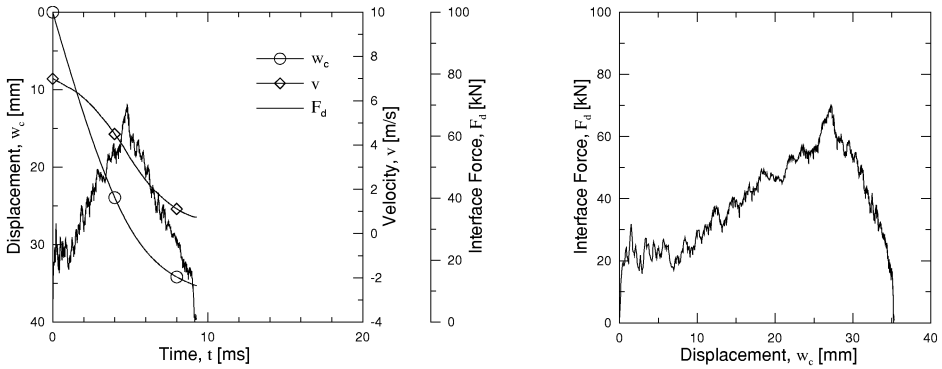

a) Displacement, velocity and force histories *b) Force-displacement curve*

Figure 69 Test C1-2; $v_i = 6.99\,m/s$*: Plugging. Containment.*

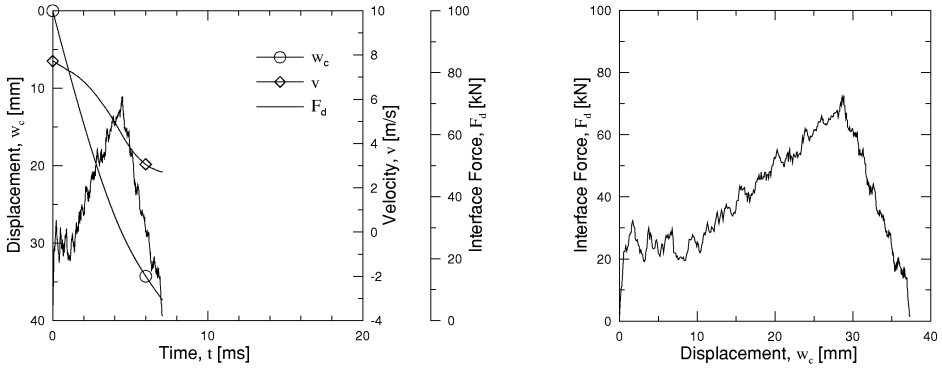

a) Displacement, velocity and force histories *b) Force-displacement curve*

Figure 70 Test C1-6; $v_i = 7.72\,m/s$ *: Plugging. Perforation.*

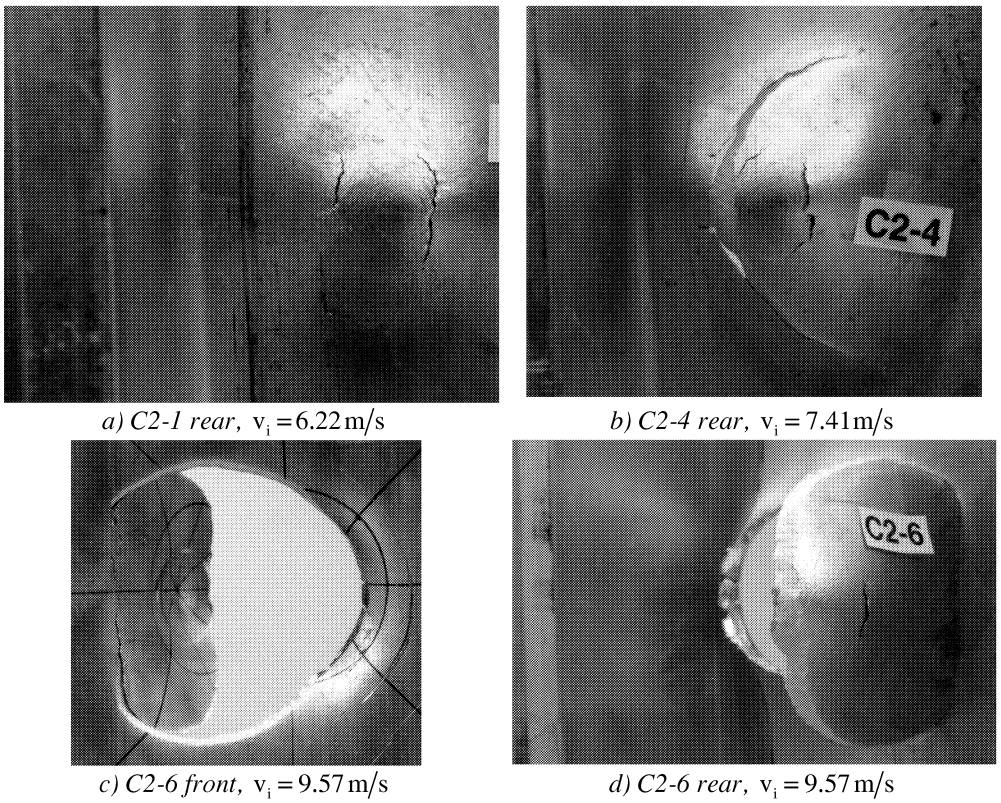

a) C2-1 rear, $v_i = 6.22\,m/s$ *b) C2-4 rear,* $v_i = 7.41\,m/s$

c) C2-6 front, $v_i = 9.57\,m/s$ *d) C2-6 rear,* $v_i = 9.57\,m/s$

Figure 71 Different failure modes for increasing impact velocities impacting next to a stiffener with a hemispherical projectile: a) cracks on each side of the centre point of the projectile, b) petaling, and c) and d) single petal with perforation.

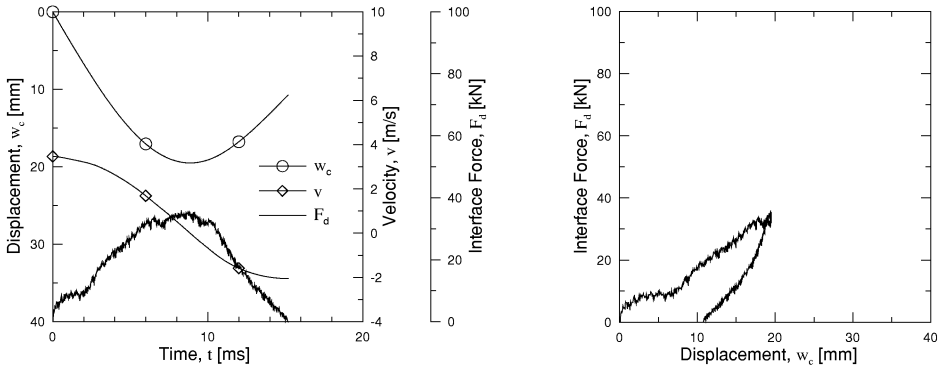

a) Displacement, velocity and force histories *b) Force-displacement curve*

Figure 72 Test C2-7; $v_i = 3.47\,m/s$ *: No fracture. Bulge. Rebound.*

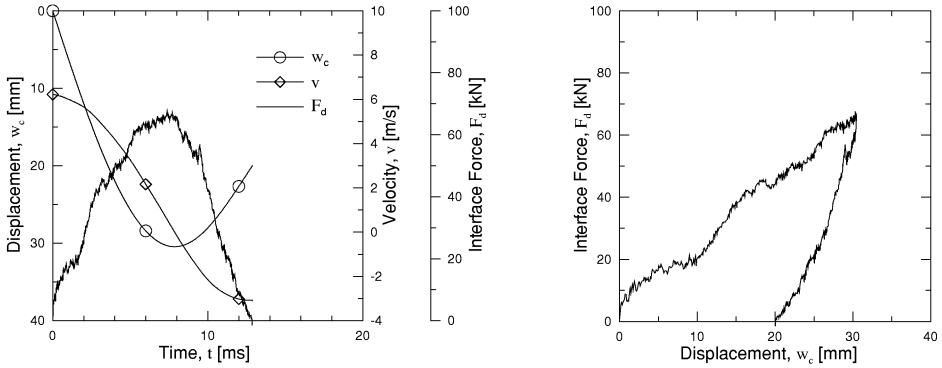

a) Displacement, velocity and force histories *b) Force-displacement curve*

Figure 73 Test C2-1; $v_i = 6.22\,m/s$ *: Fracture lines on both sides of the centre. Rebound.*

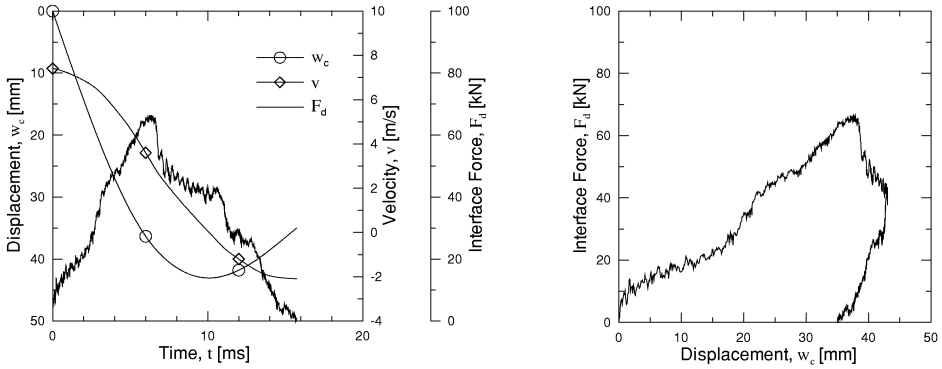

a) Displacement, velocity and force histories *b) Force-displacement curve*

Figure 74 Test C2-4; $v_i = 7.41\,m/s$ *: A single petal. Fracture lines on both sides of the centre point and one of them developed to the petal. Rebound.*

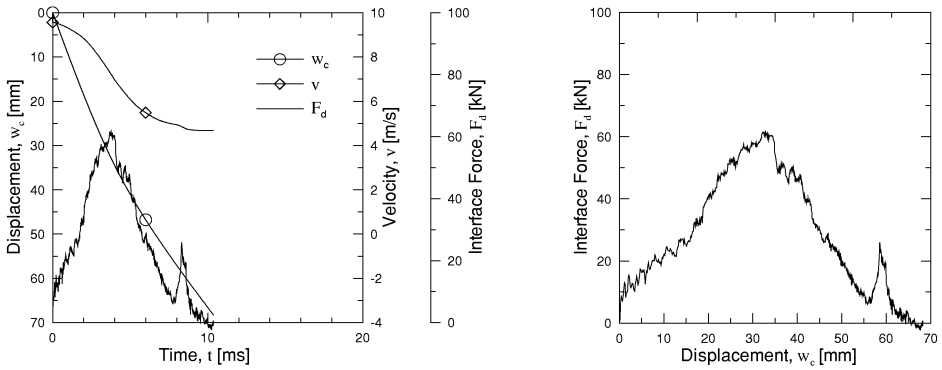

a) Displacement, velocity and force histories *b) Force-displacement curve*

Figure 75 *Test C2-6;* $v_i = 9.57\,m/s$*: A single petal and four minor petals. Fracture lines on both sides of the centre point and one of them developed to the petal. Perforation.*

4.2.2 Effect of nose shape

The effect of different nose shapes is discussed for the three different impact locations.

Load between stiffeners at the weld

The plates impacted by blunt and hemispherical projectiles are compared for approximately the same impact energy of the projectile. Figure 76a and Figure 76b show force-displacement curves for an impact in the span between the stiffeners. As shown the comparison is made for two separate impact velocities. In test A1-6 the blunt projectile did not cause any failure of the target, while the plate A2-5 experienced a crack due to the hemispherical projectile. Figure 76a show the significant difference in the maximum force, F_{dm}, and displacement of the projectile at maximum force, w_{cu}. The maximum forces in test A1-6 and A2-5 were 46.0 and 29.6 kN, respectively. Figure 76b shows the same tendency when perforation occurred. Figure 76 shows that the stiffness of the target was far less for impact with a hemispherical nosed projectile than by use of the blunt ended nose.

Test A1-4 failed by plugging and the force had a sudden drop to zero, Figure 76b. In test A2-2 the failure was by petaling, however, large central displacement occurred before the force decreased to zero. Table 6 shows that the critical forces (F_{dc}) for test series A1 and A2 were estimated to 65.4 and 36.6 kN, respectively. The ballistic limits (v_{ic}) for the test series A1 and A2 were approximately the same, i.e. 6.8 and 7.0 m/s, respectively. The estimated incipient fracture velocity, v_{iu}, for test series A1 were 4.5 m/s, whereas the corresponding velocity for test series A2 was less than 2.4 m/s. In the case of a hemispherical ended nose the plate absorbed a lot of energy after maximum force. Thus, a cracked plate can absorb significant additional energy before it is perforated.

Large elastic and plastic deformations extended from the point of load application to the supports. The permanent deformations were measured in two different sections, in the longitudinal direction, Section B, and in the transverse direction, Section A, as visualised in Figure 77. Figure 78 presents the permanent deformations, w_p, of the test specimen impacted by the blunt projectile with the lowest velocity giving cracks in the stiffened plate. The curves

in Figure 78 show that the permanent deformation was more localised in the transverse direction (Section A) than in the longitudinal direction (Section B).

The permanent deformations in the transverse direction, Section A, were compared for a blunt ended nose and for a hemispherical nose as shown in Figure 79a. The permanent deformation profiles are plotted for the tests with the lowest impact velocity giving cracks in the target. The permanent deformations were symmetric about the load position. A hemispherical ended nose gives more localisation of the permanent deformation than a blunt ended nose.

Load on a stiffener

Figure 80 shows force-displacement curves for the plates impacted on a stiffener with a blunt and hemispherical ended projectile. The impact energy was approximately 0.64 kJ and no cracks appeared in the stiffened plate, Figure 80a. As seen, both the loading and unloading took place with approximately linear stiffness in the two tests. The stiffness was slightly lower for the hemispherical projectile than the blunt projectile.

Impacting the target with an impact energy of approximately 2.05 kJ, the stiffener and the plate fractured in both cases. Table 5 lists the fracture modes of each test. By increasing the velocity above the incipient fracture velocity, v_{iu}, fracture of the stiffener occurred for test series B1. Further increase of the impact velocity gave cracks in the top flange. In test series B2 cracks in the top flange appeared for a low impact velocity, whereas fracture of the stiffener was observed for an increased impact velocity. The maximum force, F_{dm}, was less and the displacement at maximum force, w_{cu}, was larger using a hemispherical projectile than a blunt projectile for approximately the same impact energy, Figure 80b.

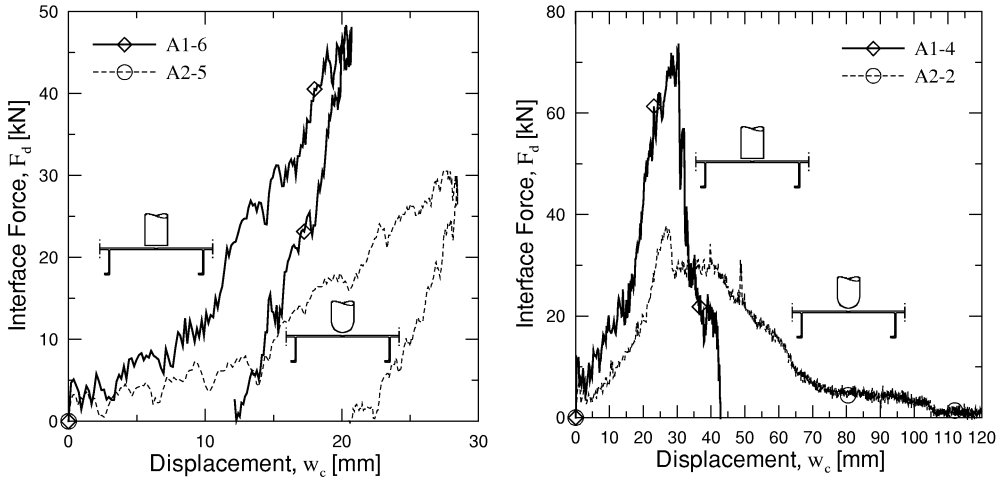

a) A1-6: $v_i = 3.72\,m/s$ *; A2-5:* $v_i = 3.47\,m/s$ *b) A1-4:* $v_i = 7.08\,m/s$ *; A2-2:* $v_i = 7.33\,m/s$

Figure 76 Force-displacement curves comparing the blunt projectile with the hemispherical projectile for impact between stiffeners for approximately same impact energy: a) no perforation, and b) perforation.

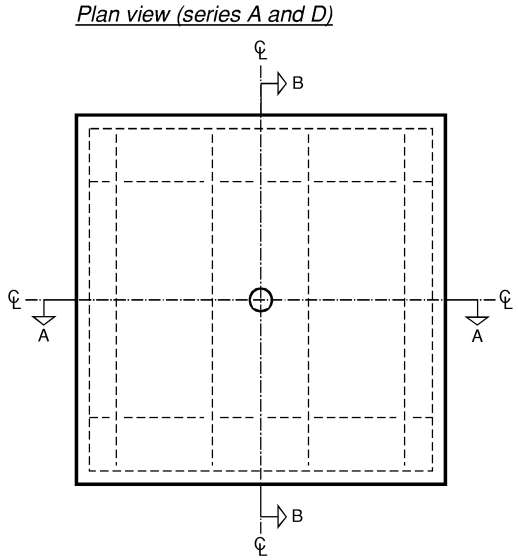

Figure 77 Sections for measurements of permanent deformations for load position in between two stiffeners.

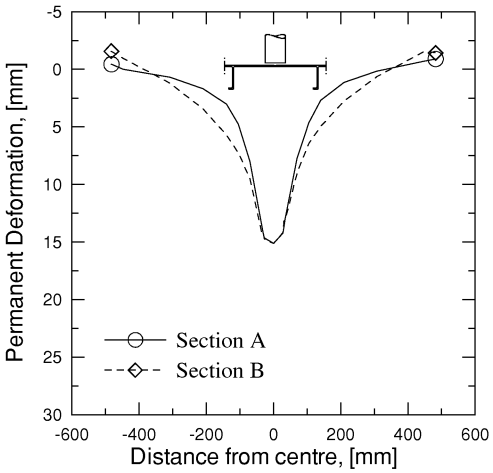

Figure 78 Permanent deformation in Sections A and B for impact in between two stiffeners with a blunt projectile.

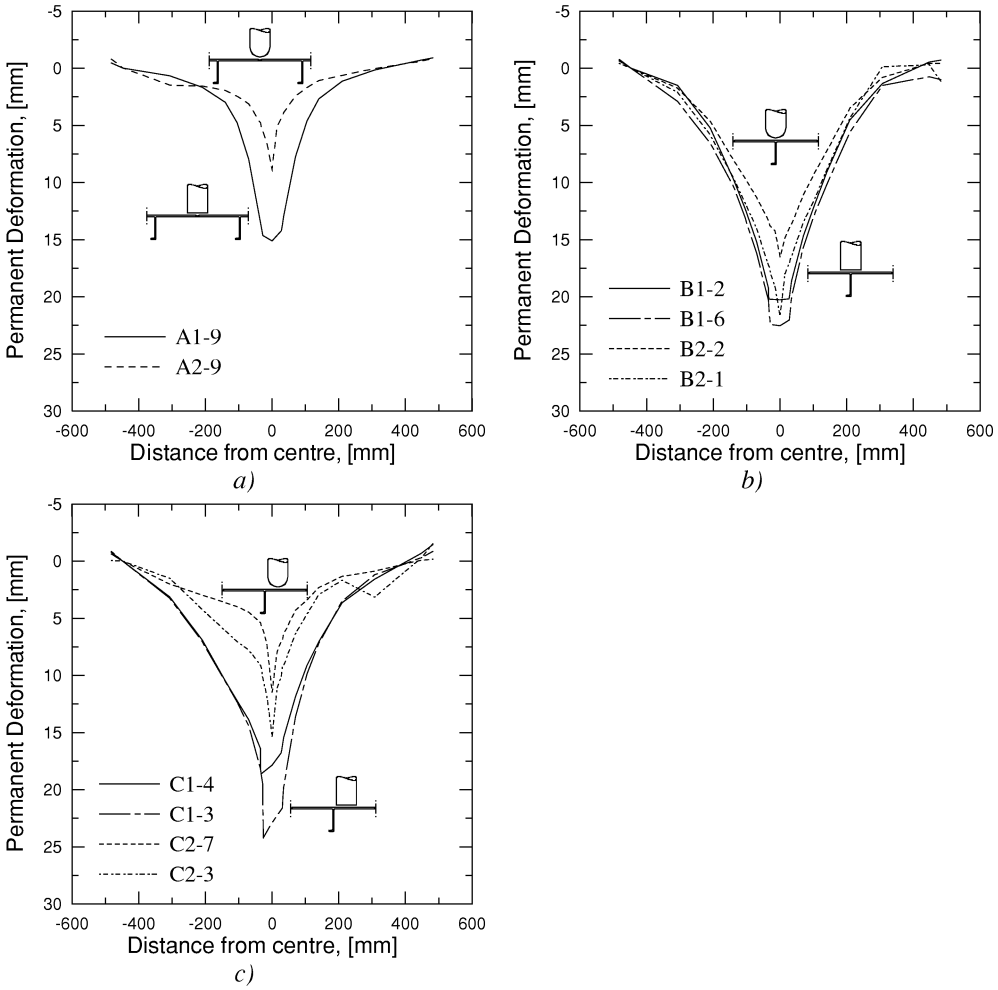

Figure 79 *Permanent deformation along Section A for blunt and hemispherical ended nose: a) load position in between stiffeners for lowest impact velocity giving cracking, b) load position on a stiffener for the highest velocity giving no failure and lowest impact velocity giving cracking, and c) load position next to a stiffener for the highest velocity giving no failure and lowest impact velocity giving cracking.*

Table 6 states that the estimated velocity giving incipient fracture, v_{iu}, in the target was less using a hemispherical projectile. The impact energy giving incipient fracture, T_{pu} using a hemispherical projectile was almost half of the energy needed using a blunt ended nose.

The permanent deformations of panels loaded on a stiffener are shown in Figure 79b for a blunt and hemispherical ended nose. The permanent deformations, w_p, of the test specimens impacted by the projectile with the lowest velocity giving cracks in the stiffened plate and with the highest impact velocity giving no failure in the target are presented. The

permanent deformations were symmetric about the load position. A hemispherical ended nose, tests B2-2 and B2-2, gives more localisation of the permanent deformation than a blunt ended nose, tests B1-2 and B1-6, as shown in Figure 79b.

Load next to a stiffener

Applying the load next to a stiffener with a velocity above the ballistic limit, plugging and petaling occurred for the blunt and hemispherical ended nose, respectively. The force-displacement curves for two targets impacted with an energy of approximately 1.06 kJ giving cracks in the top flange are shown in Figure 81a. After a phase with almost constant force level, the loading and unloading took place with almost linear stiffness for the two different nose shapes. The stiffness was slightly lower for the hemispherical projectile than the blunt projectile.

Increasing the impact energy to approximately 1.9 kJ, perforation occurred for a blunt projectile, while the hemispherical projectile caused petaling, but no perforation. The maximum force, F_{dm}, was slightly less and the displacement at maximum force, w_{cu}, was significant larger for the hemispherical than the blunt projectile, Figure 81b. Table 6 states that this resulted in ballistic limits, v_{ic}, of 7.0 and 9.1 m/s for the blunt and hemispherical projectile, respectively. The corresponding critical impact energies, T_{pc}, were 1.35 and 2.27 kJ. The estimated incipient fracture velocities, v_{iu}, showed the opposite tendency: 5.8 and 3.9 m/s for the blunt and hemispherical projectile, respectively. The corresponding energy, T_{pu}, was less than half for the hemispherical nose compared to the blunt nose. The critical forces, F_{dc}, observed in the two test series were largest for the blunt projectile.

The permanent deformations of panels, w_p, loaded next to a stiffener are shown in Figure 79c for a blunt and hemispherical ended nose. The test specimens were impacted by the projectile with the lowest velocity giving cracks in the stiffened plate and with the highest impact velocity giving no failure in the target. The permanent deformation profile was unsymmetrical due to the fact that the impact location was next to a stiffener. The permanent deformation was less beside the stiffener than on the other side of the impact point. A hemispherical ended nose, tests C2-7 and C2-3, gives more localisation of the permanent deformation than a blunt ended nose, tests C1-4 and C1-3, as shown in Figure 79c.

4.2.3 Effect of impact location

The effect of different points of load application is presented for the two different nose shapes.

Blunt projectile

Impact with a blunt ended projectile caused a shear failure mode or fracture of the stiffener depending on the point of load application. Figure 82a and Figure 82c show the force-displacement curves for impact that lead to no cracking in the targets. The stiffness development was the same for an impact on and next to a stiffener, while impact in the span between the stiffeners gave a different stiffness evolution.

Figure 82b and Figure 82d show the force-displacement curves for impact energies of approximately 1.4 kJ. The force level for plugging was somewhat reduced when moving the impact point next to the stiffener. However, the same impact energy did not cause any cracks impacting on a stiffener. The estimated incipient fracture velocity, v_{iu}, were 4.5 and 5.8 m/s

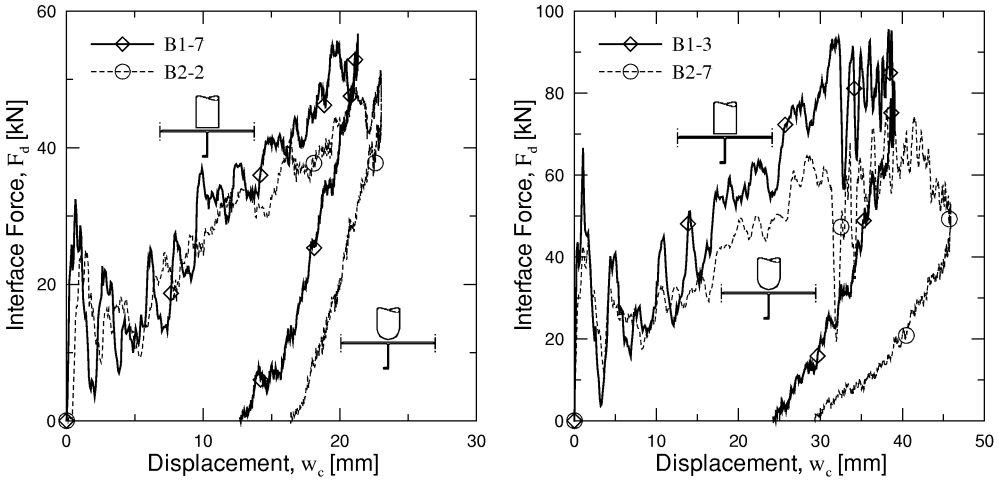

a) B1-7: $v_i = 4.78\,m/s$ *; B2-2:* $v_i = 4.84\,m/s$ *b) B1-3:* $v_i = 8.68\,m/s$ *; B2-7:* $v_i = 8.58\,m/s$

Figure 80 Force-displacement curves comparing the blunt projectile with the hemispherical projectile for impact on a stiffener for approximately same impact energy: a) no cracks, and b) cracking.

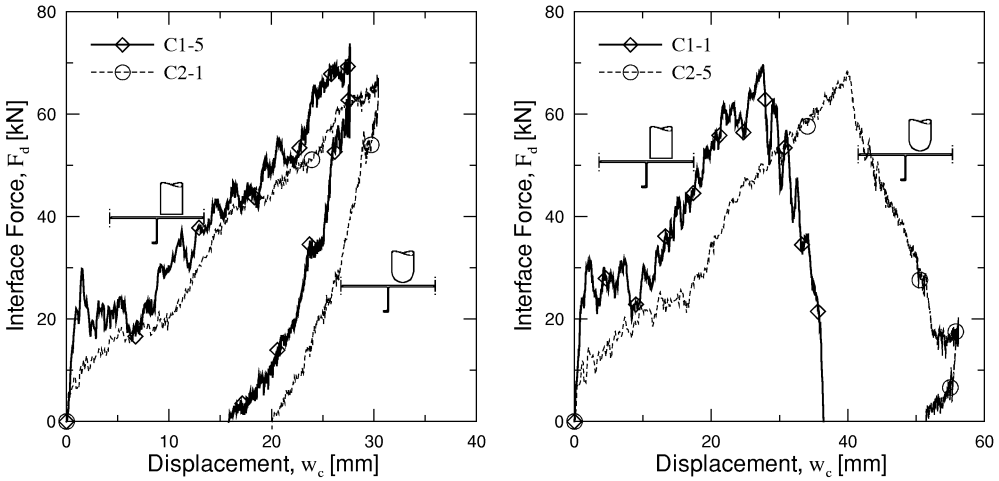

a) C1-5: $v_i = 6.19\,m/s$ *; C2-1:* $v_i = 6.22\,m/s$ *b) C1-1:* $v_i = 8.28\,m/s$ *; C2-5:* $v_i = 8.53\,m/s$

Figure 81 Force-displacement curves comparing the blunt projectile with the hemispherical projectile for impact between stiffeners for approximately same impact energy: a) no perforation, and b) C1-1: perforation and C2-5: rebound.

for impact between stiffeners and next to a stiffener, respectively. The estimated ballistic limits, v_{ic}, were approximately the same for an impact next to a stiffener as between two stiffeners, see Table 6.

The permanent deformations of three tests that were impacted by a projectile with the lowest velocity giving cracks in the target are presented in Figure 83a. The permanent deformation profile in section A for load position on a stiffener was nearly the same as for load position next to a stiffener, while the permanent deformation was less for impact between stiffener. Load applied next to a stiffener gave a nonsymmetrical profile due to the nonsymmetrical geometry of the test specimen.

Hemispherical projectile

An impact energy of approximately 0.33 kJ caused cracks when impacting the projectile between the stiffeners, while this energy gave no cracks in the other test series. The evolution of the stiffness was the same for an impact on and next to a stiffener, while impact in the span between the stiffeners gave much softer behaviour, see Figure 84a and Figure 84c.

For an impact energy of 1.5 kJ, the impact between two stiffeners gave four petals and perforation, while an impact next to a stiffener with same impact energy resulted in a single petal and projectile rebound. This amount of energy for impact on a stiffener resulted in cracks in the top flange and fracture of the stiffener. The force-displacement curves are shown in Figure 84b and Figure 84d. The maximum force, F_{dm}, was significantly less for impact in between the stiffeners compared to the two other load application points. The estimated incipient fracture velocity, v_{iu}, was less than 2.4 m/s for impact between two stiffeners, while it was considerable larger, i.e. 3.9 and 5.4 m/s, for impact next to and on a stiffener, respectively. The estimated ballistic limit, v_{ic}, was significantly less for impact between two stiffeners than next to a stiffener, see Table 6.

The permanent deformation profiles of three tests that were impacted by a projectile with the lowest velocity giving cracks in the target are given in Figure 83b. The load positions next to a stiffener and between two stiffeners gave more localised deformation at the point of load application than a load position on a stiffener.

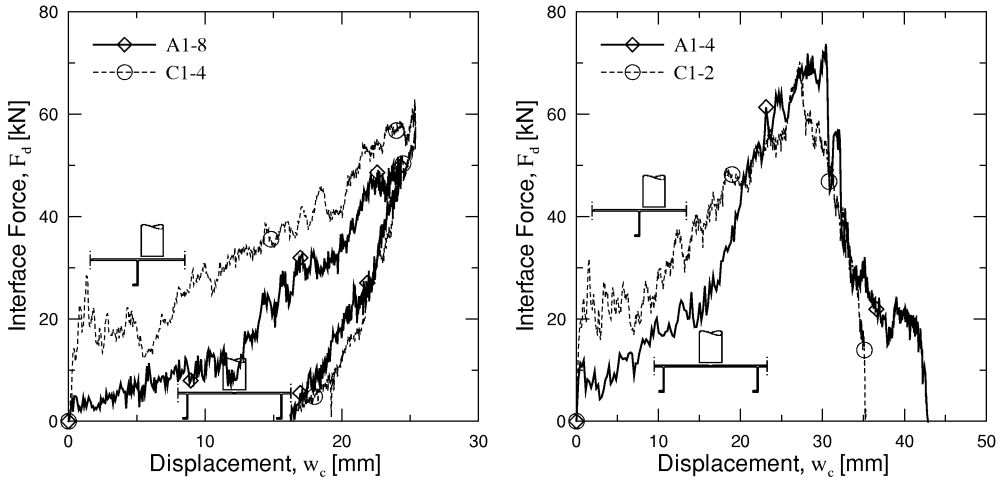

a) A1-8: $v_i = 4.08\,m/s$ *; C1-4:* $v_i = 5.47\,m/s$ *b) A1-4:* $v_i = 7.08\,m/s$ *; C1-2:* $v_i = 6.99\,m/s$

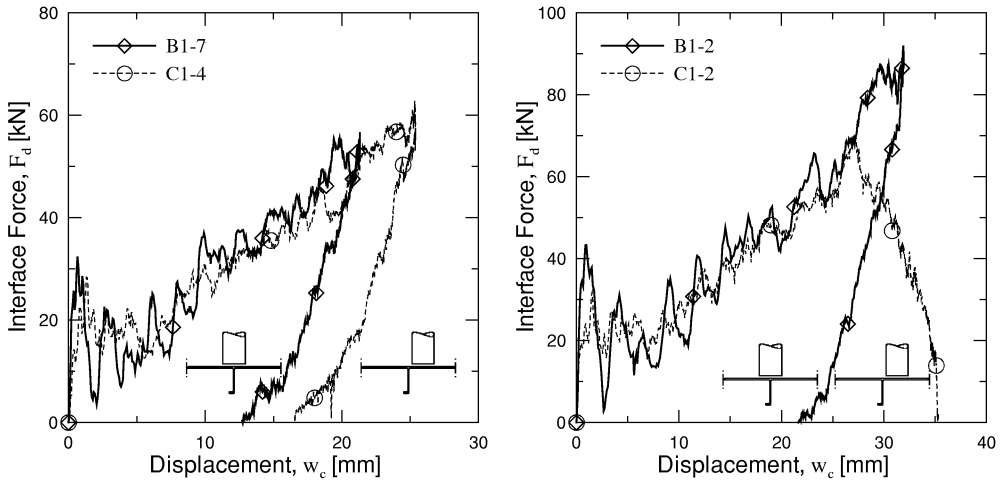

c) B1-7: $v_i = 4.78\,m/s$ *; C1-4:* $v_i = 5.47\,m/s$ *d) B1-2:* $v_i = 7.12\,m/s$ *; C1-2:* $v_i = 6.99\,m/s$

Figure 82 Force-displacement curves comparing different impact locations for the blunt projectile: a) no failure, b) plugging at an impact energy of 1.4 kJ, c) no failure, and d) impact energy of 1.4 kJ: B1-2: no failure and C1-2: plugging.

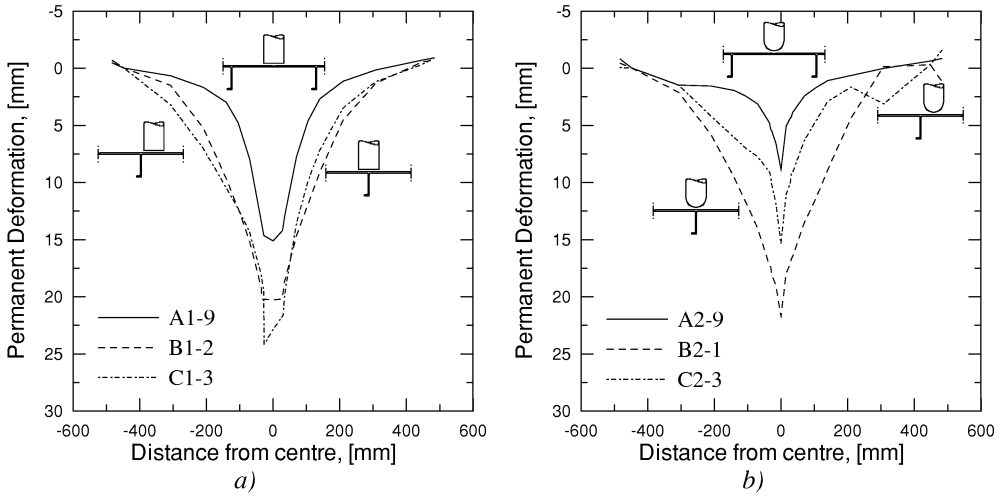

Figure 83 Permanent deformation along Section A for load position in between stiffeners (test series A), load position on a stiffener (test series B), and load position next to a stiffener (test series C) for the lowest impact velocity giving cracking: a) blunt ended nose, and b) hemispherical ended nose.

4.2.4 Summary of dynamic test results

The observations from the dynamic tests can be summarised as follows:

- The local failure mode was a function of the impact point on the target and the nose shape of the projectile.
    - A plugging failure mode occurred for the blunt projectile impacting next to a stiffener or in the span between two stiffeners. The plug was separated from the plate and was nearly circular for an impact next to a stiffener and not circular when impacting in the span between two stiffeners. The existence of the weld lead to the latter case.
    - Impact with a hemispherical projectile next to a stiffener or in the span between two stiffeners with an impact velocity above the incipient fracture velocity, resulted in two cracks in the stiffener direction in the top flange. In the case of impact on the weld, the strains were localised to the fusion line where cracks appeared. Increasing the velocity four petals developed. For an impact next to a stiffener a single petal was created.
    - Impact on the stiffener caused fracture of the stiffener and cracks in the top flange along the web.
- The estimated incipient fracture velocity was lowest for an impact between two stiffeners with a hemispherical ended projectile. An impact velocity of 2.35 m/s caused cracks in the fusion lines. The estimated incipient fracture velocity for impact next to a stiffener with a hemispherical projectile was 3.9 m/s. For a blunt ended nose an impact between two stiffeners and an impact next to a stiffener gave an incipient fracture velocity of 4.5 and 5.8 m/s, respectively.
- The ballistic limits were estimated to 6.8 and 7.0 m/s for the blunt and hemispherical projectile impacting between the stiffeners, respectively. The ballistic limit velocity

increased when impacting next to a stiffener. The values were 7.0 and 9.1 m/s for blunt and hemispherical ended projectile, respectively.

- Considerably more energy is required in order to have full penetration of the plate compared with that required for incipient fracture.
- The energy-absorbing capacity of a plate was smaller when impacting between stiffeners than next to a stiffener.

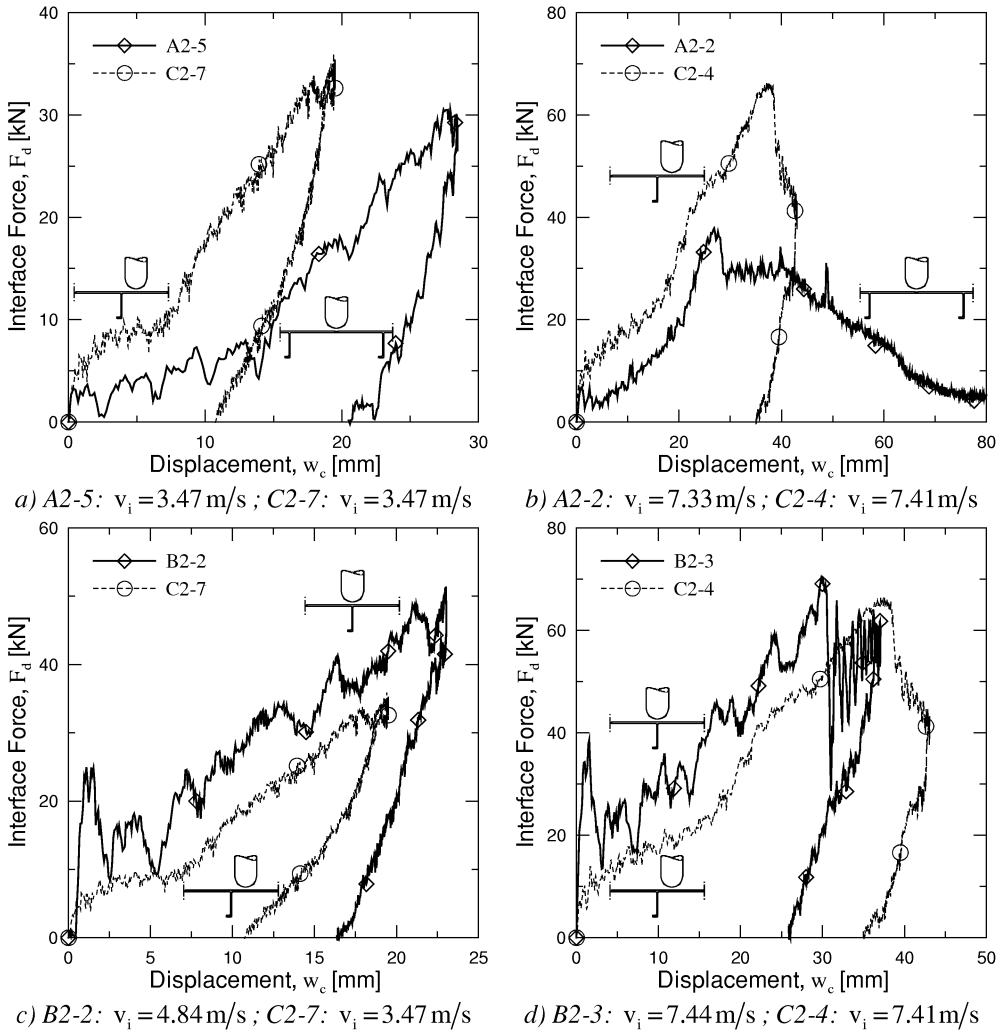

a) A2-5: $v_i = 3.47\,m/s$ *; C2-7:* $v_i = 3.47\,m/s$

b) A2-2: $v_i = 7.33\,m/s$ *; C2-4:* $v_i = 7.41\,m/s$

c) B2-2: $v_i = 4.84\,m/s$ *; C2-7:* $v_i = 3.47\,m/s$

d) B2-3: $v_i = 7.44\,m/s$ *; C2-4:* $v_i = 7.41\,m/s$

Figure 84 Force-displacement curves comparing different impact locations for the hemispherical projectile: a) impact energy of 0.33 kJ, b) impact energy of 1.5 kJ, c) no failure, and d) impact energy of 1.5 kJ.

4.3 Discussion of Experimental Observations

4.3.1 Effect of test parameters

From the experimental results given in Table 6 and Figure 46 some conclusions can be drawn. The incipient fracture velocity varied in the range between 2.3 m/s and 7.2 m/s depending on the input parameters (nose shape and impact location). The incipient fracture velocity was significant less for the hemispherical ended nose than for the blunt ended nose. The impact between the stiffeners gave lowest incipient fracture velocity followed by impact next to the stiffener and impact on a stiffener in that order. The ballistic limit velocity for blunt and hemispherical projectiles impacting between two stiffeners and the blunt projectile impacting next to a stiffener were about equal and close to 7 m/s, while the ballistic limit velocity was 9 m/s for hemispherical projectiles impacting next to a stiffener. The ballistic limit velocity for blunt ended projectiles seem to be independent of the location of impact with the exception of a direct hit on a stiffener. This is not the case for hemispherical ended projectiles which showed significant dependency on the impact location.

The observed differences in the ballistic limit velocity and incipient fracture velocity were mainly attributed to the change in failure mode (and energy absorption) with respect to the input parameters. Impacting in between two stiffeners and next to a stiffener almost the same failure mode was observed for each nose shape. The blunt projectile caused failure by plugging, and an almost circular plug was ejected from the target. The failure mode was dominated by a combination of tension and local shear. The hemispherical projectile indented the target and a modest bulge and target thinning appeared. The material in the intense tensile zone started to neck. When the tensile strain exceeded the capacity of the target material, cracks on each side of the centre point became visible. Hemispherical projectiles seemed to penetrate the target by bending the material in front of the projectile aside by forming one or four petals. The ballistic limit was significant higher when impacting next to a stiffener than in between two stiffeners using a hemispherical projectile. In the latter case the stiffener absorb some of the energy and only one petal was pushed aside during the perforation. In contrast, during perforation in the first case four petals were created and the presence of the weld lowered the capacity.

The large difference in the incipient fracture velocity for hemispherical projectile impacting in between stiffeners and next to a stiffener may be due to the difference in the localisation of the strains. In both cases the strains were localised on both sides of the centre point of the impact. Furthermore, the strains in the case of impact on the weld were localised to a rather narrow zone (the fusion zone). Hval et al. (1992) and Gråberg et al. (2002) pointed out the fusion zone as a problem area due to lower fracture toughness in the fusion zone compared to other zones in the weldment.

In Figure 46 it is shown that the difference between the critical impact energy (giving perforation) and the incipient fracture energy (giving first fracture) was larger in the case of a hemispherical projectile than for a blunt nose for those two impact locations.

Wen and Jones (1994) studied mild steel and aluminium plates impacted by blunt projectiles with velocities up to 12.2 m/s. They showed that the energy absorbing capacity of the plate was reduced significantly when struck by a mass close to the supports compared to a strike at the centre. According to Jones (1994), this behaviour was due to two factors. In the first place, membrane forces play a dominant role in absorbing the impact energies for the thinner plates stuck in the centre. The other factor was that strikes near to the support cause relatively small transverse displacements of a plate. Therefore most of the impact energy was absorbed through bending and shear effects and not membrane forces regardless of the plate

thickness. Simonsen and Lauridsen (2000) performed indentation experiments on thin, ductile steel plates with a rigid sphere. They showed that the penetration and energy absorption were dependent on the plate geometry, loading position and indentor geometry. They found that the peak force was independent of distance from indentor to the plate boundaries, while the energy absorbed up to the point of plate failure was decreasing for a decreasing distance between indentor and the plate boundary. The present study, confer Figure 46, showed the opposite tendency with regard to the energy absorbing capacity if the stiffener is assumed as a support. However, the presence of welds is an important factor in the present study and can not be disregarded.

Impacting 7 to 38 mm thick steel plates with cylindrical strikers having several nose shapes in the velocity range between 25 and 180 m/s, Ohte et al. (1982) found that the critical energy of the target was dependent on the projectile nose shapes. The hemispherical nosed projectile did not perforate for an impact energy that would have caused blunt-ended projectile to penetrate a plate. In the present study, dealing with low velocity impacts, the same as above was seen for impact next to a stiffener: significant higher ballistic limit velocity was seen for impact with a hemispherical ended nose compared to a blunt projectile. Impacting in the span between stiffeners the ballistic limits for the two nose shapes were almost equal.

Impact on the stiffener location gave other failure modes than described above, and no attempt has been made to perforate the targets due to limitations in the experimental facility. The incipient fracture velocity was larger for impact with a blunt projectile than a hemispherical projectile. The blunt projectile caused necking of the bottom flange and the first fracture appeared there. Using a hemispherical projectile a bulge was formed together with necking of the bottom flange. However, in the case of a hemispherical projectile the first crack was observed in the top flange along the web.

In addition to the local failure at the impact point, large global deformation (dishing) extended from the impact point to the supports when the projectile impacted the target. An unsymmetrical permanent deformation profile was observed due to the stiffeners. For the velocities giving incipient fracture less permanent global deformation was observed for the hemispherical projectile than the blunt projectile, Figure 79. Furthermore, the permanent deformation was least for impact in the centre between two stiffeners for the lowest velocity giving cracks in the target, Figure 83. For most test series the centre permanent displacement was several times the target plate thickness. This is often the case for low velocity impact with large mass projectiles, where the influence of global displacement causes the membrane forces to appear in the plate and where the membrane forces are an important energy absorbing mechanism (Jones 1994). Corran et al. (1983) studied projectile impact at sub-ordnance velocities on thin plates (relative to the projectile radius) and found that the displacement could be several times the plate thickness with plastic membrane stretching absorbing the majority of projectile kinetic energy. This is in contrast to ordnance velocity impacts where the deformation of plate can be neglected.

Wen and Jones (1994) observed that for mild steel and aluminium plates impacted by blunt projectiles with velocities up to 12.2 m/s the outside angles of the plugs were opposite. The diameter of the plugs separated from the aluminium plates, was less on the rear side than on the front side. In the present investigation, the outside angle of the plug varied around the plug.

In the present project, shear failure occurred in the plate on either side of the projectile lying parallel to the extrusion direction for a velocity below the ballistic limit velocity. Langseth (1988) observed that plugging failure was always initiated first on one side. According to Langseth (1988), Shadbolt (1981) observed the same and explained it by the

unstable nature of a shear failure. Another explanation may be the anisotropy of the plate due to the extrusion process, confer Chapter 3.

4.3.2 Comparison of dynamic and static tests

Figure 85 shows the dynamic force-displacement curves for the tests with the lowest velocity giving cracks in the targets together with the corresponding static force-displacement curves. In the static tests a non-linear behaviour for small displacements of the punch was found, whereas in the subsequent phase a monotonic rise in the punch load with respect to the displacement nearly up to failure was observed. During impact testing an immediate increase of the interface force between the plate and the projectile was found, see Figure 85, followed by an almost linear relationship between the load and displacement. The minor oscillations in the dynamic force displacement relationship are related to stress wave reflections in the measuring device. It is worth noting that the slopes of the dynamic curves are quite similar to the corresponding static ones. This means that after initial impact the plate behaves in a quasi-static manner and that membrane stresses control the response in both cases. This is in accordance with tests performed on stiffened steel plates by Langseth and Larsen (1993). They performed test on plates with stringers in the free span only (Langseth and Larsen 1990) and plates with continuous stringers (Langseth and Larsen 1993). They found that the behaviour of the force-displacement curves were different for plates with stringers and single plates, but the stiffness after the membrane stresses control the response are approximately equal for plates with stringers and single plates. The critical impact energy giving plugging was approximately equal in the two cases for the chosen stringer dimensions. That was the case even though the plates with stringers had different deformation patterns than single plates.

The permanent deformation profile for the static tests where incipient fracture took place are shown in Figure 86 together with the corresponding dynamic profiles for the test which had the highest velocity not giving cracks in the target and the test that had the lowest velocity giving cracks in the target. For impact on a stiffener and beside a stiffener with a blunt ended nose, and impact on a stiffener with a hemispherical ended nose, the static and dynamic permanent deformation profiles are approximately equal. The static and dynamic central displacement at maximum force when incipient fracture took place were approximately equal in those three cases. For load applied next to a stiffener with the hemispherical ended nose this was not the case. This effect may be connected to differences in the definition of cracks in the static and dynamic cases. In the dynamic tests any surface cracks were defined as failure or cracks in the target, while a sudden drop in the load was used as the corresponding initiation criterion of fracture in the static tests. There is a possibility for crack development without any significant changes in the load. However, to trace these cracks in the static test other experimental equipment must have been available or the specimens must have been unloaded, inspected and reloaded at several load levels.

The difference in the evolution of the stiffness for a blunt and a hemispherical nose is shown in Figure 36 for the static tests. The load spread zone was larger for the blunt nose than the hemispherical nose, and consequently the stiffness was less in the latter case. The same was also observed in the dynamic tests. If one compare the stiffness for the different load applications point a variation of stiffness is seen in the beginning of the impact, Figure 44. For large displacements the curves become almost linear and with approximately the same slope. Thus, the membrane forces control the response in this part.

The maximum force versus the impact energy for the dynamic tests are shown in Figure 87. All test series were divided in three different cases: no failure, cracks, and perforation of the target. The maximum static force levels are also plotted. The static maximum force level at incipient fracture was approximately the same as in the dynamic case.

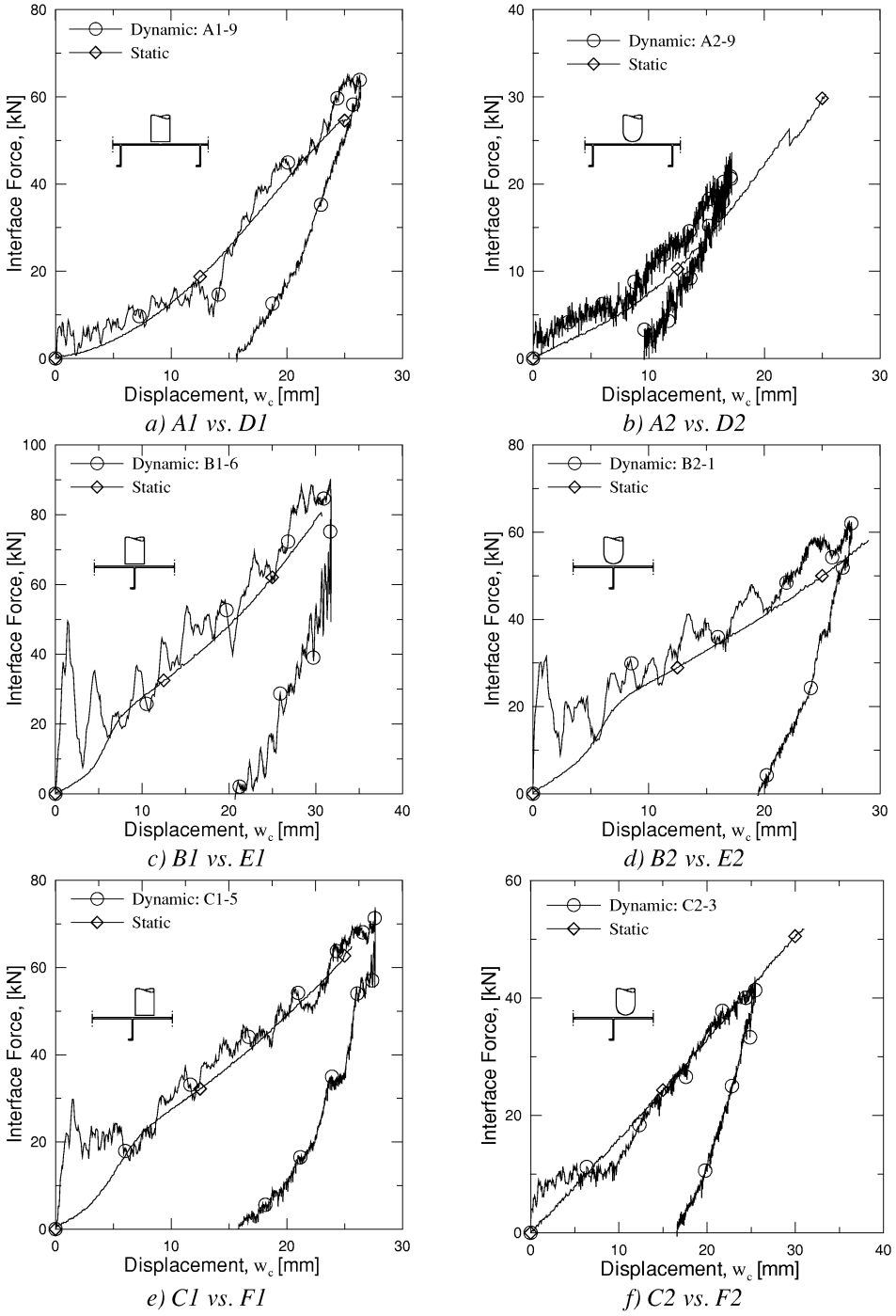

Figure 85 Dynamic and mean static force-displacement curves for the different test series.

Figure 88 shows the absorbed energy at maximum force vs. the impact energy for the dynamic tests, and the corresponding static strain energy levels. In test series A1, B1, B2 and C1 the static strain energy at maximum force predicts the impact energy giving cracking in the dynamic tests. While, in test series A2 and C2 where a hemispherical projectile impacts in between stiffeners and next to a stiffener, respectively, the static energy levels overestimates the impact energies giving cracks. A possible reason may be the difference in the definition of cracking/fracture in the static and dynamic tests, as mentioned above. Figure 88 also shows that with increased impact energies the absorbed energy in the target for the dynamic cases levels off above the static energy level. In the studied velocity range and for the blunt ended projectile, it seems like the static tests may be used to give a conservative estimate of the incipient fracture impact energy in the dynamic tests. For the hemispherical ended projectile this method may lead to non-conservative results.

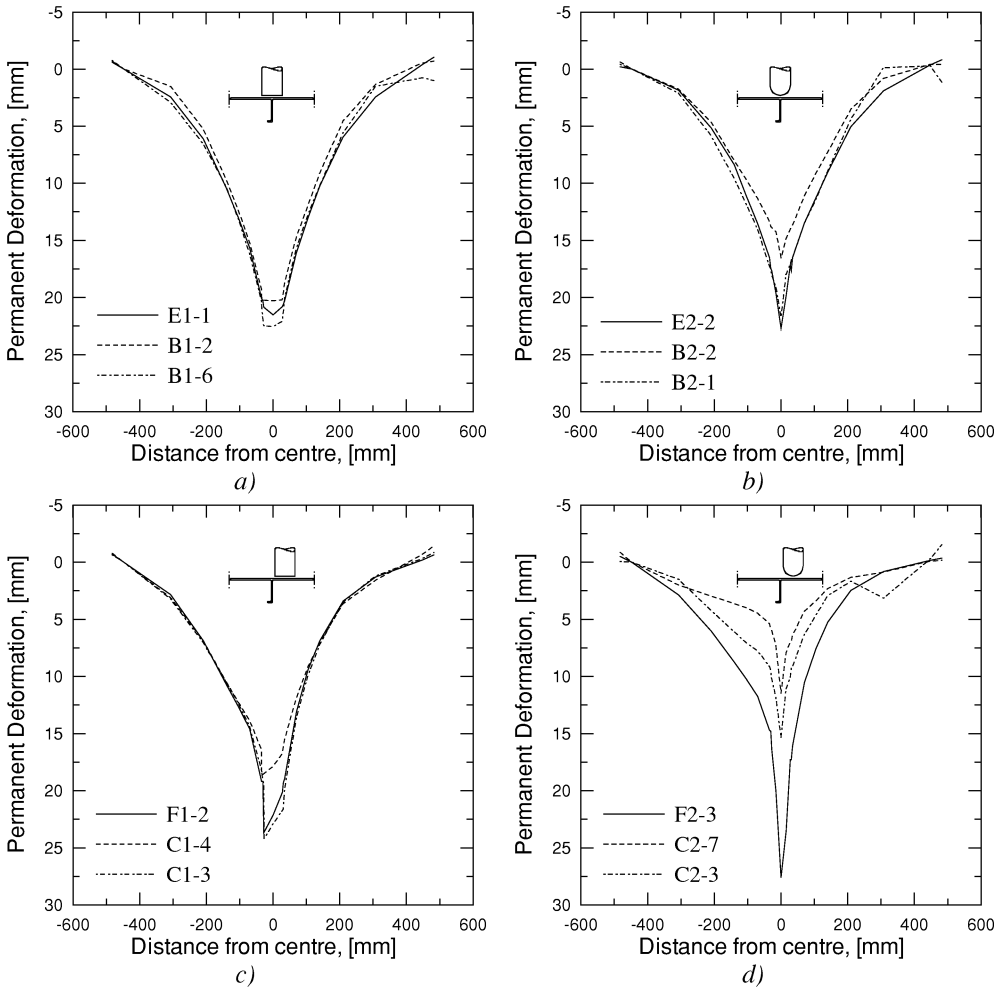

Figure 86 *Static vs. dynamic permanent deformation profiles: a) E1-1: static, B1-2: no failure, and B1-6: cracking, b) E2-2: static, B2-2: no failure, and B2-1: cracking, c) F1-2: static, C1-4: no failure, and C1-3: cracking, and d) F2-3: static, C2-7: no failure, and C2-3: cracking.*

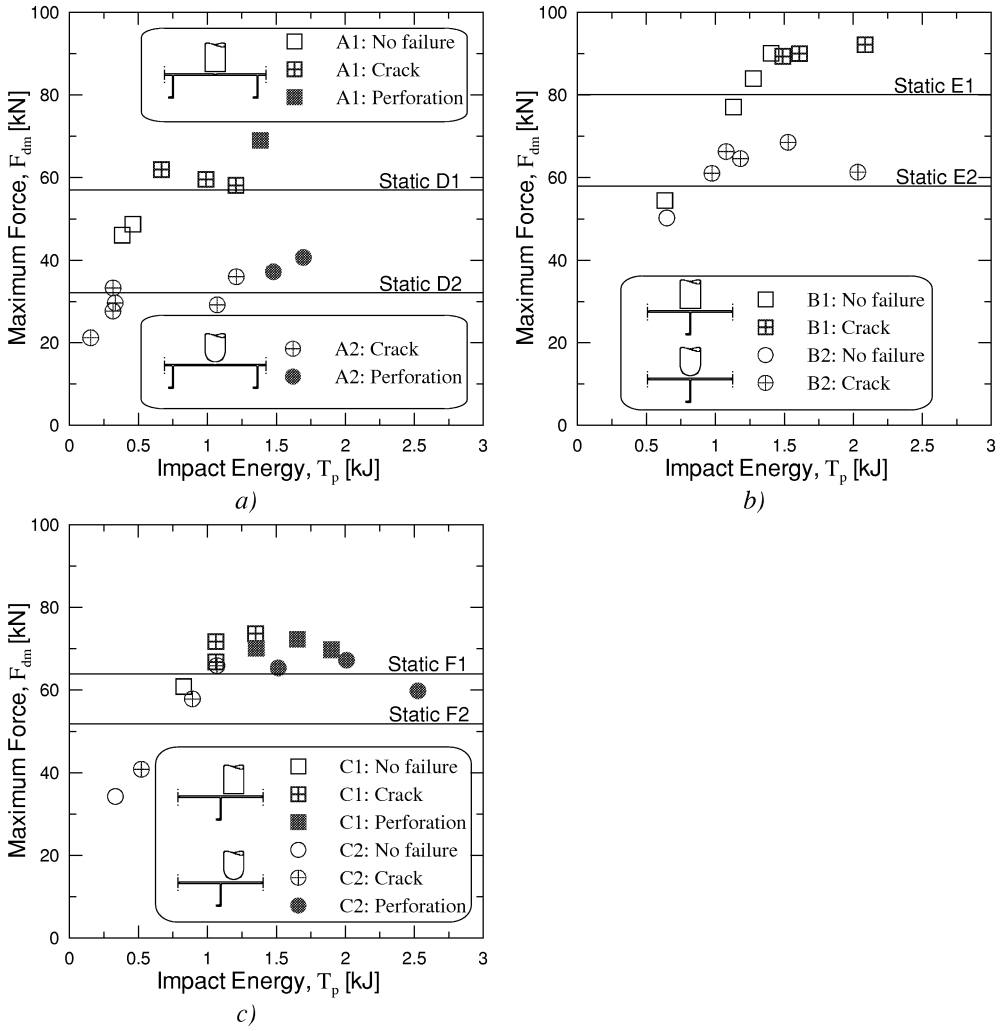

Figure 87 Impact energy versus the maximum force for a) impact between stiffeners for blunt (A1) and hemispherical projectile (A2), b) impact on a stiffener for blunt (B1) and hemispherical projectile (B2), and c) impact next to a stiffener for blunt (C1) and hemispherical projectile (C2). The mean maximum static force levels are also plotted.

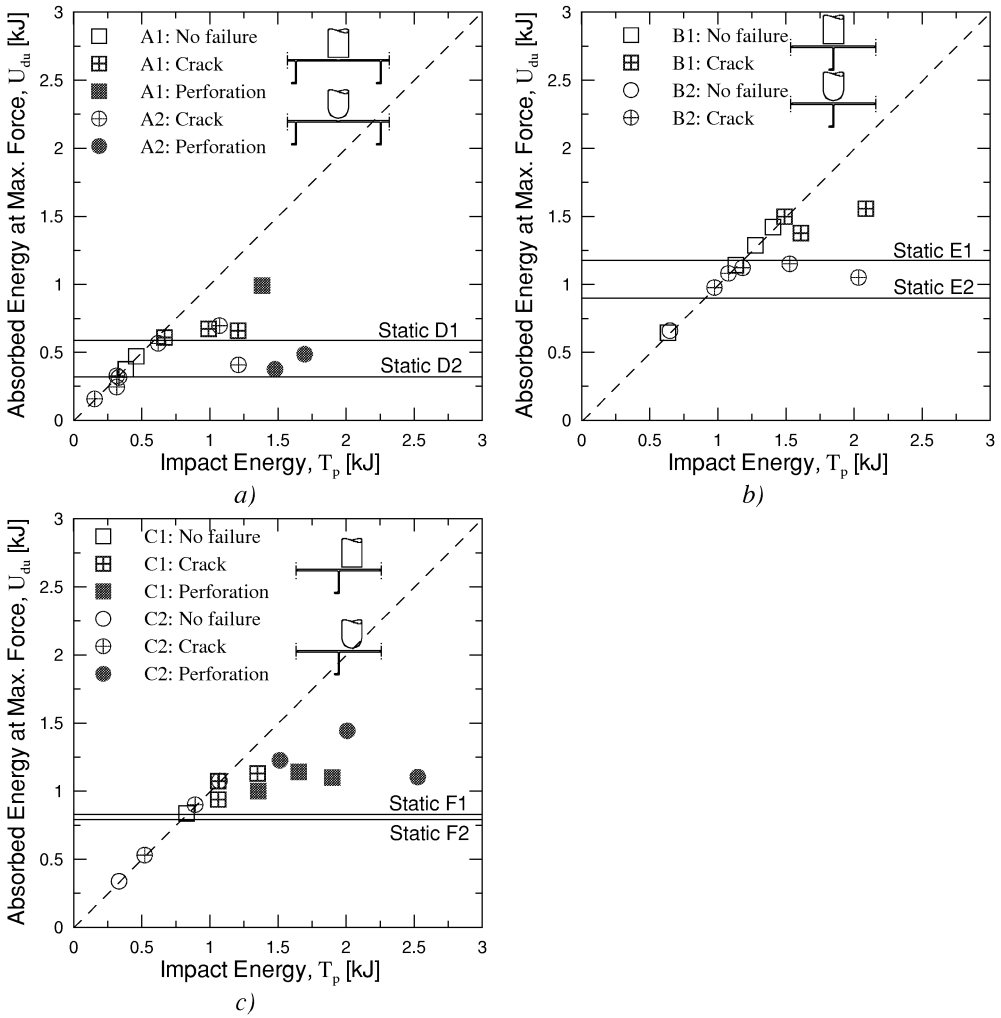

Figure 88 Impact energy versus the absorbed energy in the target at maximum force for a) impact between stiffeners for blunt (A1) and hemispherical projectile (A2), b) impact on a stiffener for blunt (B1) and hemispherical projectile (B2), and c) impact next to a stiffener for blunt (C1) and hemispherical projectile (C2). The mean static energy levels are also plotted.

5 Metallurgical Investigation

A microscopic examination was accomplished to reveal the physical phenomena underlying the local failure of the impacted plates. This metallurgical investigation has been carried out in close collaboration with Mr John Rasmus Leinum, Department of Materials Technology and Electro Chemistry, NTNU. In this chapter all figures are collected in the end of the chapter.

Large variation in strength and ductility were observed between the different extrusions, as described in Chapter 3. Therefore, the grain size and the structure of the extrusions were investigated. The Continuum Damage Mechanics model used in the numerical modelling assumes that the material is ductile. Thus fractographic investigation where carried out in a Jeol JSM 840 scanning electron microscope to establish fracture mechanisms. In addition, the different zones in the weldments were examined. Whether the initiation point of the fracture is at the rear or front side was explored, and this may provide information that is important when deciding how to perform the numerical modelling of the impacted plates. Furthermore, the investigation was providing information on the cause of the differences in fracture propagation due to the variation of the impact location and the projectile nose shape.

The studies of the cross-sections of the penetrated plates were carried out in a Leica MeF4 light microscope equipped with a ProgRes 3008 digital video camera. The hardness measurements were carried out on a Matsuzawa DVK-1S digital hardness tester with a Vickers pyramid, applying a load of 1 kg for 15 seconds. The plates studied were impacted at velocities below the ballistic limit. Four different cases were studied:

- The load applied between the stiffeners (on the weld) with a blunt ended nose: A1-3.
- The load applied next to a stiffener with a blunt ended nose: C1-3 and C1-4.
- The load applied between the stiffeners (on the weld) with a hemispherical ended nose: A2-8.
- The load applied next to a stiffener with a hemispherical ended nose: C2-2.

5.1 The load applied on the weld with a blunt projectile

The blunt ended projectile impacted the test specimen A1-3 on the weld with an impact velocity of 6.6 m/s and gave extensive cracking, but not complete perforation. The failure mode of test specimen A1-3 is shown in Figure 89. A study in the light microscope was performed to study the change in microstructure across the weld and the crack. Figure 90a and Figure 90b show macrographs of the cross section normal to the weld, Section S1-S1 in Figure 89. The four microscopic images in Figure 90 show the grain structure. Figure 90c and Figure 90d show the through thickness shear fracture, Figure 90e shows the weld, Figure 90f shows the indentation of the projectile into the plate and shear deformation was observed. It is obvious that the indentation was small on one side of the projectile and a through thickness failure was established on the other side. Figure 90 illustrates that the weld material has larger grain size than the base material and that the material in the surface has larger grain size than the material in the middle of the plate. The thickness of the recrystallised grains at the surface was less at the both sides of the weld at the contact area (Figure 90e) than outside the contact

area (Figure 90c). This means that the material in the contact area has been deformed and the recrystallised grains have become thinner due to plastic deformation.

A study in the scanning electron microscope (SEM) was done to identify the mechanisms for crack propagation during the penetration process. Cracks were not observed on the front side at Point P1 in Figure 91a. The cross-section SEM micrograph in Figure 91b and Figure 91c shows the crack on the rear side at Point P4 in Figure 91a. There were no voids at the crack tip.

Figure 92 shows a crack at the front side at Point P1 in Figure 89, i.e. in the region between the weldment and the base material. That narrow region adjacent to the fusion zone, where local melting is likely to occur, is frequently referred to as the subsolidus region (Gråberg et al. 2002). In that zone the heat influence on the base material has been so high that the low-melting point phases have melted and wet the grain boundaries leading to a reduction in fracture toughness (same as observed by Gråberg et al. (2002)). The crack propagated along the low-melting point phases that had wet the grain boundaries in the subsolidus region. SEM images were also taken approximately 350 mm from the impact point to see if cracks or voids were present in the subsolidus region. No cracks or voids were observed, but some low-melting point phases were seen in the subsolidus region, see Figure 93d.

Figure 93 shows the particle structure in the different zones 350 mm from the impact point. Figure 93a shows the base material with coarse α-AlFeMnSi particles. The hardening Mg_2Si precipitates are too small to be seen with this experimental technique. The weld consists of an eutectic particle structure of a bright α-AlFeMnSi phase and a dark Mg_2Si-phase located at the grain boundaries, Figure 93c. Figure 93b and Figure 93d show the transition region between the base material and the weldment on the front and rear side, respectively. In Figure 93d, a low melting point phase can be seen in the subsolidus region of the weld-zone.

SEM investigation of the fracture surface of the heat affected material and the weld material were performed. The fracture surface at Point P3 in Figure 89 is shown in Figure 94. The micrograph shows ductile dimples formed in the HAZ during the fracture process, and it confirms the formation of voids as the main fracture mechanism. The fracture surface in the weld which represents Point P2 in Figure 89 was examined. Figure 95 shows some dimples in the fracture surface of the weld, but the fracture mechanism is mainly intercrystalline along the weaker eutectic phases in the grain boundaries. Hence the weld material seems to be less ductile than the base material.

Vickers hardness tests across the weld at the impact point and 350 mm away from the impact point were plotted together with the hardness test on specimen 90^0-w10, reported in Chapter 3. The Vickers hardness was established in the middle of the plate thickness and at the front and rear side at Section S1-S1 in Figure 89. Figure 96 shows that the variation of the Vickers hardness in heat affected zone were approximately the same in all tests. As described in Section 1.4, this implies change in yield stress and ultimate strength with distance from the weld.

5.2 The load applied next to a stiffener with a blunt projectile

The blunt ended projectile impacted the test specimen C1-3 next to a stiffener with an impact velocity of 6.2 m/s and gave extensive cracking, but not complete perforation. Figure 97 shows the shear failure mode of the impacted plate. Figure 98a and Figure 98b show macrographs of the cross section normal to the weld, Section S1-S1 in Figure 97. Furthermore, Figure 98 shows light microscope images across the stiffener and the impact point. The sheets were orientated at 90^0 with respect to the extrusion direction. Figure 98c and

Figure 98d show the shear fracture next to the stiffener. The indentation of the projectile into the plate is seen in Figure 98e, and it is clear that the indentation is small on one side of the projectile and a through thickness failure is established on the other side. No fractures on the front side or rear side at Point P1 in Figure 97 were observed. An interesting observation is the difference between the grain size in Figure 98 and in Figure 90. It seems like the material in test C1-3 was not only recrystallised at the surface, but also partly recrystallised in the centre of the plate. This may affect the structural behaviour of the stiffened plate.

Figure 99 shows the scanning electron micrography of the crack on the rear side at Point P2 in Figure 97. Figure 99b shows the dimple structure in the fracture surface and illustrates that the fracture was ductile on the rear side of the plate. The direction of the dimples in this fracture indicates that the material on the rear side was exposed to tension, much more than shear.

Figure 100a show the fracture surface at Point P3 in Figure 97. The projectile has deformed the initial part of the fracture (the dimples), leaving a smooth surface, Figure 100b and Figure 100d. Ductile shear dimple structure is observed in the middle of the smoothed surface, Figure 100c. The fracture surface near the rear side shows indications of secondary fractures. SEM investigations of the fracture surface of the perforated plate confirmed the formation of voids as the main fracture mechanism.

The blunt ended projectile impacted the test specimen C1-4 next to a stiffener with an impact velocity of 5.47m/s. No visible cracks were observed in the specimen shown in Figure 101a before the metallurgical examination. Figure 101b shows the Section S1-S1 in Figure 101a. Figure 102a shows that no cracks are visible on the front side, while Figure 102b shows fractures on the rear side at the circumference of the projectile, Point P1 in Figure 101. Figure 102c and Figure 102d show the magnifications of two of the fractures, and no voids were seen in the crack tip. It may be reasonable to conclude that the fracture was initiated on the rear side.

5.3 The load applied on the weld with a hemispherical projectile

Test specimen A2-8 was impacted on the weld with a hemispherical projectile with an impact velocity of 3.4 m/s and gave little cracking. The failure mode is shown in Figure 103. Fracture lines in the fusion lines and across the weld were seen.

Figure 104 shows the macrograph of cross-section, Section S1-S1 in Figure 103, and light microscope images. As in test A1-3 the grain size in the weld was larger than in the base material. The grain size inside the plate as well as at the surface was the same as observed in test A1-3. Figure 104d shows a magnification of the frame in Figure 104b of a crack in the fusion zone (transition zone between the weld and heat affected material) at the rear side of the plate.

SEM fractographs of the fracture surface in the weld, at Point P1 in Figure 103, is shown in Figure 105. The fracture probably propagated along the eutectic structure (shown in Figure 93c) along the grain boundaries, that is an intergranular fracture. The eutectic network around the grains is weak relative to the matrix, thus, the fracture toughness of the weld material may be lower than in the base material.

The crack in the fusion zone, at Point P2 in Figure 103a, is shown in Figure 106a. Figure 106b shows a magnification of the frame in Figure 106a. No low-melting point phases similar to the ones in the fusion zone of the weld in test A1-3 (Figure 92), were seen in the crack tip. Nevertheless, it does not mean that such phases are non-existent in the fusion zone. It should be pointed out that these photographs correspond to one planar section through the weld and crack. The structure in planes above or below this cross section will not be exactly the same. Secondary cracks were observed beside the primary crack.

5.4 The load applied next to a stiffener with a hemispherical projectile

Test specimen C2-2 was impacted next to the stiffener with a hemispherical projectile with an impact velocity of 5.7 m/s. The failure mode is shown in Figure 107, Figure 108a and Figure 108b. The fracture lines were parallel to the stiffener. Figure 108 shows light microscope image of Section S1-S1 in Figure 107. The material was recrystallized in surface and partly recrystallized in the middle of the plate.

Scanning electron micrographs of the crack on the rear side in Section S2-S2 and Section S3-S3 in Figure 107 are shown in Figure 109. The cracks were at an angle to surface, and the crack-tips were pointing outwards from the impact point. A secondary crack at the rear side was also observed.

5.5 Discussion of the results from the metallurgical examination

The light microscope images of the different tests show that the material in test A1-3 (impacted with a blunt projectile nose between the stiffeners) and A2-8 (impacted with a hemispherical ended projectile between the stiffeners) consist of fine grains. The material in the two other tests impacted next to a stiffener, C1-3 (blunt ended nose) and C2-2 (hemispherical ended nose), was partly recrystallised. All four tests were recrystallised at the surfaces. Different levels of recrystallisation in the extrusions probably caused the significant scatter in ductility as described in Chapter 3 (as described by Lohne and Neass (1979)). The material was recrystallised prior to the impact. No evidence of temperature effects during penetration was seen.

Ductile fractures were seen in all test specimens except the fractures in connection with the welds. Crack growth in ductile fracture is essentially by a process of void coalescence (Dieter 1988). The voids and the bridges of material between the voids are elongated, and this leads to a fracture surface consisting of elongated dimples. According to Dieter (1988), the voids are usually nucleated heterogeneously at sites where the compatibility of the deformation is difficult. The dimples are equiaxed when tensile overload causes the fracture and elongated when shearing causes the fracture (Colangelo and Heiser 1987). Shear dimples on the plug and plate surfaces orientated in opposite directions suggest that the total punching action involved localised failure via plastic shearing and tensile overload. This is in accordance with the present investigation where projectile impact with a blunt ended nose caused shear on the front side at the circumference of the nose, and the material on the rear side was exposed to tension, and to much less extent of shear deformation. Scanning electron microscope observations indicated clearly that the fracture mechanism in the base material consisted of void nucleation and coalescence on the apparent shear fractures: hence, the typical dimple-type fracture was dominating.

Some cracks in the weld and low-melting phases were observed in test A1-3 impacted with a blunt projectile nose between the stiffeners. The low-melting phases near the fusion zone and the euctectic structure on the grain boundaries in the weld probably caused lower fracture toughness of the weldment and heat affected zone than in the base material. The low fracture toughness of the weldment may be a reason for that the plug was not completely circular for tests where perforation occurred when impacting on the weld.

The fracture of the test specimen impacted with a hemispherical ended projectile between the stiffeners (A2-8) was mainly across the weld and in the fusion line, and the distance between the parallel cracks was 15 mm. In test specimen impacted with a hemispherical ended projectile next to a stiffener (C2-2) the corresponding distance was 17.5 mm. In test A2-8, the weld existence caused the strains to localise in the fusion line, furthermore, the crack probably was formed and propagated along the low-melting phases in

the subsolidus region nearby the fusion line (Gråberg et al. 2002 and Hval et al. 1992). The probable low fracture toughness in this region caused the fracture, and the fracture occurred through the plate thickness in the fusion zone. In test C2-2 the fracture also started at the rear side, but the fracture propagated in an angle to the impact direction. The fracture across the weld (A2-8) was probably an intergranular fracture, and the fracture toughness was probably lower there than in the base material. This perpendicular crack between the two parallel cracks was not observed impacting next to the stiffener with a hemispherical ended nose. The incipient fracture velocity was much less impacting on the weld than next to a stiffener due to less fracture toughness of the weldment than the base material. Furthermore, the existence of the stiffener, that absorbs a lot of energy, led to a larger incipient velocity impacting next to a stiffener than between the stiffeners.

No shear band was seen, but the grains were distorted at an angle to the surface in the case of plugging, and no distortions of the grains were observed for the hemispherical ended nose. This is in accordance with examination of mild steel tubes with a thickness of 1.2 mm and an outer diameter of 50.8 mm struck by cylindrical missiles with an impact velocity near the ballistic limit (100-250 m/s) by Palomby and Stronge (1988). They observed that the grains at the separation were distorted at about 45^0 angle relative to the surface when the specimen was subjected to a flat-ended projectile and the tube failed by plugging. For the tube hit by a hemispherical-tipped missile the grains were elongated parallel to the surface and void growth was seen. They observed that a localised neck was visible at the periphery of the contact region, i.e. at a distance less than the missile radius and perforation by discing was the result. They explained this failure as a consequence of stretching combined with the dishing outside the contact area.

Wen and Jones (1994) observed that the failure first occurred on the front side and propagated to the rear side without thinning, and a through thickness failure occurred for mild steel and aluminium plates impacted by blunt projectiles with velocities up to 12.2 m/s. This is in contradiction to the present investigation where the fracture was initiated on the rear side impacting next to a stiffener or between the stiffeners (on the weld) with both nose shapes. Levy and Goldsmith (1984) struck a 3.18 mm thick aluminium plate by the 12.7 mm diameter hemispherical projectile at a speed of 89.6 m/s and the photographs indicated incipient fracture on both sides of the cap and the fracture was initiated on the rear side. Palomby and Stronge (1988) also observed initiation of fracture on the rear side when thin-walled mild steel tubes were subjected to missile impact. This is in accordance with observations in the present investigation. Levy and Goldsmith (1984) explained the fracture by tension in the bulge that induced necking and shear. They also observed that the fracture had an angle of 45^0 to the plate contour where the crack-tip were pointing outwards from the impact point similar as in the present study. Necking on each side of the cap and thereafter fracture was also observed by Goldsmith (1985) when perforating aluminium plates. In addition, the occurrence of localised necking in thin ductile plates subjected to hemispherical punch stretching is a well-known phenomenon that limits the formability of metal sheets during metal forming (Palomby and Stronge 1988).

5.6 Concluding remarks

Is seems like the fracture started on the rear side and was induced by tension. No evidence of temperature effects and no pronounced shear localisation through the thickness of the plate have been seen. Ductile dimples are formed during the crack propagation, so it is appropriate to use the Continuum Damage Mechanics model that assumes a ductile material behaviour. However, the damage evolution parameters should vary with position due to the differences in ductility of the different materials and the probably low fracture toughness in the fusion zone.

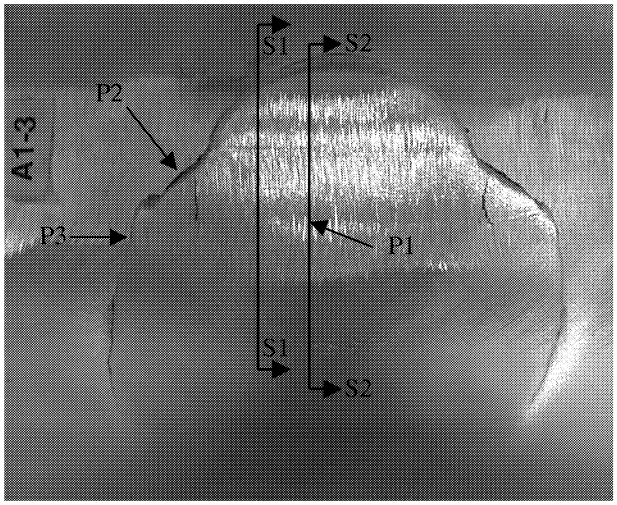

Figure 89 Shear failure of test specimen A1-3, rear side.

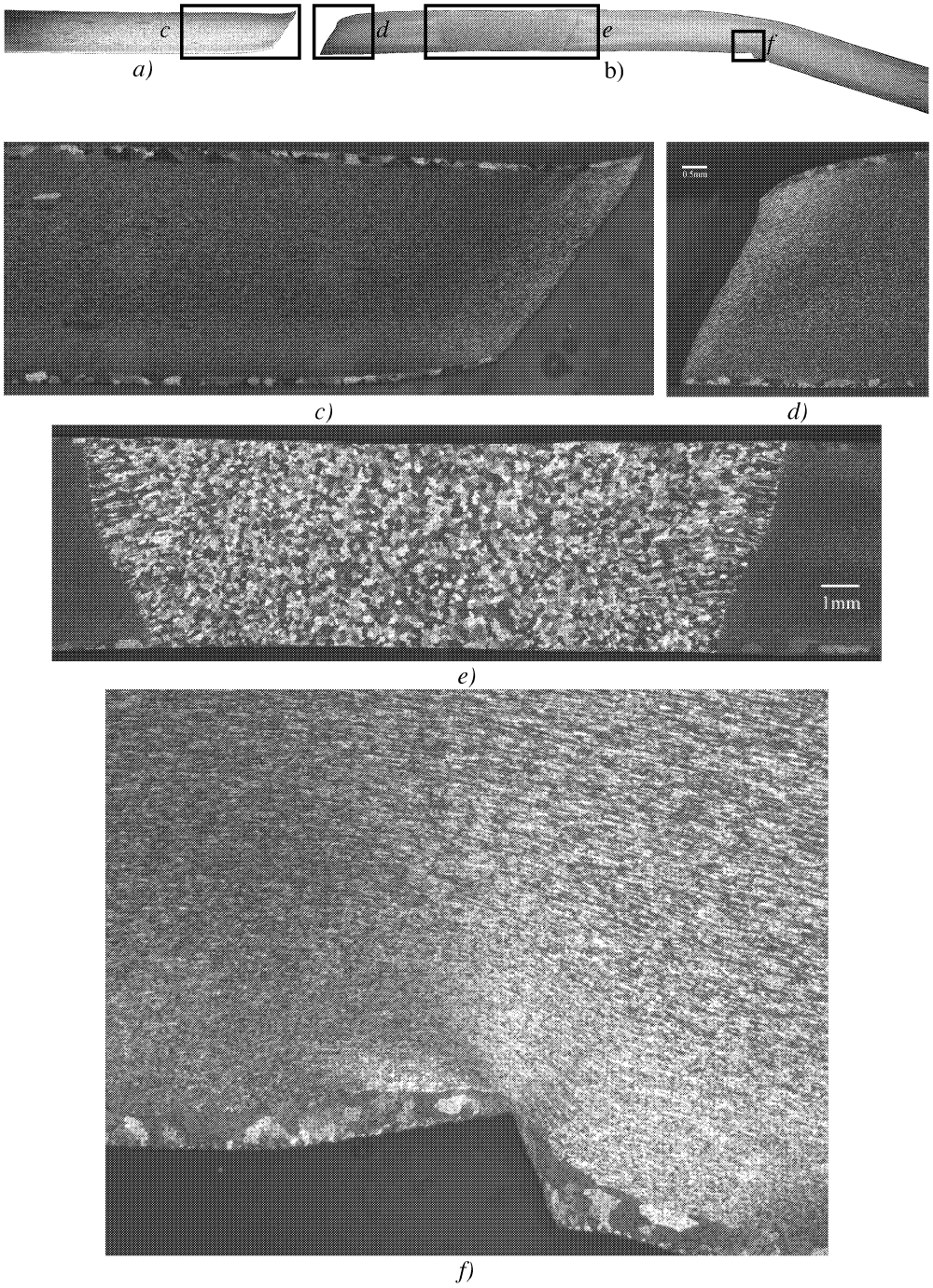

Figure 90 *Section across the weld in test specimen A1-3: a) and b) Section S1-S1 in Figure 89, c) and d) magnification of the shear fracture, d) the weld, and f) the shear localisation at the circumference of the projectile.*

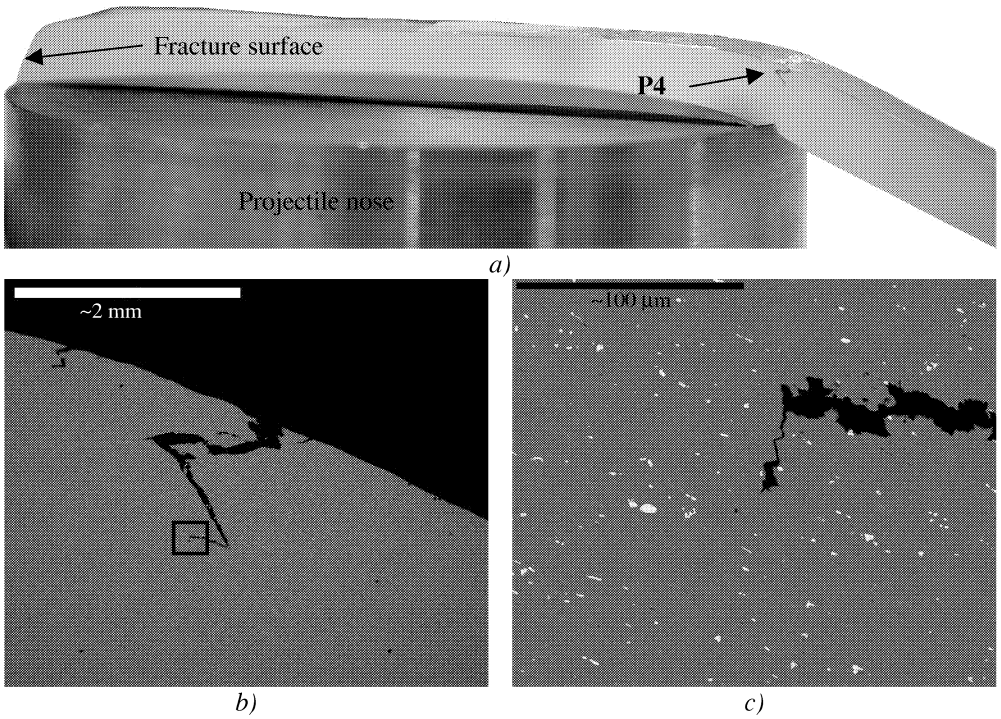

Figure 91 *a) Section S2-S2 in Figure 89 together with the projectile, b) the crack on rear side at Point P4 in a, and c) magnification of frame in b showing the crack-tip.*

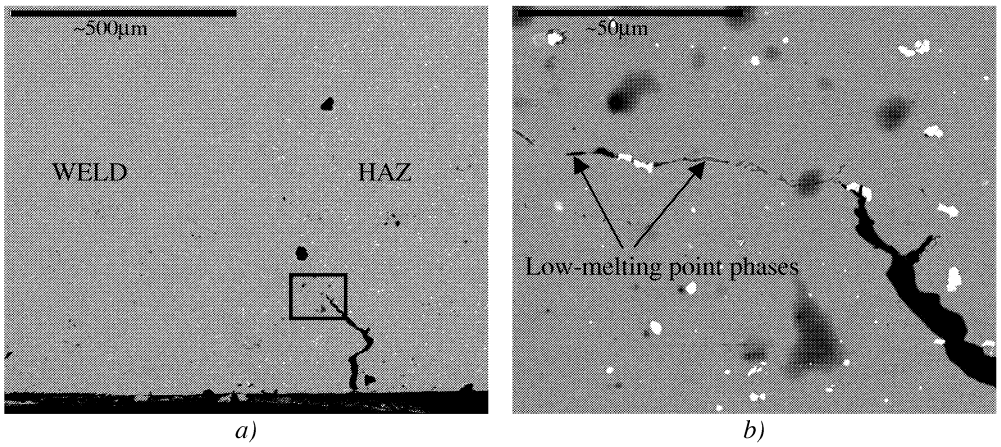

Figure 92 *a) Crack at the front side, Point P1 in Figure 89, and b) magnification of frame in a showing the formation of low-melting point phases in front of the crack-tip.*

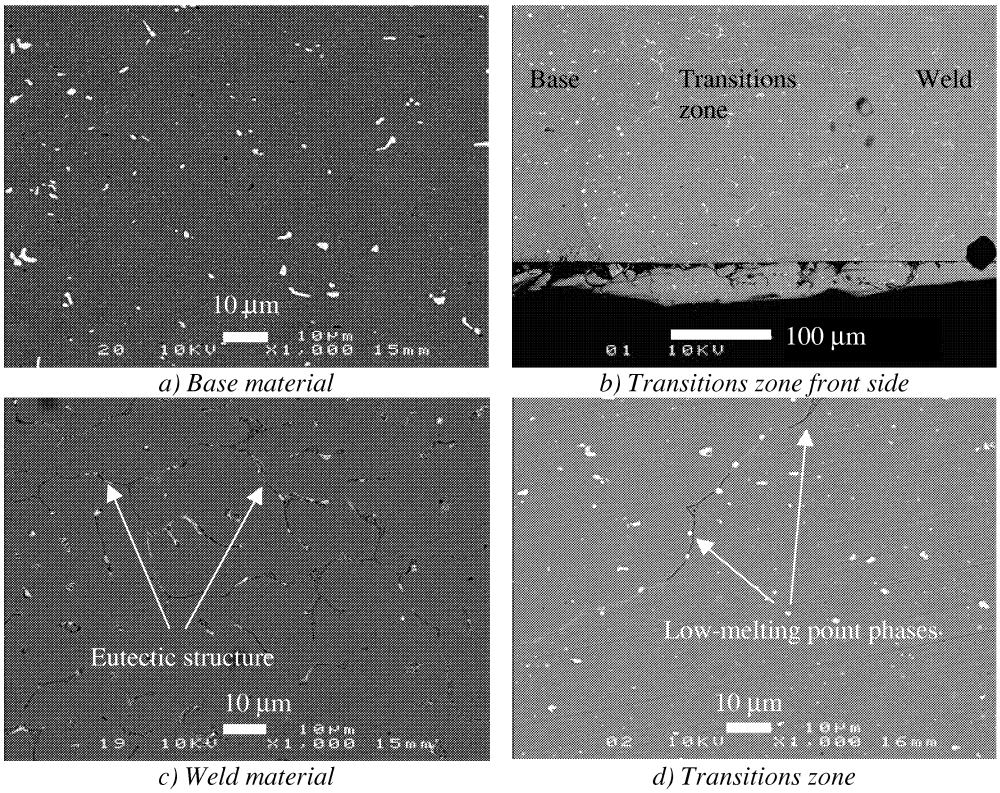

a) Base material *b) Transitions zone front side*

c) Weld material *d) Transitions zone*

Figure 93 The material structure 350 mm from the impact point.

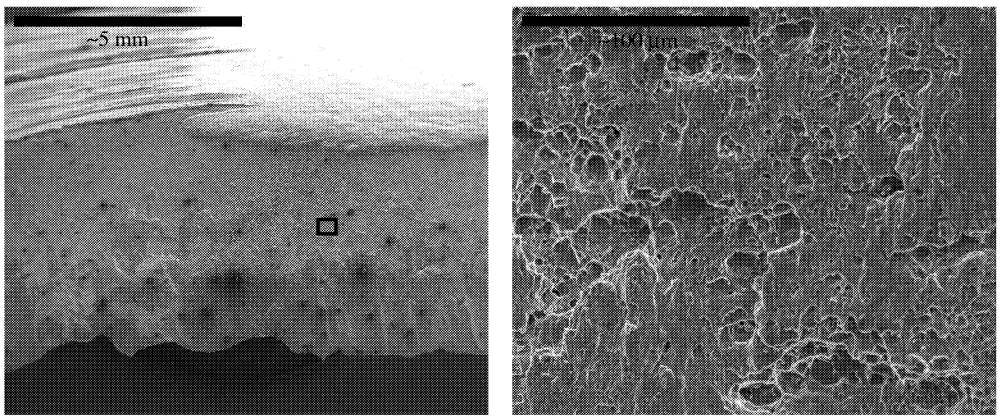

a) *b)*

Figure 94 a) Scanning electron micrography of the fracture surface in the heat affected material, and b) details from the frame in a of the ductile shear dimple structure.

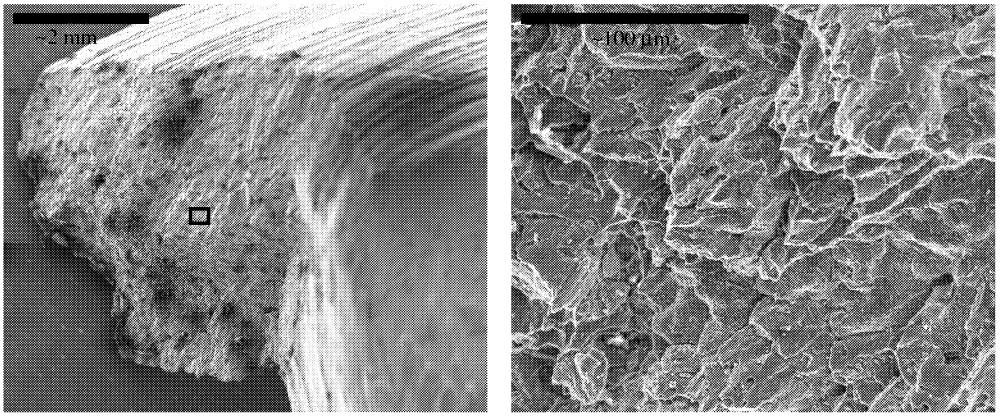

Figure 95 *a) Scanning electron micrography of the fracture surface in the weld material, and b) details from the frame in a showing the structure.*

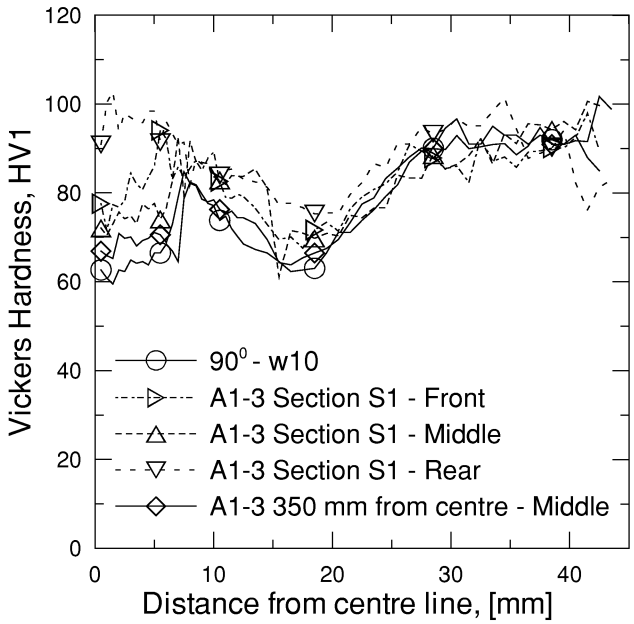

Figure 96 *Vicker hardness test across the weld.*

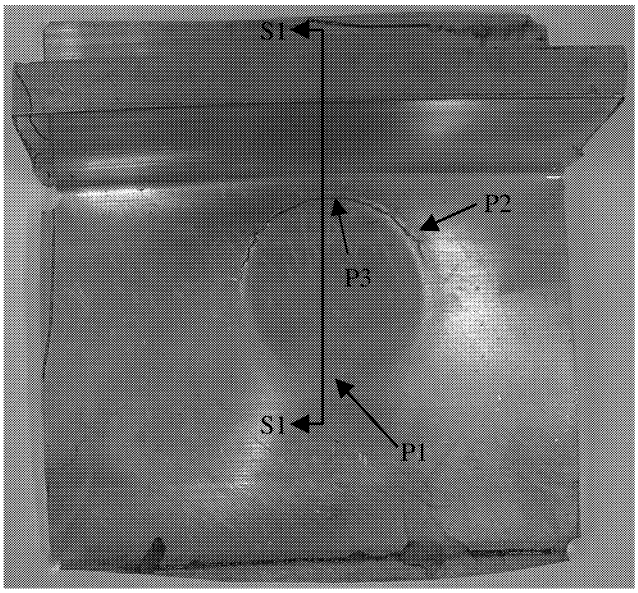

Figure 97 Shear failure of test specimen C1-3, rear side.

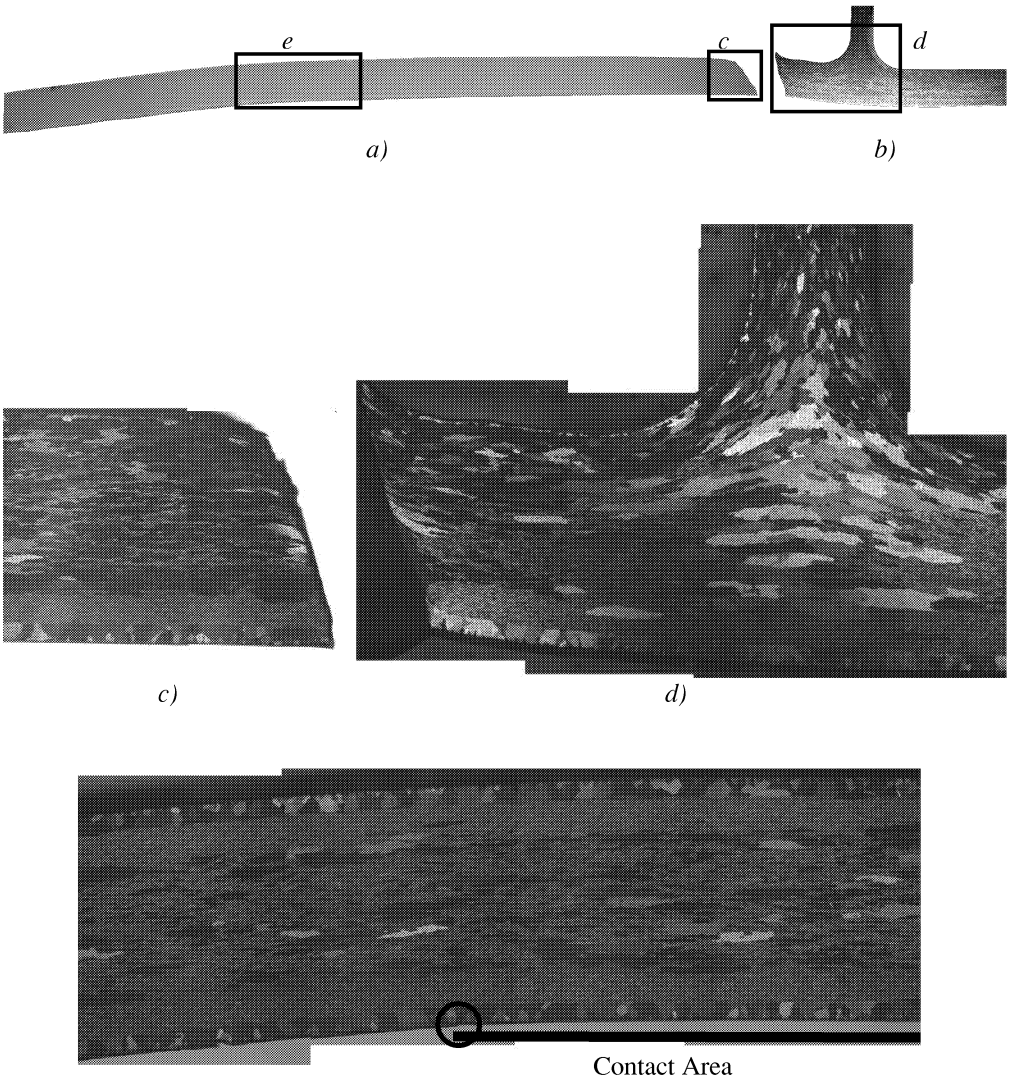

Figure 98 *Section across the fracture in test specimen C1-3: a) and b) Section S1-S1 in Figure 97, c) and d) magnification of the shear fracture, and e) the indentation at the circumference of the projectile.*

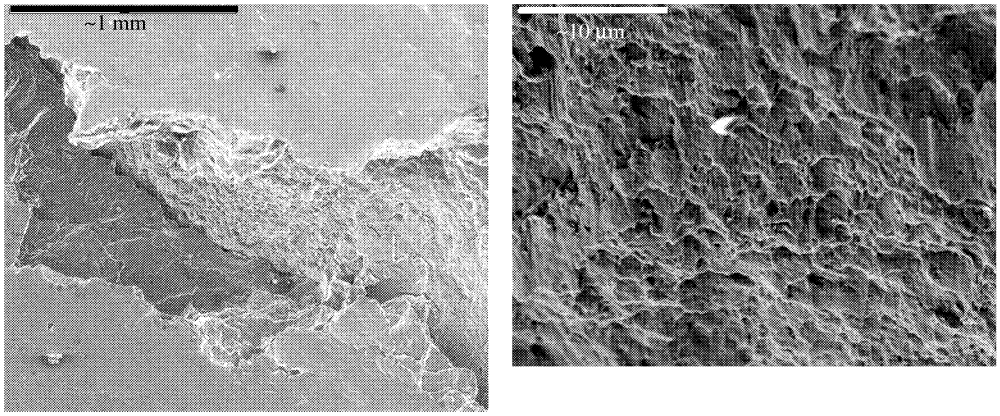

a) *b)*

Figure 99 *a) Scanning electron micrography of the crack on the rear side of test C1-3, and b) detail showing the dimple structure.*

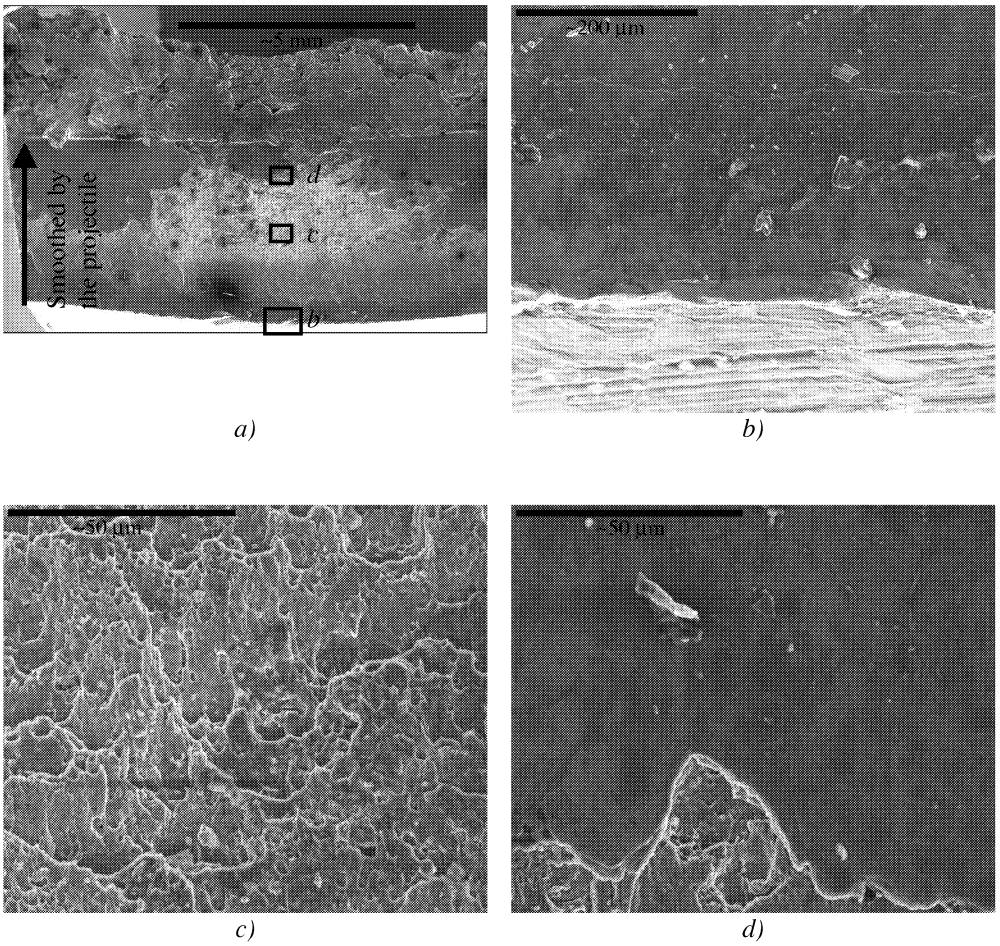

Figure 100 *a) Scanning electron micrography of the fracture surface with both a ductile dimple structure and plane areas deformed by the projectile structure, b) details of the smooth surface, c) shear dimple structure, and d) details of the smooth surface.*

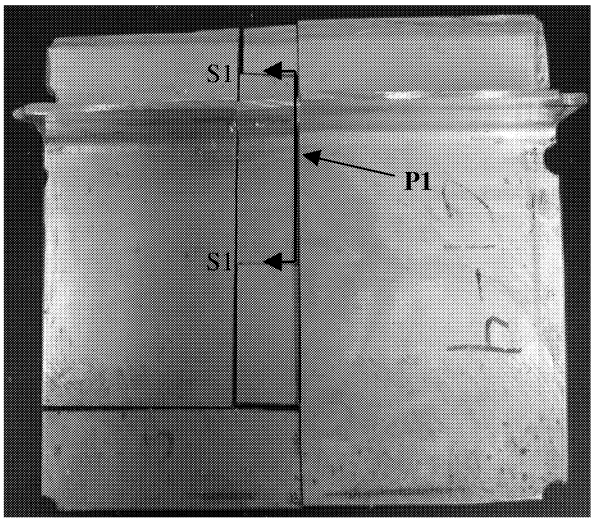

a)

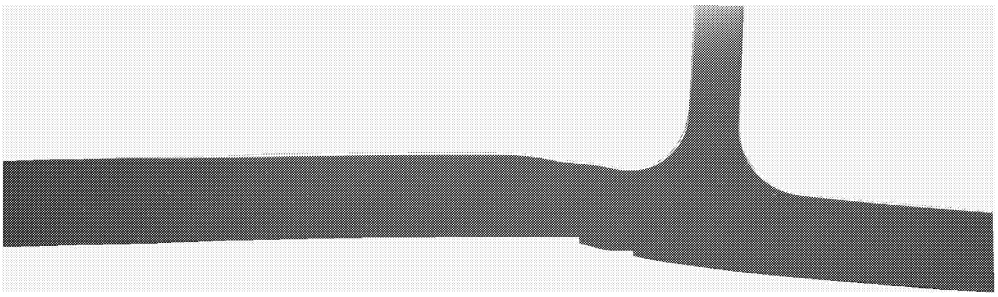

b)

Figure 101 a) Test specimen C1-4, and b) Section S1-S1 in a.

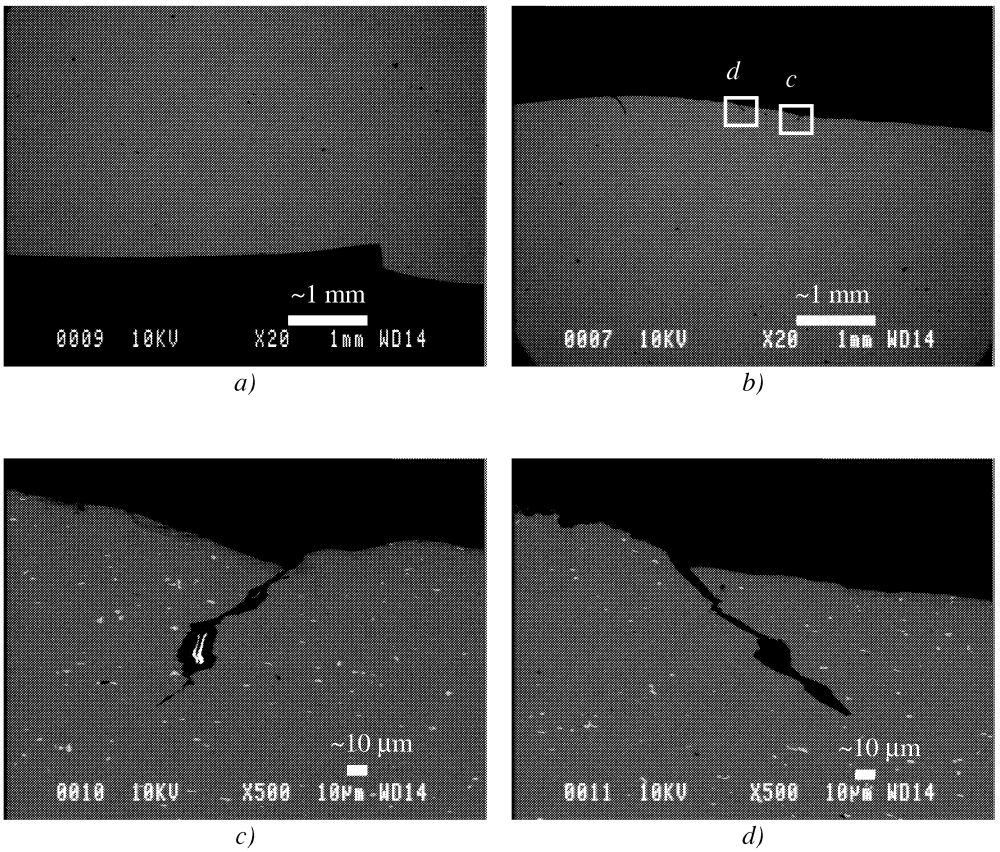

Figure 102 a) No cracks observed on front side, b) fractures on rear side, c) and d) magnification of the fractures on rear side.

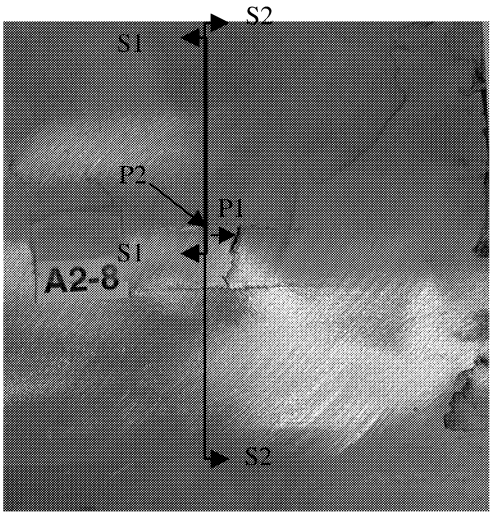

a)

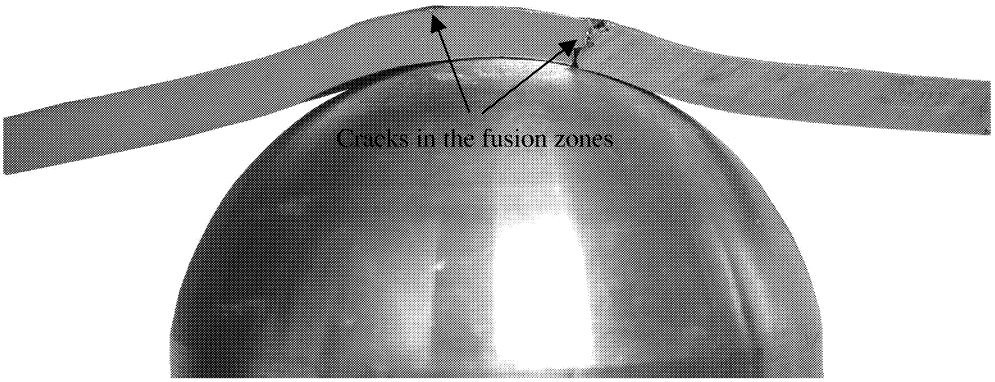

b)

Figure 103 a) Cracks in test specimen A2-8, and b) Section S2-S2 showing the fracture in the fusion line together with the projectile.

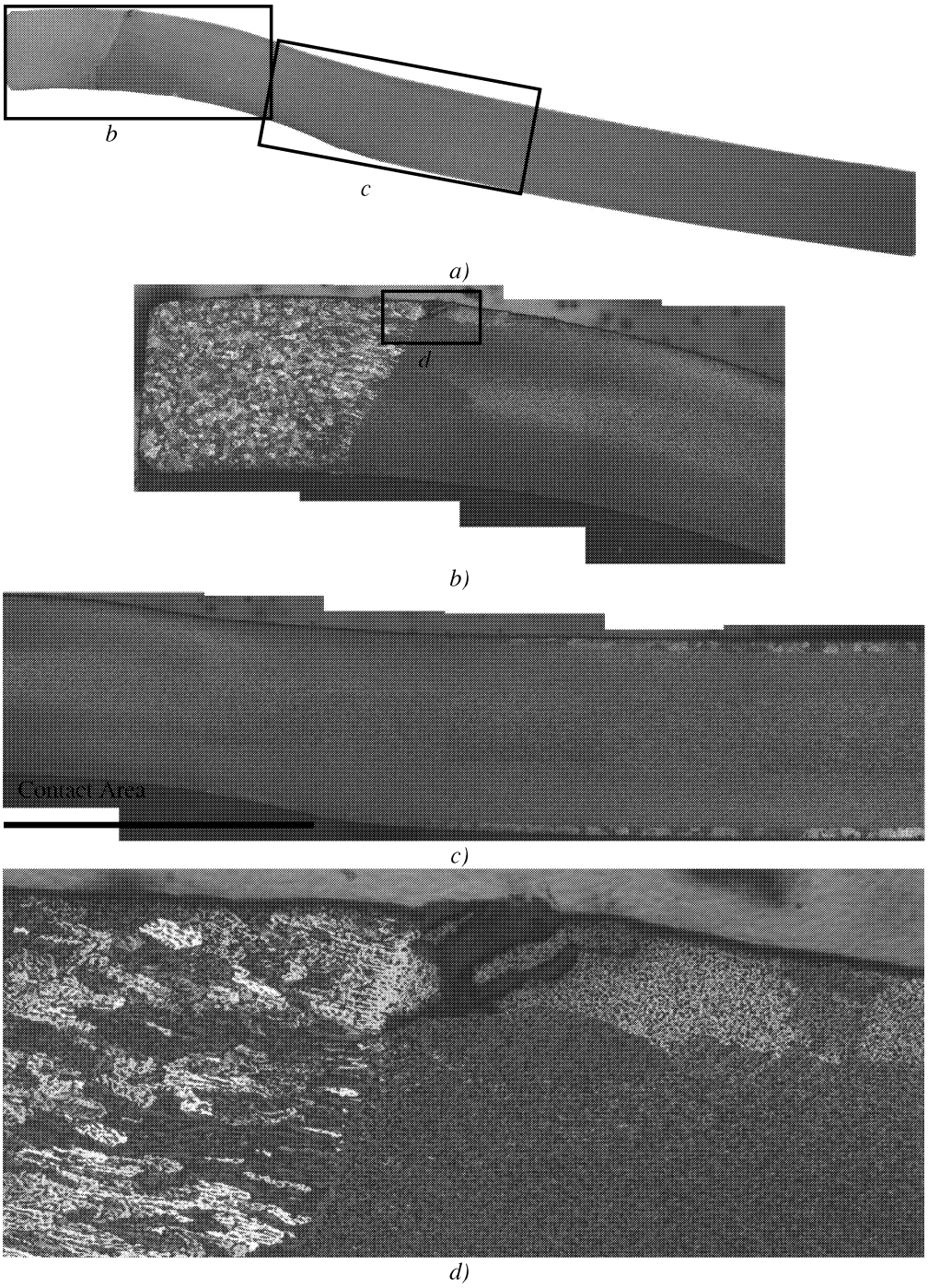

Figure 104 Section across the fracture in test specimen A2-8: a) Section S1-S1 in Figure 103, b) weld and HAZ, c) a part of the contact area and outside the contact area, and d) frame in a showing fracture on the rear side.

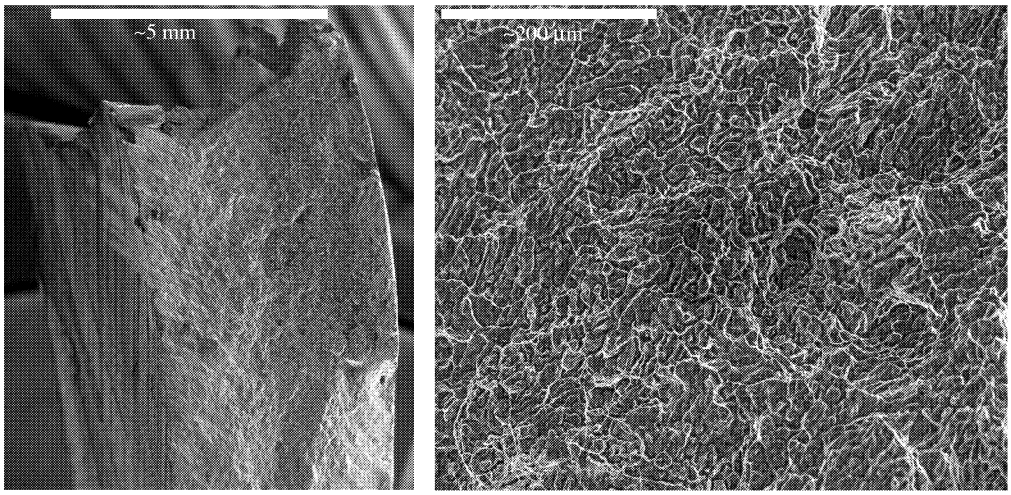

a) b)

Figure 105 a) Fracture surface in the weld (at Point P1 in Figure 103), and b) magnification of the fracture surface showing an intergranular fracture.

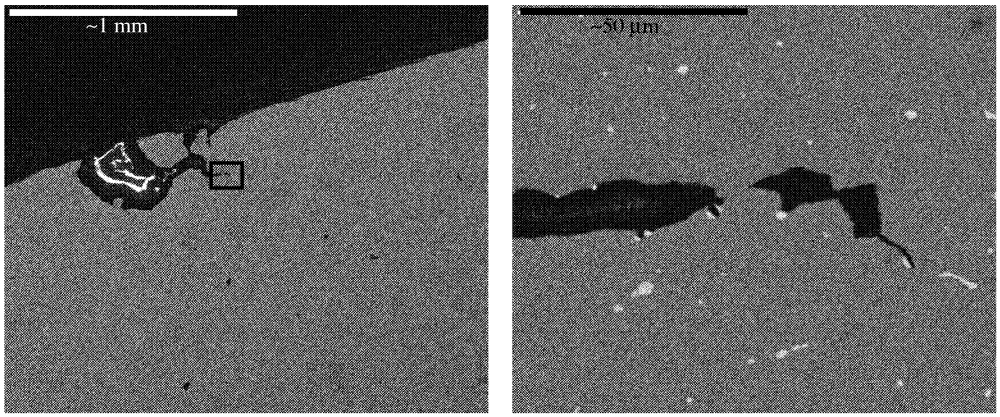

a) b)

Figure 106 a) Fracture on the rear side in the fusion line, and b) magnification of frame in a showing the crack-tip where no low-melting point phases was observed.

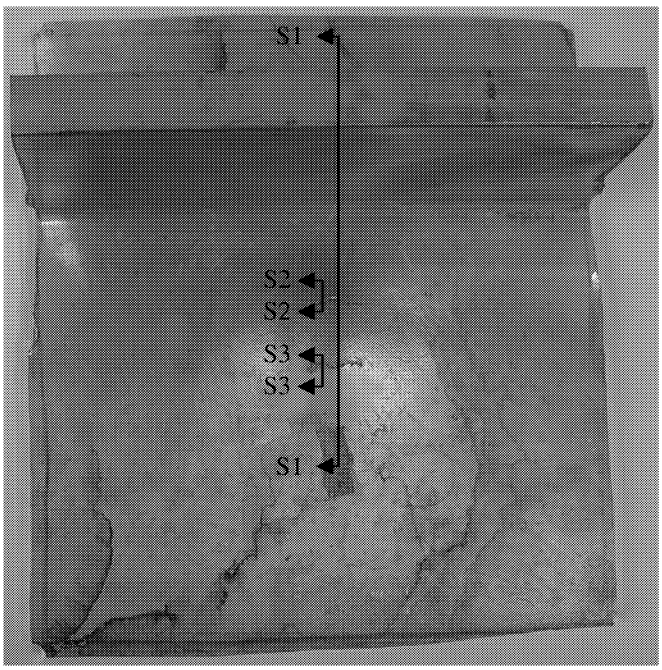

Figure 107 Cracks in test specimen C2-2.

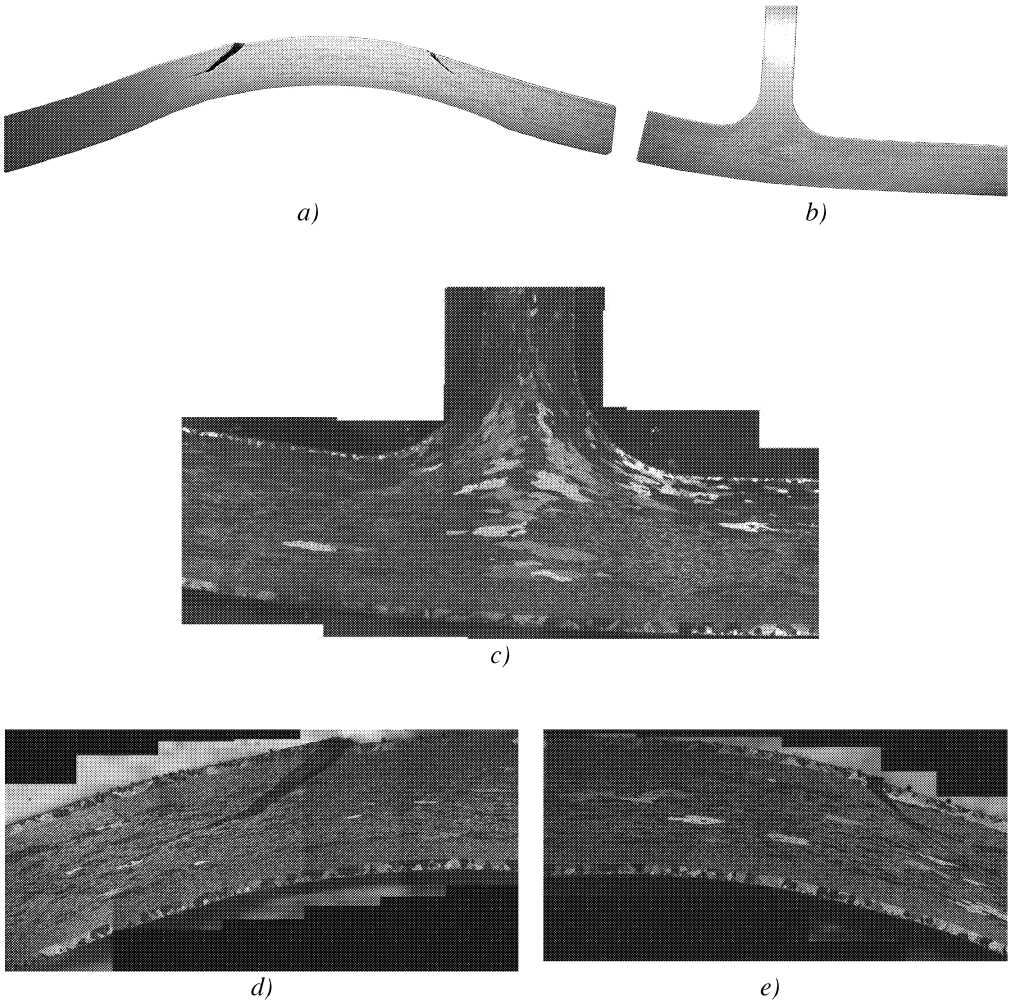

Figure 108 Section S1-S1 across the stiffener in test specimen C2-2.

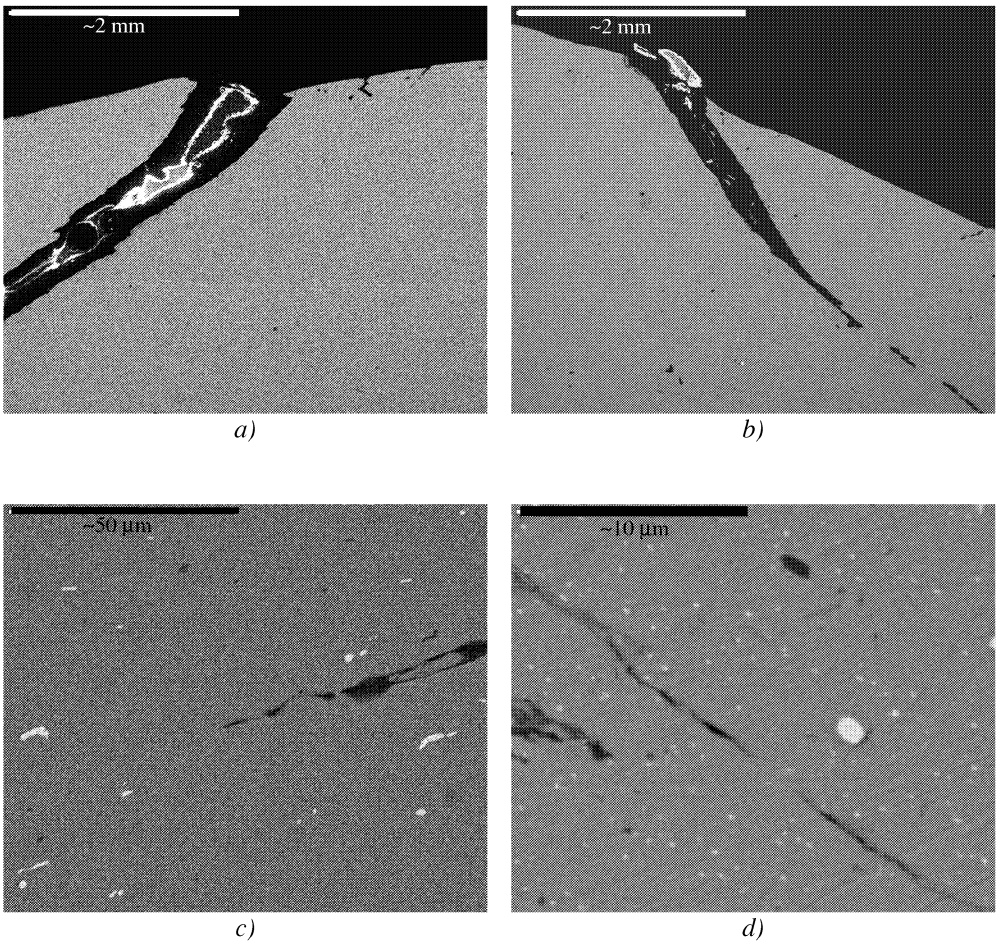

Figure 109 a) and b) scanning electron micrography of fractures on the rear side, and c) and d) the crack tips.

6 Numerical Modelling of Fracture

Numerical studies of stiffened plats subjected to impact loading have been performed using the finite element code LS-DYNA (Hallquist 1998). The main objective with these numerical simulations was to study whether the Lemaitre damage material model (Lemaitre 1996) could predict the response of the plate impacted between the stiffeners with a hemispherical ended projectile. The stiffened plate was modelled using shell elements even though brick elements may certainly give better results. Using brick elements the problem size would have been too large. In the analyses focus was placed on the measured force-displacement curves, the force at fracture, and the failure mode of the impacted plate. The finite element models were generated by the pre-processor LS-INGRID (Hallquist 1993).

The selected test for simulations was the impact test denoted A2-3, where a hemispherical projectile impacted the plate with a velocity of 7.85 m/s. A material test (denoted 0^0-32) taken from one of the impacted plates, was chosen for calibration of the hardening rule of the base material. However, to determine the material parameters of the weld and HAZ, inverse modelling has been used, i.e. tensile specimens taken across and along the weld were numerically simulated to deduce the material parameters by minimising the difference between experimental and numerical response.

6.1 Constitutive model

Assuming small deformations, the strain can be divided into elastic and plastic parts:

$$\boldsymbol{\varepsilon} = \boldsymbol{\varepsilon}^{e} + \boldsymbol{\varepsilon}^{p} \tag{13}$$

where $\boldsymbol{\varepsilon}$ is the strain tensor, $\boldsymbol{\varepsilon}^{e}$ is the elastic strain tensor, and $\boldsymbol{\varepsilon}^{p}$ is the plastic strain tensor.

In the Continuum Damage Model (CDM) proposed by Lemaitre (1996), the effective stress, the stress calculated over the section that effectively resist the forces, is defined as

$$\tilde{\boldsymbol{\sigma}} = \frac{\boldsymbol{\sigma}}{1-D} \tag{14}$$

where $\boldsymbol{\sigma}$ is the stress tensor, and D is the isotropic damage variable, where $0 \le D \le 1$. For a virgin material D equals zero and for a fully broken element D is equal to one. Fracture occurs as D reaches the critical damage, D_c:

$$D = D_c \quad \Rightarrow \quad \text{crack initiation}$$

D_c may vary between $D_c \simeq 0$ for brittle failure to $D_c \simeq 1$ for pure ductile fracture, but usually D_c is in the range 0.2 to 0.5. Even though the critical damage depends upon the material and the loading condition, it is for simplicity assumed that D_c is a material constant.

The strain equivalence principle states (Lemaitre 1996):
"Any strain constitutive equation for a damaged material may be derived in the same way as for virgin material except that the usual stress is replaced by the effective stress."

According to that principle the elastic stress-strain relation is defined by

$$\boldsymbol{\sigma} = (1-D)\,\mathbf{C} : \boldsymbol{\varepsilon}^{e} \tag{15}$$

where $\mathbf{C}$ is the fourth order tensor of elastic moduli.

The yield function, separating the elastic and plastic domain of the stress space, is given as

$$f = \frac{\sigma_{eq}}{1-D} - \sigma_Y = 0 \tag{16}$$

where σ_Y is the yield strength in uniaxial tension, and von Mises equivalent stress reads:

$$\sigma_{eq} = \sqrt{\frac{3}{2}\boldsymbol{\sigma}^D : \boldsymbol{\sigma}^D} \tag{17}$$

$\boldsymbol{\sigma}^D$ is the deviatoric stress tensor.

Langseth et. al. (1999) found that numerical simulations of impacted aluminium plates showed no difference in the plate response between analyses performed with kinematic and isotropic hardening. Assuming isotropic hardening the uniaxial stress strain curve in present study was modelled by

$$\sigma_Y = \sigma_0 + R^* = \sigma_0 + \sum_{i=1}^{2} Q_i \left(1 - \exp(-C_i r)\right) \tag{18}$$

where R^* is the isotropic strain hardening variable, σ_0 is the proportionality limit, Q_i and C_i are the hardening parameters, and r is the damage accumulated plastic strain. This hardening relationship is part of material model 104 in LS-DYNA (Hallquist 1998), originally based on work of Berstad et al. (1999).

An associated flow rule, i.e. the flow potential equals the yield criterion, is chosen. This flow rule defines the evolution of the plastic strain tensor and the accumulated plastic strain as

$$\dot{\boldsymbol{\varepsilon}}^p = \dot{\lambda}\frac{\partial f}{\partial \boldsymbol{\sigma}}; \quad \dot{r} = -\dot{\lambda}\frac{\partial f}{\partial R} \tag{19}$$

where $\dot{\lambda} \geq 0$ is the plastic multiplier.

In LS-DYNA (Hallquist 1998) the evolution of damage is defined as

$$\dot{D} = \begin{cases} 0 & \text{for} \quad r \leq r_D \\ \dfrac{Y}{S(1-D)}\dot{r} & \text{for} \quad r > r_D \end{cases} \tag{20}$$

where r_D is the strain threshold for damage initiation, and S is a positive material constant. The strain energy density release rate is defined as

$$Y = \frac{1}{2}\boldsymbol{\varepsilon}^e : \mathbf{C} : \boldsymbol{\varepsilon}^e \tag{21}$$

The loading-unloading conditions can be stated as

$$\dot{\lambda} \geq 0; \quad f \leq 0; \quad \dot{\lambda} f = 0 \tag{22}$$

which are sometimes referred to as Kuhn-Tucker conditions.

This constitutive model coupled to an element kill algorithm is available in LS-DYNA material model 104 (Hallquist 1998 and Berstad et al. 1999). The critical damage criterion is used to predict the onset of fracture, i.e. D_c controls the element erosion. In this study, the parameters S and D_c are based on inverse modelling of tensile test specimens.

6.2 Identification of material parameters

Uniaxial tensile test 0^0-32 ($\sigma_{0.2} = 255\,\text{MPa}$ and $\sigma_u = 292\,\text{MPa}$), taken from one of the extrusions of the impacted plate denoted A2-3 and described in Chapter 3, was used to calibrate the hardening rule for the base material. The hardening parameters and the proportionately limit were estimated by minimising the sum of squares between the model and the experimental data for data points in the range from initial loading until the onset of diffuse necking. The parameters are given in Table 7. Damage was included as described in the previous section. Lemaitre (1996) suggests that damage may evolve already from zero strain in aluminium alloys. Owing to this statement the damage strain threshold, r_D, was assumed to be equal to zero. The damage evolution parameters S and D_c were chosen based on work by Lademo (1999). Damage lowers the strength of the material, and this was taken into account by slightly altering the hardening parameters. The altered hardening parameters and the damage evolution parameters are given in Table 8.

The weld material was calibrated using the uniaxial tensile test of the weld, 0^0-w10, see Figure 30 and Figure 29a. Another method could have been to use the material curves found by use of the strain gauges at the minimum hardness in the weld and in the heat-affected zone, see Figure 29b. Those material curves were considered to be too conservative, and the test, 0^0-w10, was considered to be an average material curve better suited in our numerical simulations of the weld material. The damage evolution parameter, S, was chosen as 1.8 MPa and the critical damage was found from the measured data points as $D_c = 0.046$. The hardening parameters were calibrated and altered to include damage as described above.

The geometry of the tensile test specimen is as shown in Figure 23. The thickness was constant 4.16 mm. The finite element model is depicted in Figure 110. The failure process is observed to evolve without symmetry and hence the whole tensile test specimen was modelled. The model consists of 3924 Belytscko-Tsay shell elements that had one point reduced in-plane integration and five integration points through the thickness. Material model 104 in LS-DYNA was applied combining ductile damage with elasto-plasticity. In all numerical simulations, Young's modulus was taken as 70000 MPa and a value of 0.33 was adopted for Poisson's ratio.

The load was applied through the pins in each end of the specimen. The pins were modelled as rigid bodies tied to the specimen. It is important in quasi-static analysis using the explicit solver LS-DYNA to apply the loading smoothly in order to avoid introducing high frequency components into the calculated response. Thus, the prescribed velocity of pins were given as

$$v^*(t) = \frac{1}{2} \cdot \frac{4 \cdot 0.3 \cdot 0.045}{7\, t_{tot}} \left(1 - \cos\left(\min\left\{ \frac{4\pi t}{t_{tot}}, \pi \right\} \right) \right) \tag{23}$$

during a fictive time period $0 \le t \le t_{tot} = 10\,\text{ms}$. This lead to approximately 82600 time steps. The rate of the kinetic energy was checked and found to be small. The load factor, the ratio between a true static case and a dynamic case as defined by Ilstad (1999), was checked for the analysis of the base material and is plotted versus the displacement in Figure 111. (The displacement was measured across the 20 mm middle part of the specimen.) The load factor wills deviate from unity in cases with significant inertia forces and wills also become "unstable" after fracture of the specimen. Here, as observed from Figure 111, the result of the analyses can be treated as quasi-static. The velocity was further increased with a factor of 2.25 and the response still remained unaltered.

The simulated force versus displacement of the crosshead for the weld material is shown in Figure 112 together with the measured curve. Another analyses with the same parameters except a critical damage of $D_c = 0.15$ is also plotted in Figure 112. It shows that the value of critical damage is not essential. The focus must be placed on modelling of the plastic instability phenomenon. Figure 113 shows that the fracture mode in the simulation is a shear failure mode making an angle of 54.7^0 to the load axis as should be expected from classical theories, (Hill 1950).

The heat-affected zone was modelled using homogenised material parameters for each zone. The two curves were found by inverse modelling of tensile test, 90^0-w10, orientated across the weld. The same finite element mesh as for test 0^0-w10 was used. The tensile specimen was divided in four different regions: the base material, the weld material, the HAZ1 material, and the HAZ2 material as shown in Figure 114. The length of the weld zone was 20 mm, and the length of each of the HAZ-zones was 10 mm in the simulations. The material parameters previously established for the base and weld material was used, while some trial-and-error analyses lead to the parameters for HAZ1 and HAZ2, see Table 8.

The simulated force versus displacement of the crosshead is shown in Figure 115 together with the measured curve. A reasonable good agreement is found up to onset of diffuse necking of the tensile test specimen. The ductility is somewhat smaller in the simulations than in the test. The equivalent plastic strain is plotted in Figure 116 and it illustrates that there exist four localised necks in the HAZ and one of them develops to a fracture. The fracture also appeared in the HAZ in the experiment, but made an angle of 90^0 to the load axis (see Figure 30). Examination of the test specimen revealed a shear type of failure through the thickness of the gauge section as illustrated by a photograph of a fractured specimen from the base material in Figure 117. Consequently, it is believed that modelling the specimens with brick elements could have derived a better agreement with the tests.

Table 7 Hardening parameters.

Material	E [GPa]	σ_0 [MPa]	Q_1 [MPa]	C_1	Q_2 [MPa]	C_2
Base	70.0	193	80.5	$3.21 \cdot 10^3$	68.9	20.3
Weld	70.0	134	69.0	27.7	130	5.80
HAZ1	70.0	110	45.9	$4.94 \cdot 10^3$	90.5	42.5
HAZ2	70.0	136	45.9	$4.94 \cdot 10^3$	90.5	42.5

Table 8 Hardening parameters after including damage and the damage evolution parameters.

Material	E [GPa]	σ_0 [MPa]	Q_1 [MPa]	C_1	Q_2 [MPa]	C_2	r_D	S [MPa]	D_C
Base	70.0	193	80.9	$3.21 \cdot 10^3$	80.0	17.4	0	3.6	0.1
Weld	70.0	136	60.5	25.2	156	5.91	0	1.8	0.046
HAZ1	70.0	110	46.1	$4.94 \cdot 10^3$	95.4	39.8	0	1.2	0.1
HAZ2	70.0	136	46.3	$4.94 \cdot 10^3$	94.6	40.4	0	1.8	0.1

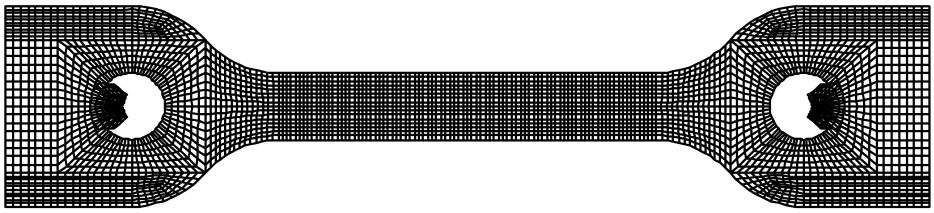

Figure 110 Finite element mesh of the tensile test specimen.

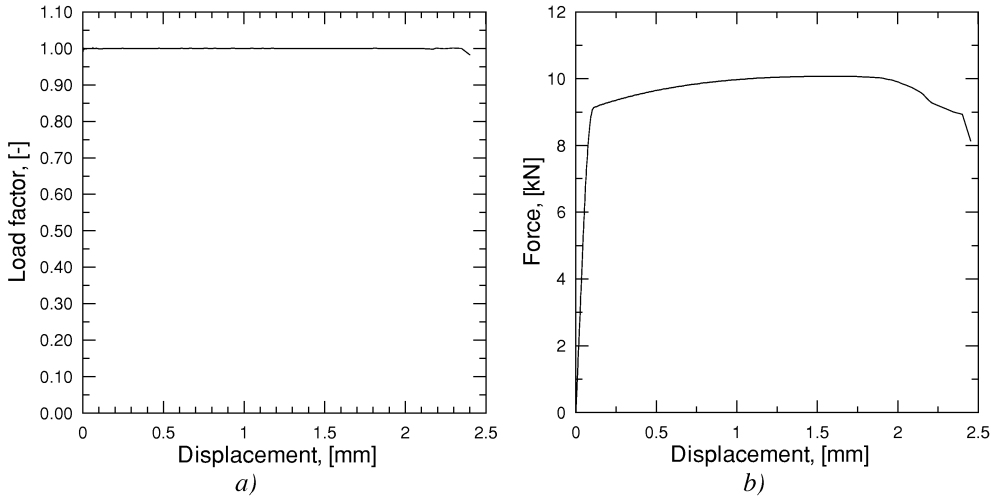

Figure 111 Simulation of tensile test of the base material: a) load factor versus the displacement, and b) force-displacement curve.

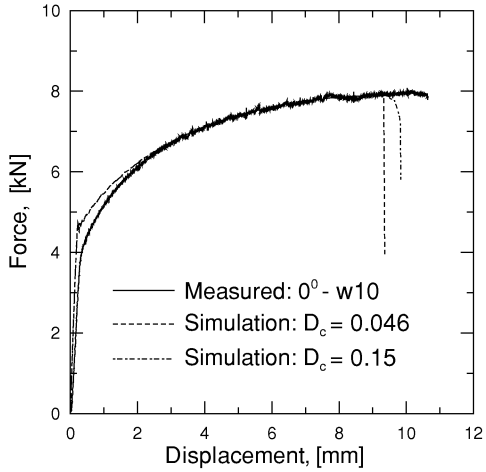

Figure 112 Force versus displacement of crosshead for the two analyses of the weld material, test specimen 0^0-w10.

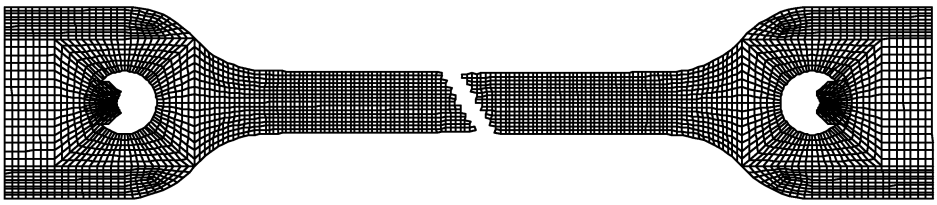

Figure 113 Fracture mode for the simulation of 0^0-w10, the weld material.

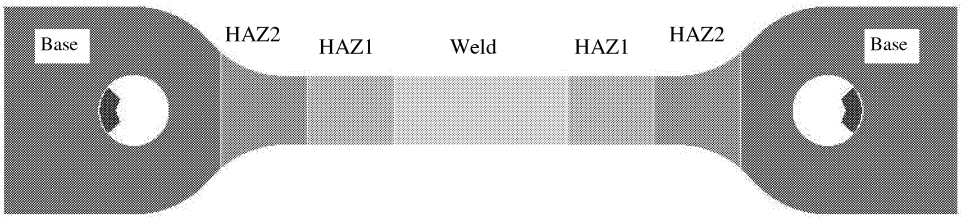

Figure 114 The different materials in the finite element model of 90^0-w10.

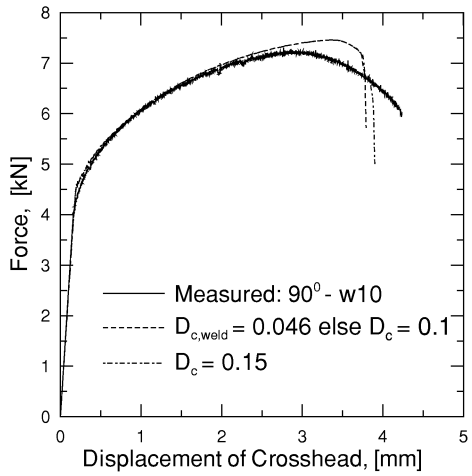

Figure 115 Force versus displacement of crosshead for the material test across the weld, 90^0-w10.

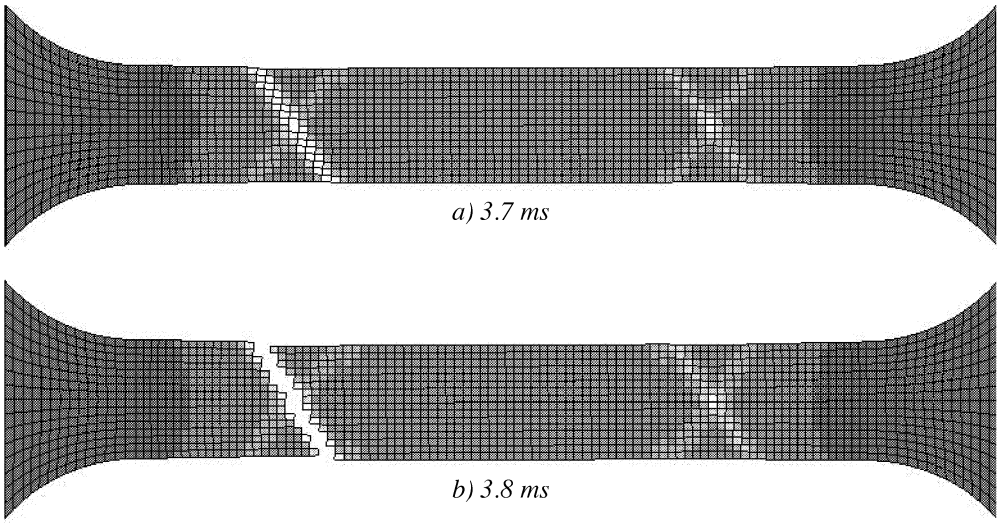

Figure 116 Equivalent plastic strain a) before and b) after fracture of the specimen across the weld, 90^0-w10.

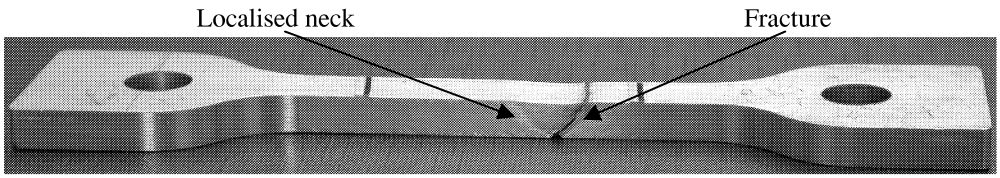

Figure 117 Example of fractured tensile test specimen.

6.3 Numerical simulation of impacted plate

The geometry of the plate and the support condition are modelled very similar to that used in the experimental test set-up, see Figure 13. The Belytschko-Tsay shell element is used and the element mesh is depicted in Figure 118. The idealised support conditions were simply supported and the nodes at the supports were fixed in the direction normal to the plate. The failure process is observed to evolve without symmetry and hence the whole specimen was modelled. The plate consists of 90 elements in both the length and transverse direction. The stiffeners consist of 82 elements in length direction. The bottom flange has 2 elements in the width, and the web has 6 elements in the height. The edge stiffeners are modelled with 7 elements in the height.

In the central part of the plate the mesh is refined using adaptive re-meshing. An h-adaptive method is included in LS-DYNA. In an h-adaptive method (Hallquist 1998) the elements are subdivided into smaller elements whenever an error indicator shows that the subdivision of the elements will provide improved accuracy. In this study, the original element is divided in four when the thickness becomes below a user-defined value.

Using commercial codes such as LS-DYNA, some adjustments have to be performed to get reasonable results. In this study, all adaptive re-meshing was performed before the projectile impacted the specimen, otherwise run-time problems occurred. Four adaptive levels were used in the present study. This resulted in a mesh with 13244 and 99152 shell elements in the whole plate before and after re-meshing, respectively. The elements had a length of 0.625 mm at the impact point after re-meshing. The four-node Belytschko-Tsay shell element was used with one point reduced in-plane integration and five integration points through the thickness in order to represent bending. A stiffness based hourglass control was adopted in the numerical simulations. The four different materials, as explained in the previous section and listed in Table 8, were modelled. The different materials are given different shadings in Figure 118 showing the central part of the plate using three levels of re-meshing.

The projectile was modelled as a rigid body consisting of 6400 shell elements. The projectile was given the same initial velocity as measured in test A2-3, $v_i = 7.85\,\mathrm{m/s}$. Contact between the projectile and the target was modelled using a “nodes to surface” penalty formulation without friction. The thickness of the shells was not considered in the contact routine, and this was another adjustment performed to avoid problems during the numerical simulation.

Figure 119 show photographs of a test at the impact point. Cracks in the fusion lines were developed for a velocity above the incipient fracture velocity. Increasing the velocity further, fracture across the weld developed and then four petals were created for a velocity of 7.85 m/s (test A2-3). The numerical simulation using a critical damage of 0.046 in the weld material and 0.10 in the rest of the plate are shown in Figure 121. The elements in the centre row parallel to the weld were eroded before any instability at the fusion line was developed. Then four petals were created. As shown in Figure 120 the maximum force is much lower in this analysis than in the experiment.

By increasing the critical damage for all materials to 0.15, instability in the element row closest to the fusion line develops. Figure 122 show plots of the equivalent plastic strains. The plastic strains were localised at the fusion line between the weld and the HAZ zone. Elements in the element row closest to one of the fusion lines were eroded, but no petals were created during the first 5 ms of the analyses. Figure 120 shows the force versus time and force versus displacement curves for the numerical simulation and the laboratory test. The maximum force and the stiffness of the plate were predicted quite well.

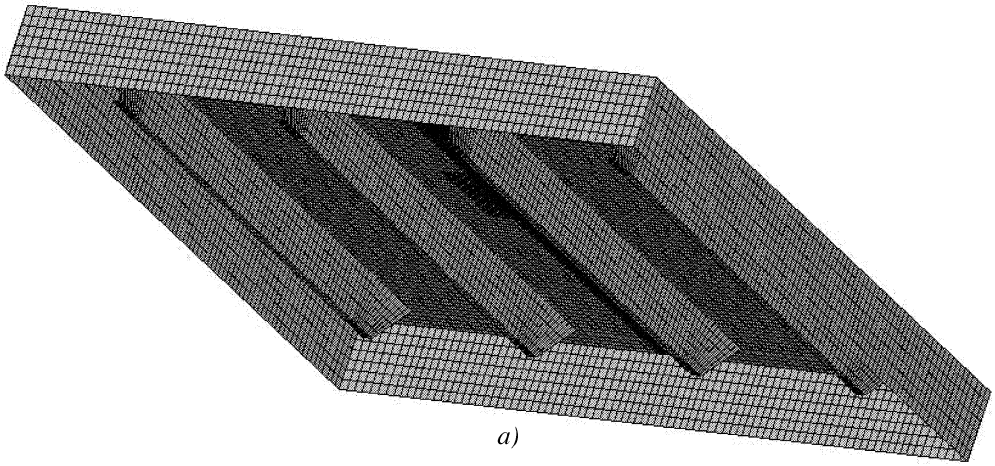

a)

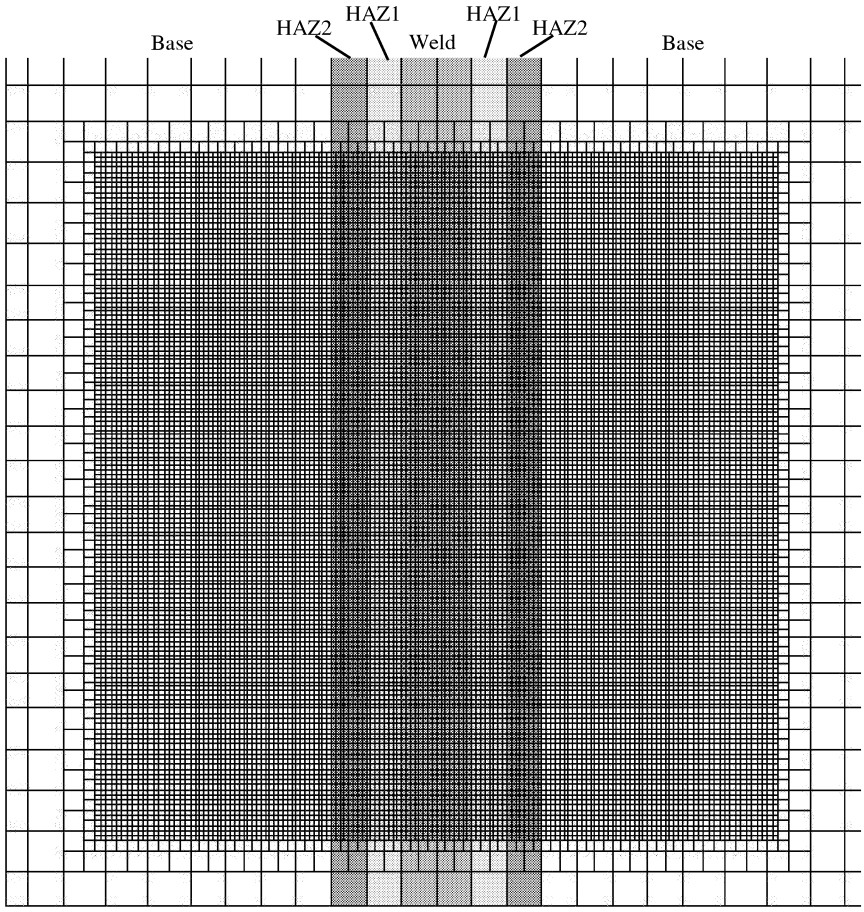

b)

Figure 118 The element mesh of a) the stiffened plate, and b) the middle section of the plate.

It is worth noting that these simulations were performed without friction between the target and the projectile. As observed in Figure 122b the fractured zone developed more rapidly along one of the fusion lines. Without any friction the target material is likely to move transversely and consequently no petals will develop. A more comprehensive study including friction will clarify this effect. Another element of uncertainty is the homogenisation of the material parameters in different zones. The variation of material properties in these zones is thereby absent. This effect could have been reduced by dividing the material into far more regions. This has to some extent been studied in numerical simulations of uniaxial tensile tests of butt welds where the results were found to be sensitive to the number of different material zones (Kjosavik 2001).

The material is anisotropic, and incorporation of an anisotropic material model may lead to increased accuracy of the results. Limited yield strength anisotropy was found, but the anisotropy in flow properties was large. This means that an anisotropic criterion could have an influence on the localisation of the strains and thereby the propagation of fracture.

The element size also influences the results. The sensitivity of the element size was studied in welded aluminium structures (Hildrum et al. 2001 and Hildrum et al. 2002). It was found that the localisation of the strains was very sensitive to the element size and that small elements were of vital importance to trig and develop the instability phenomenon. Use of brick elements may certainly give better description of strain localisation and shear instability through the thickness. However, as pointed out in parallel study (Hildrum et al. 2001), numerous brick elements also have to be used in the thickness direction. The problem size will be unwieldy for this plate impact study for the time being.

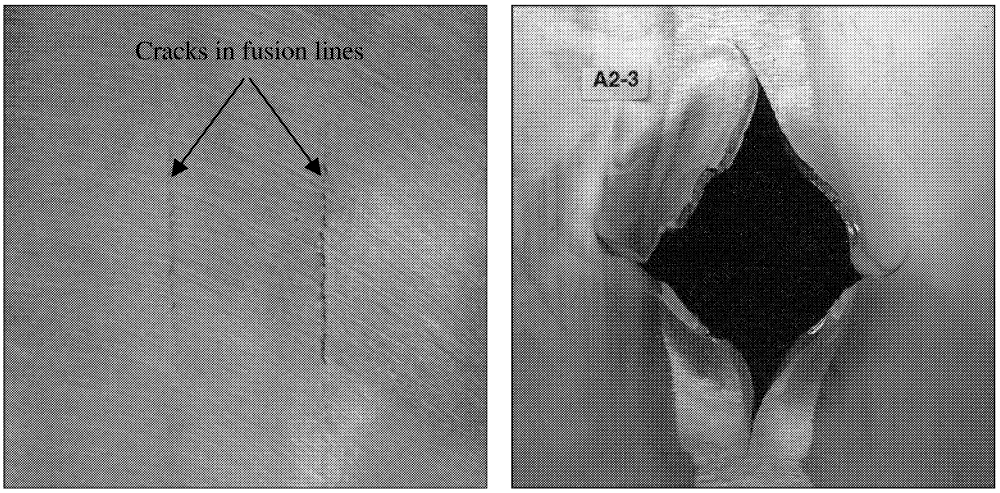

Figure 119 Experimental tests: a) fracture lines in the fusion line using a impact velocity of 2.4 m/s, and b) a petaling failure mode in test A2-3.

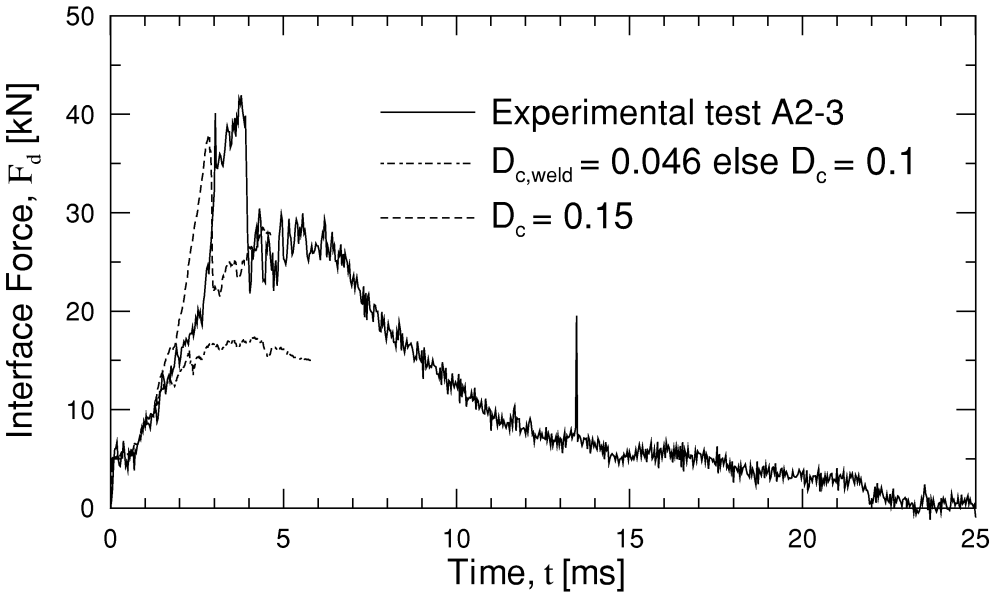

a)

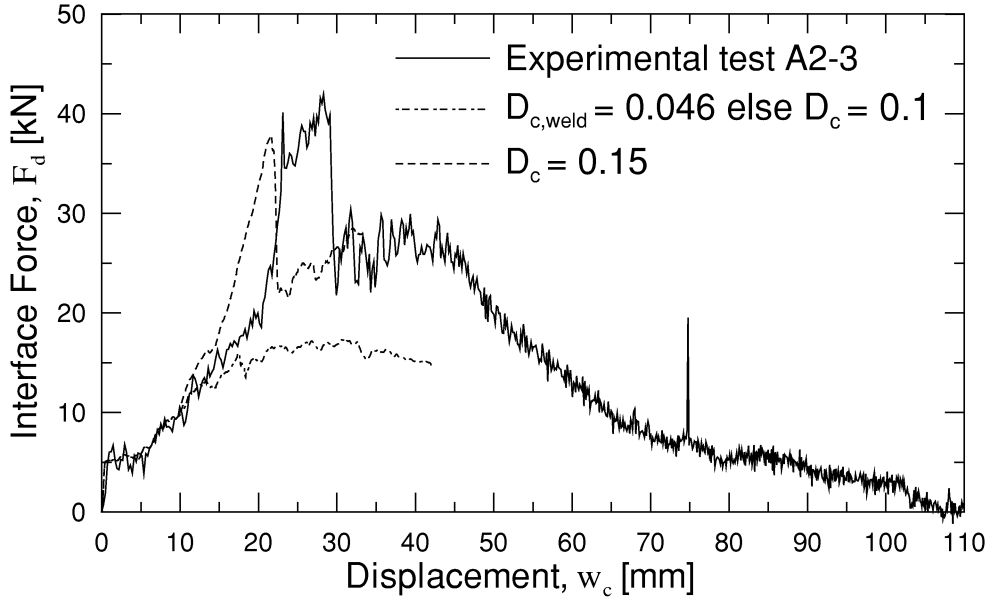

b)

Figure 120 Experimental test versus simulations: a) force-time curves, and b) force-displacement curves.

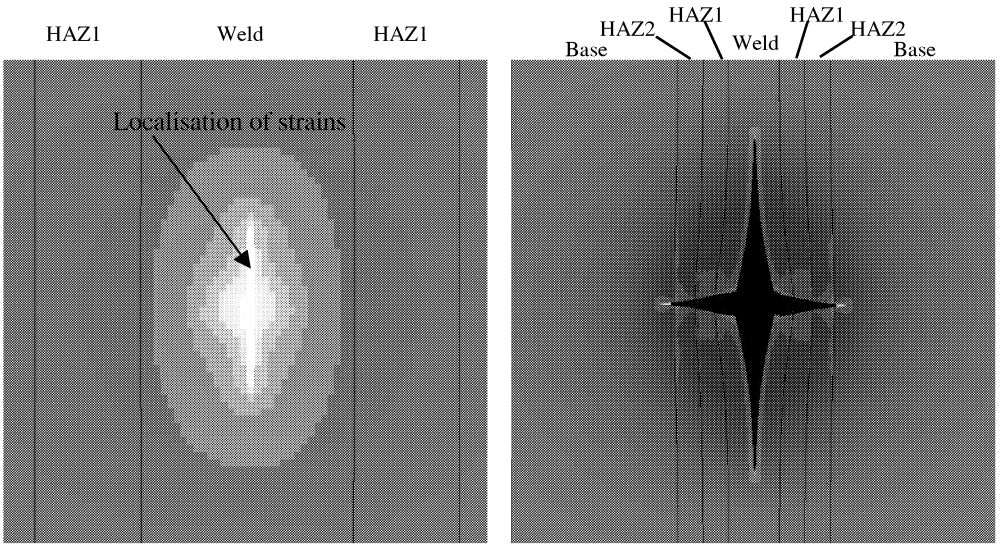

Figure 121 Plastic strains in analysis where $D_{c,weld} = 0.046$ else $D_c = 0.1$: a) the middle part of the plate at 1.8 ms, and b) the fracture at 5 ms.

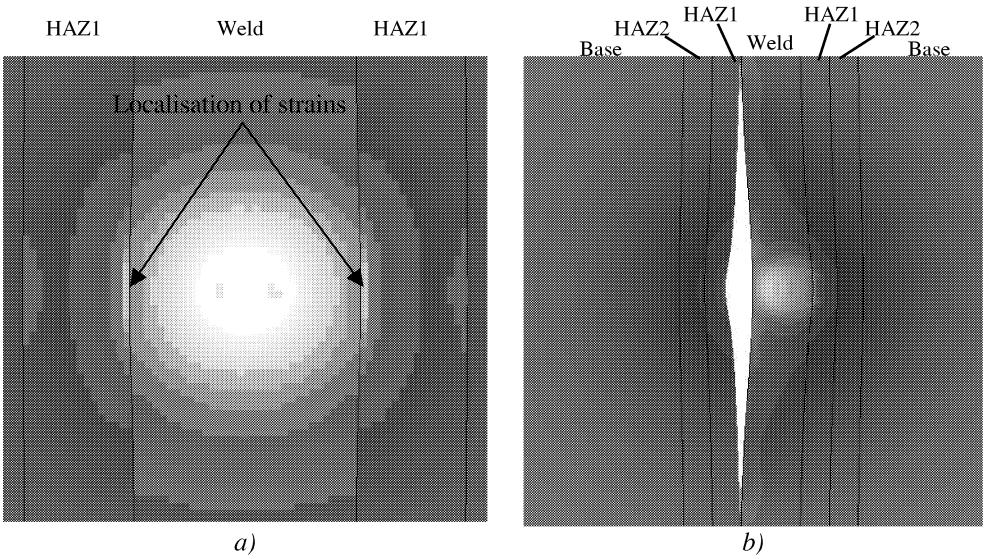

Figure 122 Plastic strains in analysis where $D_c = 0.15$ for all materials: a) the middle part of the plate at 3.2 ms, and b) the fracture at 5 ms.

7 Conclusions and Recommendations for Further Work

7.1 Conclusions

The present study has provided impacts tests in which projectiles with two different nose shapes (blunt and hemispherical) were used to penetrate a stiffened aluminium plate on three different locations (between stiffeners, on a stiffener, and next to a stiffener). Based on the experimental observations and the numerical simulations, the most important results and conclusions are as follows:

- Material tests revealed large variations in the tensile properties of AA6082 temper T6. The strength varied considerably between the extrusions, as well as it depended on the orientation of the specimen relative to the extrusion axis.
- The incipient fracture velocity and the ballistic limit velocity of the stiffened aluminium plate were severely affected by the nose shape of the projectile and the impact position on the target under the given conditions.
- The estimated incipient fracture velocity (giving cracks in the target) varied in the range between 2.3 m/s and 7.2 m/s. That velocity was significant less for the hemispherical ended nose than the blunt ended nose. The impact between the stiffeners gave lowest incipient fracture velocity followed by impact next to the stiffener and impact on a stiffener in that order.
- The estimated ballistic limit velocity varied in the range between 6.8 m/s and 9.1 m/s. The ballistic limit was almost equal for impact between two stiffeners using both nose shapes and for impact next to a stiffener with the blunt ended projectile. The hemispherical ended projectile impacting next to a stiffener lead to significant higher ballistic limit.
- The observed differences in the ballistic limit velocity and incipient fracture velocity were mainly attributed to the change in failure mode (and energy absorption) with respect to the input parameters. The blunt projectile caused failure by plugging, while petaling failure modes were observed for impact with a hemispherical ended projectile. In addition to the local failure at the impact point, large global deformation (dishing) extended from the impact point to the supports.
- In the studied velocity range and for the blunt ended projectile, it seems like the static tests may be used to give a conservative estimate of the incipient fracture impact energy in the dynamic tests. For the hemispherical ended projectile this method may lead to non-conservative results.
- Impacting in between two stiffeners (on the weld) cracks appeared in the fusion zone, probably due to low fracture toughness in that zone.
- The fracture was initiated on the rear side in impacts next to a stiffener or between the stiffeners (on the weld) with both nose shapes. Ductile fractures were observed in all test specimens except the fractures in connection with the welds. No evidence of temperature effects and no pronounced shear localisation through the thickness of the plate were seen.

- Numerical simulations of perforation of a stiffened plate impacted with a hemispherical ended projectile between two stiffeners were performed using LS-DYNA. Inverse modelling of tensile test specimens was performed to identify the material parameters. The weld and heat affected zone were modelled with reduced strength compared to the parent material and the Lemaitre damage model was employed to simulate fracture. The numerical simulation described the maximum force quite well. Furthermore, the model predicts the instability phenomenon and fracture process as observed in the experiments reasonably well.

7.2 Suggestions for further work

Based on the present project, the challenge seems to be to model the event at the impact point, i.e. the initiation and evolution of the fracture. Hence, material modelling to define engineering fracture criteria to be used in large-scale numerical analyses of impacted welded stiffened aluminium plates seems to be the most appropriate continuation of the present work. The activities and research needs could be as follows:

- The parameters (point of load application and nose shape) and impact velocity may be varied to explore whether the present numerical model is capable of predicting the other failure modes.
- The element size is of crucial importance when modelling plastic instability such as necking. Even though it was not possible to refine the element mesh further in the present study, the rapid growth of computational power already enables use of more elements. Further investigation with smaller element size may provide better agreement between the experimental and numerical failure modes.
- Modelling the plate using brick elements (or brick elements in combination with shell elements) may certainly give better description of the strain localisation and shear instability through the thickness of the impacted plates. This may be possible in the future due to the rapid growth of computational power.
- Additional material characterisation should be performed to establish a more accurate shape of the yield surface. The yield properties may affect the initiation of plastic instability and thereby the failure mode of the plate.
- The weld modelling capability in LS-DYNA may be explored and compared with the present experiments and numerical simulations.
- A parametric study may be performed to find the most important parameters (e.g. material properties, thickness of plate and projectile mass) influencing the response and to establish a database.

References

Aalberg, A., Langseth, M. and Larsen, P.K. (2001): Stiffened aluminium panels subjected to axial compression, *Thin-Walled Structures*, **39**, pp. 861-885.

Altenpohl, D. (1982): *Aluminum Viewed from Within. An Introduction into the Metallurgy of Aluminium Fabrication*, Aluminium-Verlag, Düsseldorf, ISBN 3-87017-138-3.

Ashby, M.F. and Jones, D.R.H. (1980*): Engineering Materials 1: An Introduction to their Properties and Applications*, Butterworth Heineman Ltd, Oxford, ISBN 0 7506 2766 2.

Backman, M.E. and Goldsmith, W. (1978): The mechanics of penetration of projectiles into targets, *Int. Journal of Engng Science*, **16**, pp. 1-99.

Berstad, T., Hopperstad, O.S., Lademo, O.-G. and Malo, K.A. (1999): Computational Model of Ductile Damage and Fracture in Shell Analysis, *Second European LS-DYNA Conference*, Gothenburg, Sweden, pp. A 37-44.

Børvik, T. (2001): *Ballistic Penetration and Perforation of Steel Plates*, Dr ing. Thesis, Department of Structural Engineering, Norwegian University of Science and Technology, Trondheim, Norway, ISBN 82-7984-154-7.

Cobden, R. (1994): Aluminium: Physical Properties, Characteristics and Alloys. TALAT Lecture 1501. *Aluminium Training Partnership*.

Colangelo, V.J. and Heiser, F.A. (1987): *Analysis of Metallurgical Failures*, Second edition, John Wiley & Sons, Inc., New York, ISBN 0-471-89168-1.

Corbett, G.G, Reid, S.R., and Johnson, W. (1996): Impact loading of plates and shells by free-flying projectiles: A review, *Int. J. Impact Engng,* **18** (2), pp. 141-230.

Corran, R.S.J., Shadbolt, P.J. and Ruiz, C., (1983): Impact loading of plates – an experimental investigation, *Int. J. Impact Engng,* **1** (1), pp. 3-22.

Dieter, G.E. (1988): *Mechanical Metallurgy SI Metric Edition*, McGraw-Hill Book Company, London, ISBN 0-07-100406-8.

Edwards, M.R. and Mathewson A. (1997): The ballistic properties of tool steel as a potential improvised armour plate. *Int. J. Impact Engng,* **19** (4), pp. 297-309.

Estensen, A.B., (1998): *Impact loading on stiffened aluminium plates*, siv.ing. Hovedoppgave (masters-level thesis), Department of Structural Engineering, Norwegian University of Science and Technology, Trondheim, Norway (in Norwegian).

Goldsmith, W. (1985): Initiation of perforation in thin plates by projectiles, *Metal forming and impacts mechanics*, S.R: Reid (ed.), pp. 271-288.

Goldsmith, W. (1999): Review. Non-ideal projectile impact on targets, *Int. Journal of Engng Science*, **22**, pp. 95-395.

Grong, Ø., (1997*): Metallurgical Modelling of Welding*, Second edition, Institute of Materials, London, ISBN 1 86125 036 3.

Grong, Ø. and Myhr, O.R., (1993): Modelling of the Strength Distribution in the Heat Affected Zone of 6082-T6 Aluminium Weldments, *Mathematical Modelling of Weld Phenomena*, Cerjak and Easterling (eds.), Institute of Materials, London.

Gråberg, S., Bratland, D.A., Grong, Ø. and Reiso, O. (2002): Effect of local melting on the HAZ toughness of GMA welded AA6082 and AA6005 extrusions containing Cu, *To be published in 8th International Conference on Aluminium Alloys (ICAA8)*, Cambridge, Great Britain.

Hallquist, J.O. (1993): *LS-INGRID – A pre-processor and tree-dimensional mesh generator for the programs LS-DYNA, LS-NIKE and TOPAZ*, Livermore Software Technology Corporation, Livermore, California.

Hallquist, J.O. (1998): *LS-DYNA theoretical manual*, Livermore Software Technology Corporation, Livermore, California.

Hildrum, H.G. and Malo, K.A. (2001*): An Introductory FEM Study of Strain Localisation in Welded Aluminium Structures. Part I: Isotropic Material*, Department of Structural Engineering, Norwegian University of Science and Technology, Report No.: R-22-01, Trondheim, Norway.

Hildrum, H.G., Berstad, T., Hopperstad, O.S. and Malo, K.A. (2002*): An Introductory FEM Study of Strain Localisation in Welded Aluminium Structures. Part II: Fillet Weld*, Department of Structural Engineering, Norwegian University of Science and Technology, Report No.: R-3-02, Trondheim, Norway.

Hill, R. (1950): *The mathematical theory of plasticity*, The Clarendon Press, Oxford, Great Britain.

Hval, M., Thaulow, Chr. and Anglevik, K. (1992): Significance of defects in thick welded AlMgSi1 (AA6082) aluminium extrusion, *5th International Conference on Aluminium Weldments*, Munich, Kosteas et al. (eds.), Germany.

Hosford, W.F. and Caddell, R.M. (1993): *Metal forming: Mechanics and metallurgy*, Second edition, PRT Pretence Hall, ISBN 0-13-588526-4.

Ilstad, H. (1999): *Validation of Numerical Collapse Behaviour of Thin-Walled Corrugated Panels*, Dr ing. Thesis, Department of Structural Engineering, Norwegian University of Science and Technology, Trondheim, Norway, ISBN 82-471-0474-1.

Johnson, W., Ghosh, S.K. and Reid S.R. (1980): Piercing and hole-flanging of sheet metals: a survey, *Memoires Scientifiques Revue Metallurgie*, pp. 585-606.

Jones, N. (1994): Low velocity perforation of metal plates, *Shock and Impact on Structures,* Brebbia and Sánchez-Gálvez (eds.), pp.53-71, Computational Mechanics Publications, Boston, ISBN 1853122971.

Jones, N. (1997): Dynamic Inelastic Failure of Structures, *Transactions of the Japan Society of Mechanical Engineers*, **12**, pp. 2485-2495.

Jones, N. and Kim, S.-B. (1997 a): A Study on the Large Ductile Deformations and Perforation of Mild Steel Plates Struck by a Mass – Part I: Experimental Results. *ASME Journal of Pressure Vessel Technology,* **119**, pp. 178-184.

Jones, N. and Kim, S.-B. (1997 b): A Study on the Large Ductile Deformations and Perforation of Mild Steel Plates Struck by a Mass – Part II: Discussion. *ASME Journal of Pressure Vessel Technology,* **119**, pp. 185-191.

Jones, N., Kim, S.-B. and Li, Q.M. (1997 c): Response and Failure of Ductile Circular Plates Stuck by a Mass, *ASME Journal of Pressure Vessel Technology,* **119**, pp. 332-342.

Kjosavik, M. (2001): *Finite element analysis of welded aluminium connections*, siv.ing. Hovedoppgave (masters-level thesis), Department of Structural Engineering, Norwegian University of Science and Technology, Trondheim, Norway (in Norwegian).

Lademo, O.-G. (1999): *Engineering Models of Elastoplasticity and Fracture of Aluminium Alloys*, Dr ing. Thesis, Department of Structural Engineering, Norwegian University of Science and Technology, Trondheim, Norway, ISBN 82-471-0367-2.

Lademo, O.-G. Hopperstad and Langseth, M., (1999): On the strain-rate effect and anisotropy of AA7108, *Impact Response of Materials and Structures*, 3rd International Symposium on Impact Engineering, V.P.W. Shim, S. Tanimura, C.T. Lim (eds.), Oxford University Press, ISBN 0 19 588546 3.

Lademo, O.-G., Hopperstad, O.S., Berstad, T. and Langseth, M., (2001): Numerical Simulations of Ductile Failure in Extruded Aluminium Alloys Using a Coupled Model of Elastoplasticity and Damage, *Third European LS-DYNA Conference*, 18-19 June, Paris.

Lademo, O.-G., Hopperstad, O.S. and Pedersen, K.P. (2002): Formability modelling of aluminium extrusions, to be published.

Langseth, M. (1988): *Dropped objects' plugging capacity of steel plates*, Dr ing. Thesis, Division of Structural Engineering, Norwegian University of Trondheim, Norwegian Institute of Technology, Trondheim, Norway, ISBN 82-7119-042-3.

Langseth, M. and Larsen, P. K. (1990): Dropped objects' plugging capacity of steel plates: an experimental investigation. *Int. J. Impact Engng,* **9** (3), pp. 289-316.

Langseth, M. and Larsen, P. K. (1992): The behaviour of square steel plates subjected to a circular blunt ended load. *Int. J. Impact Engng,* **12** (4), pp. 617-638.

Langseth, M. and Larsen, P. K. (1993): Dropped objects' plugging capacity of stiffened panels. *Structural Dynamics – EURODYN'93*. Moan et al. (eds.). Balkema, Rotterdam, ISBN 90 5410 336 1.

Langseth, M. and Larsen, P. K. (1994): Dropped objects' plugging capacity of aluminium alloy plates. *Int. J. Impact Engng,* **15** (3), pp. 225-241.

Langseth, M. and Hopperstad, O.S. (1996): Static and dynamic axial crushing of square thin-walled aluminium extrusion. *Int. J. Impact Engng,* **18** (7-8), pp. 949-968.

Langseth, M., Hopperstad, O.S and Berstad, T. (1999): Impact Loading of Plates: Validation of Numerical Simulations by Testing. *International Journal of Offshore and Polar Engineering*, **9** (1), pp. 10-15, ISSN 1053-5381.

Lemaitre, J. (1996): *A Course on Damage Mechanics*, Second Edition, Springer-Verlag, Germany, ISBN 3-540-60980-6.

Levy, N. and Goldsmith, W. (1984): Normal Impact and Perforation of Thin Plates by Hemispherically-tipped Projectiles – II. Experimental Results, *Int. J. Impact Engng,* **2** (4), pp. 299-324.

Lindhom, U.S., Bessey, R.L. and Smith, G.V. (1971): Effect of Strain Rate on Yield Strength, Tensile Strength, and Elongation of Three Aluminium Alloys, *Journal of Materials*, **6** (1), pp. 119-133.

Lohne, O. and Neass, O.J. (1979): The effect of dispersoids and grain size on mechanical properties of AlMgSi-alloys, *Strength of metals and alloys*, P. Haasen et al. (eds.), pp. 781-788.

Matusiak, M. (1999): *Strength and Ductility of Welded Structures in Aluminium Alloys*, Dr ing. Thesis, Department of Structural Engineering, Norwegian University of Science and Technology, Trondheim, Norway, ISBN 82-471-0487-3.

Marciniak, Z. and Kuczinsky, K. (1967): Limit Strains in the Process of Stretch-Forming Sheet Metal, *Int. J. Mechanical Sciences*, **9**, pp. 609-620.

Norwegian Petroleum Directorate (1994): *Regulations relating to loadbearing structures in the petroleum activities* (Unofficial translation), ISBN 82-7257-417-9.

Ohte, S., Yoshizawa, H., Chiba, N., and Shida, S. (1982): Impact Strength of Steel Plates Struck by Projectiles. *Bulletin of the JSME*, **25** (206), pp. 1226-1231.

Palomby, C. and Stronge, W.J. (1988): Blunt Missile Perforation of Thin Plates and Shells by Discing, *Int. J. Impact Engng,* **7** (1), pp. 85-100.

Shadbolt, P.J. (1981): *Impact Loading of Plates*, Ph.D. Thesis, University of Oxford.

Simonsen, B.C. and Lauridsen, L.P. (2000): Energy absorption and ductile failure in metal sheets under lateral indentation by a sphere. *Int. J. Impact Engng,* **24** , pp. 1017-1039.

Tibballs, J.E. (1995): *Forming and Age-hardening Aluminium Alloys AlZn5Mg1 (AA708) and AlMg1MnSi1 (AA6082) A Review of Literature and experimental Methods*, Department of Physics, University of Oslo, report 95-03, ISSN-0332-5571.

Tryland, T. (1999): *Aluminium and Steel Beams under Concentrated Loading*, Dr ing. Thesis, Department of Structural Engineering, Norwegian University of Science and Technology, Trondheim, Norway, ISBN 82-471-0397-4.

Wen, H.-M. and Jones, N. (1992): Semi-Empirical Equations for the Perforation of Plates stuck by a Mass, *Structures under Shock and impact*, Vol. II, P.S. Bulson (ed.), pp. 369-380 (Computational Mechanics Publications, Southampton and Boston, and Thomas Telford, London).

Wen, H.-M. and Jones, N. (1993): Experimental investigation of the scaling laws for metal plates stuck by large masses. *Int. J. Impact Engng,* **13** (3), pp. 485-505.

Wen, H.-M. and Jones, N. (1994): Experimental investigation into the dynamic plastic response and perforation of a clamped circular plate stuck transversely by a mass, *Journal of Mechanical Engineering Science*, **208**, pp. 113-137.

Wen, H.-M. and Jones, N. (1996): Low-Velocity Perforation of Punch-Impact-Loaded Metal Plates, *ASME Journal of Pressure Vessel Technology,* **118**, pp. 181-187.

Zukas, J.A., Nicholas, T., Swift, H.F., Greszczuk, L.B. and Curran, D.R. (1982): *Impact Dynamics*, John Wiley & Sons, Inc., New York, ISBN 0-89464-661-3.

URN:NBN:no-3315

Appendix A Specification of the extrusion (WET 0143 A)

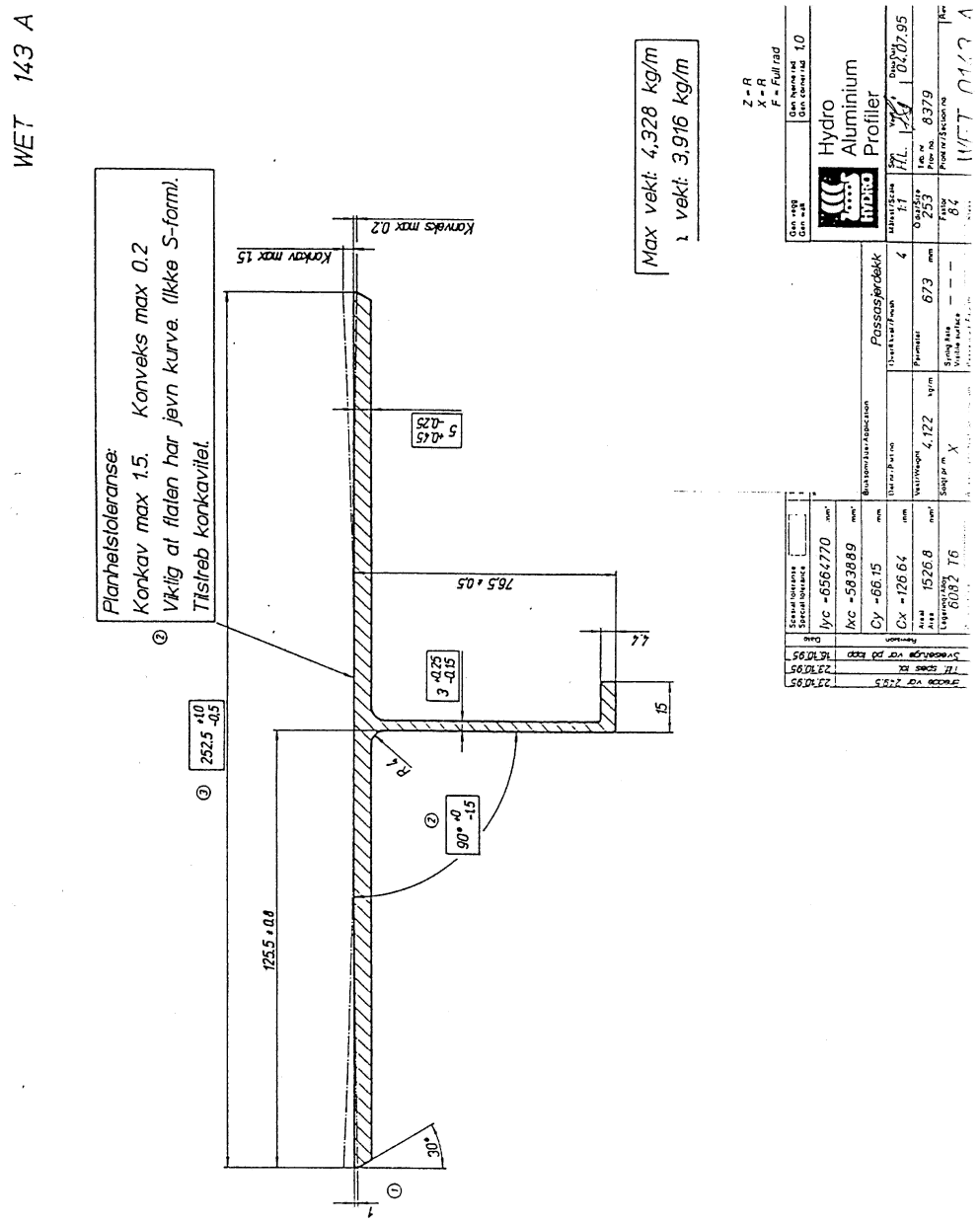

Figure A-1 The specification of the extrusion.

Appendix B Uniaxial Tension Tests

Table B-1 Geometry of tensile test specimens

Series	Test no.	Part of extrusion	Extrusion no.	Length of test specimen	Mean thickness [mm]	Mean Area [mm^2]
A	0^0-01	Top flange	20	110 mm	4.87	38.74
	0^0-02	Top flange	13	110 mm	4.82	38.29
	0^0-03	Top flange	16	110 mm	4.84	40.88
	0^0-04	Top flange	17	110 mm	4.87	38.79
	0^0-06	Top flange	16	110 mm	4.86	38.77
	0^0-07	Top flange	20	110 mm	4.86	38.71
	45^0-01	Top flange	20	110 mm	4.87	38.79
	45^0-02	Top flange	13	110 mm	4.82	38.58
	45^0-03	Top flange	16	110 mm	4.84	41.21
	45^0-04	Top flange	17	110 mm	4.82	38.40
	90^0-01	Top flange	20	110 mm	4.86	40.98
	90^0-02	Top flange	13	110 mm	4.82	38.39
	90^0-03	Top flange	16	110 mm	4.85	38.88
	90^0-04	Top flange	16	110 mm	4.85	38.68
B	0^0-10	Top flange	1	110 mm	5.00	39.97
	0^0-11	Top flange	1	110 mm	5.00	39.80
	0^0-12	Top flange	3	110 mm	5.00	40.05
	0^0-13	Top flange	3	110 mm	5.01	39.91
	0^0-14	Top flange	5	110 mm	4.99	39.75
	0^0-15	Top flange	5	110 mm	5.01	40.10
	0^0-16	Top flange	7	110 mm	4.99	39.69
	0^0-17	Top flange	7	110 mm	4.99	39.69
	0^0-18	Top flange	9	110 mm	4.98	39.86
	0^0-19	Top flange	9	110 mm	4.99	39.70
	0^0-50	Web	1	110 mm	3.00	23.82
	0^0-51	Web	3	110 mm	2.99	23.92
	0^0-52	Web	5	110 mm	2.99	23.82
	0^0-53	Web	7	110 mm	2.97	23.64
	0^0-54	Web	9	110 mm	2.98	23.87
	0^0-80	Bottom flange	1	80 mm	3.09	15.43
	0^0-81	Bottom flange	3	80 mm	3.01	14.96
	0^0-82	Bottom flange	5	80 mm	3.01	15.02
	0^0-83	Bottom flange	7	80 mm	3.01	15.03
	0^0-84	Bottom flange	9	80 mm	2.99	14.85

Table B-1 Cont. Geometry of tensile test specimens.

Series	Test no.	Part of extrusion	Extrusion no.	Length of test specimen	Mean thickness [mm]	Mean Area [mm^2]
C	0^0-30	Top flange	41	110 mm	5.09	40.48
	0^0-31	Top flange	33	110 mm	4.84	38.75
	0^0-32	Top flange	24	110 mm	4.84	38.55
	0^0-33	Top flange	31	110 mm	4.83	38.40
	0^0-34	Top flange	45	110 mm	4.84	38.76
	0^0-35	Top flange	48	110 mm	4.85	38.57
	0^0-36	Top flange	55	110 mm	4.79	38.07
	0^0-37	Top flange	62	110 mm	4.84	38.75
	0^0-38	Top flange	70	110 mm	5.11	40.69
	0^0-39	Top flange	68	110 mm	5.09	40.48

Table B-2 Uniaxial tension test results.

Series	Test no.	E [GPa]	$\sigma_{0.2}$ [MPa]	σ_u [MPa]	ε_u	ε_f	R
A	0^0-01	59.7	279	309	0.085	0.102	0.34
	0^0-02	56.4	268	303	0.069	0.103	0.41
	0^0-03	55.8	275	303	0.071	0.111	0.41
	0^0-04	57.5	271	302	0.082	0.120	0.40
	0^0-06	58.8	275	300	0.074	0.087	0.36
	0^0-07	65.4	283	313	0.072	0.106	0.37
	45^0-01	60.7	266	296	0.056	0.060	-
	45^0-02	61.0	256	287	0.058	0.063	1.33
	45^0-03	56.5	268	295	0.064	0.082	0.77
	45^0-04	-	-	-	-	-	-
	90^0-01	68.8	281	315	0.066	0.090	0.70
	90^0-02	69.9	268	303	0.058	0.098	0.68
	90^0-03	55.6	275	307	0.085	0.113	0.66
	90^0-04	55.2	273	304	0.080	0.110	0.64
B	0^0-10	99.1	311	331	0.064	0.124	0.39
	0^0-11	69.3	310	329	0.060	0.119	0.37
	0^0-12	106.6	312	332	0.068	0.106	0.41
	0^0-13	66.4	309	327	0.071	0.126	0.37
	0^0-14	78.3	313	329	0.064	0.110	0.35
	0^0-15	83.8	309	325	0.064	0.118	0.32
	0^0-16	93.2	309	328	0.069	0.113	0.38
	0^0-17	92.9	307	329	0.066	0.100	0.34
	0^0-18	81.3	312	330	0.071	0.129	0.36
	0^0-19	80.2	312	331	0.069	0.084	0.47
	0^0-50	84.8	300	320	0.066	0.098	0.38
	0^0-51	66.5	301	320	0.066	0.108	0.39
	0^0-52	83.1	307	321	0.068	0.094	0.39
	0^0-53	83.5	300	318	0.068	0.082	0.39
	0^0-54	72.1	303	320	0.066	0.097	0.40
	0^0-80	-	280	307	0.069	0.081	-
	0^0-81	-	284	312	0.069	0.096	-
	0^0-82	-	299	321	0.072	0.126	-
	0^0-83	-	-	-	-	-	-
	0^0-84	-	294	317	0.074	0.096	-
C	0^0-30	84.5	257	285	0.071	0.106	0.38
	0^0-31	85.3	266	294	0.077	0.111	0.40
	0^0-32	87.7	255	292	0.079	0.142	0.41
	0^0-33	95.9	261	290	0.080	0.090	0.41
	0^0-34	80.9	261	293	0.072	0.092	0.41
	0^0-35	90.1	232	270	0.058	0.078	0.50
	0^0-36	80.3	262	296	0.077	0.119	0.44
	0^0-37	95.9	263	295	0.058	0.111	0.38
	0^0-38	97.3	245	277	0.050	0.135	0.36
	0^0-39	74.8	239	270	0.077	0.090	0.43

Appendix C Static Tests

Table C-1 Localisation and thickness of test specimens with reference to Figure 11.

Test no.	Extrusion no. *)	Thickness Plate [mm]	Thickness Flange [mm]	Thickness Web [mm]	Width Flange [mm]
D1-1	16-19;17-18	4.85 **)	-	-	-
D1-2	18-21;19-20	4.86 **)	-	-	-
D1-3	18-21;19-20	4.86 **)	-	-	-
D2-1	25-28;26-27	-	-	-	-
D2-2	18-21;19-20	4.86 **)	-	-	-
D2-3	12-15;13-14	4.82 **)	-	-	-
E1-1	45-49;47	4.84	4.35	2.97	14.80
E1-2	44-48;46	4.87	4.43	3.01	14.82
E1-3	49-53;51	4.82	4.34	2.97	14.79
E2-2	45-49;47	4.85	4.35	2.98	14.81
E2-3	49-53;51	4.82	4.34	2.98	14.87
E2-4	48-52;50	4.84	4.35	2.97	14.81
F1-1	33-37;35	-	-	-	-
F1-2	1-5;3	4.97	-	-	-
F1-3	6-10;8	4.96	-	-	-
F1-4	2-6;4	4.98	-	-	-
F2-1	65-69;67	5.10	-	-	-
F2-2	64-68;66	5.06	-	-	-
F2-3	65-69;67	5.08	-	-	-

*) Extrusion numbers and impacted extrusion(s)
**) Thickness taken from tensile test specimens

Appendix D Dynamic Tests

The mass of the projectile varies within a test series due to a minor modification of the cover protecting the strain gauges during the tests.

Table D-1 Mass of projectile and geometry of test specimens.

Test no.	Mass [kg]	Impact location	Nose Shape	Thickness Plate [mm]	Thickness Flange [mm]	Thickness Web [mm]	Width Flange [mm]	Extrusion no. **)
A1-6	55.22	Between stiffeners	Blunt	4.84 *)	-	-	-	22-25;23-24
A1-8	55.22	Between stiffeners	Blunt	4.82 *)	-	-	-	12-15;13-14
A1-9	55.37	Between stiffeners	Blunt	5.06	-	-	-	8-11;9-10
A1-5	55.22	Between stiffeners	Blunt	4.85 *)	-	-	-	16-19;17-18
A1-7	55.22	Between stiffeners	Blunt	4.82 *)	-	-	-	12-15;13-14
A1-3	55.22	Between stiffeners	Blunt	4.82 *)	-	-	-	12-15;13-14
A1-4	55.22	Between stiffeners	Blunt	-	-	-	-	33-36;34-35
A1-2	55.22	Between stiffeners	Blunt	4.85 *)	-	-	-	14-17;15-16
A1-1	55.22	Between stiffeners	Blunt	4.83 *)	-	-	-	29-32;30-31
A2-9	55.20	Between stiffeners	Hemispherical	5.07	-	-	-	8-11;9-10
A2-8	55.20	Between stiffeners	Hemispherical	5.06	-	-	-	8-11;9-10
A2-7	55.03	Between stiffeners	Hemispherical	4.83 *)	-	-	-	29-32;30-31
A2-5	55.03	Between stiffeners	Hemispherical	-	-	-	-	25-28;26-27
A2-4	55.03	Between stiffeners	Hemispherical	4.85 *)	-	-	-	14-17;15-16
A2-6	55.03	Between stiffeners	Hemispherical	4.86 *)	-	-	-	18-21;19-20
A2-1	55.03	Between stiffeners	Hemispherical	-	-	-	-	26-29;27-28
A2-2	55.03	Between stiffeners	Hemispherical	-	-	-	-	26-29;27-28
A2-3	55.03	Between stiffeners	Hemispherical	4.84 *)	-	-	-	22-25;23-24
B1-7	55.37	On stiffener	Blunt	4.93	4.35	2.97	14.83	48-52;50
B1-1	55.37	On stiffener	Blunt	4.81	4.34	2.96	14.77	59-63;61
B1-5	55.37	On stiffener	Blunt	4.86	4.36	3.00	14.85	44-48;46
B1-2	55.37	On stiffener	Blunt	4.84	4.35	2.98	14.84	54-58;56
B1-6	55.37	On stiffener	Blunt	4.86	4.41	2.96	14.83	44-48;46
B1-4	55.37	On stiffener	Blunt	4.79	4.33	2.96	14.83	49-53;51
B1-3	55.37	On stiffener	Blunt	4.84	4.35	2.97	14.80	58-62;60
B2-2	55.20	On stiffener	Hemispherical	4.85	4.35	2.98	14.81	54-58;56
B2-1	55.20	On stiffener	Hemispherical	4.84	4.34	2.97	14.79	58-62;60
B2-6	55.20	On stiffener	Hemispherical	4.80	4.34	2.96	14.79	59-63;61
B2-5	55.20	On stiffener	Hemispherical	4.86	4.35	2.98	14.80	55-59;57
B2-4	55.20	On stiffener	Hemispherical	4.84	4.34	2.96	14.81	59-63;61
B2-3	55.20	On stiffener	Hemispherical	4.86	4.35	2.98	14.81	55-59;57
B2-7	55.20	On stiffener	Hemispherical	4.84	4.34	2.97	14.80	54-58;56

*) Thickness is taken form tensile test specimens

**) Extrusion numbers and impacted extrusion(s)

Table D-1 Cont. Mass of projectile and geometry of test specimens.

Test no.	Mass [kg]	Impact location	Nose Shape	Thickness Plate [mm]	Thickness Flange [mm]	Thickness Web [mm]	Width Flange [mm]	Extrusion no. **)
C1-4	55.37	Beside stiffener	Blunt	5.06	-	-	-	64-68;66
C1-3	55.37	Beside stiffener	Blunt	5.05	-	-	-	64-68;66
C1-5	55.37	Beside stiffener	Blunt	4.96	-	-	-	7-11;9
C1-7	55.37	Beside stiffener	Blunt	4.98	-	-	-	3-7;5
C1-2	55.37	Beside stiffener	Blunt	4.96	-	-	-	2-6;4
C1-6	55.37	Beside stiffener	Blunt	5.07	-	-	-	64-68;66
C1-1	55.37	Beside stiffener	Blunt	4.96	-	-	-	1-5;3
C2-7	55.20	Beside stiffener	Hemispherical	4.96	-	-	-	7-11;9
C2-3	55.20	Beside stiffener	Hemispherical	4.97	-	-	-	3-7;5
C2-2	55.20	Beside stiffener	Hemispherical	4.96	-	-	-	7-11;9
C2-1	55.20	Beside stiffener	Hemispherical	4.96	-	-	-	1-5;3
C2-4	55.20	Beside stiffener	Hemispherical	4.97	-	-	-	3-7;5
C2-5	55.20	Beside stiffener	Hemispherical	5.08	-	-	-	66-70;68
C2-6	55.20	Beside stiffener	Hemispherical	4.96	-	-	-	4-8;6

**) Extrusion numbers and impacted extrusion(s)

Summaries of the dynamic experimental tests arranged in order of increasing impact velocity, v_i, within each test series are presented in Table D-2. The definitions used are as follows; T_p is the impact energy of the projectile. The maximum force, F_{dm}, is the measured maximum interface force between the target and the projectile. Owing to oscillations on the measured interface force curve, the maximum force was estimated. The central displacement, w_{cu}, is defined as the calculated displacement of the projectile at maximum force. U_{du} is the calculated energy absorbed by the target at maximum force.

The maximum central displacement, w_{cm}, is defined as the calculated maximum displacement of the projectile at incipient fracture. U_{dm} is the calculated maximum energy absorbed by the target. The residual velocity, v_r, is defined as the calculated velocity of the projectile immediately after impact that is when the interface force is equal to zero. The duration of the impact/penetration, t_d, is defined as the interval to the instant when the force is first reduced to zero. w_{cd} is the calculated centre displacement of the projectile at the instant when the force is first reduced to zero. The permanent centre displacement of the plate, w_{cp}, was measured after impact. The penetration cases rebound, containment, and perforation are defined in Chapter 1.

Table D-2 Dynamic test result table.

Test no.	v_i [m/s]	T_p [kJ]	F_{dm} [kN]	U_{du} [kJ]	w_{cu} [mm]	w_{cm} [mm]	U_{dm} [kJ]	v_r [m/s]	t_d [ms]	w_{cd} [mm]	w_{cp} [mm]	Penetration	Failure mode
A1-6	3.72	0.382	46.0	0.375	20.3	20.7	0.393	-2.50	13.4	12.2	-	Rebound	No failure
A1-8	4.08	0.459	48.7	0.471	24.3	24.3	0.472	-2.43	13.7	16.2	-	Rebound	No failure
A1-9	4.90	0.666	61.9	0.609	25.3	26.4	0.680	-3.14	13.0	15.6	15.1	Rebound	Failure
A1-5	5.07	0.709	-	-	-	-	-	-	-	-	18.5	Rebound	Shear failure
A1-7	5.98	0.988	59.5	0.673	23.0	30.7	1.005	-2.42	16.1	19.3	-	Rebound	Shear failure
A1-3	6.61	1.206	58.1	0.659	27.1	55.5	1.217	0.84	21.1	55.5	-	Rebound	Shear failure
A1-4	7.08	1.383	69.0	0.990	30.4	42.9	1.328	1.68	10.0	42.9	-	Perforation	Plugging
A1-2	7.33	1.485	-	-	-	-	-	-	-	-	-	Perforation	Plugging
A1-1	7.67	1.624	-	-	-	-	-	-	-	-	-	Perforation	Single petal
A2-9	2.35	0.152	21.2	0.158	17.0	17.2	0.162	-1.60	18.4	9.6	8.9	Rebound	Tensile failure
A2-8	3.38	0.315	33.3	0.328	22.6	22.8	0.327	-2.09	16.6	13.7	-	Rebound	Tensile failure
A2-7	3.38	0.314	27.7	0.245	22.9	26.3	0.329	-1.59	19.6	17.9	-	Rebound	Tensile failure
A2-5	3.47	0.331	29.6	0.316	27.4	28.5	0.346	-1.66	18.9	20.5	-	Rebound	Tensile failure
A2-4	4.74	0.619	-	0.566	32.4	35.7	0.638	-0.60	17.7	34.1	-	Rebound	Tensile failure
A2-6	6.24	1.070	29.2	0.696	39.4	55.7	1.100	-1.08	26.8	48.0	-	Rebound	Four petals
A2-1	6.63	1.209	36.0	0.408	27.0	64.7	1.244	-0.26	25.6	63.8	-	Rebound	Four petals
A2-2	7.33	1.477	37.2	0.376	26.8	134.1	1.507	1.24	54.8	134.0	-	Perforation	Four petals
A2-3	7.85	1.695	40.6	0.486	28.3	116.5	1.493	3.10	26.2	116.4	-	Perforation	Four petals
B1-7	4.78	0.633	54.4	0.644	21.3	21.3	0.645	-2.50	12.4	12.7	-	Rebound	No failure
B1-1	6.39	1.130	77.0	1.141	29.7	29.8	1.146	-3.13	12.1	19.8	-	Rebound	No failure
B1-5	6.78	1.274	83.9	1.286	29.3	29.3	1.290	-3.49	11.5	18.6	-	Rebound	No failure
B1-2	7.12	1.403	90.0	1.420	31.9	31.9	1.420	-3.42	11.5	21.6	20.3	Rebound	No failure
B1-6	7.33	1.487	89.3	1.496	31.7	31.8	1.504	-3.19	12.2	20.7	22.6	Rebound	Failure of stiffener
B1-4	7.62	1.608	89.9	1.376	31.4	34.9	1.627	-3.76	13.0	21.1	-	Rebound	Failure of stiffener
B1-3	8.68	2.084	92.1	1.555	32.2	39.0	2.105	-3.94	13.2	24.2	-	Rebound	Failure of stiffener/top flange
B2-2	4.84	0.647	50.2	0.659	23.0	23.0	0.660	-2.16	12.6	16.4	16.6	Rebound	No failure
B2-1	5.94	0.974	61.0	0.976	27.3	27.6	0.989	-2.69	12.3	19.4	21.7	Rebound	Failure of top flange
B2-6	6.25	1.077	66.2	1.080	29.7	29.9	1.093	-2.90	12.3	21.7	-	Rebound	Failure of top flange
B2-5	6.54	1.181	64.6	1.121	31.1	32.7	1.199	-2.77	15.0	21.3	-	Rebound	Failure of top flange/stiffener
B2-4	6.85	1.296	-	-	-	-	-	-	-	-	-	Rebound	Failure of top flange/stiffener
B2-3	7.44	1.527	68.5	1.150	29.9	37.1	1.547	-3.26	14.1	25.9	-	Rebound	Failure of top flange/stiffener
B2-7	8.58	2.032	61.3	1.050	28.6	45.9	2.057	-3.19	17.3	29.3	-	Rebound	Failure of top flange/stiffener
C1-4	5.47	0.827	60.9	0.838	25.3	25.4	0.841	-2.61	12.6	16.5	18.6	Rebound	No failure
C1-3	6.19 *)	1.060	66.8	0.939	26.2	28.4	1.076	-2.59	13.1	18.6	24.2	Rebound	Shear failure
C1-5	6.19	1.060	71.7	1.074	27.6	27.7	1.075	-3.12	12.8	15.8	-	Rebound	Shear failure
C1-7	6.98	1.348	73.6	1.131	31.7	35.2	1.367	-2.21	14.5	25.8	-	Rebound	Shear failure
C1-2	6.99	1.353	70.1	1.002	27.2	35.3	1.357	0.75	9.3	35.3	-	Containment	Plugging
C1-6	7.72	1.651	72.3	1.142	28.8	37.3	1.467	2.72	7.1	37.3	-	Perforation	Plugging
C1-1	8.28	1.897	69.8	1.101	27.6	36.4	1.478	3.98	5.8	36.4	-	Perforation	Plugging
C2-7	3.47	0.332	34.3	0.339	19.4	19.5	0.343	-2.05	15.2	10.7	11.5	Rebound	No failure
C2-3	4.34	0.520	40.9	0.531	25.4	25.5	0.534	-2.34	14.9	16.6	15.3	Rebound	Failure of top flange
C2-2	5.68	0.891	57.9	0.901	31.2	31.3	0.908	-2.88	13.9	21.1	-	Rebound	Failure of top flange
C2-1	6.22	1.069	65.9	1.076	30.3	30.4	1.085	-3.08	12.9	20.0	-	Rebound	Failure of top flange
C2-4	7.41	1.513	65.4	1.227	37.1	43.1	1.537	-2.08	15.7	35.0	-	Rebound	Single petal
C2-5	8.53	2.008	67.2	1.444	40.0	56.2	2.038	-0.96	22.1	51.4	-	Rebound	Single petal
C2-6	9.57	2.525	59.8	1.104	32.8	68.3	1.959	4.68	10.4	68.3	-	Perforation	Single petal

*) Assumed

Appendix E Dynamic Tests Curves

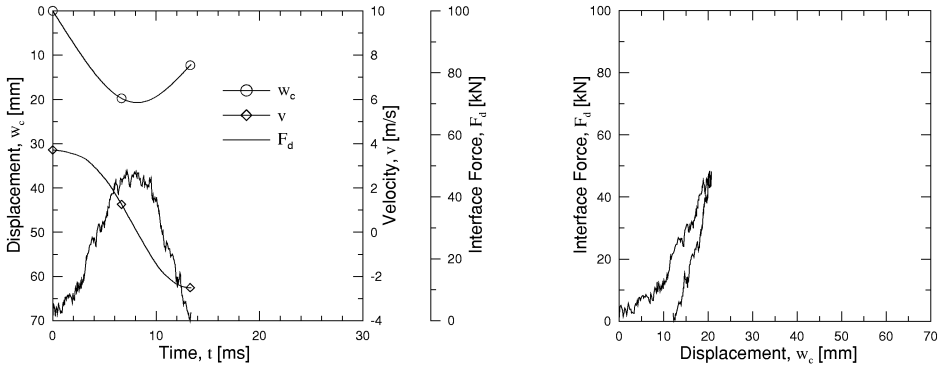

a) Displacement, velocity and force histories *b) Force-displacement curve*

Figure E-1 Test A1-6; $v_i = 3.72\,m/s$ *: No cracks. Rebound.*

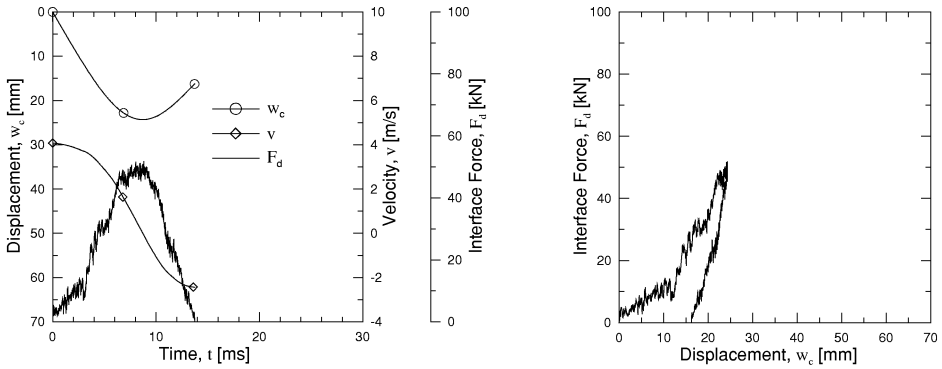

a) Displacement, velocity and force histories *b) Force-displacement curve*

Figure E-2 Test A1-8; $v_i = 4.08\,m/s$ *: No cracks. Rebound.*

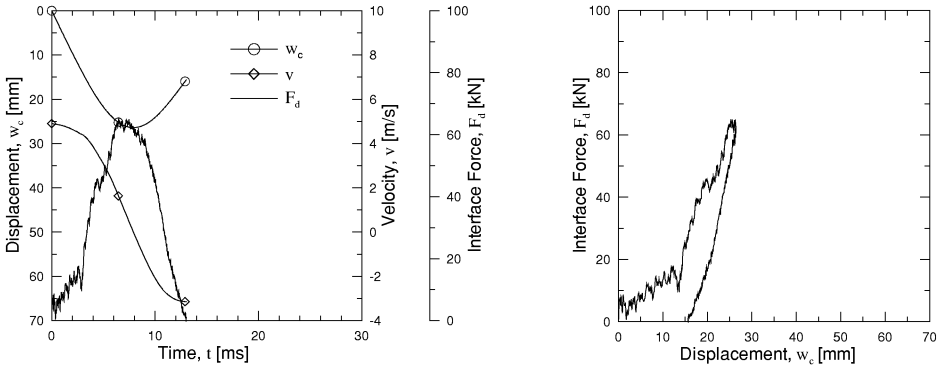

a) Displacement, velocity and force histories *b) Force-displacement curve*

Figure E-3 Test A1-9; $v_i = 4.70\,m/s$ *: Cracks in both fusion lines on the rear side with a length of approximately 100 mm. Orange peeling on the rear side. Rebound.*

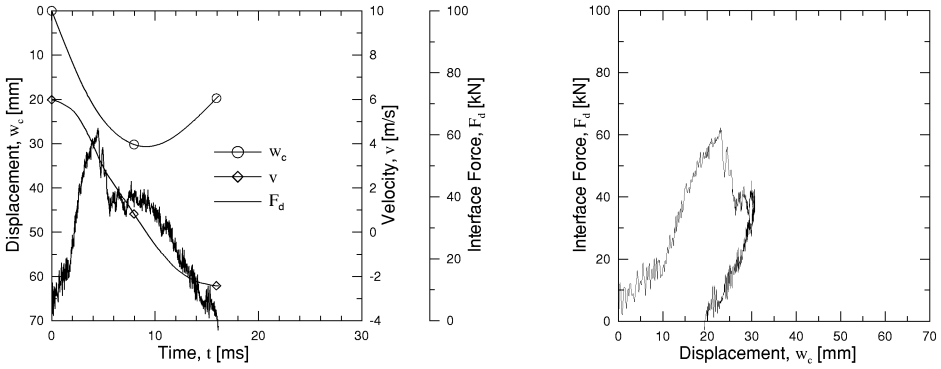

a) Displacement, velocity and force histories *b) Force-displacement curve*

Figure E-4 Test A1-7; $v_i = 6.24\,m/s$ *: Shear failure half way around the nose circumference. Cracks in both fusion lines on the rear side. Orange peeling on the rear side. Rebound.*

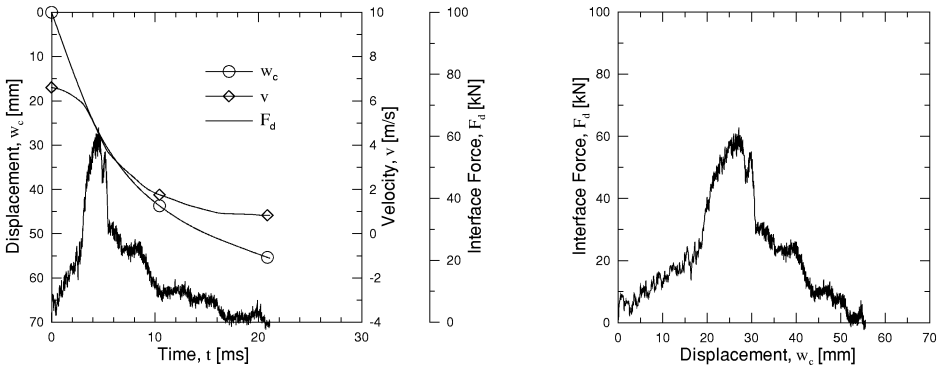

a) Displacement, velocity and force histories *b) Force-displacement curve*

Figure E-5 Test A1-3; $v_i = 6.61\,m/s$ *: Shear failure half way around the nose circumference and cracks in transverse direction with a width of 80 mm. Orange peeling on the rear side. Rebound.*

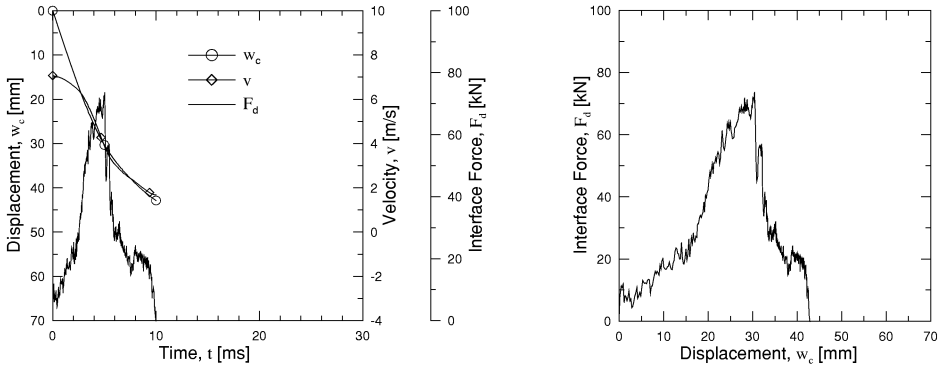

a) Displacement, velocity and force histories *b) Force-displacement curve*

Figure E-6 Test A1-4; $v_i = 7.08\,m/s$*: Plugging. Cracks in the fusion lines. Not completely circular plug. Perforation.*

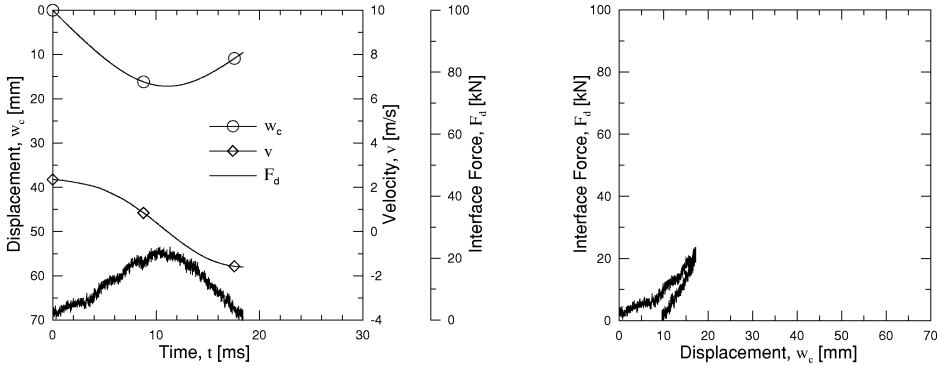

a) Displacement, velocity and force histories *b) Force-displacement curve*

Figure E-7 Test A2-9; $v_i = 2.35\,m/s$*: Cracks in the fusion lines. Rebound.*

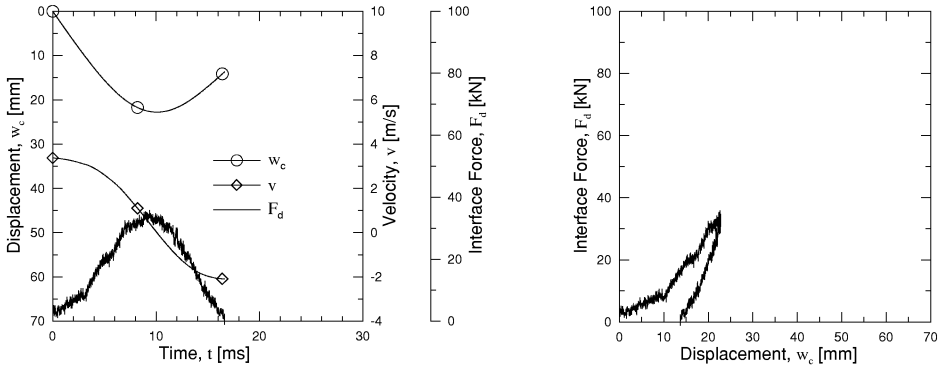

a) Displacement, velocity and force histories *b) Force-displacement curve*

Figure E-8 Test A2-8; $v_i = 3.38\,m/s$*: Cracks in the fusion lines and across the weld between the fusion lines on the rear side (H-crack) and L-crack on the front side. Rebound.*

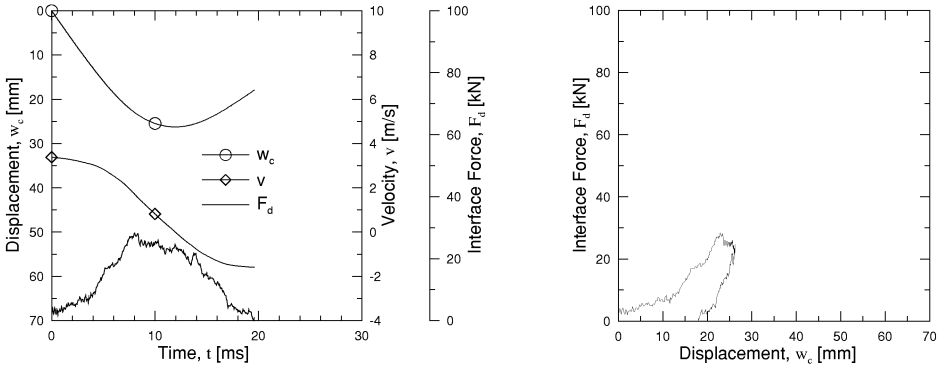

a) Displacement, velocity and force histories *b) Force-displacement curve*

Figure E-9 Test A2-7; $v_i = 3.38\,m/s$: Cracks in the fusion lines and across the weld between the fusion lines on the rear side (H-crack) and L-crack on the front side. Rebound.

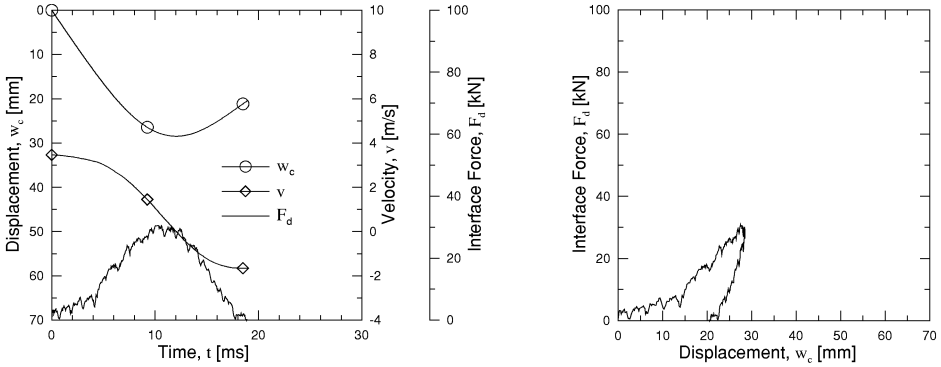

a) Displacement, velocity and force histories *b) Force-displacement curve*

Figure E-10 Test A2-5; $v_i = 3.47\,m/s$: Cracks in the fusion lines and across the weld between the fusion lines on the rear side (H-crack) and L-crack on the front side. Rebound.

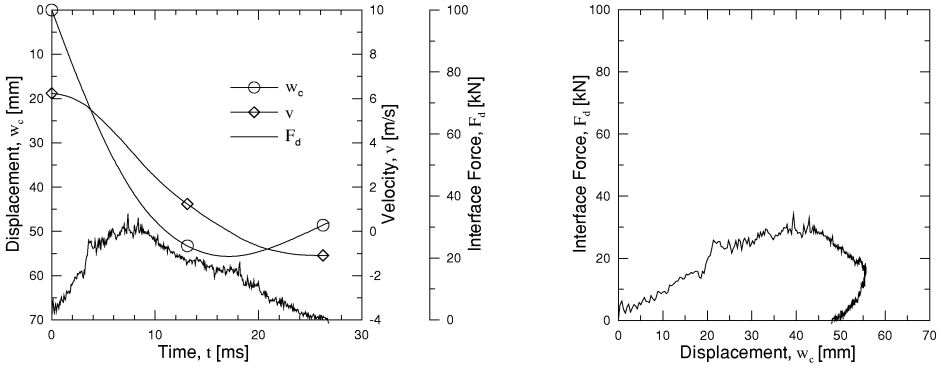

a) Displacement, velocity and force histories *b) Force-displacement curve*

Figure E-11 Test A2-6; $v_i = 6.24\,m/s$: 4 petals. Rebound.

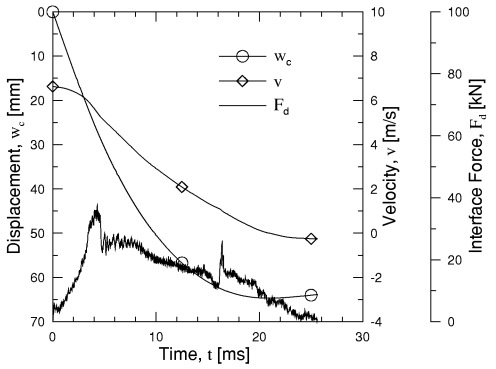

a) Displacement, velocity and force histories

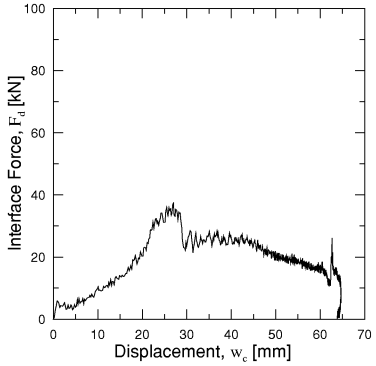

b) Force-displacement curve

Figure E-12 Test A2-1; $v_i = 6.63\,m/s$ *: 4 petals. Rebound.*

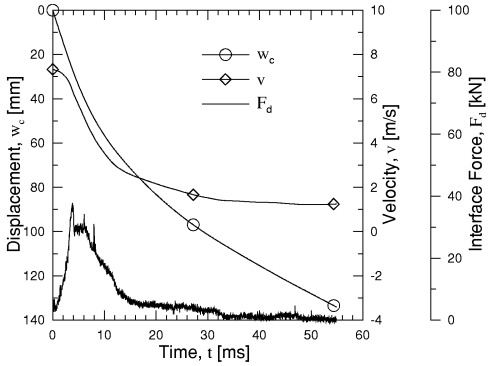

a) Displacement, velocity and force histories

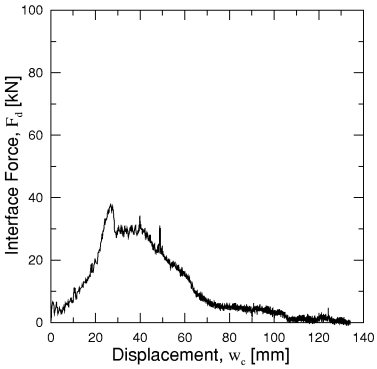

b) Force-displacement curve

Figure E-13 Test A2-2; $v_i = 7.33\,m/s$ *: 4 petals. Perforation.*

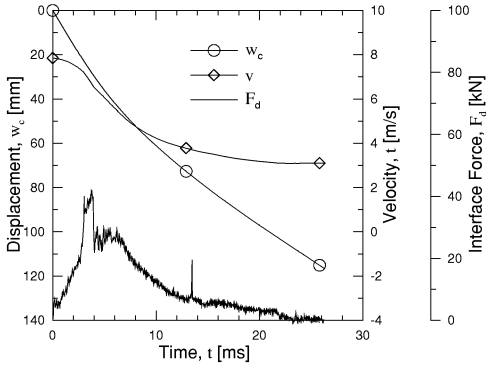

a) Displacement, velocity and force histories

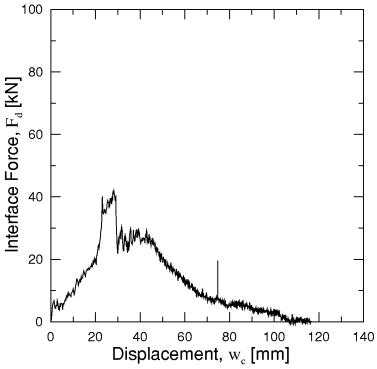

b) Force-displacement curve

Figure E-14 Test A2-3; $v_i = 7.85\,m/s$ *: 4 petals. Perforation.*

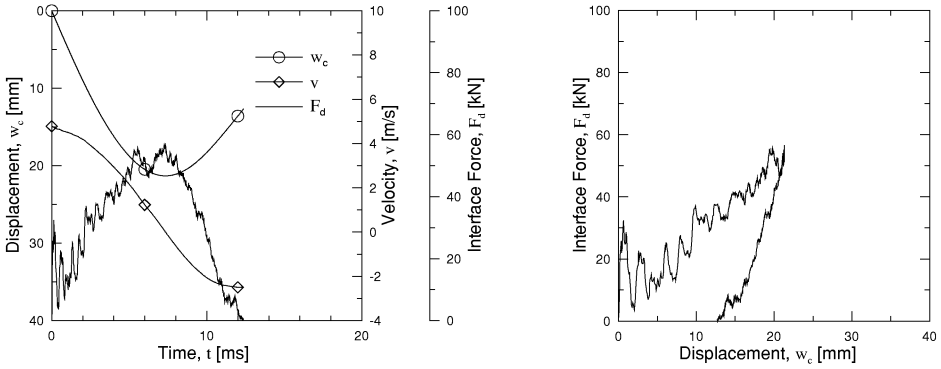

a) Displacement, velocity and force histories *b) Force-displacement curve*

Figure E-15 Test B1-7; $v_i = 4.78\,m/s$*: No cracks. Diffuse necking of the bottom flange. Orange peeling of the bottom flange and lower parts of the web. Rebound.*

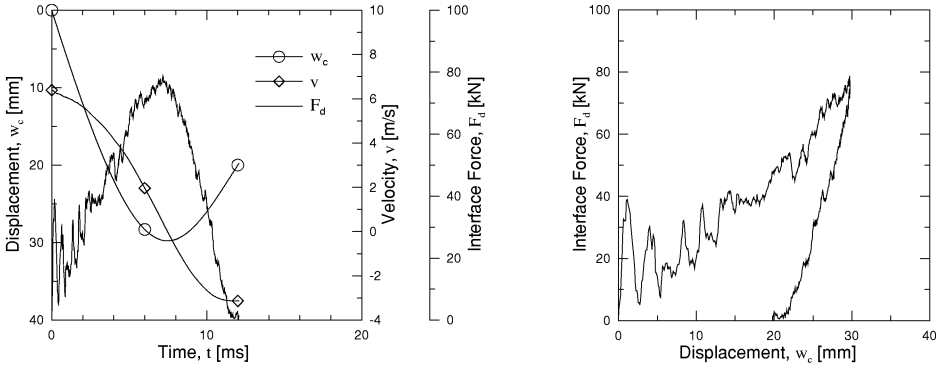

a) Displacement, velocity and force histories *b) Force-displacement curve*

Figure E-16 Test B1-1; $v_i = 6.39\,m/s$*: No cracks. Diffuse necking of the bottom flange. Orange peeling of the bottom flange and lower parts of the web. Rebound.*

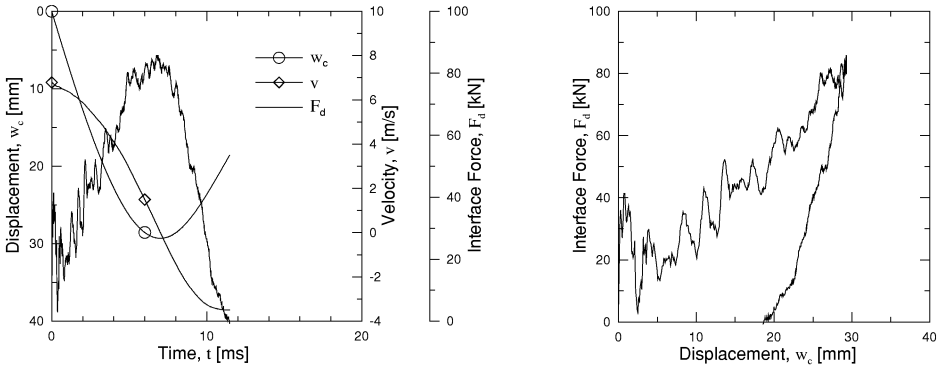

a) Displacement, velocity and force histories *b) Force-displacement curve*

Figure E-17 Test B1-5; $v_i = 6.78\,m/s$*: No cracks. Diffuse necking of the bottom flange. Orange peeling of the bottom flange and lower parts of the web. Rebound.*

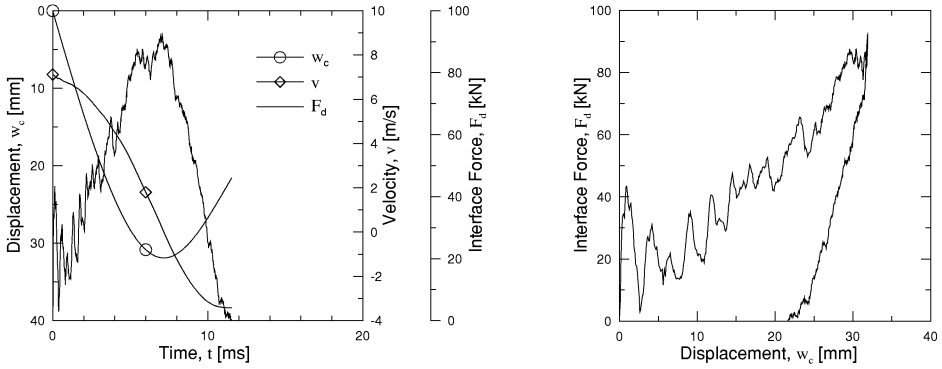

a) Displacement, velocity and force histories *b) Force-displacement curve*

Figure E-18 Test B1-2; $v_i = 7.12\,m/s$*: No cracks. Diffuse necking of the bottom flange (probably just before tensile fracture). Orange peeling of the bottom flange, of lower parts of the web, and of the nose circumference. A flat part of the top flange can be seen. Rebound.*

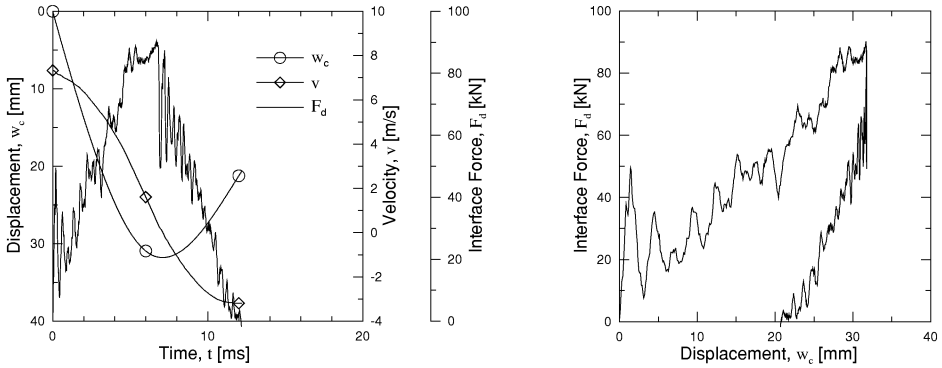

a) Displacement, velocity and force histories *b) Force-displacement curve*

Figure E-19 Test B1-6; $v_i = 7.33\,m/s$*: Tensile fracture of the bottom flange and of the 2/3 lower part of the web. Orange peeling on the rear side around the nose circumference. Rebound.*

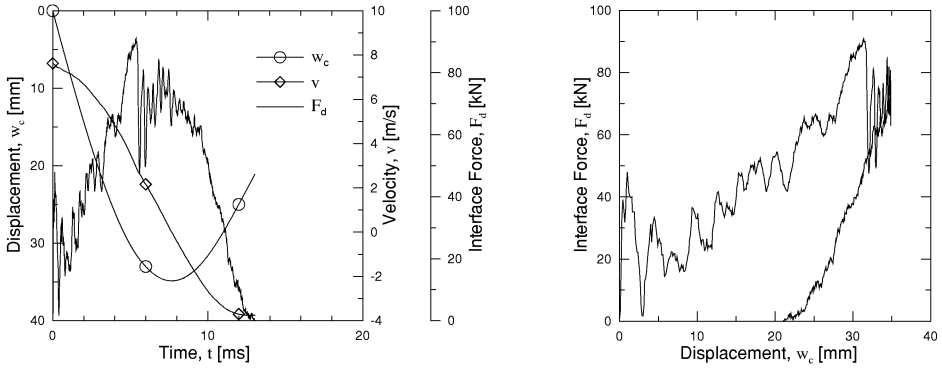

a) Displacement, velocity and force histories *b) Force-displacement curve*

Figure E-20 Test B1-4; $v_i = 7.62\,m/s$*: Tensile fracture of the bottom flange and the web. Orange peeling on the rear side around the nose circumference. Rebound.*

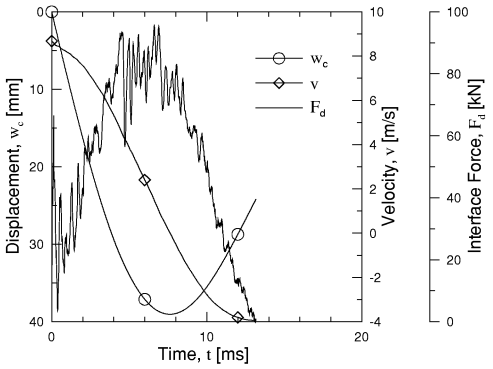

a) Displacement, velocity and force histories

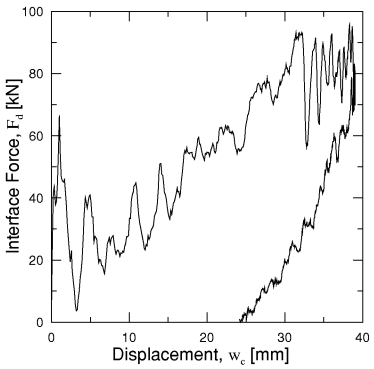

b) Force-displacement curve

Figure E-21 Test B1-3; $v_i = 8.68\,m/s$*: Tensile fracture of the bottom flange and the web. shear failure half way around the nose circumference. Rebound.*

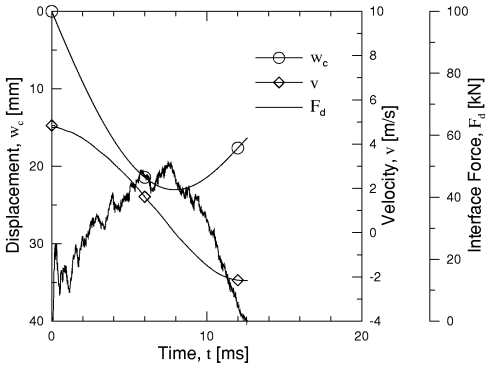

a) Displacement, velocity and force histories

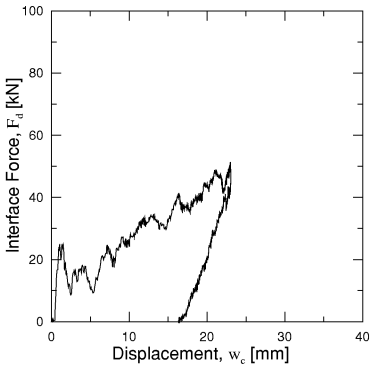

b) Force-displacement curve

Figure E-22 Test B2-2; $v_i = 4.84\,m/s$*: No cracks. Orange peeling of the bottom flange. Bulge. Rebound*

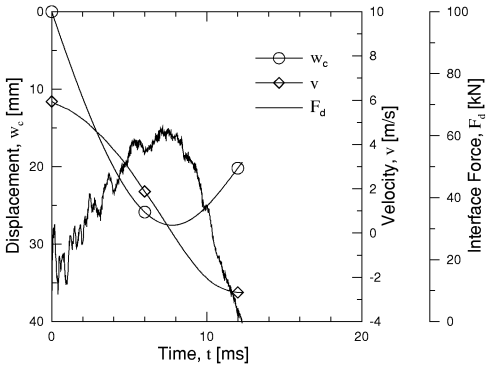

a) Displacement, velocity and force histories

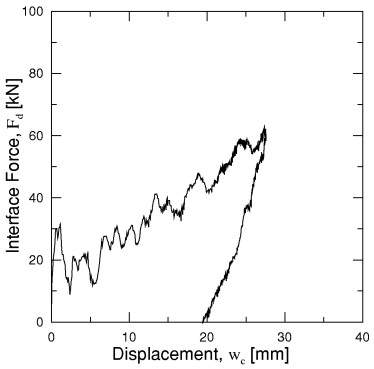

b) Force-displacement curve

Figure E-23 Test B2-1; $v_i = 5.94\,m/s$*: Fracture of the top flange along the web (13 mm). Diffuse necking of the bottom flange. Bulge. Rebound.*

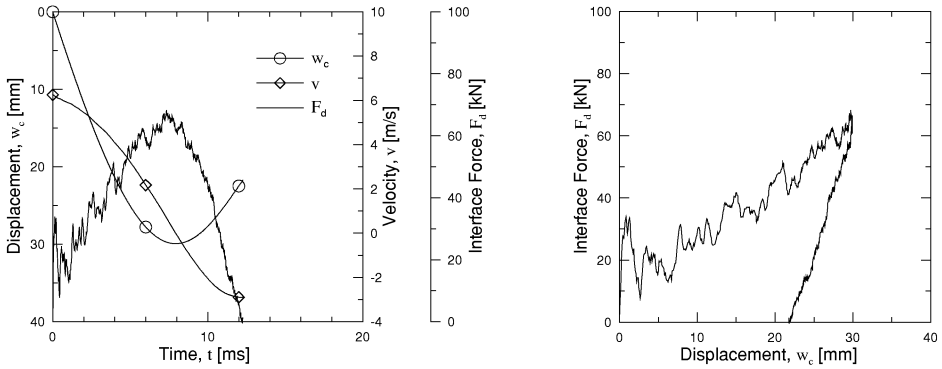

a) Displacement, velocity and force histories *b) Force-displacement curve*

Figure E-24 Test B2-6; $v_i = 6.25\,m/s$*: Fracture of the top flange along the web (20 mm). Diffuse necking of the bottom flange. Bulge. Rebound.*

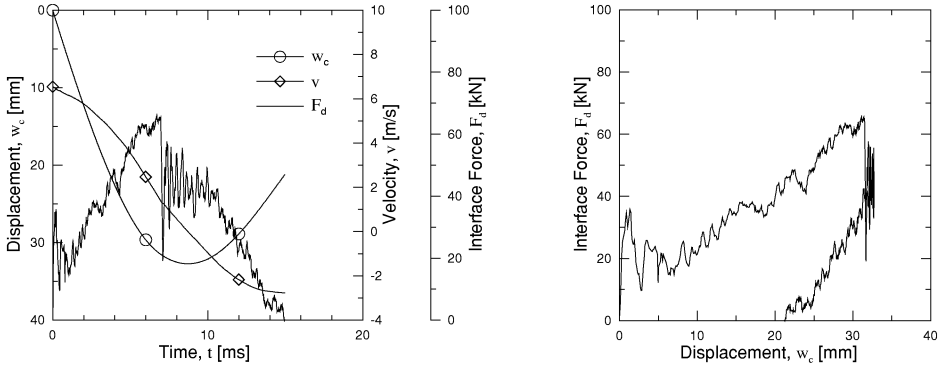

a) Displacement, velocity and force histories *b) Force-displacement curve*

Figure E-25 Test B2-5; $v_i = 6.54\,m/s$*: Fracture of the top flange along the web on both sides of the web (10-15 mm), tensile fracture of the bottom flange. Bulge. Rebound.*

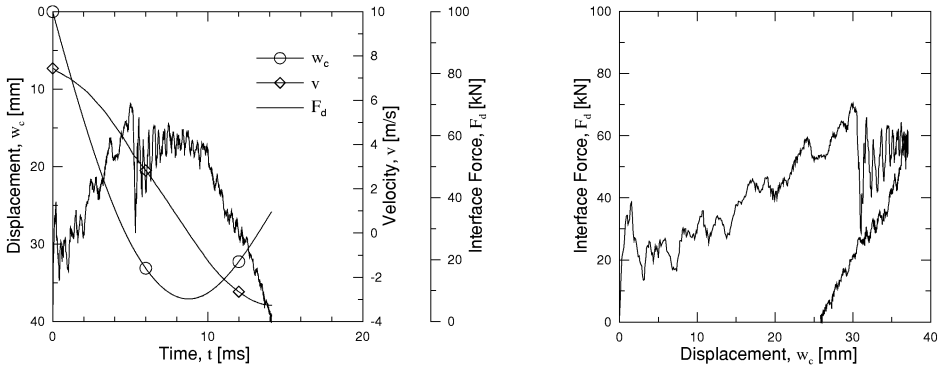

a) Displacement, velocity and force histories *b) Force-displacement curve*

Figure E-26 Test B2-3; $v_i = 7.44\,m/s$*: Fracture of the top flange along the web (38 mm). Tensile fracture of the bottom flange and the web. Bulge. Rebound.*

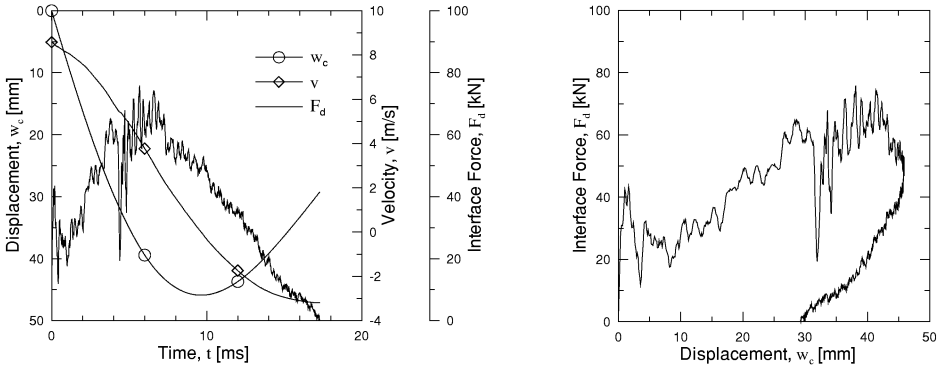

a) Displacement, velocity and force histories *b) Force-displacement curve*

Figure E-27 Test B2-7; $v_i = 8.58\,m/s$*: Fracture of the top flange along the web on both sides of the web (185 and 14 mm). Tensile fracture of the bottom flange and web, but not in the transition zone between the web and top flange. Bulge. Rebound.*

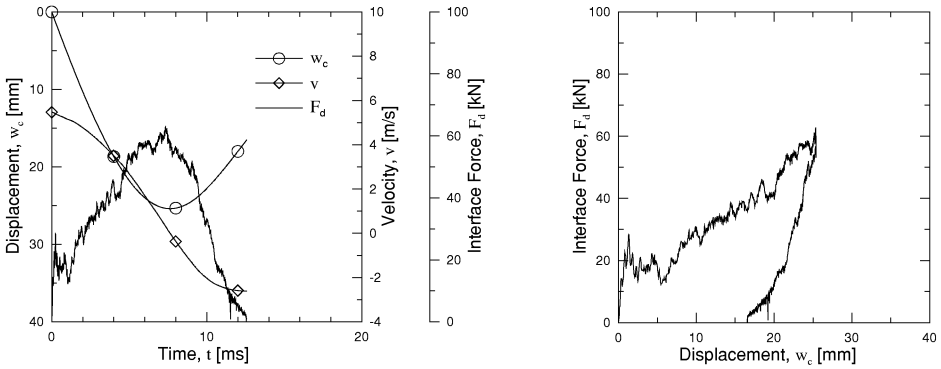

a) Displacement, velocity and force histories *b) Force-displacement curve*

Figure E-28 Test C1-4; $v_i = 5.47\,m/s$*: No fracture. Orange peeling of the bottom flange and around the nose circumference. Rebound.*

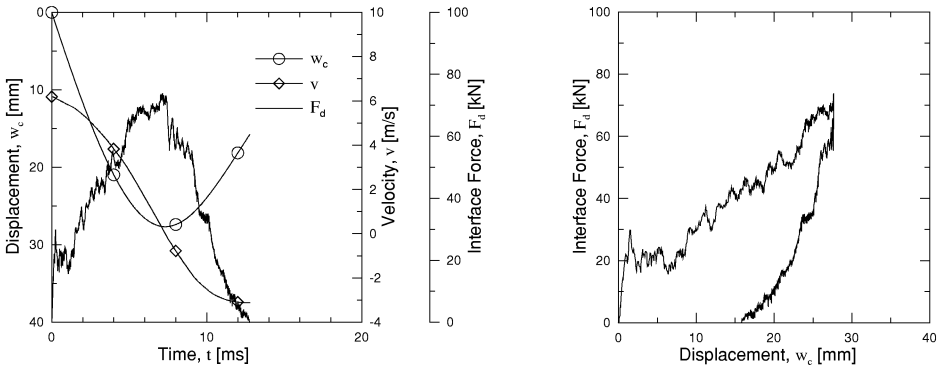

a) Displacement, velocity and force histories *b) Force-displacement curve*

Figure E-29 Test C1-5; $v_i = 6.19\,m/s$*: Shear failure of the top flange a quarter around the circumference of the nose. Diffuse necking of the bottom flange and lateral displacement of the bottom flange. Rebound.*

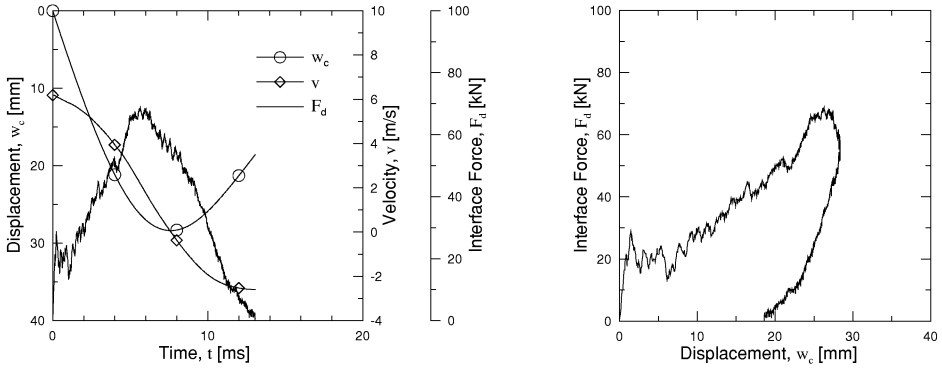

a) Displacement, velocity and force histories *b) Force-displacement curve*

Figure E-30 Test C1-3; $v_i = 6.19\,m/s$ *(assumed): Shear failure of the top flange half way around the nose circumference. Diffuse necking of the bottom flange and lateral displacement of the bottom flange. Rebound.*

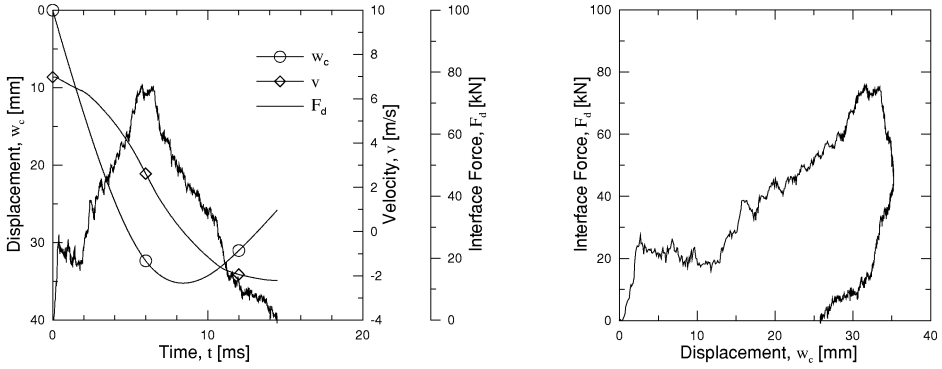

a) Displacement, velocity and force histories *b) Force-displacement curve*

Figure E-31 Test C1-7; $v_i = 6.98\,m/s$*: Shear failure of the top flange half way around the nose circumference. Diffuse necking of the bottom flange and lateral displacement of the bottom flange. Rebound.*

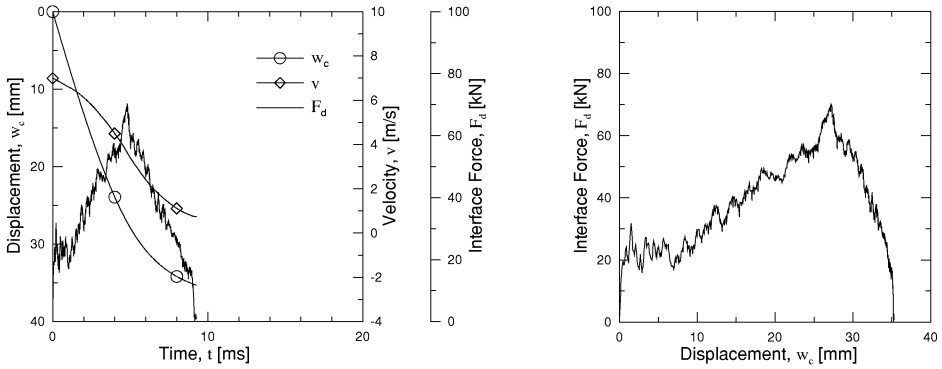

a) Displacement, velocity and force histories *b) Force-displacement curve*

Figure E-32 Test C1-2; $v_i = 6.99\,m/s$*: Plugging. Orange peeling of the top flange around the nose circumference. Diffuse necking of the bottom flange and lateral displacement of the bottom flange. Containment.*

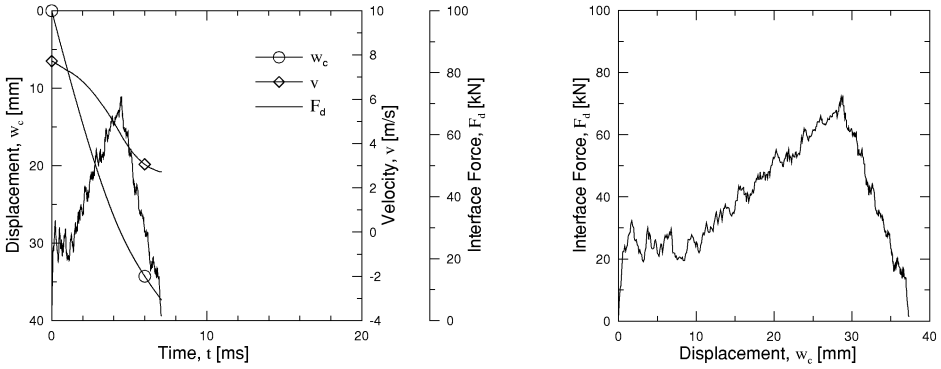

a) Displacement, velocity and force histories *b) Force-displacement curve*

Figure E-33 Test C1-6; $v_i = 7.72\,m/s$*: Plugging. Orange peeling of the top flange around the nose circumference. Diffuse necking of the bottom flange and lateral displacement of the bottom flange. Perforation.*

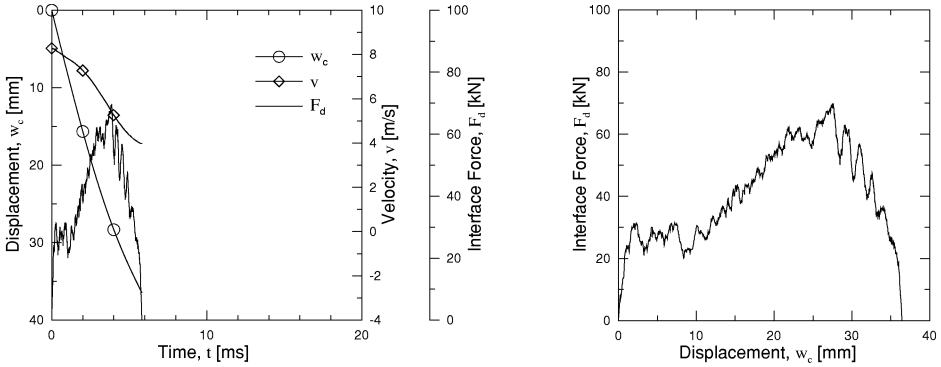

a) Displacement, velocity and force histories *b) Force-displacement curve*

Figure E-34 Test C1-1; $v_i = 8.28\,m/s$*: Plugging. Orange peeling of the top flange around the circumference of the nose. Diffuse necking of the bottom flange and lateral displacement of the bottom flange. Perforation.*

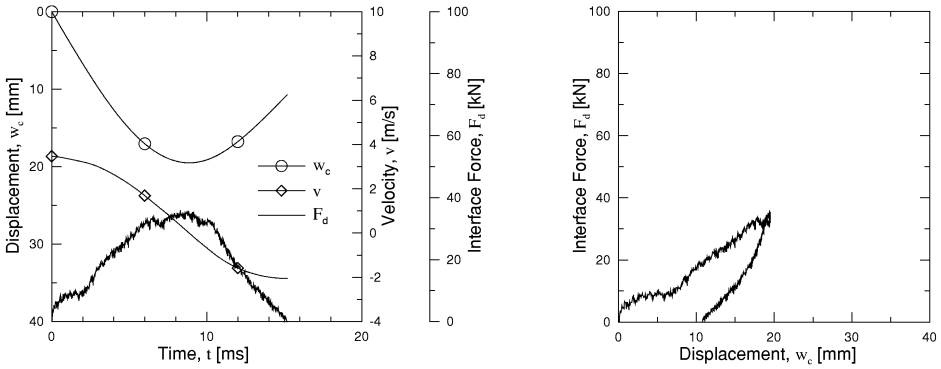

a) Displacement, velocity and force histories *b) Force-displacement curve*

Figure E-35 Test C2-7; $v_i = 3.47\,m/s$*: No fracture. Orange peeling on the rear side. Bulge. Rebound.*

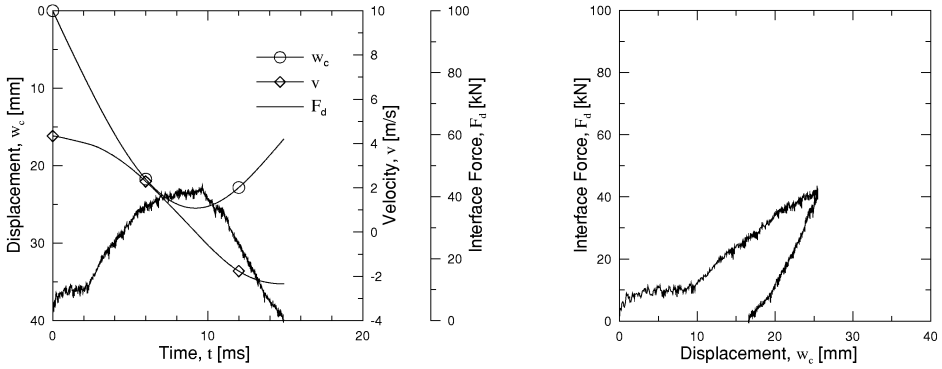

a) Displacement, velocity and force histories *b) Force-displacement curve*

Figure E-36 Test C2-3; $v_i = 4.34\,m/s$*: Fracture lines on the stiffener side of the mid point (11 mm). Orange peeling on the rear side. Bulge. Rebound.*

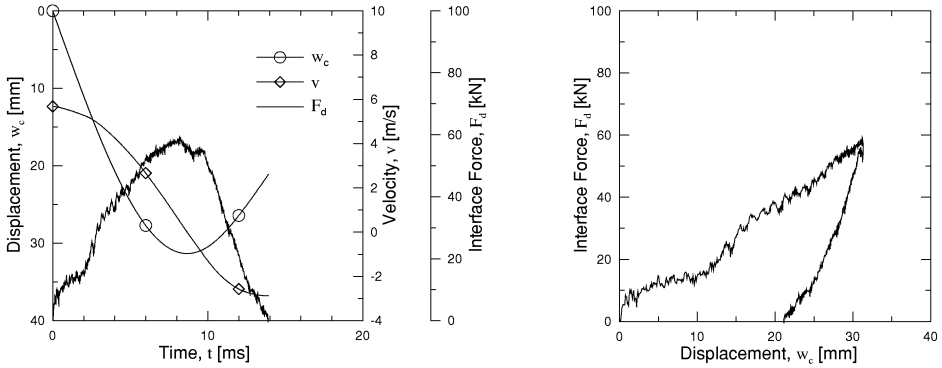

a) Displacement, velocity and force histories *b) Force-displacement curve*

Figure E-37 Test C2-2; $v_i = 5.68\,m/s$*: Fracture lines on both sides of the centre point (17 and 12 mm with a distance of 17.5 mm). Orange peeling on the rear side. Diffuse necking of the bottom flange and lateral displacement of the bottom flange. Bulge. Rebound.*

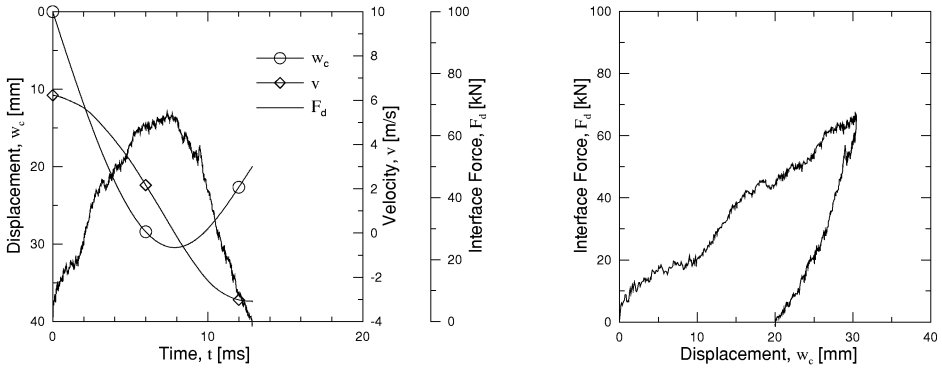

a) Displacement, velocity and force histories *b) Force-displacement curve*

Figure E-38 Test C2-1; $v_i = 6.22\,m/s$*: Fracture lines on both sides of the centre. Orange peeling on the rear side. Diffuse necking of the bottom flange and lateral displacement of the bottom flange. Bulge. Rebound.*

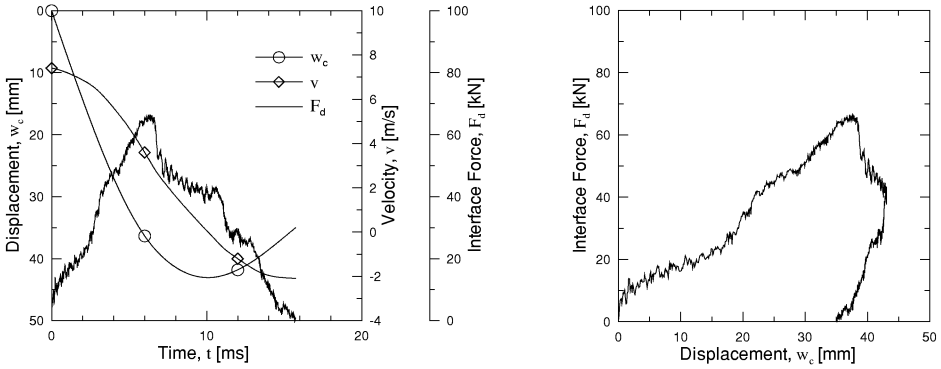

a) Displacement, velocity and force histories *b) Force-displacement curve*

Figure E-39 Test C2-4; $v_i = 7.41 m/s$ *: A single petal. Fracture lines on both sides of the centre point and one of them developed to the petal. Orange peeling on the rear side. Lateral displacement of the bottom flange. Bulge. Rebound.*

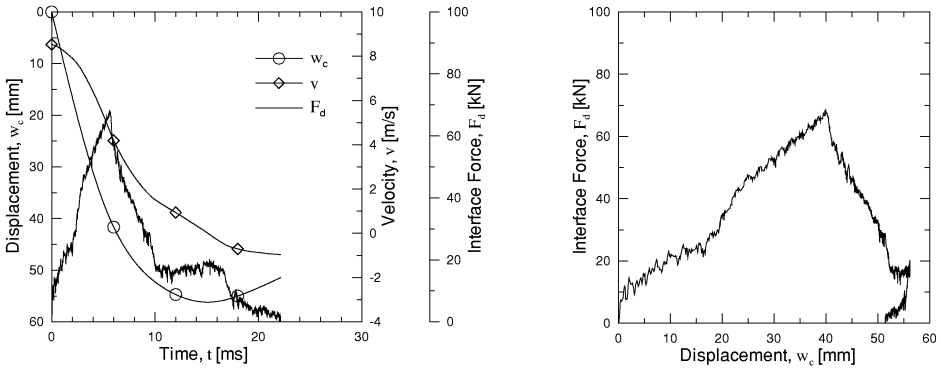

a) Displacement, velocity and force histories *b) Force-displacement curve*

Figure E-40 Test C2-5; $v_i = 8.53 m/s$ *: A single petal. Fracture lines on both sides of the centre point and one developed to the petal. Orange peeling on the rear side. Diffuse necking and lateral displacement of the bottom flange. Bulge. Rebound.*

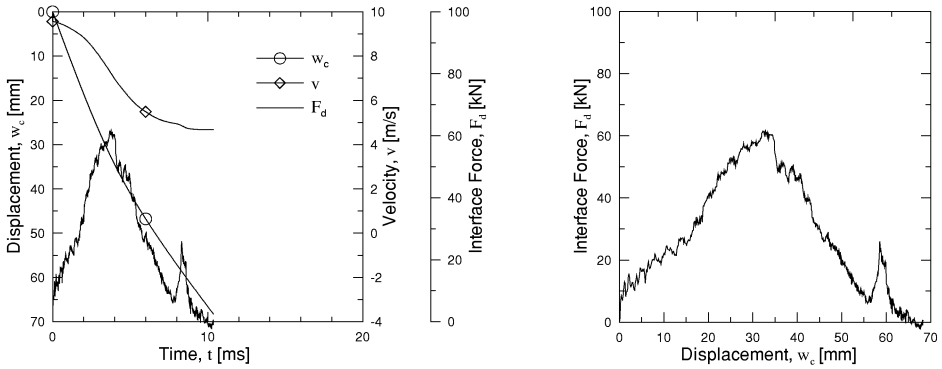

a) Displacement, velocity and force histories *b) Force-displacement curve*

Figure E-41 Test C2-6; $v_i = 9.57\,m/s$*: A single petal and four small petals/cracks. Fracture lines on both sides of the centre point and one of them developed to the petal. Orange peeling on the rear side. Diffuse necking and lateral displacement of the bottom flange. Bulge. Perforation.*

URN:NBN:no-3315

DEPARTMENT OF STRUCTURAL ENGINEERING
NORWEGIAN UNIVERSITY OF SCIENCE AND TECHNOLOGY

N–7491 TRONDHEIM, NORWAY
Telephone: +47 73 59 47 00 Telefax: +47 73 59 47 01

"Reliability Analysis of Structural Systems using Nonlinear Finite Element Methods",
C. A. Holm, 1990:23, ISBN 82-7119-178-0.

"Uniform Stratified Flow Interaction with a Submerged Horizontal Cylinder",
Ø. Arntsen, 1990:32, ISBN 82-7119-188-8.

"Large Displacement Analysis of Flexible and Rigid Systems Considering Displacement-Dependent Loads and Nonlinear Constraints", K. M. Mathisen, 1990:33, ISBN 82-7119-189-6.

"Solid Mechanics and Material Models including Large Deformations",
E. Levold, 1990:56, ISBN 82-7119-214-0, ISSN 0802-3271.

"Inelastic Deformation Capacity of Flexurally-Loaded Aluminium Alloy Structures",
T. Welo, 1990:62, ISBN 82-7119-220-5, ISSN 0802-3271.

"Visualization of Results from Mechanical Engineering Analysis",
K. Aamnes, 1990:63, ISBN 82-7119-221-3, ISSN 0802-3271.

"Object-Oriented Product Modeling for Structural Design",
S. I. Dale, 1991:6, ISBN 82-7119-258-2, ISSN 0802-3271.

"Parallel Techniques for Solving Finite Element Problems on Transputer Networks",
T. H. Hansen, 1991:19, ISBN 82-7119-273-6, ISSN 0802-3271.

"Statistical Description and Estimation of Ocean Drift Ice Environments",
R. Korsnes, 1991:24, ISBN 82-7119-278-7, ISSN 0802-3271.

G. Petkovic, 1991:35

"Turbidity Current Modelling",
B. Brørs, 1991:38, ISBN 82-7119-293-0, ISSN 0802-3271.

"Zero-Slump Concrete: Rheology, Degree of Compaction and Strength. Effects of Fillers as Part Cement-Replacement",
C. Sørensen, 1992:8, ISBN 82-7119-357-0, ISSN 0802-3271.

"Nonlinear Analysis of Reinforced Concrete Structures Exposed to Transient Loading",
K. V. Høiseth, 1992:15, ISBN 82-7119-364-3, ISSN 0802-3271.

"Finite Element Formulations and Solution Algorithms for Buckling and Collapse Analysis of Thin Shells",
R. O. Bjærum, 1992:30, ISBN 82-7119-380-5, ISSN 0802-3271.

"Response Statistics of Nonlinear Dynamic Systems",
J. M. Johnsen, 1992:42, ISBN 82-7119-393-7, ISSN 0802-3271.

"Digital Models in Engineering. A Study on why and how engineers build and operate digital models for decisison support",
J. Høyte, 1992:75, ISBN 82-7119-429-1, ISSN 0802-3271.

"Sparse Solution of Finite Element Equations",
A. C. Damhaug, 1992:76, ISBN 82-7119-430-5, ISSN 0802-3271.

"Some Aspects of Floating Ice Related to Sea Surface Operations in the Barents Sea",
S. Løset, 1992:95, ISBN 82-7119-452-6, ISSN 0802-3271.

"Modelling of Cyclic Plasticity with Application to Steel and Aluminium Structures",
O. S. Hopperstad, 1993:7, ISBN 82-7119-461-5, ISSN 0802-3271.

"The Free Formulation: Linear Theory and Extensions with Applications to Tetrahedral Elements with Rotational Freedoms",
G. Skeie, 1993:17, ISBN 82-7119-472-0, ISSN 0802-3271.

"Høyfast betongs motstand mot piggdekkslitasje. Analyse av resultater fra prøving i Veisliter'n",
T. Tveter, 1993:62, ISBN 82-7119-522-0, ISSN 0802-3271.

"A Nonlinear Finite Element Based on Free Formulation Theory for Analysis of Sandwich Structures",
O. Aamlid, 1993:72, ISBN 82-7119-534-4, ISSN 0802-3271.

"The Effect of Curing Temperature and Silica Fume on Chloride Migration and Pore Structure of High Strength Concrete",
C. J. Hauck, 1993:90, ISBN 82-7119-553-0, ISSN 0802-3271.

"Failure of Concrete under Compressive Strain Gradients",
G. Markeset, 1993:110, ISBN 82-7119-575-1, ISSN 0802-3271.

"An experimental study of internal tidal amphidromes in Vestfjorden",
J. H. Nilsen, 1994:39, ISBN 82-7119-640-5, ISSN 0802-3271.

"Structural analysis of oil wells with emphasis on conductor design",
H. Larsen, 1994:46, ISBN 82-7119-648-0, ISSN 0802-3271.

"Adaptive methods for non-linear finite element analysis of shell structures",
K. M. Okstad, 1994:66, ISBN 82-7119-670-7, ISSN 0802-3271.

"On constitutive modelling in nonlinear analysis of concrete structures",
O. Fyrileiv, 1994:115, ISBN 82-7119-725-8, ISSN 0802-3271.

"Fluctuating wind load and response of a line-like engineering structure with emphasis on motion-induced wind forces",
J. Bogunovic Jakobsen, 1995:62, ISBN 82-7119-809-2, ISSN 0802-3271.

"An experimental study of beam-columns subjected to combined torsion, bending and axial actions",
A. Aalberg, 1995:66, ISBN 82-7119-813-0, ISSN 0802-3271.

"Scaling and cracking in unsealed freeze/thaw testing of Portland cement and silica fume concretes",
S. Jacobsen, 1995:101, ISBN 82-7119-851-3, ISSN 0802-3271.

"Damping of water waves by submerged vegetation. A case study of laminaria hyperborea",
A. M. Dubi, 1995:108, ISBN 82-7119-859-9, ISSN 0802-3271.

"The dynamics of a slope current in the Barents Sea",
Sheng Li, 1995:109, ISBN 82-7119-860-2, ISSN 0802-3271.

"Modellering av delmaterialenes betydning for betongens konsistens",
Ernst Mørtsell, 1996:12, ISBN 82-7119-894-7, ISSN 0802-3271.

"Bending of thin-walled aluminium extrusions",
Birgit Søvik Opheim, 1996:60, ISBN 82-7119-947-1, ISSN 0802-3271.

"Material modelling of aluminium for crashworthiness analysis",
Torodd Berstad, 1996:89, ISBN 82-7119-980-3, ISSN 0802-3271.

"Estimation of structural parameters from response measurements on submerged floating tunnels",
Rolf Magne Larssen, 1996:119, ISBN 82-471-0014-2, ISSN 0802-3271.

“Numerical modelling of plain and reinforced concrete by damage mechanics”,
Mario A. Polanco-Loria, 1997:20, ISBN 82-471-0049-5, ISSN 0802-3271.

“Nonlinear random vibrations - numerical analysis by path integration methods”,
Vibeke Moe, 1997:26, ISBN 82-471-0056-8, ISSN 0802-3271.

“Numerical prediction of vortex-induced vibration by the finite element method”,
Joar Martin Dalheim, 1997:63, ISBN 82-471-0096-7, ISSN 0802-3271.

“Time domain calculations of buffeting response for wind sensitive structures”,
Ketil Aas-Jakobsen, 1997:148, ISBN 82-471-0189-0, ISSN 0802-3271.

"A numerical study of flow about fixed and flexibly mounted circular cylinders",
Trond Stokka Meling, 1998:48, ISBN 82-471-0244-7, ISSN 0802-3271.

“Estimation of chloride penetration into concrete bridges in coastal areas”,
Per Egil Steen, 1998:89, ISBN 82-471-0290-0, ISSN 0802-3271.

“Stress-resultant material models for reinforced concrete plates and shells”,
Jan Arve Øverli, 1998:95, ISBN 82-471-0297-8, ISSN 0802-3271.

URN:NBN:no-3315

“Chloride binding in concrete. Effect of surrounding environment and concrete composition”,
Claus Kenneth Larsen, 1998:101, ISBN 82-471-0337-0, ISSN 0802-3271.

“Rotational capacity of aluminium alloy beams”,
Lars A. Moen, 1999:1, ISBN 82-471-0365-6, ISSN 0802-3271.

“Stretch Bending of Aluminium Extrusions”,
Arild H. Clausen, 1999:29, ISBN 82-471-0396-6, ISSN 0802-3271.

“Aluminium and Steel Beams under Concentrated Loading”,
Tore Tryland, 1999:30, ISBN 82-471-0397-4, ISSN 0802-3271.

"Engineering Models of Elastoplasticity and Fracture for Aluminium Alloys",
Odd-Geir Lademo, 1999:39, ISBN 82-471-0406-7, ISSN 0802-3271.

"Kapasitet og duktilitet av dybelforbindelser i trekonstruksjoner",
Jan Siem, 1999:46, ISBN 82-471-0414-8, ISSN 0802-3271.

“Etablering av distribuert ingeniørarbeid; Teknologiske og organisatoriske erfaringer fra en norsk ingeniørbedrift”,
Lars Line, 1999:52, ISBN 82-471-0420-2, ISSN 0802-3271.

“Estimation of Earthquake-Induced Response”,
Símon Ólafsson, 1999:73, ISBN 82-471-0443-1, ISSN 0802-3271.

“Coastal Concrete Bridges: Moisture State, Chloride Permeability and Aging Effects”
Ragnhild Holen Relling, 1999:74, ISBN 82-471-0445-8, ISSN 0802-3271.

”Capacity Assessment of Titanium Pipes Subjected to Bending and External Pressure”,
Arve Bjørset, 1999:100, ISBN 82-471-0473-3, ISSN 0802-3271.

“Validation of Numerical Collapse Behaviour of Thin-Walled Corrugated Panels”,
Håvar Ilstad, 1999:101, ISBN 82-471-0474-1, ISSN 0802-3271.

“Strength and Ductility of Welded Structures in Aluminium Alloys”,
Miroslaw Matusiak, 1999:113, ISBN 82-471-0487-3, ISSN 0802-3271.

“Thermal Dilation and Autogenous Deformation as Driving Forces to Self-Induced Stresses in High Performance Concrete”,
Øyvind Bjøntegaard, 1999:121, ISBN 82-7984-002-8, ISSN 0802-3271.

“Some Aspects of Ski Base Sliding Friction and Ski Base Structure”,
Dag Anders Moldestad, 1999:137, ISBN 82-7984-019-2, ISSN 0802-3271.

"Electrode reactions and corrosion resistance for steel in mortar and concrete",
Roy Antonsen, 2000:10, ISBN 82-7984-030-3, ISSN 0802-3271.

"Hydro-Physical Conditions in Kelp Forests and the Effect on Wave Damping and Dune Erosion. A case study on Laminaria Hyperborea",
Stig Magnar Løvås, 2000:28, ISBN 82-7984-050-8, ISSN 0802-3271.

URN:NBN:no-3315

"Random Vibration and the Path Integral Method",
Christian Skaug, 2000:39, ISBN 82-7984-061-3, ISSN 0802-3271.

"Buckling and geometrical nonlinear beam-type analyses of timber structures",
Trond Even Eggen, 2000:56, ISBN 82-7984-081-8, ISSN 0802-3271.

”Structural Crashworthiness of Aluminium Foam-Based Components”,
Arve Grønsund Hanssen, 2000:76, ISBN 82-7984-102-4, ISSN 0809-103X.

“Measurements and simulations of the consolidation in first-year sea ice ridges, and some aspects of mechanical behaviour”,
Knut V. Høyland, 2000:94, ISBN 82-7984-121-0, ISSN 0809-103X.

”Kinematics in Regular and Irregular Waves based on a Lagrangian Formulation”,
Svein Helge Gjøsund, 2000-86, ISBN 82-7984-112-1, ISSN 0809-103X.

”Self-Induced Cracking Problems in Hardening Concrete Structures”,
Daniela Bosnjak, 2000-121, ISBN 82-7984-151-2, ISSN 0809-103X.

"Ballistic Penetration and Perforation of Steel Plates",
Tore Børvik, 2000:124, ISBN 82-7984-154-7, ISSN 0809-103X.

"Freeze-Thaw resistance of Concrete. Effect of: Curing Conditions, Moisture Exchange and Materials",
Terje Finnerup Rønning, 2001:14, ISBN 82-7984-165-2, ISSN 0809-103X

"Structural behaviour of post tensioned concrete structures. Flat slab. Slabs on ground",
Steinar Trygstad, 2001:52, ISBN 82-471-5314-9, ISSN 0809-103X.

"Slipforming of Vertical Concrete Structures. Friction between concrete and slipform panel."
Kjell Tore Fosså, 2001:61, ISBN 82-471-5325-4, ISSN 0809-103X.

“Improved Fatigue Performance of Threaded Drillstring Connections by Cold Rolling”,
Steinar Kristoffersen, 2002:11, ISBN: 82-421-5402-1, ISSN: 0809-103X.

"Deformations in Concrete Cantilever Bridges: Observations and Theoretical Modelling",
Peter F. Takâcs, 2002:23, ISBN 82-471-5415-3, ISSN: 0809-103X.

URN:NBN:no-3315

URN:NBN:no-3315